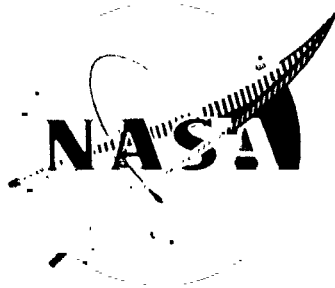


NASA CR-72514
PWA FR-3015



INTERIM REPORT
STUDY OF
INDUCER LOAD AND STRESS

by

H. J. Barten, L. L. Coons, and R. E. Javis

PRAIT & WHITNEY AIRCRAFT
FLORIDA RESEARCH AND DEVELOPMENT CENTER

Prepared for
NATIONAL AERONAUTICS AND SPACE ADMINISTRATION

NASA Lewis Research Center
Contract NAS3-11216
D. D. Scheer, Project Manager

FACILITY FORM 602	N 69-20879	
	<small>(ACCESSION NUMBER)</small>	<small>(THRU)</small>
	153	1
	<small>(PAGES)</small>	<small>(CODE)</small>
	OK 72514	28
	<small>(NASA CR OR TMX OR AD NUMBER)</small>	<small>(CATEGORY)</small>

NOTICE

This report was prepared as an account of Government-sponsored work. Neither the United States, nor the National Aeronautics and Space Administration (NASA), nor any person acting on behalf of NASA:

- A.) Makes any warranty or representation, expressed or implied, with respect to the accuracy, completeness, or usefulness of the information contained in this report, or that the use of any information, apparatus, method, or process disclosed in this report may not infringe privately owned rights; or
- B.) Assumes any liabilities with respect to the use of, or for damages resulting from the use of, any information, apparatus, method, or process disclosed in this report.

As used above, "person acting on behalf of NASA" includes any employee or contractor of NASA, or employee of such contractor, to the extent that such employee or contractor of NASA or employee of such contractor prepares, disseminates, or provides access to any information pursuant to his employment or contract with NASA, or his employment with such contractor.

Requests for copies of this report should be referred to:

National Aeronautics and Space Administration
Scientific and Technical Information Facility
P.O. Box 33
College Park, Md. 20740

NASA CR-72514

PWA FR-3015

INTERIM REPORT

STUDY OF

INDUCER LOAD AND STRESS

by

H. J. Barten, L. L. Coons, and R. E. Davis

PRATT & WHITNEY AIRCRAFT
FLORIDA RESEARCH AND DEVELOPMENT CENTER
BOX 2691, WEST PALM BEACH, FLORIDA 33402

Prepared for

NATIONAL AERONAUTICS AND SPACE ADMINISTRATION

2 April 1969

Contract NAS3-11216

NASA Lewis Research Center
Cleveland, Ohio
D. D. Scheer, Project Manager
Chemical Rockets Division

PRECEDING PAGE BLANK NOT FILMED.

FOREWORD

This interim report presents a summary of the work conducted under the first three tasks of Contract NAS3-11216, by the Florida Research and Development Center of Pratt & Whitney Aircraft, Mr. W. E. Young, Program Manager. The Contract is sponsored by the Lewis Research Center of the National Aeronautics and Space Administration, Cleveland, Ohio, and was administered under the technical direction of the Chemical Rockets Division with Mr. D. D. Scheer, Project Manager. This report covers the period 15 February 1968 to 15 October 1968.

ABSTRACT

A program of analysis, design, fabrication and testing is being conducted to develop computer programs for predicting rocket engine turbo-pump inducer hydrodynamic loading, stress magnitude and distribution, and vibration characteristics. This interim report covers the analysis and design portion of the program. Methods of predicting blade loading, stress, and vibration characteristics were selected from a literature search and used as a basis for the computer programs. A test inducer was designed representative of typical rocket engine inducers and instrumentation was selected to provide measurements of blade surface pressures and stresses for correlation with the prediction system. Subsequent fabrication and testing will be covered in the final report.

CONTENTS

SECTION		PAGE
	TABLES	ix
I	INTRODUCTION	3
II	WORK ACCOMPLISHED	5
	A. Task I - Literature Survey	5
	B. Task II - Formulation of Computer Programs	9
	C. Task III - Design of Test Inducer	90
III	CONCLUDING REMARKS	107
	APPENDIX A - Literature Survey	109
	APPENDIX B - Resumes of Source Material	119
	APPENDIX C - Formulation of Hydrodynamic Computer Program	125
	APPENDIX D - Nomenclature	139

ILLUSTRATIONS

FIGURE		PAGE
1	Distinct Vapor Cavity Forms During Cavitation	11
2	Thickness Distribution of Typical Blade	12
3	Typical Velocity Diagram	14
4	Schematic of Flow Passage	14
5	Semi-Infinite Cascade	15
6	Exponential Decay of Deviation Angle	16
7	Inducer Exit Velocity Diagrams	17
8	Circular Arc Cavity Shape	23
9	Paddle Wheel Geometry and Operating Conditions	24
10	Paddle Wheel Test Case - Radial Equilibrium	24
11	NASA 12-Degree Inducer Noncavitating Head Coefficient vs Flow Coefficient	25
12	NASA 12-Degree Inducer Noncavitating Efficiency vs Flow Coefficient	26
13	Typical Inducer Exit Velocity Triangle	27
14	NASA 12-Degree Inducer Exit Deviation Angle vs Radius	27

ILLUSTRATIONS (Continued)

FIGURE		PAGE
15	NASA 12-Degree Inducer Ideal Total Head Rise Coefficient vs Radius	28
16	NASA 12-Degree Inducer Total Head Loss Coefficient vs Radius	29
17	NASA 12-Degree Inducer Actual Total Head Rise Coefficient vs Radius	30
18	NASA 12-Degree Inducer Efficiency vs Radius	31
19	NASA 12-Degree Inducer Outlet Flow Coefficient vs Radius	31
20	Flat Plate Cascade Cavitation Test Case	32
21	NASA 12-Degree Inducer Head Coefficient vs Net Positive Suction Head	33
22	NASA 12-Degree Inducer Cavitating Performance	34
23	Turbopump Inducer	36
24	Geometric Parameters of Middle Surface of Inducer Blade.	36
25	Local $ \bar{x}, \bar{y}, \bar{z} $ and Common $ x, y, z $ Rectangular Coordinate System for Triangular Element.	37
26	Triangulation of Inducer Blade.	38
27	Generalized Nodal Local Membrane Displacements and Forces On Flat Triangular Element	41
28	Generalized Nodal Bending Displacements and Forces On Flat Triangular Element	41
29	Common Node of 6 Neighboring Triangles.	46
30	Division of System Into Subsystems.	47
31	Definition of Quasi-Normal Coordinate System.	50
32	Geometry for Deriving $\{R_1\}$	54
33	Geometry for Deriving $\{\psi\}_N$	58
34	Geometry for Deriving $\{\psi\}$	59
35	Geometry of Triangular Element With Linearly Varying Thickness	60
36	Generalized Nodal Local Membrane Displacements and Forces On Flat Triangular Element	62
37	Generalized Nodal Bending Displacements and Forces On Flat Triangular Element	65

ILLUSTRATIONS (Continued)

FIGURE		PAGE
38	Generalized Nodal Bending Displacements and Forces On Flat Triangular Element.	67
39	Geometry of Rotating Triangular Element.	69
40	Definition of Quasi-Normal Coordinate System	75
41	Breakup of 45-Degree Sector Into 12 Triangular Elements and 9 Free Nodes.	76
42	Breakup of 45-Degree Sector Into 48 Triangular Elements and 30 Free Nodes	77
43	Radial Displacements In Rotating 45-Degree Sector	77
44	Radial Membrane Stresses In Rotating 45-Degree Sector With 30 Free Nodes.	78
45	Radial Membrane Stresses In Rotating 45-Degree Sector at Midchord	78
46	Transverse Midchord Displacement of Uniformly Loaded 45-Degree Cantilevered Sector	79
47	Radial Bending Stresses In Uniformly Loaded 45-Degree Cantilever Sector With 30 Free Nodes	79
48	Radial Bending Stresses In Uniformly Loaded 45-Degree Cantilevered Sector Midchord 	80
49	Breakup of 2-Inch by 3-Inch Rectangle Into 48 Triangular Elements and 30 Free Nodes	80
50	Radial Displacements In Rotating Rectangle With 30 Free Nodes	81
51	Radial Stresses In Rotating Rectangle With 30 Free Nodes.	81
52	Transverse Midchord Displacement of Uniformly Loaded Cantilever With 30 Free Nodes	82
53	Radial Bending Stress In Uniformly Loaded Cantilever With 30 Free Nodes.	82
54	Breakup of Circular Disk Into 96 Triangular Elements and 48 Free Nodes	83
55	Radial Displacements In 48 Node Spinning Disk.	84
56	Radial and Tangential Membrane Stresses In 48 Node Spinning Disk.	84
57	Breakup of 1-Inch by 2-Inch Rectangular Plate Into 64 Triangular Elements and 40 Free Nodes.	85
58	First Bending Mode of Cantilever Plate	87
59	Second Bending Mode of Cantilever Plate.	87

ILLUSTRATIONS (Continued)

FIGURE		PAGE
60	First Torsion Mode of Cantilever Plate.	88
61	Third Bending Mode of Cantilever Plate.	88
62	Task III Inducer Flow Path and Blade Angle Distribution.	92
63	Task III Inducer Mean Passage Velocity Profile.	93
64	Task III Inducer Noncavitating Performance.	94
65	Task III Inducer Cavitating Performance	95
66	Task III Inducer Design Blade Loading Distribution, 100% Speed, 100% Flow [No Cavity]	96
67	Task III Inducer Design Blade Loading Distribution, 100% Speed, 100% Flow, NPSH = 20 ft [6.1m]	96
68	Task III Inducer Design Blade Loading Distribution, 100% Speed, 100% Flow, NPSH = 65 ft [19.8M].	97
69	Effect of Cavity Shape On Streamline Curvature.	98
70	Task III Inducer Design Stress Level Distribution, 100% Speed, 100% Flow [No Cavity]	99
71	Task III Inducer Design Stress Level Distribution, 100% Speed, 100% Flow, NPSH = 65 ft [19.8M].	99
72	Task III Inducer Design Stress Level Distribution, 100% Speed, 100% Flow, NPSH = 20 ft [6.1m]	100
73	Task III Inducer First Four Vibratory Mode Shapes	101
74	Strain Gage Locations - Blades No. 1, 2, and 3.	102
75	Pressure Scanning Valve In Inducer Hub.	103
76	Schematic of Pressure Scanning Valve	10
77	Pressure Tap Locations - Blades 1 and 2	104
78	Miniature Transducer Locations - Blade No. 3	105
79	Inducer Test Rig.	106

TABLES

TABLE		PAGE
I	Comparison of Exact and Computed Modes and Natural Frequencies of 1 by 2 by 0.1 in. Thick Cantilevered Rectangular Steel Plates.	86
II	Mode Shapes and Comparison of Natural Frequencies of 6-Degree (0.105-rad) Inducer	89
III	Basic Design Parameters.	91

SUMMARY

Cavitating inducers are widely used in rocket engine turbopump designs to prevent cavitation in the pump main stages. This results in higher turbopump operating speeds and/or reduced pump inlet pressure requirements. Inducer hydrodynamic performance can be accurately predicted from empirical loss and deviation data. The prediction of operating stresses presents a problem, however, because (1) there is a lack of information on blade pressure loading and (2) the complexity of the inducer blade shape prevents simple steady and vibratory stress analysis. Consequently, inducer mechanical design is usually based on several approximations, with liberal safety factors being applied. This approach results in relatively heavy inducers with undesirably thick blades.

This study was therefore undertaken to provide analytic tools, in the form of computer programs, for the prediction of (1) design and off-design hydrodynamic blade loading under cavitating and noncavitating conditions, (2) stresses due to hydrodynamic and centrifugal loading, and (3) blade resonant frequencies and relative stress distribution. The study consists of (1) a literature survey to establish the current state-of-the-art, (2) formulation of computer programs and correlation with existing data, (3) design and fabrication of a test inducer and test rig, (4) a test program in which blade pressures, resonant frequencies, and stresses are measured and compared with predictions, and (5) development of the computer programs based on the test results.

The literature survey, analytic formulations, and test rig designs have been completed and the results are presented in this report. Inducer internal flow was calculated from a mean streamline analysis using finite increments. Stress and vibration characteristics were calculated using a matrix analysis of finite triangular elements.

Computer program predictions were compared with experimental data or exact solutions for inducer cavitating and noncavitating performance, inducer resonant frequencies, cantilevered plate resonant frequencies, inducer stress (bladder between blades), and flat plate stress. The correlation was satisfactory in all cases.

An inducer and test rig were designed with provisions for measurement of blade steady and vibratory pressures with resultant steady and vibratory strains. These data will later be compared with computer program predictions for further refinement of the programs.

PRECEDING PAGE BLANK NOT FILMED

SECTION I
INTRODUCTION

Inducers are universally used as the first stage in liquid rocket engine turbopumps because of the weight reduction and performance gains they provide. Inducers can operate at low inlet pressures, reducing the required propellant tank pressure. Low tank pressures mean lighter propellant tanks. At the same time, the inducer supplies the main stage of the turbopump with a much higher pressure than is possible by tank pressurization, thus allowing the turbopumps to operate at much higher speeds. Higher turbopump speeds mean lighter and more efficient pumps. As might be expected, the inducer must pay the penalty for the advantages realized by the engine system. Because of the low tank pressures, the inducer must operate almost continuously in a state of partial cavitation while still providing the necessary head rise. When operating with inlet pressures high enough to prevent cavitation, blade steady stresses become severe. As inlet pressure is lowered and a vapor cavity forms, the steady stresses are reduced. However, the collapse of the vapor cavity is often violent and unstable, resulting in fluctuating blade loads that can cause blade fatigue failure.

Inducer hydrodynamic design has been refined through the correlation of empirical data with design theory to the point where excellent performance, i.e., head rise, efficiency and suction capabilities, can be accurately predicted and achieved. However, in the area of mechanical or structural design, the state-of-the-art has not kept pace, and it is this lack of advance that may limit further improvements in hydrodynamic performance. The reason for this is (1) the inability of existing design tools to accurately predict the blade loadings that occur in the inducer from pressure and centrifugal forces and (2) the absence of a satisfactory method of predicting the stresses that result even were these forces known. As a consequence, the inducer blades must be designed conservatively, i.e., overly thick, to ensure that failure will not occur during engine operation. The blade thickness directly affects the blockage in the inducer inlet and is detrimental to inducer suction performance.

It was this deficiency in rocket engine inducer design that led to the initiation of Contract NAS3-11216, "Study of Inducer Loads and Stresses." The objective of this contract work is to develop computer programs that can accurately predict inducer blade pressure distributions and resonant frequencies, along with their resultant stresses. The combined analytical and experimental effort is divided into the following six tasks:

- I. Literature Survey
- II. Formulations of Analytical Models and Computer Programs
- III. Hydrodynamic and Mechanical Design of Test Inducer
- IV. Detailed Design of Test Inducer
- V. Fabrication of Test Hardware
- VI. Experimental Testing and Computer Program Verification.

This interim report covers the work performed in the first three tasks of the program, the results of which are discussed in detail.

PRECEDING PAGE BLANK NOT FILMED

SECTION II
WORK ACCOMPLISHED

A. TASK I - LITERATURE SURVEY

1. General

A literature survey was conducted to determine the current state-of-the-art in the following aspects of inducer structural design:

1. Methods used in the prediction of design and off-design hydrodynamic loading under cavitating and noncavitating conditions
2. Methods used in the prediction of stresses due to hydrodynamic and centrifugal loading
3. Methods used in the prediction of inducer blade resonant frequencies and associated stress distributions

These methods were selected based on the following criteria:

1. Comprehensiveness - ability to account for important physical characteristics (geometric and hydrodynamic)
2. Simplicity - practical design tool
3. Success of similar methods in other applications
4. Availability of empirical substantiation.

As will be noted in the subsequent discussion, it became necessary or desirable to modify some methods and combine attractive features of others to more adequately satisfy these criteria.

The literature survey was conducted through the library facilities of United Aircraft Corporation and the Defense Documentation Center. From these sources, approximately 1800 abstracts were collected, of which over 100 were found to be pertinent to the work requirements of the program. These selected abstracts were categorized and are presented in Appendix A under the following main headings.

Section 1 - Blade Hydrodynamic Loading Under Cavitating and Noncavitating Conditions

Section 2 - Blade Stresses (Stresses in Curved Plates)

Section 3 - Blade Vibrations (Vibrations of Curved Plates)

Resumes of those articles from which material was drawn are presented in Appendix B.

2. Hydrodynamic Loading of Inducer Blades

Exact, approximate, and experimental methods can be used in defining flow through inducer passages. Examples of each of these methods are presented below.

a. Exact Methods

Exact methods may employ conformal mapping techniques for solution of the exact potential flow equations. This type solution is for ideal or no-loss flow and normally is solved only for a two-dimensional flow field. Examples of solutions to specific cases have been presented by several authors. Exact solutions for single case flow between flat plate cascades was presented by von Karman and Burgers (Reference 1). Stripling and Acosta (Reference 2) extended the potential flow flat plate theory to include the effects of cavitation. Fanti (Reference 3) presents the modified flat plate theory to exactly account for potential flow about airfoils of arbitrary shape in an arbitrary cascade. Jakobsen (Reference 4) presents the most general of the exact cascade flow theory by accounting for varying airfoil shape and complete cavitation. However, he only presents solutions for flat plates and circular arc airfoils.

b. Approximate Methods

The term "approximate method" used here refers to methods that give an approximate analytical description of a three-dimensional flow field. These methods could be divided into two subgroups referred to as three-dimensional and quasi-three-dimensional methods. A three-dimensional approximate method may employ a numerical relaxation or finite difference solution of the potential flow equations. A quasi-three-dimensional solution may involve either a two-dimensional finite difference solution to the basic flow equations with an assumed solution in the third dimension or a one-dimensional solution with assumed solutions in the other two dimensions.

The finite difference solution of the basic flow equations is a standard method. This type solution has been used by Stanitz (Reference 5), Stockman (Reference 6), and Cooper (Reference 7) among others. Stanitz and Stockman present quasi-three-dimensional solutions whereas Cooper presents both three-dimensional and quasi-three-dimensional solutions. Loss calculations can easily be incorporated into methods involving a finite difference solution of a potential flow field. This type solution applies equally well to either cavitating or noncavitating flow.

The most general type solution between the exact and approximate solutions is the three-dimensional approximate solution because of its ability to describe completely a flow field in three dimensions, including the effects of three-dimensional flow, cavitation and flow losses. It was found, however, in Reference 7 that use of a three-dimensional approximate model (referred to as "exact" in that reference) required such large quantities of computer time that it would not be practical to consider it for use in the present inducer stress design system. A quasi-three-dimensional solution was found to execute much more rapidly on the computer, as stated in Reference 7. It is noted, however, that in models such as this one, flow incidence effects on blade loading in the region of the blade leading edge have not always been properly considered.

Therefore, in the hydrodynamic portion of the Task II effort the quasi-three-dimensional analysis was used for defining the flow field within the inducer passage while using the results of exact potential flow solu-

tions for defining the flow field on and near the blade leading edge. The complete hydrodynamic model will solve both cavitating and noncavitating flow problems accounting for leading edge/flow incidence effects and internal flow losses.

c. Experimental Methods

Experimental methods in general rely heavily on particular test results for use in analysis. Although these techniques are generally less complex in nature, their uses are restricted to specific machines and flow conditions. Because of these restrictions these methods were not considered for use as prediction methods in this program. However, they may be useful later in Task II for making comparisons between the loadings predicted by the computer program and experimental data.

3. Stresses and Vibrations in Inducer Blades

Stresses and vibrations in inducers with idealized geometry such as constant helix angle, hub diameter, and blade thickness can probably be determined by classical methods similar to those discussed by Wan (Reference 8), Reissner (Reference 9), and Knowles (Reference 10). Varying geometry that is used in conventional inducers would prevent the use of classical methods because of the increase in the number of variables, and approximate numerical methods are the only practical alternative. A survey of the literature indicates that matrix analysis of finite elements should be applicable to the inducer problem, using existing digital computer techniques.

In the finite element analysis, the object is divided into polygonal elements, usually rectangles or triangles, and internal distributed forces are replaced by statically equivalent forces at element nodes. By selection of appropriate displacement polynomials, the stiffness matrix, which associates the nodal forces with nodal displacements, can be obtained. This matrix depends upon the geometry of the element, and for the inducer, selection of a base element in the shape of a flat triangle would be practical. The change in the directions of the normals of these base elements will then account for blade curvature. Techniques for handling triangular elements that are variable in direction are discussed by Argyris for elements under membrane loading (Reference 11) and McGrattan and North (Reference 12). Although the latter paper involves vibrations, its application to elements in three dimensions is pertinent to the inducer stress program.

a. Stresses in Inducer Blades

Stiffness matrices for triangles can be obtained by direct methods, as discussed by Turner, Clough, and Topp (Reference 13), or by conventional strain energy methods as discussed by Utku (Reference 14) and others. An analytical expression for the stiffness matrix of an arbitrarily shaped triangle is very cumbersome and it is more practical to obtain its numerical elements on a computer by consideration of the strain energy. This matrix will yield the relation between nodal forces and displacements associated with the triangle. Because of blade curvature, normals of the base triangular elements will not lie in the same direction and the stiffness matrices must be transformed to correspond

to a common direction. This technique is discussed in detail in Reference 11. After they are transformed, the summation of nodal forces to zero and the equating of nodal displacements at common nodes yields a set of simultaneous displacement equations. The values for displacements are then used to determine stresses. External load conditions in this instance are pressure loading and centrifugal loading.

b. Vibrations of Inducer Blades

After the stiffness matrix is obtained, the frequency equation and nodes can be obtained by consideration of the matrix equation of motion as discussed by McGrattan and North (Reference 12). This will involve a determination of the flexibility matrix, which can be obtained by inversion of the stiffness matrix on the computer.

Similar means have been used by divisions of United Aircraft Corporation to calculate frequencies and node shapes for radial impellers. Results agree well with experimental test data.

4. References

1. Durand, W. F., "Flow Through a Lattice Composed of Air Foils," p 91-96. Aerodynamic Theory, Volume II (General Aerodynamical Theory - Perfect Fluids by T. von Karman and J. M. Burgers. First Edition, 1963.)
2. Stripling, L. B., and A. J. Acosta, "Cavitation in Turbopumps," ASME - Papers 61-WA-112 13 p. 61-WA-98 11 p for meeting Nov 26-Dec 1 1961. Paper WA-112 (Pt. 1).
3. Fanti, R., "Elementary Incompressible Solution for the Performance of Airfoils of Arbitrary Shape in an Arbitrary Cascade," United Aircraft Corporation Research Department, Report R-23010-12, Feb 23, 1953.
4. Jakobsen, J. K., "Supercavitating Cascade Flow Analysis," Trans ASME, J1 of Basic Engineering, Dec, 1964, p. 805-814.
5. Stanitz, J. D., "Some Theoretical Aerodynamic Investigations of Impellers in Radial - and Mixed-Flow Centrifugal Compressors," ASME Gas Turb Power Fall Meeting, Minneapolis, September 1951. Paper 51-F-13, 25 pp. -- Trans. ASME 74, 4, 473-497, May 1952.
6. Stockman, N. O., and J. L. Kramer, "Method for Design of Pump Impellers Using a High Speed Digital Computer," NASA TN D-1562, 1963.
7. Cooper, P. and H. B. Bosch, "Three-Dimensional Analysis of Inducer Fluid Flow," NASA CR-54836, February 11, 1966.
8. Wan, F. Y. M., "A Class of Unsymmetrical Stress Distributions in Helicoidal Shells," Quarterly of Applied Mathematics, Volume 24, November 4, 1967.

9. Reissner, E., "On Finite Twisting and Bending of Circular Ring Sector Plates and Shallow Helicoidal Shells," Quarterly of Applied Mathematics, Volume 11, 1963, p 473-483.
10. Knowles, J. K., and E. Reissner, "Torsion and Extension of Helicoidal Shell," Quarterly of Applied Mathematics, Volume 17, p 409-422, 1959.
11. Argyris, J. H., "Recent Advances in Matrix Methods of Structural Analysis," Progress in Aeronautical Sciences, Volume 4, The Macmillan Company, 1964.
12. McGrattan, R. J., and E. L. North, "Vibration Analysis of Shells Using Discrete Mass Techniques," Transactions of ASME, November 1967, p 766-772.
13. Turner, M. J., R. W. Clough, H. C. Martin and L. J. Topp, "Stiffness and Deflection Analysis of Complex Structures," Journal of the Aeronautical Sciences, Volume 25, No. 9, September 1956, p 805-823.
14. Utku, S., "Stiffness Matrices for Thin Triangular Elements of Nonzero Gaussian Curvature," AIAA Journal, Volume 5, No. 9, September 1967, p 1659-1667.

B. TASK II - FORMULATION OF COMPUTER PROGRAMS

1. Computer Program for Predicting Hydrodynamic Loading Under Cavitating and Noncavitating Conditions
 - a. Introduction

To predict inducer blade stresses under cavitating and noncavitating conditions, it is first necessary to obtain the pressure distribution on the surfaces of the blades. The pressure differential across the blade causes a normal force called the hydrodynamic loading. If this information is available from tests, then the hydrodynamic loading can be combined with the centrifugal loading on the blades to predict the blade stresses.

This test information is usually not available. It is known, however, that a large proportion of the blade stress in inducers is caused by the hydrodynamic loading. Therefore, it is essential that accurate methods for predicting the blade hydrodynamic loadings be used. At present, there are no known accurate methods available for calculating pressure distributions on the blade surface. As a part of Task II, a computer program for the prediction of hydrodynamic loading, under cavitating and noncavitating conditions, has been formulated and programmed.

b. Description of Analytical Model

(1) Basic Flow Model

The basic flow model selected as a result of the Task II literature survey is a mean streamline, two-dimensional meridional flow model. It is assumed that the average flow conditions in the blade-to-blade space can be represented on a meridional surface so that only a two-dimensional, streamline balancing relaxation analysis is required to establish mean velocities, pressures, and flow angles.

The relationship for the angle of the flow relative to the blade angle and the flow path hub and tip contour are established by appropriate assumptions concerning the deviation caused by inlet loading (incidence) and trailing edge unloading (normally called the deviation). Another deviation of the flow angle from the blading angle is caused by the formation of a cavity.

Superimposed upon the meridional flow is an assumed form of solution for the blade-to-blade flow conditions. In the selected model, it is assumed (1) that the pressure differential across the flow passage (i.e., from blade to blade) can be determined by the conservation of angular momentum of the fluid flow and (2) that the average flow conditions are found from the meridional analysis.

(2) Viscous Effects

The effects of viscosity include (1) boundary layer growth, which tends to block the flow passage to change the work input capability of the inducer and increase the exit dumping loss, and (2) friction on the walls of the flow passage, which reduces the bulk or freestream total pressure. Thus, the viscosity of the fluid affects both the head input and head output.

(3) Cavitation Effects

A second nonideal fluid characteristic is the vaporization of the fluid when the local pressure reaches saturation pressure. In the selected model, it is assumed that the fluid will vaporize whenever the fluid reaches some critical value of pressure. Furthermore, this value is assumed to be constant and equal to the equilibrium saturation pressure of the bulk fluid at the inlet to the inducer. There are no effects of transient heat transfer processes or of local subcooling of the liquid to suppress the cavitation.

The assumption is made that the liquid and vapor are separated by centrifugal effects both in the meridional surface and in the blade-to-blade surface (due to flow curvature). Thus, the cavitation model incorporates the concept of a distinct vapor cavity displacing an otherwise incompressible liquid. (See figure 1.) Because the vapor merely displaces the liquid in the flow model it is assumed that the actual blade can be replaced by a pseudo-blade consisting of the real blade plus the cavity. The blade angle is replaced by the mean angle of the pseudo-blade; i.e.,

the average of the real blade angle and the angle of the surface of discontinuity between the vapor and the liquid. This then produces a local "deviation" caused by cavitation, which will add to the mean deviation due to leading edge loading and trailing edge unloading. It will be shown later that this effect tends to unload the blade whenever the flow curvature becomes too severe for the available local pressure above saturation pressure.

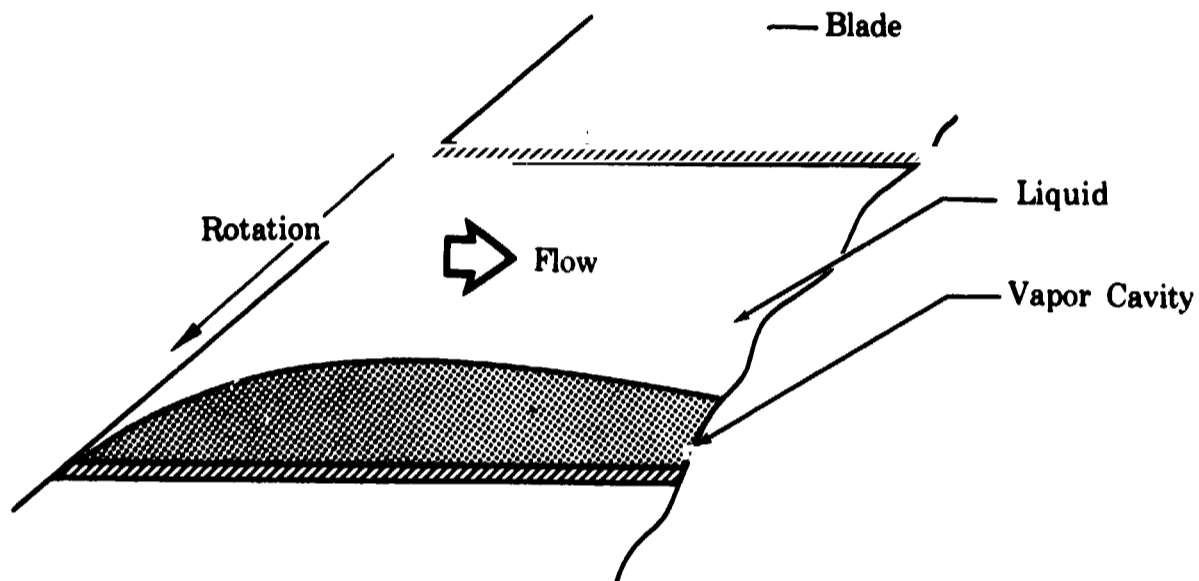


Figure 1. Distinct Vapor Cavity Forms During Cavitation

FD 25645A

c. Discussion of Basic Relations

(1) Geometric Relations

The information about the geometry of the inducer required to begin the analysis includes the flowpath inner and outer radii versus axial distance and some description of the blade angle (β^*) and thickness (t) distributions. In the model selected, it is assumed that one surface of the inducer blade is generated by a straight line (generatrix) passing through the hub and tip radii given previously. The other surface is assumed to be generated by a straight line inclined at some angle (γ - the taper angle) and displaced some distance (the blade thickness) with respect to the other generatrix (figure 2). To allow for nonradial element blading, it is assumed that the product of radius (R) times the tangent of the blade angle varies linearly from the values for the hub and tip. Thus,

$$R \tan \beta^* = R_T \tan \beta_T^* - \frac{R_T - R}{R_T - R_H} \left[R_T \tan \beta_T^* - R_H \tan \beta_H^* \right] \quad (1)$$

from which the local value of β^* can be found for any value of R .

The local blade thickness may be obtained from the given blade tip thickness (t_T) and the taper angle (γ):

$$t = t_T + \frac{\gamma(R_T - R)}{\cos \lambda_L} \quad (2)$$

where λ_L is the angle of lean of the generatrix measured from a vertical line (See figure 2.)

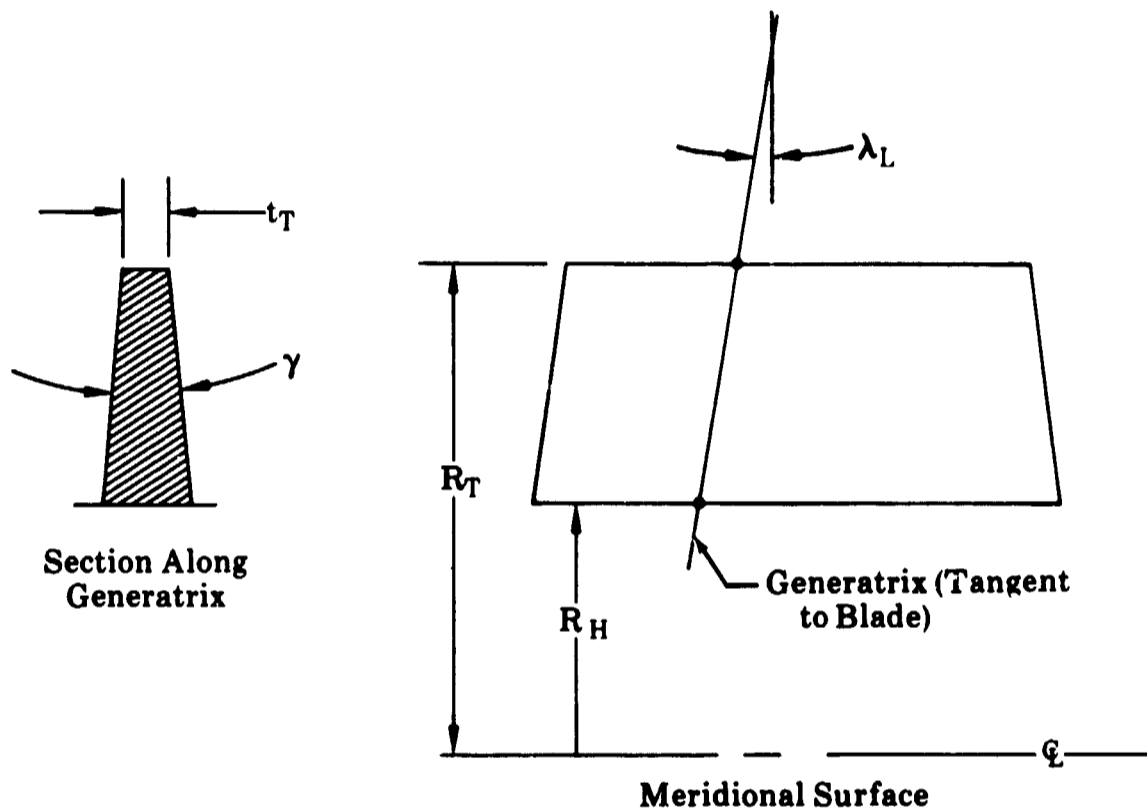


Figure 2. Thickness Distribution of Typical Blade

FD 25872A

The distance between surfaces of adjacent blades (measured in the circumferential direction) is given by

$$\tau = \frac{2\pi R}{N_b} - \frac{t}{\sin\beta^*} \quad (3)$$

where τ is the spacing and N_b is the number of blades.

Although the flow in an inducer is primarily axial, the hub or tip contour often has a varying radius. The streamlines then may be forced to change radius and, because of the inducer rotation about its axis, Coriolis forces will cause blade pressure loading. It is assumed that the change in slopes of the hub and tip contours will be gradual so that the angle of the streamline across the flow path will vary linearly with radius from the value at the hub (ψ_H) to the value at the tip (ψ_T). Thus,

$$\psi = \psi_H + \frac{R - R_H}{R_T - R_H} (\psi_T - \psi_H) \quad (4)$$

The hub and tip values are found from the input values for the radius and axial distance (Z):

$$\tan \psi = \frac{\Delta R}{\Delta Z}$$

(2) Flow Relations

The velocity diagram at any point in the flow is shown in figure 3. From trigonometry

$$\begin{aligned} V_m &= W_m = W \sin \beta \\ W_u &= W \cos \beta \\ V_u &= U - W_u \\ \alpha &= \text{Arc tan } (V_m/V_u) \\ V &= V_m/\sin \alpha \end{aligned}$$

The relative flow angle (β) is found from the blade angle and the deviation angle at any point

$$\beta = \beta^* - \text{deviation}$$

The relative flow velocity (W) is found from the volumetric flow (Q) and the flow area normal to the flow direction (A)

$$W = Q/A$$

where:

$$A = \tau_l (\Delta y) \cos \psi (\sin \beta) \quad (5)$$

and τ_l is that portion of the circumferential distance between two blades that is occupied by liquid, and Δy is the vertical distance between streamlines. (See figure 4). The value of τ_l is obtained by adjusting the geometric blade spacing (τ) by the boundary layer displacement thickness (δ^*) and the vapor cavity height (b), measured circumferentially:

$$\tau_l = \tau - \frac{2\delta^*}{\sin \beta^*} - b \quad (6)$$

The factor of two on δ^* accounts for layers on the surfaces of both blades bounding the flow channel, i.e., the stream tube.

Blockage due to hub and shroud surface boundary layers is accounted for by reducing the hub and tip stream tube heights (Δy) by their respective displacement thickness, δ^* :

$$\Delta y = \Delta y - \delta^*$$

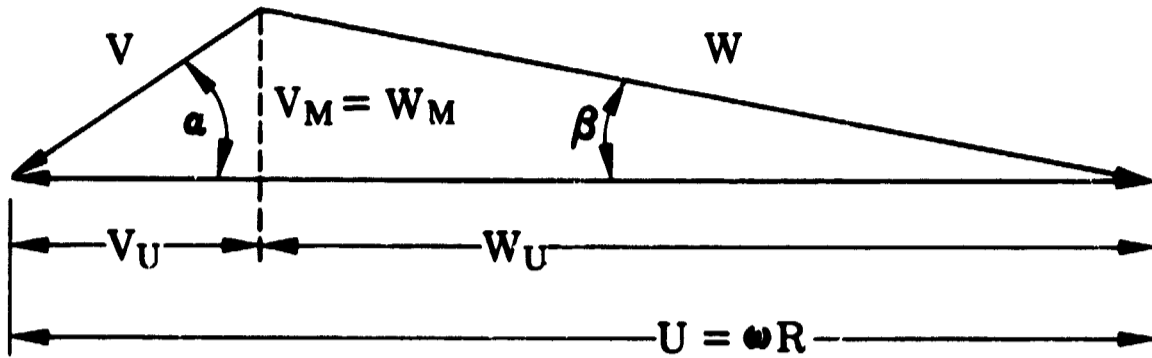


Figure 3. Typical Velocity Diagram

FD 25809

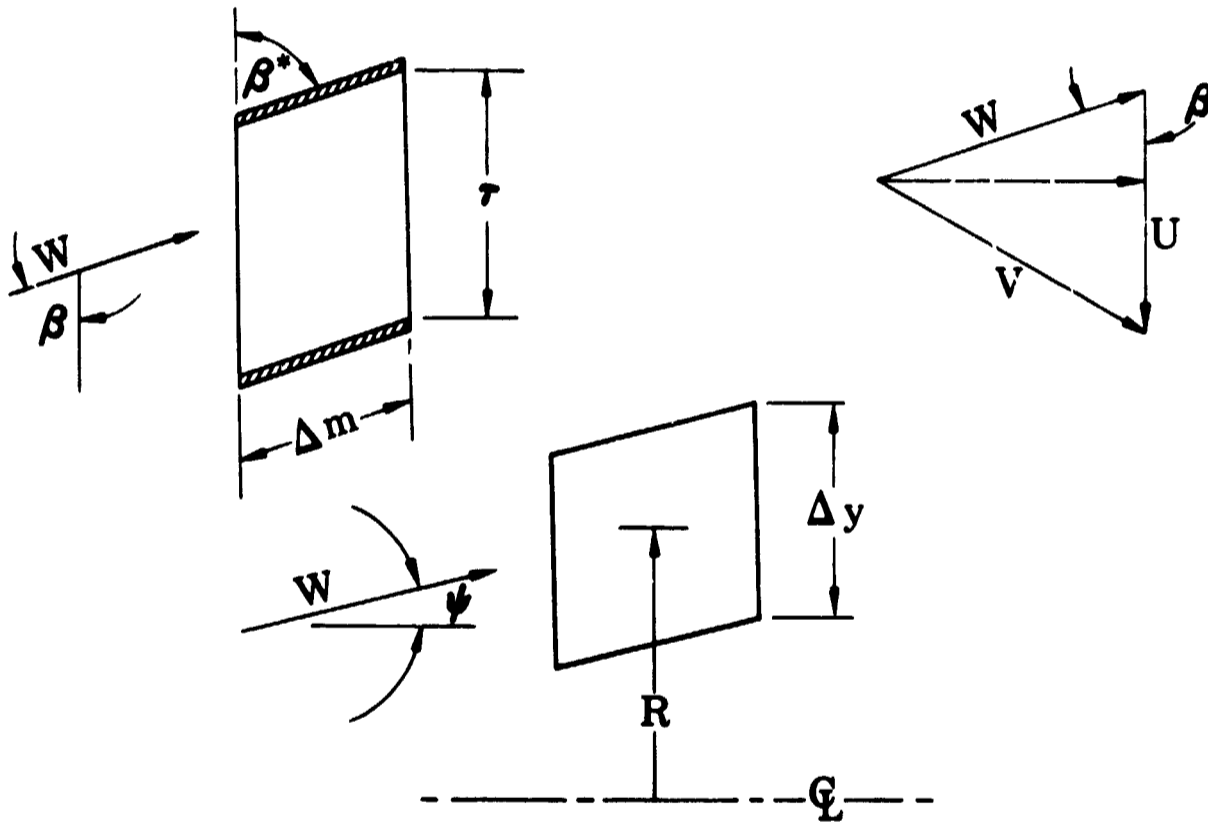


Figure 4. Schematic of Flow Passage

FD 25644A

(3) Deviation

It is assumed that the flow will tend to follow the mean direction of the passage formed by the blades (or by the pseudo-blades). However, because of fluid inertia, changes of angle at the leading and trailing edges, required to satisfy boundary conditions, cannot take place discontinuously. Therefore, relations for the distribution of deviation angle in terms of inlet and exit boundary values must be established. The method selected is based on the exact analysis of a two-dimensional, nonstaggered flat plate cascade.

(a) Leading Edge Loading

Refer to the flow conditions shown in figure 5. The relation for the component of velocity normal to the blades (V_u) is found from complex transformation to be:

$$iV = \frac{u \sin \alpha_0}{\sqrt{\text{Exp} (2\pi z/\tau) - 1}} \quad (7)$$

where i = (imaginary) and z is the complex coordinate, $z = x + iy$

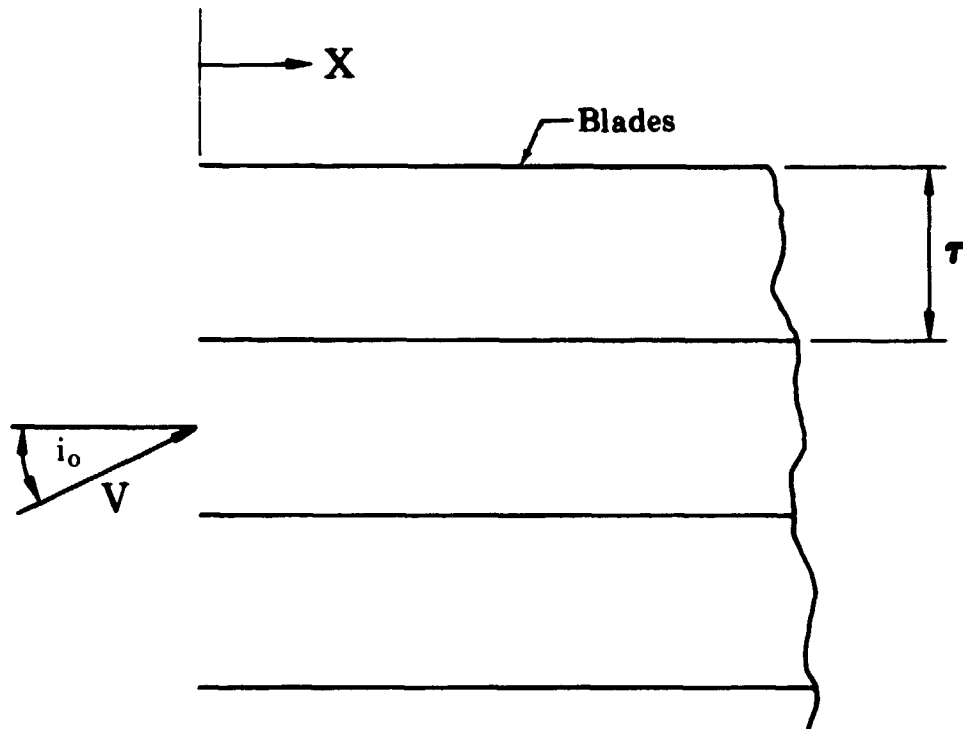


Figure 5. Semi-Infinite Cascade

FD 25810A

The ratio of this velocity (V) to the through-flow velocity is the tangent of the local flow direction. Evaluating this at the mid-stream position ($z = x + iy/2$), the distribution of deviation angle (δ) is found to be

$$\tan \delta = \frac{\tan \alpha_0}{\sqrt{1 + \text{Exp} (2\pi x/\tau)}} \quad (8)$$

For the staggered cascade, the normal spacing is $\tau \sin \beta^*$ and the distance x is measured along the mid-stream locus as m . Thus

$$\tan \delta = \frac{\tan \alpha_0}{\sqrt{1 + \text{Exp} (2\pi m/\tau \sin \beta^*)}} \quad (9)$$

It is interesting to note that as m increases an approximation of this expression is

$$\tan \delta = \tan \alpha_0 \text{Exp} (-\pi m/\tau \sin \beta^*) \quad (10)$$

This is the same form of exponential decay found in actuator disk theory for the variation of streamline slope upstream and downstream of a blade row. A plot of the ratio, $\tan \delta / \tan \alpha_0$, versus m/τ_n (where $\tau_n = \tau \sin \beta^*$) is shown in figure 6. Note that at a distance of one normal gap ($m/\tau_n = 1$) the ratio is only 0.04; that is, approximately 96% of the upstream incidence has been taken out. This indicates that blade hydrodynamic loading due to flow incidence will decay in approximately one normal gap measured from the leading edge along the mid-passage. This leading-edge deviation is designated by subscript as δ_1 .

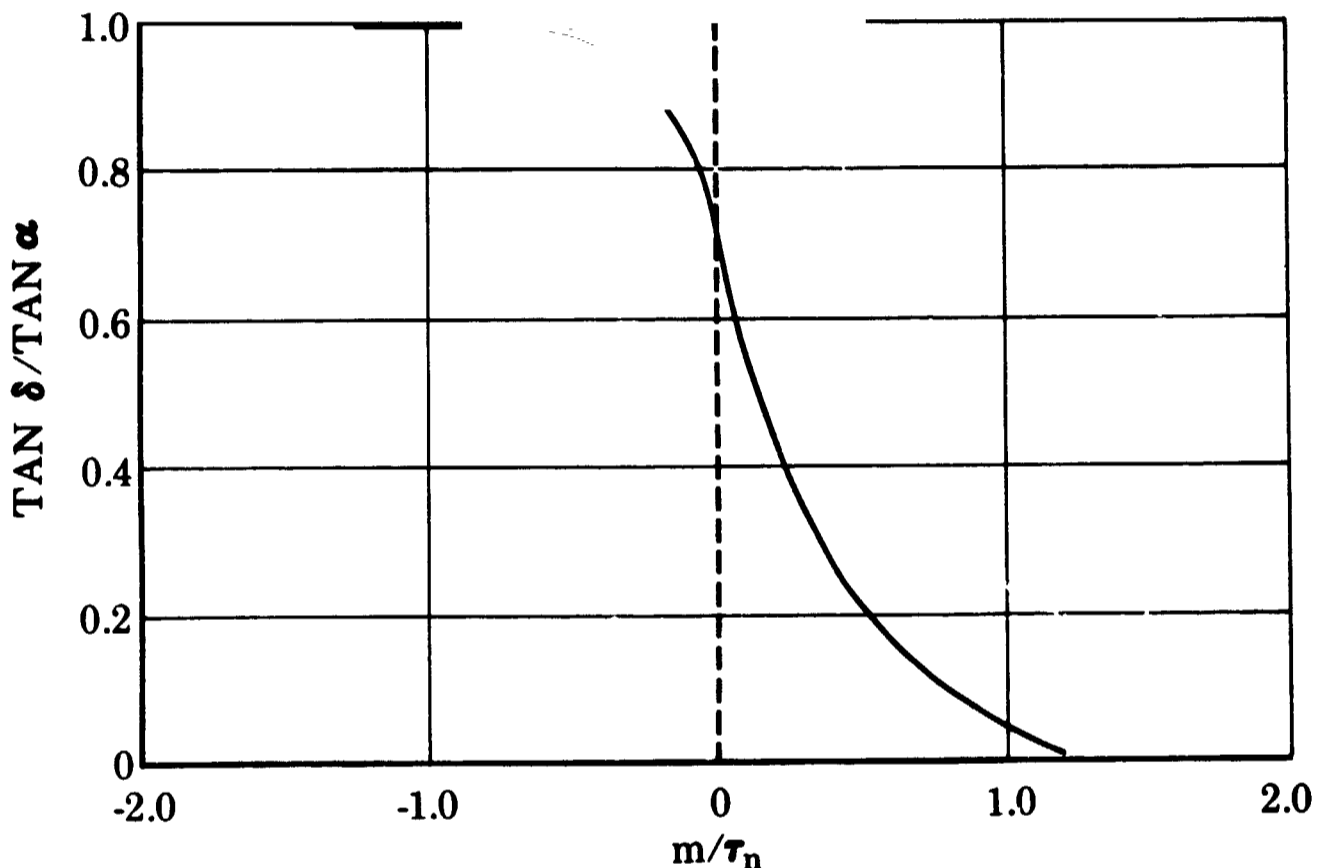


Figure 6. Exponential Decay of Deviation Angle

FD 25569

(b) Trailing Edge Unloading

Because of boundary layer, blade thickness, and cavitation effects, the flow aft of the blade trailing edge will have a relative flow angle (β) different from the blade angle (β^*) at the trailing edge. Figure 7 illustrates the effect of "dumping" the flow downstream of the blades. Because angular momentum is conserved, the tangential component of absolute velocity (V_u) remains constant while the axial component (V_m) decreases so that β is reduced, creating a deviation. Because of fluid inertia, this deviation cannot occur discontinuously. Therefore, an exponential decay of deviation (δ_2) as a function of distance from the trailing edge is used. The value of exit deviation is treated as analogous to the inlet incidence, α_0 .

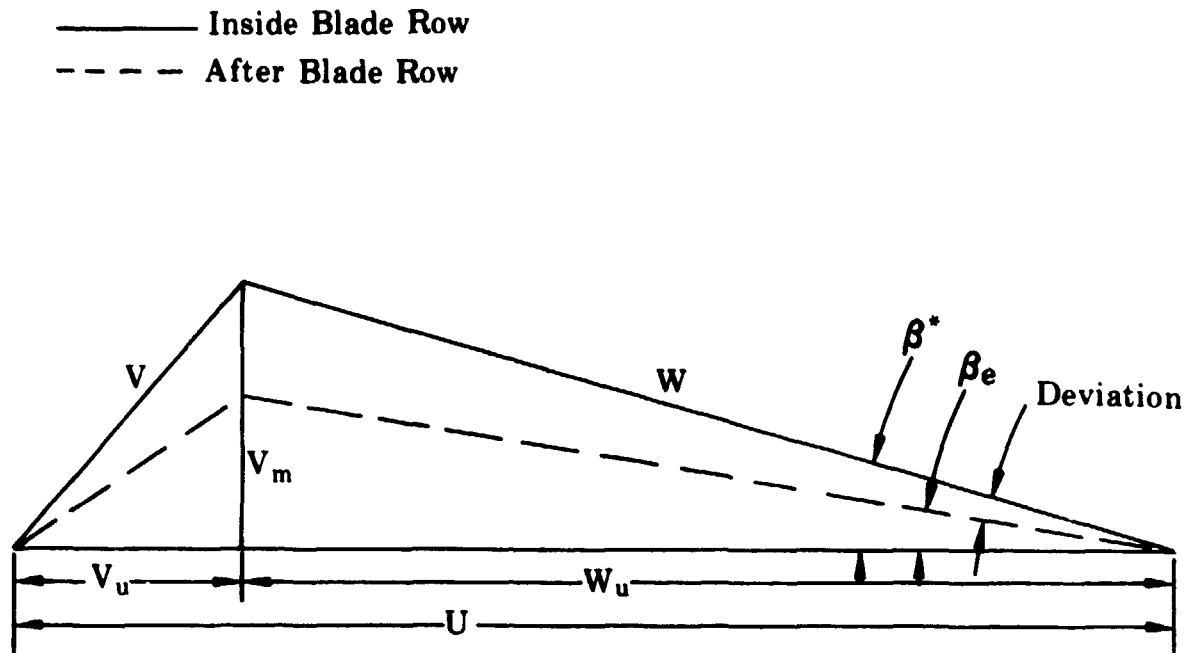


Figure 7. Inducer Exit Velocity Diagrams

FD 25642A

(c) Deviation Due to Cavitation

In the concept of the selected model, cavitation causes a change in the "effective" blade angle. In this sense, the cavity forms part of a pseudo-blade rather than causing deviation, i.e.,

$$\beta^{*eff} = \beta^* - \delta\beta^*$$

where $\delta\beta^*$ is one-half the slope of the vapor cavity surface relative to the real blade. However, for reference purposes this deviation is considered as a part of the total deviation:

$$\text{Deviation} = \beta^* - \beta = \delta_1 + \delta_2 + \delta\beta^*$$

(4) Radial Equilibrium

The flow in the inducer must satisfy equilibrium of radial momentum. The static pressure (P) within each stream tube is found from the Bernoulli equation

$$P = P_{orel} - \frac{\rho}{2g} W^2 \quad (11)$$

where P_{orel} is the local total relative pressure and ρ is the fluid density.

The radial gradient of static pressure for each stream tube can be found from conservation of momentum in the radial direction. There are two effects causing a radial pressure gradient - first, the rotation of the inducer causes a centrifugal pressure gradient

$$\left(\frac{dP}{dr}\right)_1 = \frac{\rho}{g} \frac{(V_u)^2}{R} \quad (12)$$

Substituting $V_u = U - W_u = \omega R - W \cos \beta$, where ω is rotational velocity,

$$\left(\frac{dP}{dr}\right)_1 = \frac{\rho}{g} \frac{(\omega R - W \cos \beta)^2}{R} \quad (13)$$

Secondly, the change in radial velocity (i.e., streamline curvature) causes a radial pressure gradient:

$$\left(\frac{dP}{dr}\right)_2 = -\frac{\rho}{g} v_m^2 \frac{d\Psi}{dm} \frac{\cos \Psi}{\sin \beta} + v_m \frac{\sin \Psi}{\sin \beta} \frac{dv_m}{dm} \quad (14)$$

where dm is the element of path length. Substituting $v_m = W \sin \beta$,

$$\left(\frac{dP}{dr}\right)_2 = -\frac{\rho}{g} W^2 \sin^2 \beta \cos \Psi \frac{d\Psi}{dm} - W \sin \Psi \sin \beta \frac{dW}{dm} - W^2 \sin \Psi \cos \beta \frac{d\beta}{dm} \quad (15)$$

The total pressure gradient is, therefore:

$$\begin{aligned} \frac{dP}{dr} &= \left(\frac{dP}{dr}\right)_1 + \left(\frac{dP}{dr}\right)_2 \\ &= \frac{\rho}{g} \left[\frac{(\omega R - \omega \cos \beta)^2}{R} - \omega^2 \sin^2 \beta \cos \Psi \frac{d\Psi}{dm} - W \sin \Psi \sin \beta \frac{dW}{dm} \right. \\ &\quad \left. - W^2 \sin \Psi \cos \beta \frac{d\beta}{dm} \right] \end{aligned} \quad (16)$$

(5) Streamline Relaxation

The radial position of each streamline at each axial station is determined by satisfying the condition of radial equilibrium with the least error or by an error less than some tolerance level. The error in local static pressure gradient is found by comparing the calculated dP/dr with the finite difference value determined from adjacent stream tubes:

$$\text{Error} = \frac{\Delta P}{\Delta r} - \frac{dP}{dr}$$

where

$$\Delta P = P(I) - P(I-1)$$

and

$$\Delta r = R(I) - R(I-1)$$

The root-mean-square error of all stream tubes is computed and minimized by iterating on the position of the streamlines. The positions (in percent of passage height) are corrected by a small incremental step in the direction determined by the error in pressure gradients of the stream tubes above and below each streamline. The size of the incremental correction is reduced after a fixed number of iterations to improve the accuracy. A limit is placed on the total number of iterations to limit computing time.

(6) Blade Loading

After the radial positions of the streamlines are located through the relaxation procedure, the meridional solution at the axial station is completely determined. Then it is possible to superimpose a solution for the blade-to-blade pressure difference. This pressure difference, measured in the circumferential direction, is also the blade hydrodynamic pressure loading, ΔP_b . The value of ΔP_b is found from conservation of angular momentum of the fluid between any two axial stations. The total blade pressure force in the tangential direction is:

$$F = (\Delta P_b) (\Delta y \cos \Psi) (\Delta m \sin \beta^*) l_b \quad (17)$$

The moment arm is the radius R . Therefore, the torque is:

$$T = F \cdot R = (\Delta P_b) (\Delta y \cos \Psi) (\Delta m \sin \beta^*) (N_b) (R) \quad (18)$$

From Euler's turbomachinery equation, the change in fluid angular momentum is equal to this torque

$$\dot{m} \cdot \Delta(RV_u) = T \quad (19)$$

The continuity of mass is given by

$$\dot{m} = \rho(\Delta y \cos \Psi) (\tau \sin \beta) (W) (N_b) \quad (20)$$

Substituting for \dot{m} and T , the momentum equation reduces to

$$\Delta P_b = \frac{\rho W \tau}{R} \cdot \frac{\sin \beta}{\sin \beta^*} \cdot \frac{\Delta(RV_u)}{\Delta m} \quad (21)$$

If the increment Δm is taken small enough,

$$\frac{\Delta(RV_u)}{\Delta m} \approx \frac{d(RV_u)}{dm} = V_u \frac{dR}{dm} + R \frac{dV_u}{dm} \quad (22)$$

Substituting $V_u = \omega R - W \cos \beta$

and

$$\frac{dV_u}{dm} = \frac{\omega dR}{dm} + W \sin \beta \frac{d\beta}{dm} - \cos \beta \frac{dW}{dm}$$

then

$$\frac{d(RV_u)}{dm} = (2\omega R - W \cos \beta) \frac{dR}{dm} + WR \sin \beta \frac{d\beta}{dm} - R \cos \beta \frac{dW}{dm} \quad (23)$$

and

$$\Delta P_b \approx \frac{\rho W T}{R} \cdot \frac{\sin \beta}{\sin \beta^*} \left[2\omega R \frac{dR}{dm} - W \cos \beta \frac{dR}{dm} + WR \sin \beta \frac{d\beta}{dm} - R \cos \beta \frac{dW}{dm} \right] \quad (24)$$

Factoring out $\sin \beta$ and noting that

$$\frac{1}{\sin \beta} \frac{dR}{dm} = \sin \psi$$

and dividing through by the relative dynamic pressure (q)

where

$$q = \frac{\rho W^2}{2g}$$

$$\text{then, } \frac{\Delta P_b}{q} = \frac{2 \tau \sin^2 \beta}{\sin \beta^*} \left[\frac{2 \omega \sin \psi}{W} - \frac{\cos \beta \sin \psi}{R} + \frac{d\beta}{dm} - \frac{\cot \beta}{W} \frac{dW}{dm} \right] \quad (25)$$

The first term inside the brackets represents the blade loading caused by Coriolis forces. The second term derives from curvature of the flow in absolute space about the axis at constant relative angle (β). The third term represents the contribution of flow curvature due to the rate of change of the relative flow direction. The last term is the contribution of mean diffusion to the tangential loading ΔP_b . For inducers with low blade camber ($d\beta/dm \approx 0$) and axial flow ($\sin \psi \approx 0$), the last term will dominate and primarily determine the blade hydrodynamic loading.

(7) Inlet and Exit Calculations

Special inlet calculations are required to establish streamline locations, incidence angles, and other relative inlet conditions. An exit station downstream of the blade trailing edge is included to evaluate effects of dumping of the flow and to provide exit pressures and velocities for performance evaluation.

(8) Performance Calculations

The overall performance calculations include mass average and radial distribution of performance parameters such as work input, head rise, and efficiency. Other pertinent parameters, such as NPSH, Reynolds number, suction specific speed, flow coefficient, and head coefficient are included in these calculations.

(9) Boundary Layer Calculations

A simple turbulent-flow, zero-pressure-gradient, boundary layer model is used to determine the values of boundary layer displacement thickness (δ^*) and skin friction coefficient (f). It is assumed that there is

little secondary flow in the inducer so that migration of the boundary layer flow from the pressure surface to the suction surface is not significant. The values of δ^* and f are based on the local mean velocity (W) and the distance from the leading edge (m).

$$\delta^* = 0.04625 (m) (Re_m)^{-1/5} \quad (26)$$

$$f = 0.0576 (Re_m)^{-1/5} \quad (27)$$

where Re_m is the length Reynolds Number.

(10) Loss System

The loss system considers two causes of losses in total relative pressure between any two adjacent axial stations:

(a) The loss due to skin friction

$$\Delta P_{o_{rel}} = \frac{(f) (\Delta m) (W.P.)}{A} q \quad (28)$$

where $W.P.$ is the perimeter of the wetted surface. For the hub or tip stream tubes, these perimeters include the hub or shroud surfaces between blades in addition to the blade walls. All other stream tubes have only the blade walls as wetted surfaces. For the typical inducer, the velocity gradient between stream tubes should be low enough that viscous or Reynolds stresses between stream tubes are low compared with the wall stresses. This is true because the boundary layer thickness normally is small compared with the height of the hub or tip stream tubes.

(b) The loss due to diffusion

Whenever the velocity gradient (dW/dm) is negative, the losses will increase due to increased boundary layer momentum thickness. This conceivably could be handled by a more complex boundary layer model, including effects of pressure gradient. A simpler approach, selected for the present model, is to use diffuser empirical loss data, and to express the gradient in terms of a local equivalent diffusion angle, ϕ_{eq} (in degrees)

$$\phi_{eq} = 114.6 \tan^{-1} \left[\frac{1}{\Delta m} \left(\frac{A}{\pi} \right)^{1/2} \left(1 - \frac{W}{W'} \right)^{1/2} \right] \quad (29)$$

The pressure loss for a diffuser is usually expressed as

$$\frac{\Delta P}{q} = f(\phi_{eq}) \left[1 - \frac{A_{in}}{A_{out}} \right]^2 \quad (30)$$

Substituting $W/W' = A_{in}/A_{out}$,

where W' is the value of relative velocity at the previous axial station,

$$\frac{\Delta P}{q} = f(\phi_{eq}) \left[\frac{W' - W}{W'} \right]^2 \quad (31)$$

The function $f(\phi_{eq})$ is determined from empirical data (SAE Aerospace Applied Thermodynamics Manual, Section 1):

$$\begin{aligned}
 \phi_{eq} > 46.0 & \quad f(\phi_{eq}) = 1.0 \\
 \phi_{eq} < 0 & \quad f(\phi_{eq}) = 0.0 \\
 14 < \phi_{eq} \leq 46.0 & \quad f(\phi_{eq}) = 0.02577 \phi_{eq} - 0.1855 \\
 0 < \phi_{eq} \leq 14 & \quad f(\phi_{eq}) = (0.74506) \times 10^{-3} \phi_{eq}^2 + (0.79874) \times 10^{-3} \phi_{eq} - \\
 & \quad (0.4006) \times 15^{-4}
 \end{aligned}$$

(11) Relations for Cavitation

In the present flow model, cavitation is handled through the concept of a distinct vapor cavity forming on the suction surface of the blade. As discussed above, this cavity tends to act as a pseudo-blade, displacing the flow and allowing it to turn more gradually. It is this more gradual turning that allows the pressure at the vapor-liquid interface (i.e., the "suction surface" of the pseudo-blade) to be equal to the saturation pressure. If the blade loading increases due to increased incidence, or if the static pressure decreases due to decrease in inlet pressure, then the cavity should grow and assume a shape so that the "suction surface" pressure will always equal saturation pressure.

Stripling and Acosta (ASME Paper No. 61-WA-98) have solved the problem of two-dimensional, plane, flat cascade potential flow with a free streamline, along which the pressure is equal to saturation pressure. The solution for the detailed shape of the cavity involves complex variables. However, the solution for the maximum cavity height (h_0) and the distance from the leading edge to the point of maximum height (c) are easily obtained. These relations have been taken directly from Stripling and Acosta and are included in the engineering formulation of the program (Appendix C).

A simple shape which can be used to approximate the solution of Stripling and Acosta is the circular arc shown in figure 8. The circular arc passes through the leading edge and the point of maximum height (c, h_0). The local height (h) is expressed functionally as

$$h/h_0 = f\left(\frac{m}{c}, R_c\right) \quad (32)$$

where the radius of the circular arc, R_c , is expressed functionally as

$$R_c = f(h_0, c) \quad (33)$$

The slope of the cavity relative to the blade is dh/dm . This is related to the correction of blade angle for the pseudo blade, as discussed in paragraph Blc(3c) above:

$$\delta\beta^* = \frac{1}{2} \frac{dh}{dm} \quad (34)$$

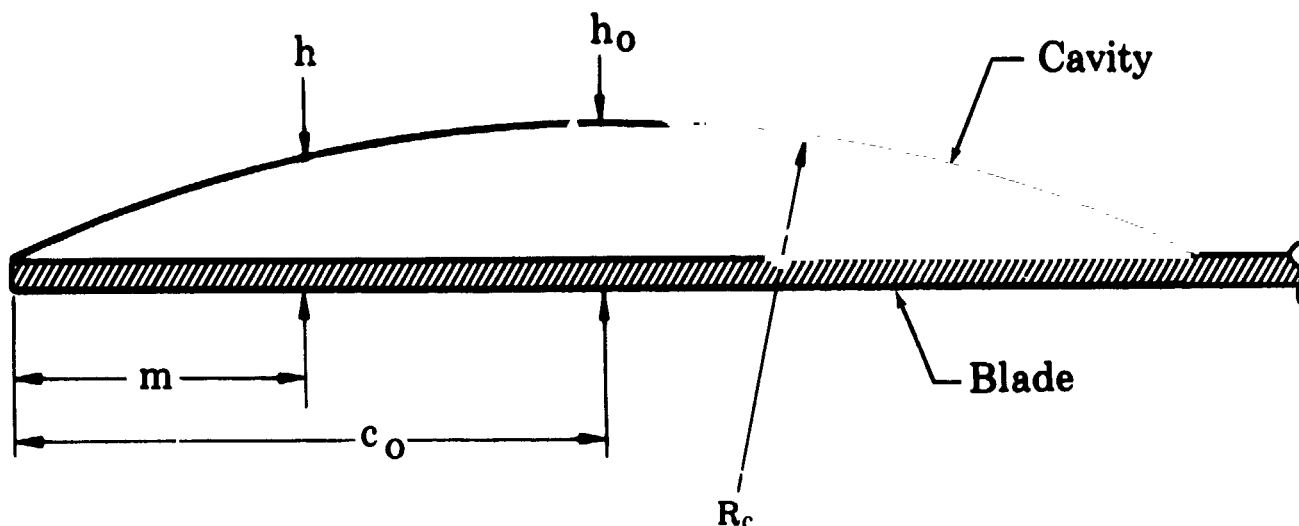


Figure 8. Circular Arc Cavity Shape

FD 25870A

The flow model of Stripling and Acosta does not involve the cavity past the point of maximum height. For the present inducer flow model, it is assumed that the collapse of the cavity beyond this point is symmetrical with the growth of the cavity ahead of the maximum point. An exponential smoothing function is used in the vicinity of the point of collapse of the cavity to avoid a discontinuity of effective blade angle.

d. Typical Results of Analyses

(1) Test Cases

In this section, typical results from the hydrodynamic analysis program will be presented for four separate test cases. Two of the test cases were used for verification of the flow model operating under noncavitating conditions, and the other two cases were used in evaluating the model during cavitating operation. The test cases were as follows:

1. Noncavitating

- a. Paddle wheel
- b. NASA 12-deg (0.21-rad) helical inducer (NASA TND-1170)

2. Cavitating

- a. Cavitating flat plate cascade
- b. NASA 12-deg (0.21-rad) helical inducer (NASA TND-1170)

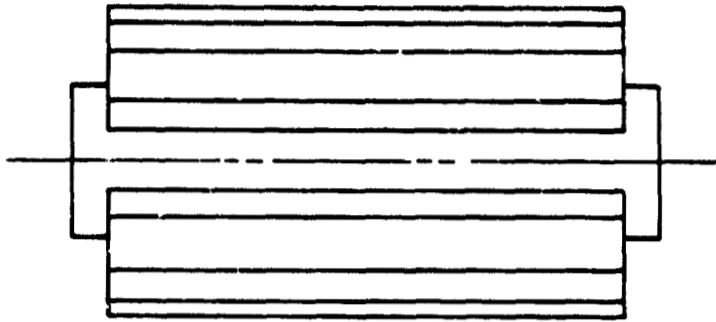
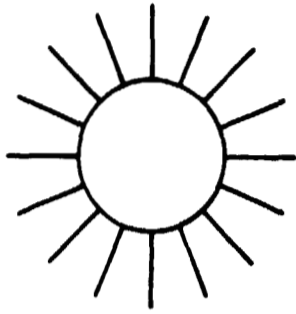
(2) Noncavitating Test Cases

(a) Paddle Wheel

The purpose of this test case was to select a simplified geometry that would allow solution of the radial momentum differential equation by direct integration, resulting in an exact expression for the radial pressure and axial velocity distributions. Details of the paddle wheel geometry and operating conditions are shown in figure 9.

GEOMETRY

1. To Scale
2. Zero Blade Thickness



OPERATING CONDITIONS

1. Noncavitating
2. No Inlet Deviation
3. No Exit Deviation
4. Nonviscous Flow

Figure 9. Paddle Wheel Geometry and Operating Conditions

FD 25899

A comparison of the exact analytical and program calculated radial pressure profile is shown in figure 10. As this figure shows, the program results are in complete agreement with the exact analytical solution. The conclusion drawn from this comparison is that the streamline balance procedure as used by the hydrodynamic program operates as desired in satisfying radial equilibrium.

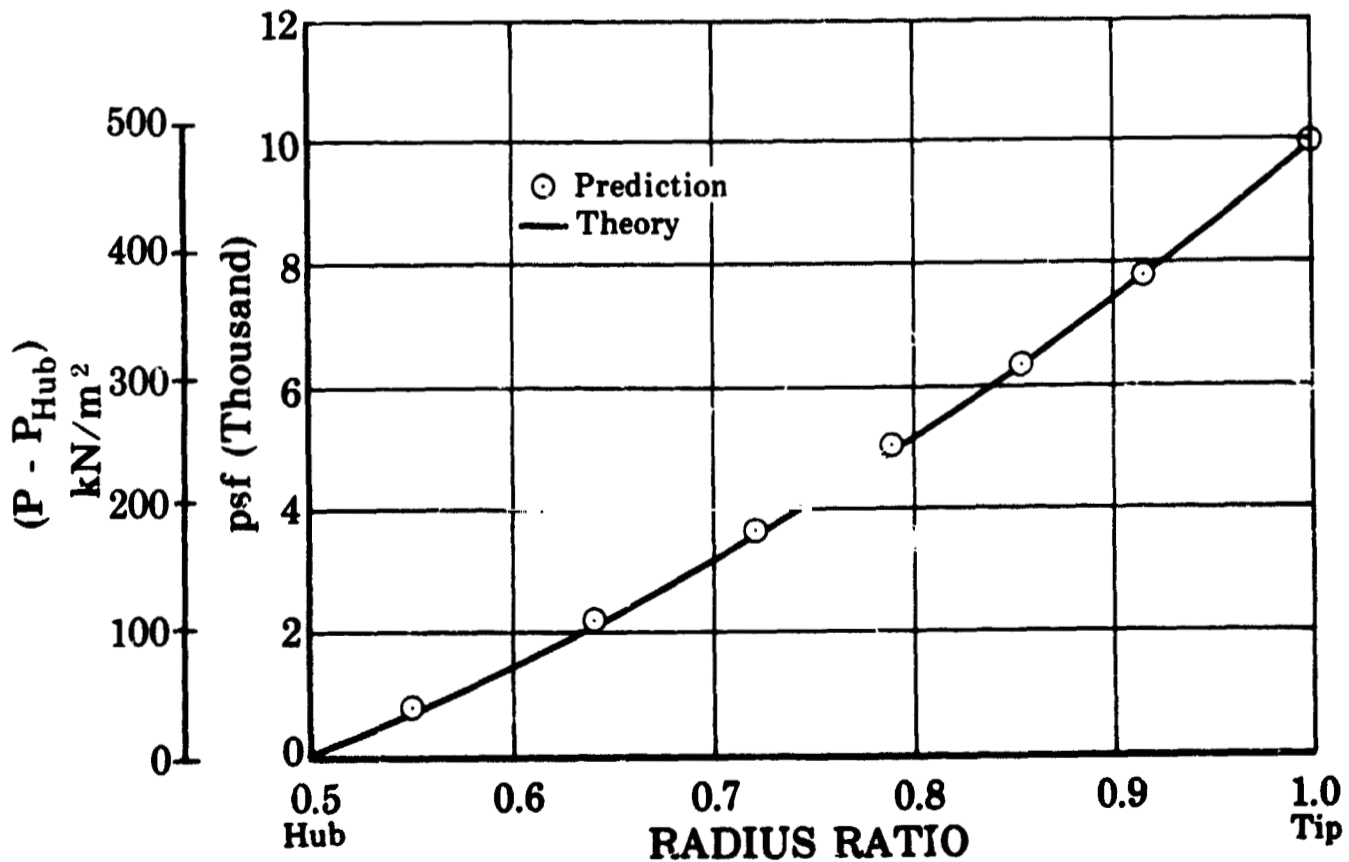


Figure 10. Paddle Wheel Test Case - Radial Equilibrium

FD 25397

It would be desirable as a next step in the noncavitating analysis to compare the actual measured blade suction and pressure surface static pressures for a given geometry with those calculated using the hydrodynamic program. Unfortunately, accurate data of this type are not available. The next best method of demonstrating noncavitating program reliability would be the program's ability to predict inducer performance, including radial distribution of the exit parameters.

(b) NASA 12-deg (0.21-rad) Inducer (NASA TND-1170)

Selection of this inducer for aiding in program checkout was based upon the availability of an extensive amount of noncavitating test data. This inducer is also believed to be typical of most inducer designs and, therefore, would provide a reasonably rigorous checkout of program capability.

Noncavitating inducer performance was investigated for several flow coefficients, resulting in direct performance comparisons as well as comparisons in radial distribution for several important exit flow parameters. These comparisons are individually discussed below.

(1) Overall Performance

(a) Head vs Flow

A head-flow curve, plotted as head coefficient as a function of flow coefficient, is shown in figure 11. Close agreement between the experimental and the predicted program results is shown. Some deviation between the experimental and the predicted program results,

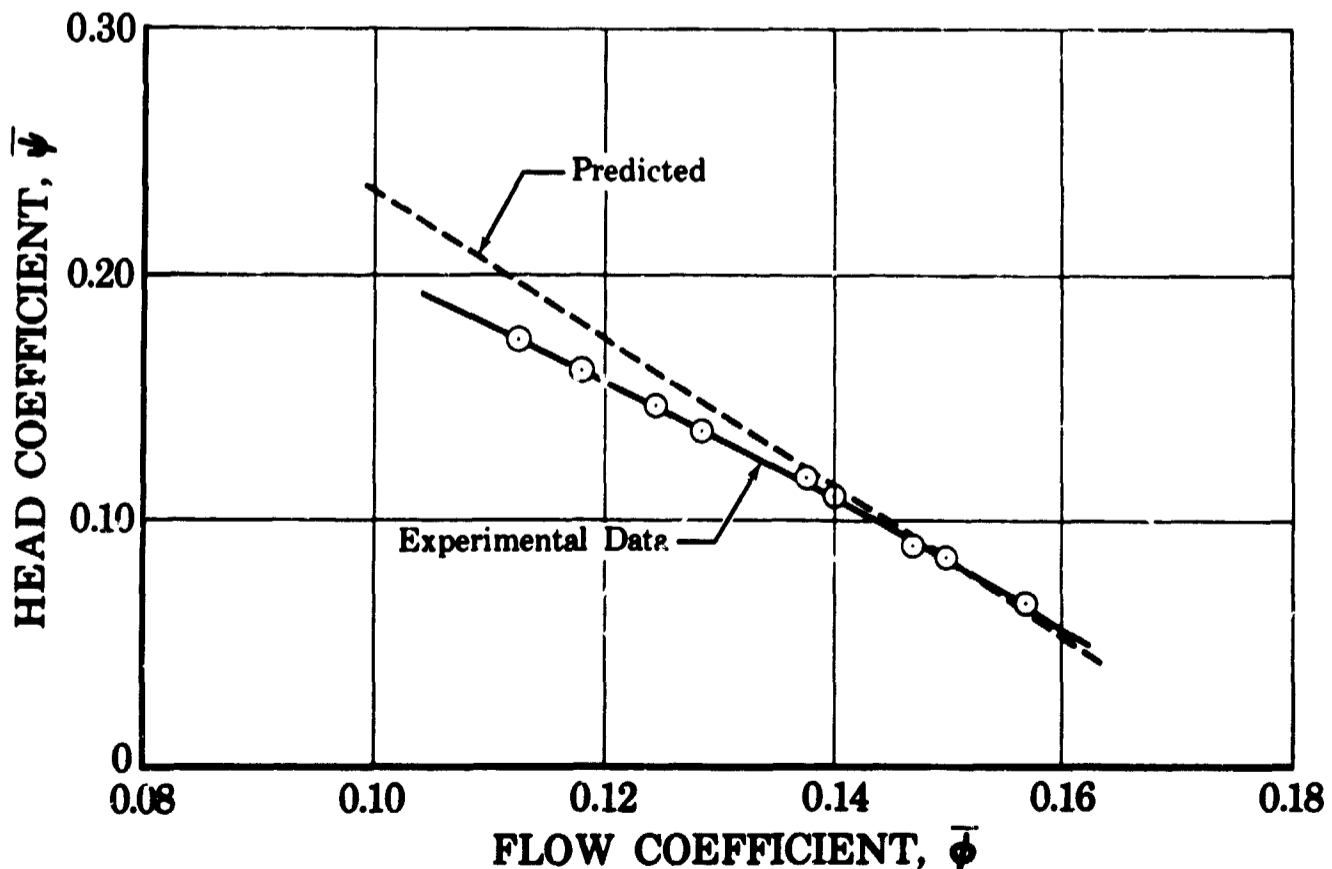


Figure 11. NASA 12-Degree Inducer Noncavitating Head Coefficient vs Flow Coefficient

FD 25808

appearing at the lower flow coefficients, is believed to be the result of flow separation in the actual case occurring both along the hub at the exit and along the tip at the inlet. This results in increased flow losses and decreased work in the actual case, which appear in the form of decreased head coefficient.

(b) Efficiency vs Flow

Figure 12 shows a comparison between the experimental and calculated inducer efficiencies as a function of the average inlet flow coefficient. Experimental data scatter prevents drawing any definite conclusions other than that the program predicts the inducer efficiency with reasonable accuracy.

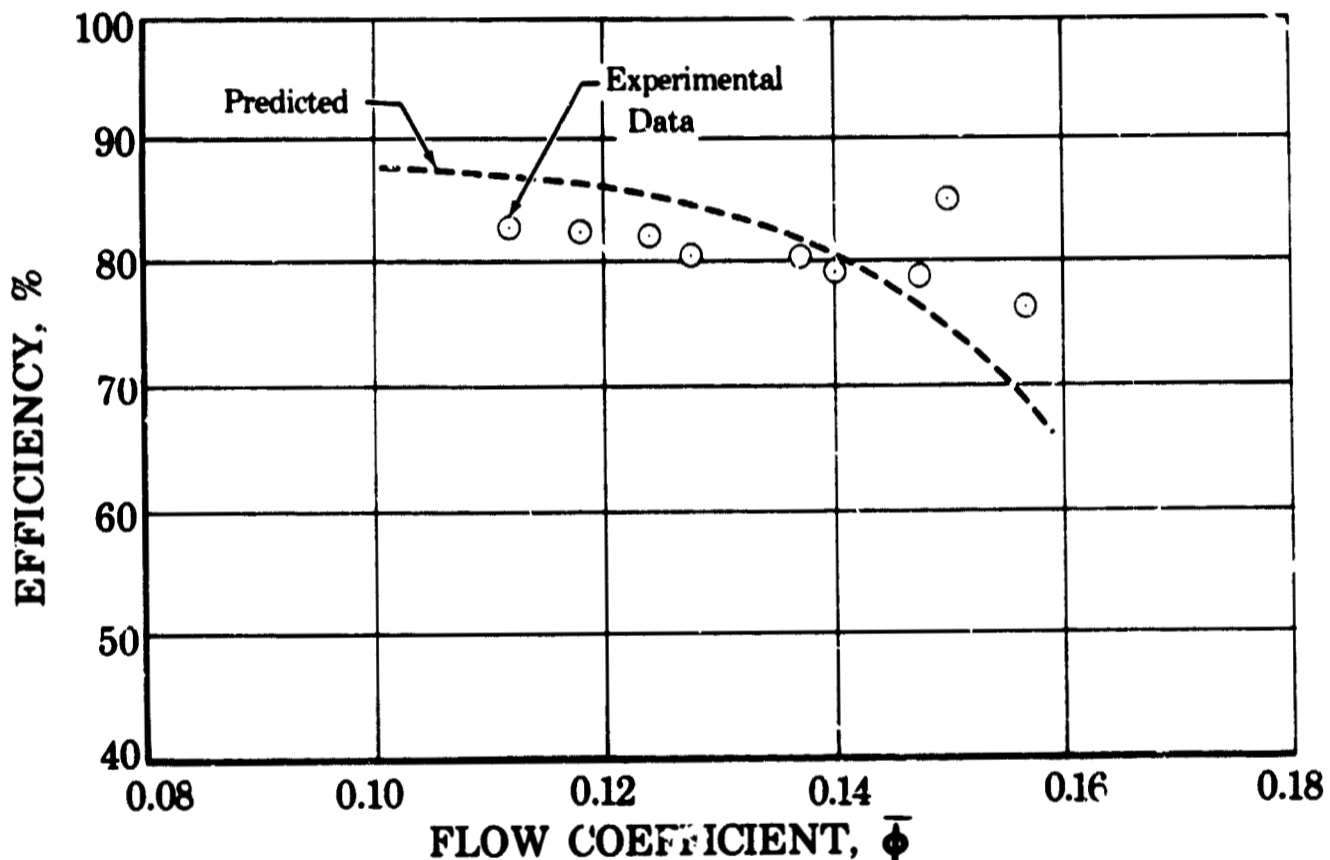


Figure 12. NASA 12-Degree Inducer Noncavitating Efficiency vs Flow Coefficient FD 25807

(2) Radial Distribution

(a) Exit Deviation

Of primary importance in predicting inducer performance is the ability to accurately predict exit flow deviation. In general, inducers are low head rise machines having low angle blading. Consider, for example, the NASA 12-deg (0.21-rad) inducer presently being discussed, which is typical of many inducer designs. If we look at a typical exit velocity triangle as shown in figure 13, it becomes obvious that minor discrepancies in the deviation angle can result in large variations in fluid tangential velocity, V_u . For zero inlet prewhirl, the ideal head rise is proportional to V_u . From this, it is seen that small errors in deviation can result in larger errors in ideal (and, therefore, actual) head rise.

$U = \text{Constant}$
 $V_m = \text{Constant}$
 $W'_u = W_u + \Delta V_u$

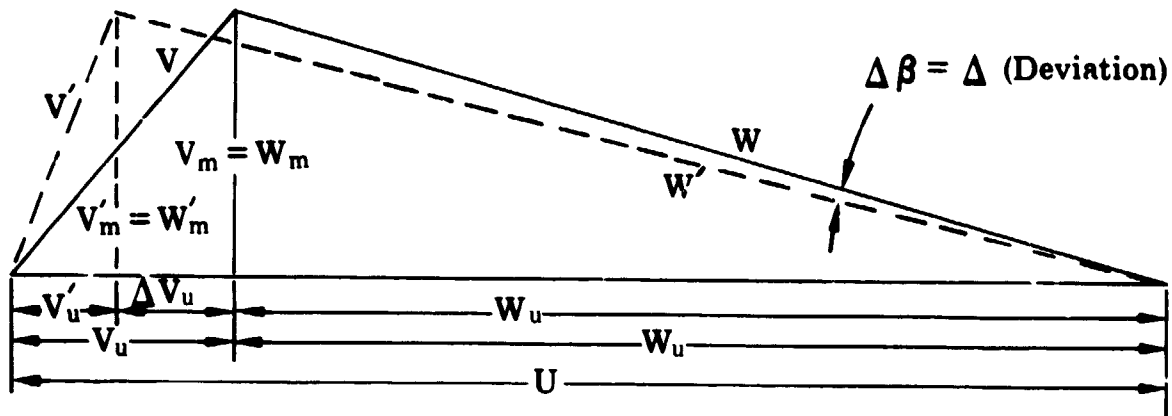


Figure 13. Typical Inducer Exit Velocity Triangle

FD 25871

Figure 14 is an illustration of the radial distribution of exit deviation angle. As this figure shows, good agreement between experimental and analytical radial distributions of exit deviation was achieved. This type of agreement is reflected in the close comparison between the experimental and program values of average head coefficient. Again, the calculated deviation agrees more closely with the flow coefficient of 0.157 than with the lower flow coefficient, 0.147.

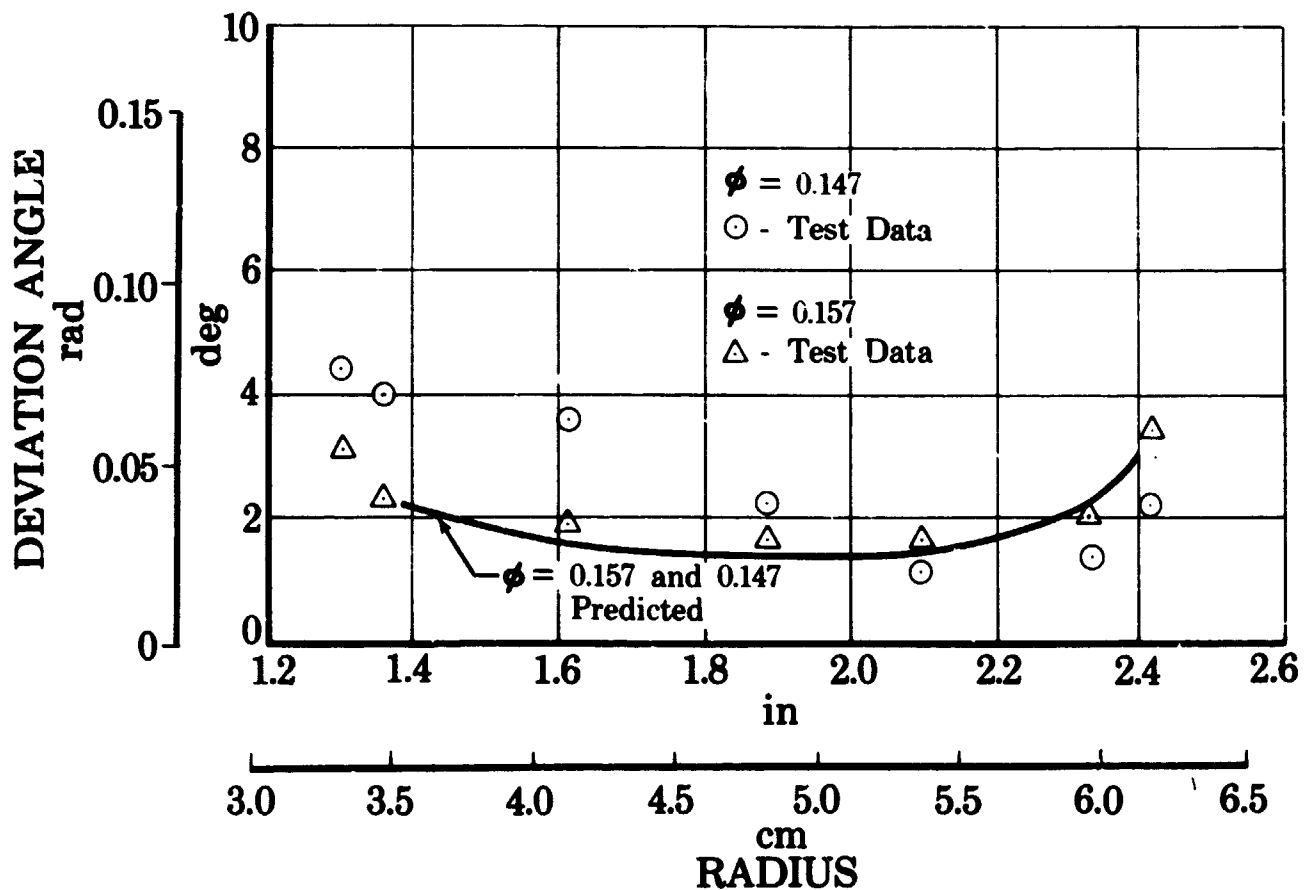


Figure 14. NASA 12-Degree Inducer Exit Deviation Angle vs Radius

FD 25405

(b) Ideal Total Head Rise Coefficient

Ideal head rise coefficient as a function of radius is shown in figure 15. The largest differences between the experimental and the program values of ideal head rise coefficient occur at the hub where the lowest actual head rise occurs. For this reason, relatively large local discrepancies in ideal head rise coefficient can occur near the hub without significantly affecting overall or mass-average inducer performance.

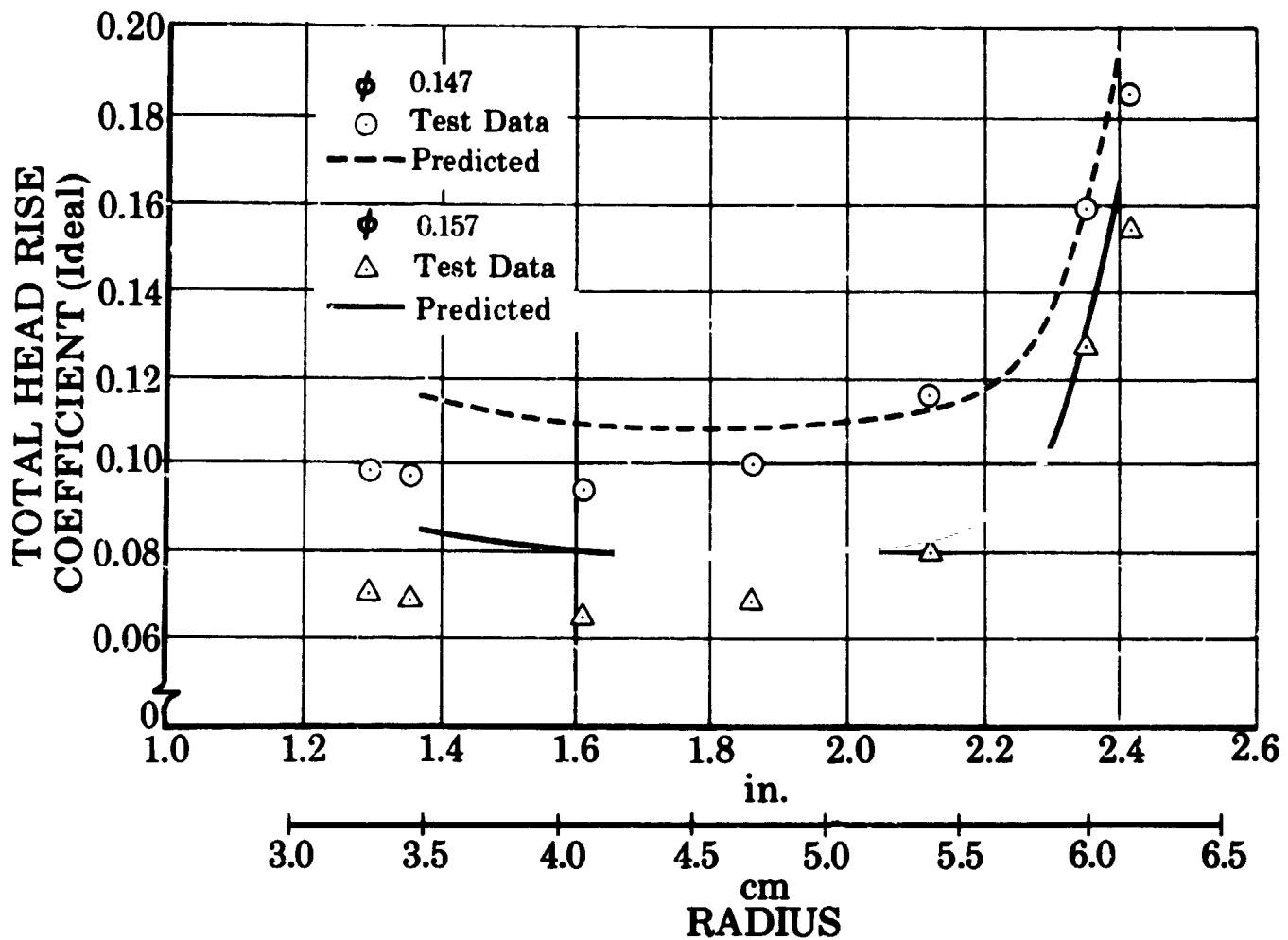


Figure 15. NASA 12-Degree Inducer Ideal Total Head Rise Coefficient vs Radius

FD 25400

(c) Total Head Loss Coefficient

Total head loss coefficient, $\bar{\omega}$ is mathematically defined as:

$$\bar{\omega} = \frac{\text{Loss in Total Relative Head}}{\text{Inlet Relative Dynamic Head}}$$

It is a measure of relative total head loss resulting from dumping and internal flow losses.

Figure 16 shows this loss coefficient as a function of radius. Again, close agreement between the experimental and the predicted program values occurs near the inducer tip while agreement decreases as the hub is approached.

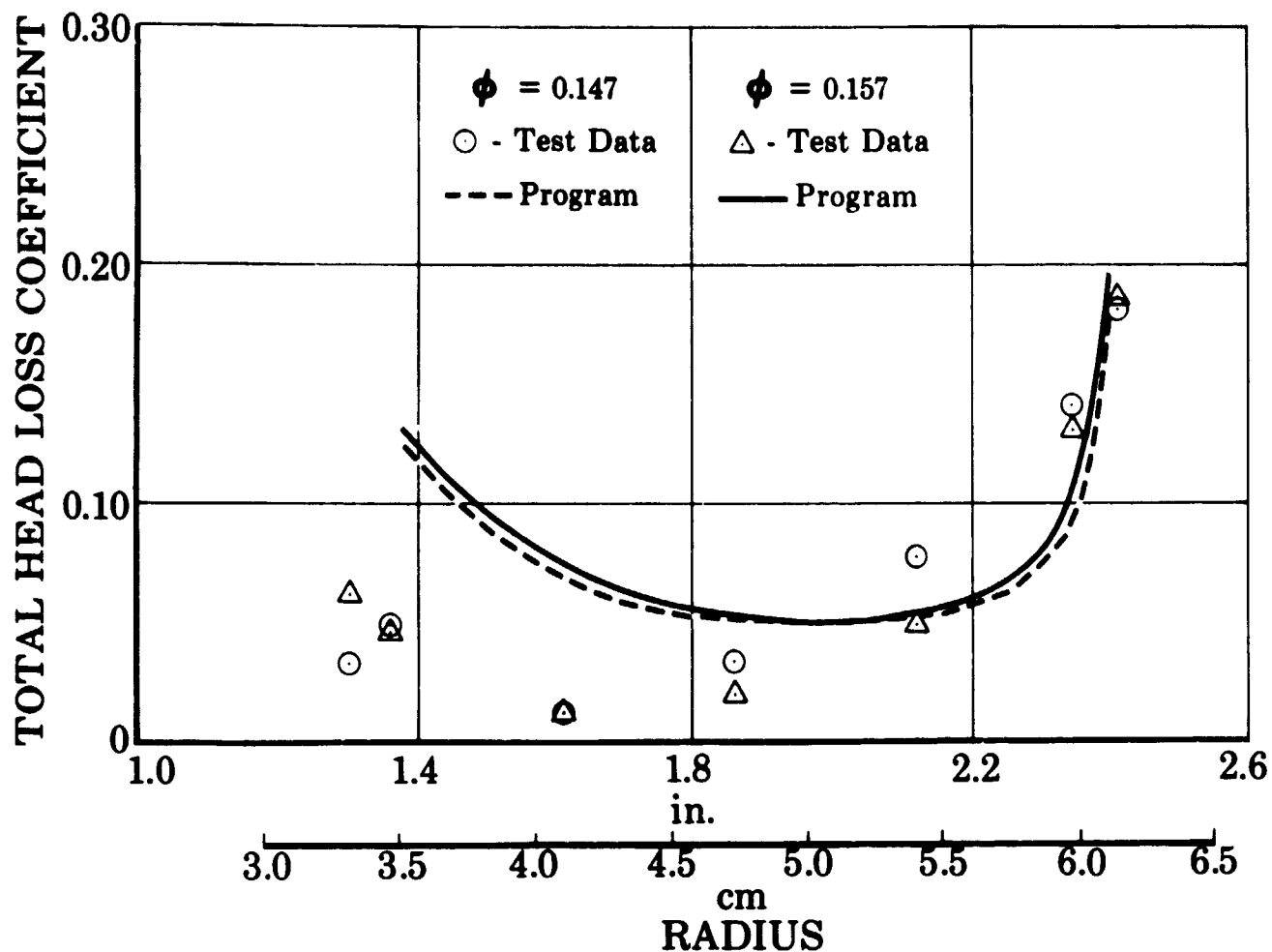


Figure 16. NASA 12-Degree Inducer Total Head Loss Coefficient vs Radius

FD 25409A

In the present loss system, an approximation in wetted perimeter within the blade passage at the hub and tip is based on a mean-height stream tube width instead of the actual hub and tip passage widths. This affects both the hub and the tip wetted perimeter, increasing the wetted perimeter at the hub and decreasing it slightly at the tip. Correcting the wetted perimeter for the actual passage width will result in a decrease in the flow losses along the hub and an increase at the tip. The relative error in the wetted perimeter and, hence in the skin friction losses, is more significant at the hub than at the tip. This is because the relatively large radius ratio (mean/inner) of the hub stream tube results in an appreciable difference between the mean stream tube width and the actual stream tube width at the hub. The mean stream tube width for the tip is a reasonable approximation for calculating the wetted perimeter because of the small radius ratio of the tip stream tube.

(d) Actual Total Head Rise Coefficient

The actual total head rise is equal to the ideal head rise minus the head losses. Figure 17 shows the variation of total head rise coefficient with inducer radius. Very close agreement occurs between the experimental and the predicted values not only at the tip, but also at the hub. Close agreement at the hub is partially because of the offsetting of high predicted ideal head rise with high predicted flow losses. If the flow losses had not offset the high predicted ideal head rise, the mass averaged actual head would still have agreed very well with the experimental value.

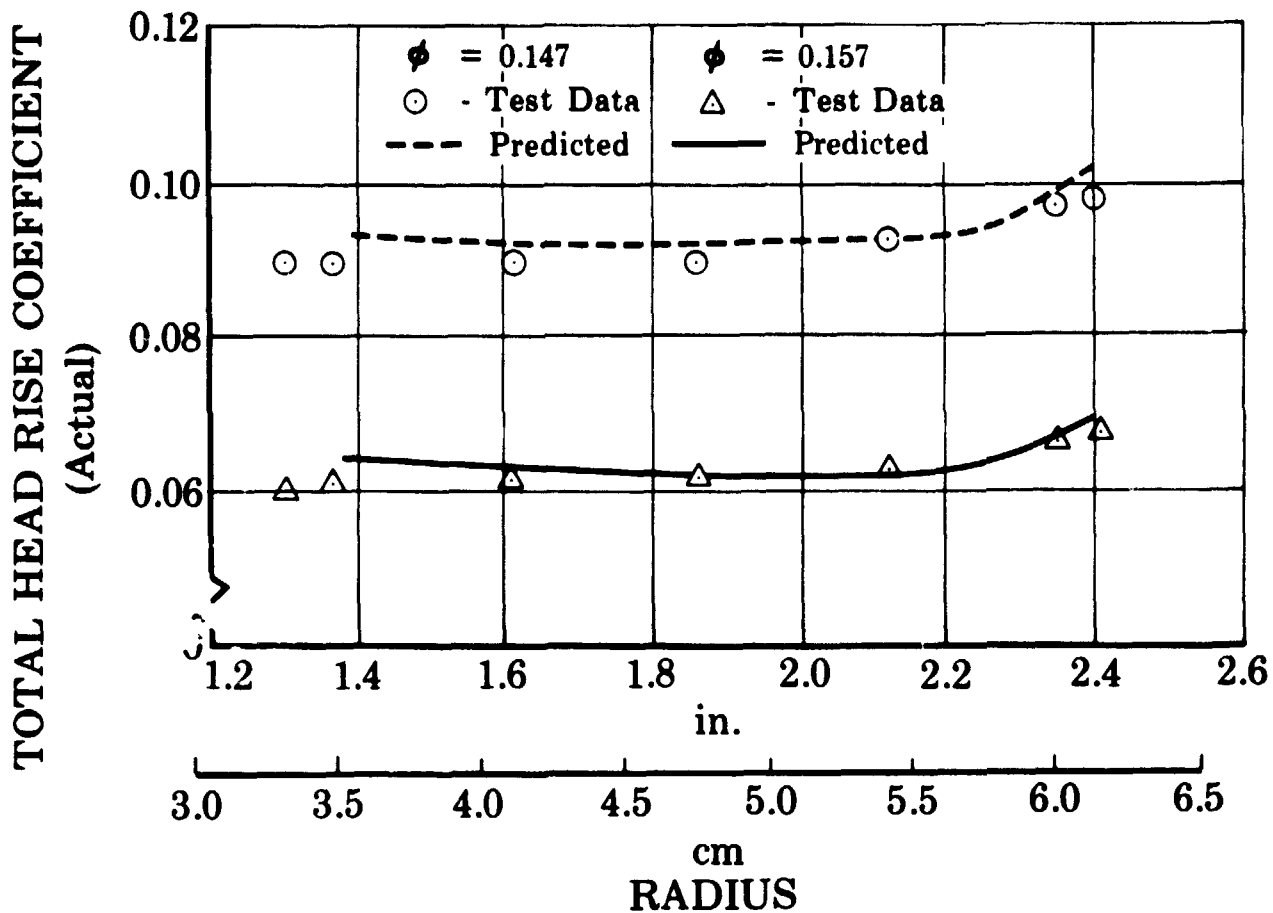


Figure 17. NASA 12-Degree Inducer Actual Total Head Rise Coefficient vs Radius

FD 25407

(e) Efficiency

Efficiency is merely a ratio of the actual to the ideal head rise. If the predicted actual and the ideal head rise agree well with data, it is expected that efficiency will also agree well. This is illustrated in figure 18.

(f) Axial Velocity

Figure 19 illustrates the agreement between the calculated and the test values of axial velocity (flow coefficient) at the exit. Good agreement here demonstrates correct radial distribution of boundary layer blockage and flow losses. The condition of radial equilibrium results in the correct radial distribution of axial velocity only if the total relative pressure and flow area are distributed correctly.

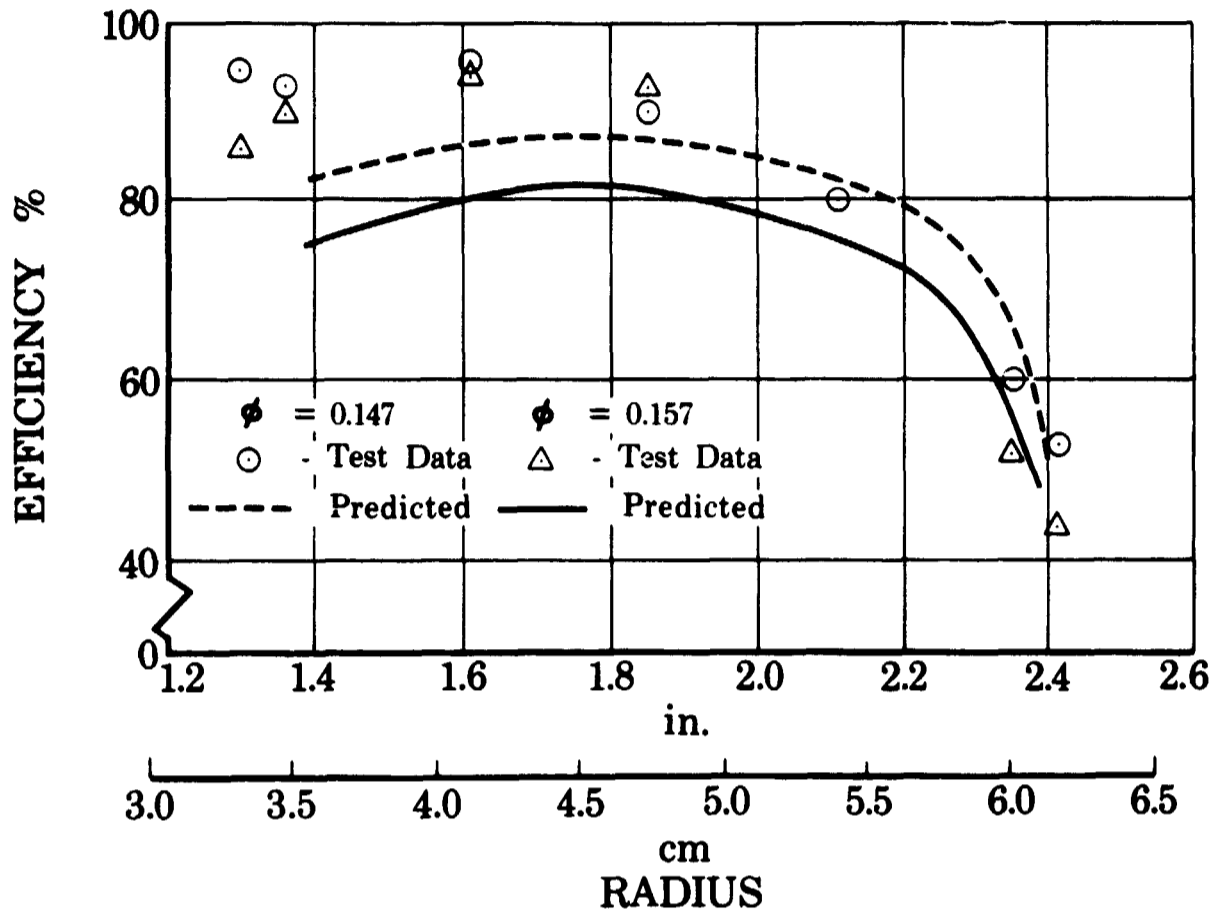


Figure 18. NASA 12-Degree Inducer Efficiency vs Radius

FD 25401

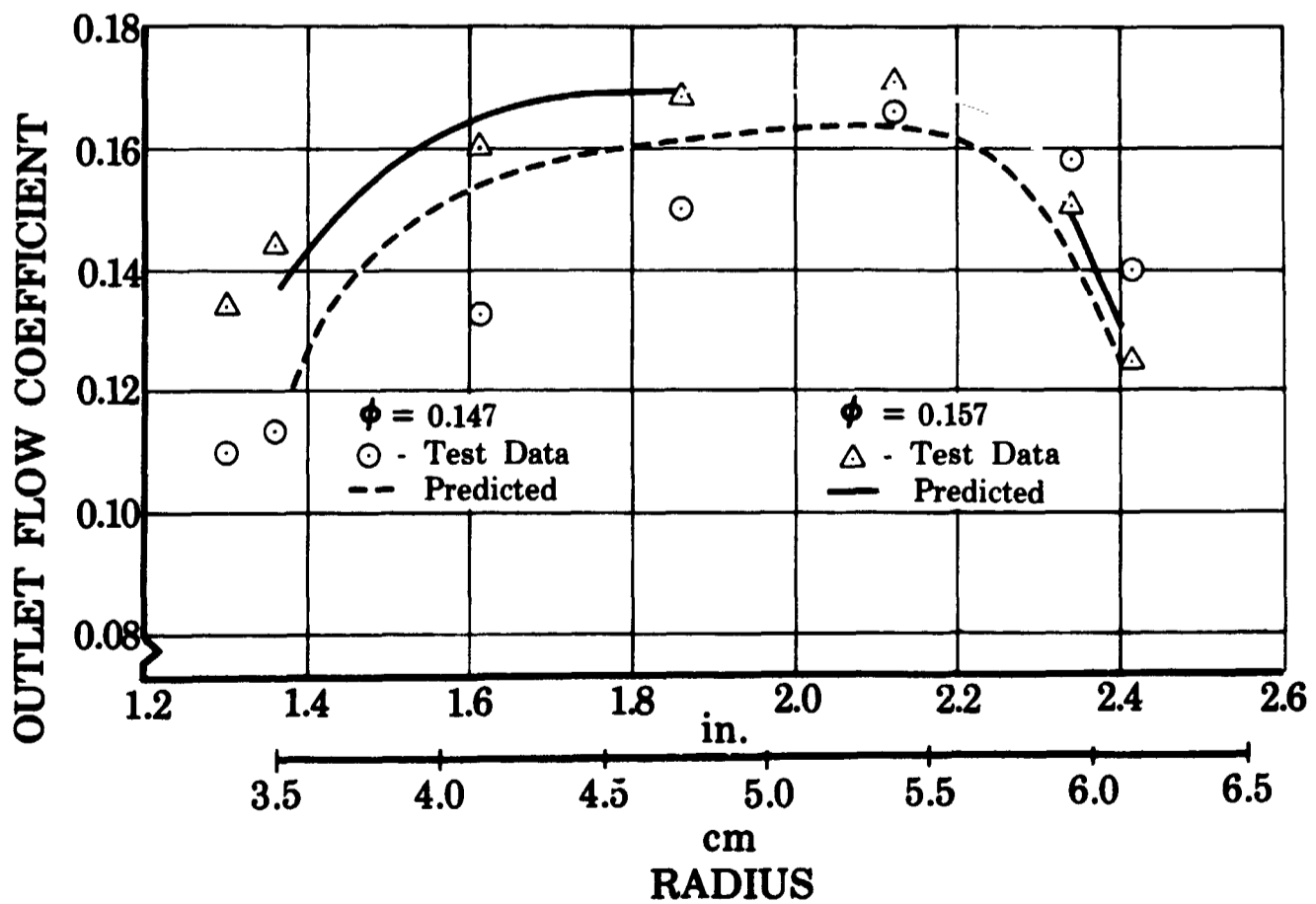


Figure 19. NASA 12-Degree Inducer Outlet Flow Coefficient vs Radius

FD 25402

(3) Cavitating Test Cases

(a) Cavitating Flat Plate Cascade

In paragraph Blc(11) above, the method of treating the cavity shape that is based on the work of Stripling and Acosta was discussed. In the referenced ASME paper (No. 61-WA-112), the authors presented plots of cavity shape for specific inlet conditions. Figure 20 compares the circular arc approximation from the analytical model and the exact solution of the authors. The agreement substantiates the validity of the circular arc cavity approximation, at least up to the point of maximum cavity height.

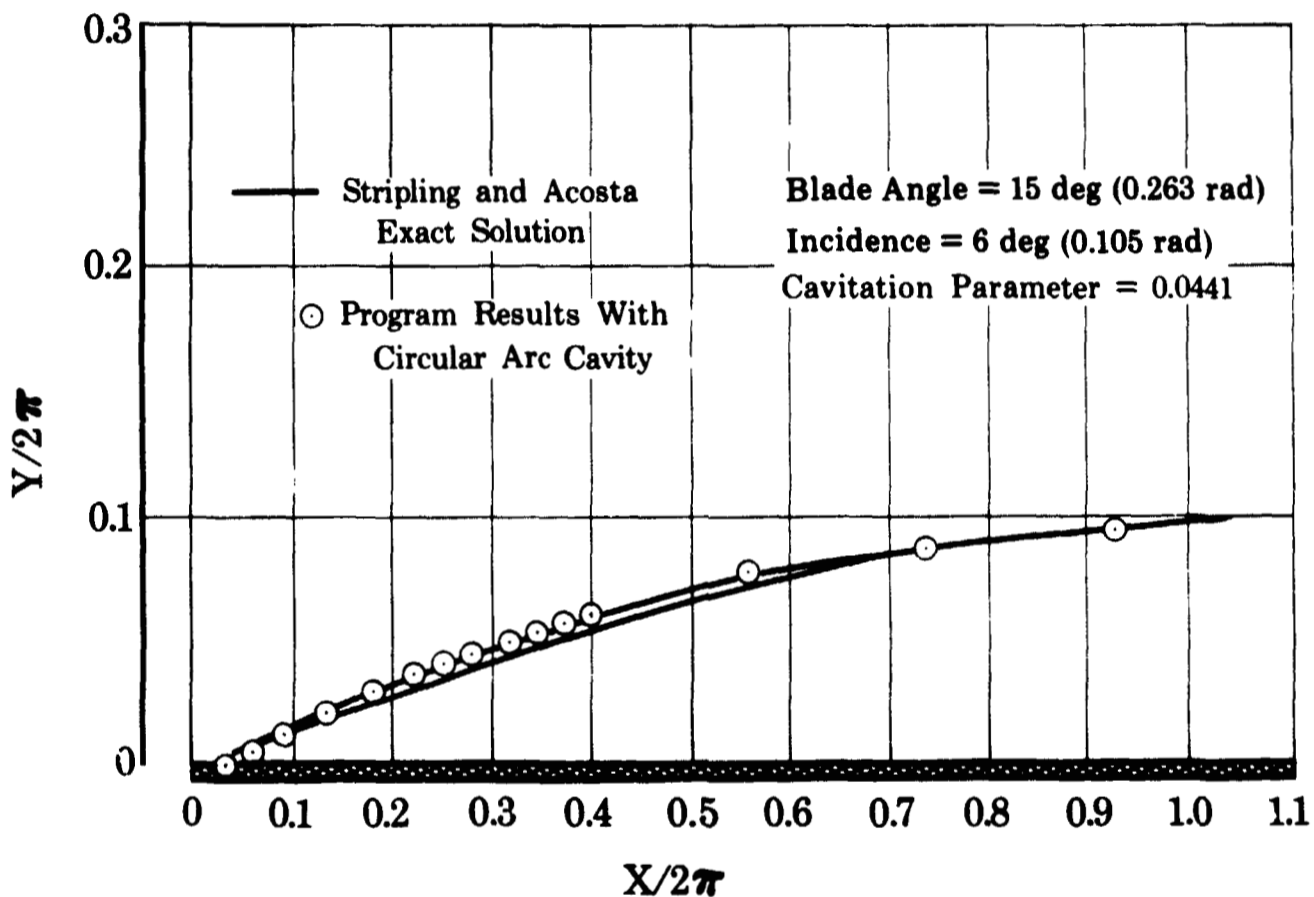


Figure 20. Flat Plate Cascade Cavitation Test Case

FD 25395

(1) NASA 12-deg (0.21-rad) Inducer (Cavitating)

(a) Illustration of Head Breakdown

Figure 21 illustrates the effect of the net positive suction head (NPSH) on the inducer average head coefficient. This figure demonstrates the ability of the hydrodynamic program to predict head breakdown or head fall-off.

The data shown here are for an inlet flow coefficient of 0.147 and consist of only four test points. The analytical prediction contains an abrupt increase in head coefficient just prior to complete head breakdown. The increase occurs when the cavity first reaches, and then progresses beyond, the blade trailing edge and is caused by the sudden increase in the effective blade exit angle. Although this type of

abrupt increase in head coefficient has been measured in other inducers, it is difficult to determine whether any abrupt increase actually occurred in the measured data. In any event, it is believed that the sudden increase predicted by the program is unrealistic and should be eliminated, possibly by a better smoothing function on effective blade angle. Preferably, some improvement in the cavity shape model behind the point of maximum height would provide a smoother transition.

It should be noted that the NPSH at complete head breakdown (i.e., choking) predicted by the program agrees very well with the test value.

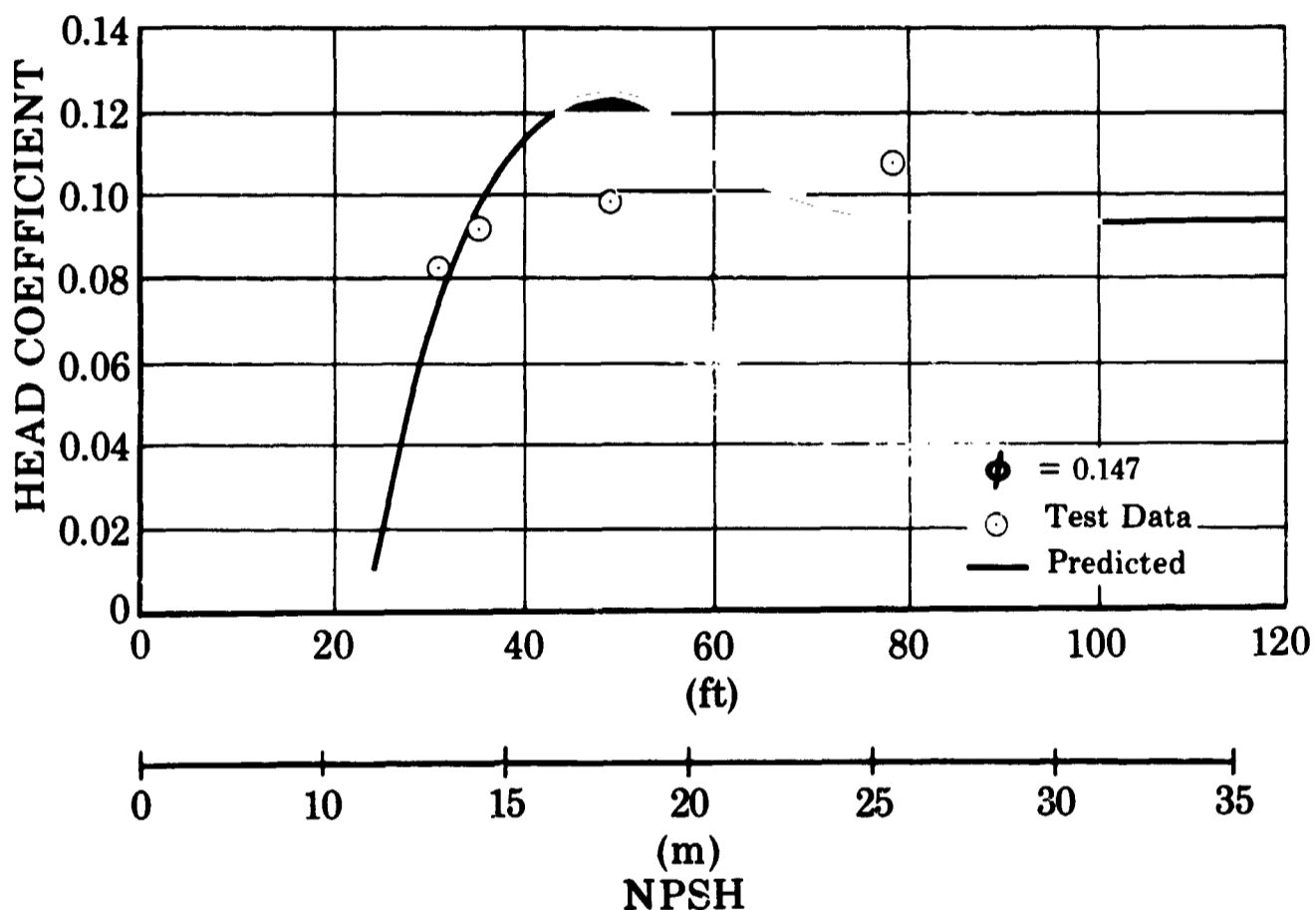


Figure 21. NASA 12-Degree Inducer Head Coefficient vs Net Positive Suction Head

FD 25398

(b) Nondimensional Inducer Performance

The overall head rise of an inducer operating under varying flow conditions (cavitating and noncavitating) can be recorded in nondimensional form. Figure 22 illustrates the overall head rise performance of the NASA 12-deg (0.21-rad) inducer recorded in the form $\Psi/\Psi_{\text{(noncavitating)}}$ as a function of cavitation parameter, k . As shown in this figure, the hydrodynamic program very closely agrees with the nondimensional overall head rise performance measured over a wide range of operating conditions and closely predicts the point of complete head breakdown. The sudden increase in head coefficient appearing in figure 21 and discussed above is omitted from figure 22.

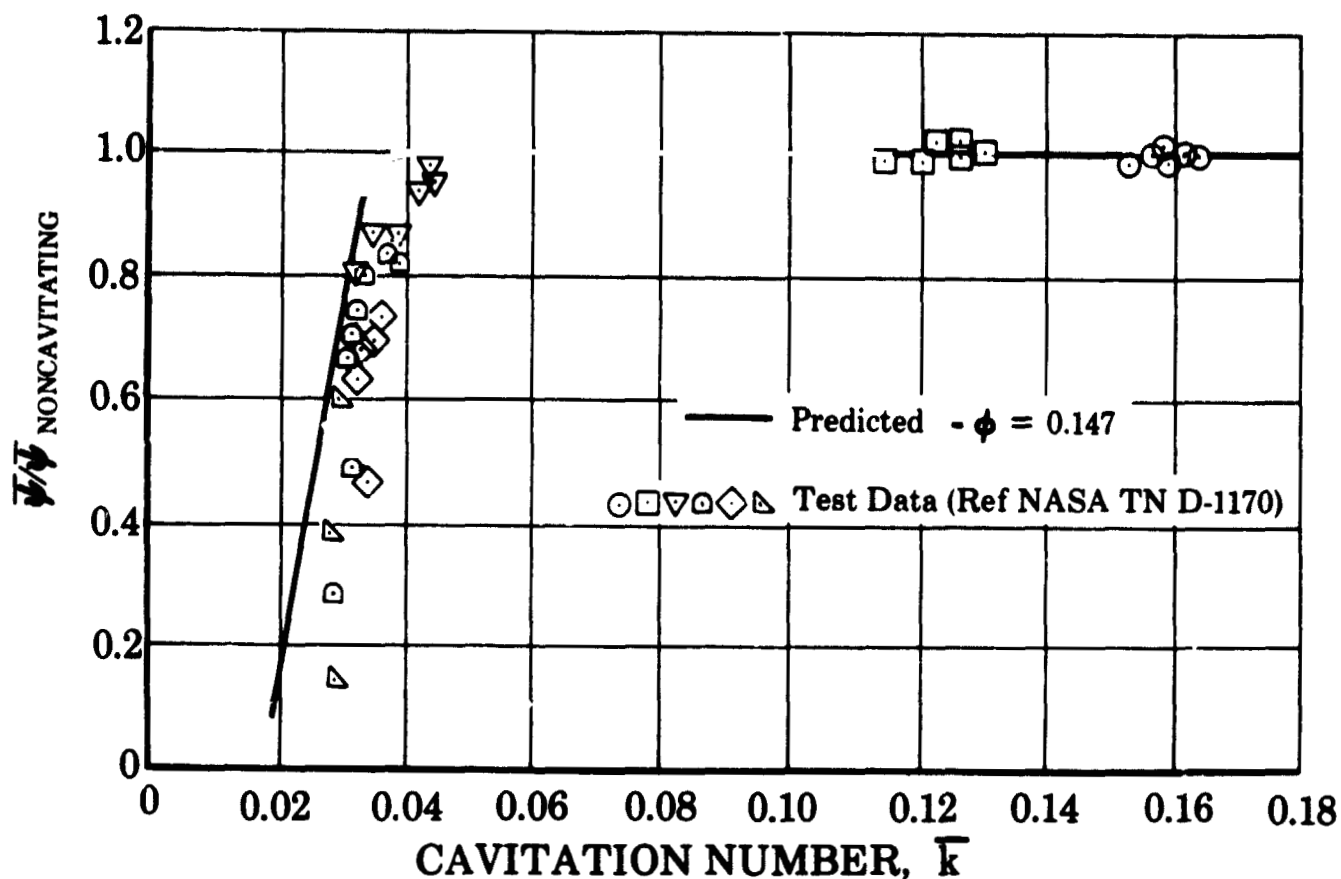


Figure 22. NASA 12-Degree Inducer Cavitating Performance FD 25399

e. Future Developments

It is anticipated that in Task VI information will be obtained from the testing that will either substantiate the present model or lead to improvements. In particular, the blade pressure distributions will provide a basis for determining the deviation angles and the extent and shape of the cavity. These pressure loadings can be used to solve the indirect flow problem and determine the shape of the liquid flow passage. From this, the cavity shape can be deduced.

Improvements in the deviation angle and boundary layer blockage would improve the agreement between the calculated and the test values of velocities and angles, as shown in the previous section for the NASA 12-deg (0.21-rad) inducer. Development of the loss system should include a more accurate estimate of the diffusion losses. This might be accomplished through the use of a boundary layer model that includes the influence of pressure gradients.

Finally, the input-output information and format should be arranged to provide that a minimum of work is required to translate information from the hydrodynamic analysis to the stress analysis.

2. Computer Programs for Predicting Stresses and Vibration Characteristics of Inducer Blades

a. Introduction

Computer programs for determining stress and vibratory characteristics in three-dimensional inducer blades have been developed.

The programs are based on the matrix displacement method using discrete flat triangular elements to define the blade surface.

The inducer blade middle surface is generated by a skew line that moves at a fixed distance from the axis of the inducer. The numerical (x,y,z) coordinates of this surface are thus directly defined by the wrap angle θ and elevation of the generating line. This surface is then replaced by flat triangular elements that are joined at the vertices or nodes that lie on the surface. The curvature of the surface is thus approximated by the change in direction of the normals to the triangular elements. Each element has a local rectangular coordinate system $(\bar{x},\bar{y},\bar{z})$ associated with it. Displacement functions, which are expressed in terms of local coordinates, yield stiffness, centrifugal load, pressure load, and inertia matrices expressed in terms of generalized nodal forces and generalized nodal displacements.

For the stress program, these matrices are first transformed to a common rectangular coordinate system. Assembly of these matrices, by satisfying compatibility and equilibrium at common nodes and boundary conditions, yields a set of simultaneous equations with nodal displacements as unknowns. Displacements that satisfy this set of equations are then used to calculate stresses.

The vibration program is handled differently than the stress program because only 50 degrees of freedom can be handled by an existing latent root or eigen-value program. This allows a breakup of only eight free nodes each of which has six degrees of freedom. For this reason, the number of degrees of freedom per free node was reduced to one by first assuming that the dominant displacement is normal to the surface and then using matrix condensation techniques. In this instance, local stiffness and inertia matrices were transformed to a rectangular coordinate system in which the normal direction at a node is in the mean direction of the normals of a set of triangular elements which have common vertices at a node. Assembly of these matrices by satisfying nodal compatibility and equilibrium followed by a matrix condensation yields frequency equations from which frequency and mode shapes are obtained.

b. Description of Analytical Model

(1) Blade Generation

A typical inducer is shown in figure 23. The inducer blade is normally machined by a straight milling cutter whose axis is tilted and may pass at a fixed distance from the axis of the inducer while the inducer blank advances and rotates at the desired lead. The middle surface of the inducer blade is used for purposes of analysis and geometric parameters that define the right-handed (x,y,z) coordinates of the surface as hub radius R_H , off-set radius, R_G , tilt angle λ , lead height z_H , radius R along projection of generator, and wrap angle θ as shown in figure 24. The (x,y,z) coordinates in terms of these parameters are:

$$\begin{aligned}x &= R_G \cos \theta - R \sin \theta \\y &= R_G \sin \theta + R \cos \theta \\z &= z_H + (R - R_H) \tan \lambda\end{aligned}$$



Figure 23. Turbopump Inducer

FE 70544

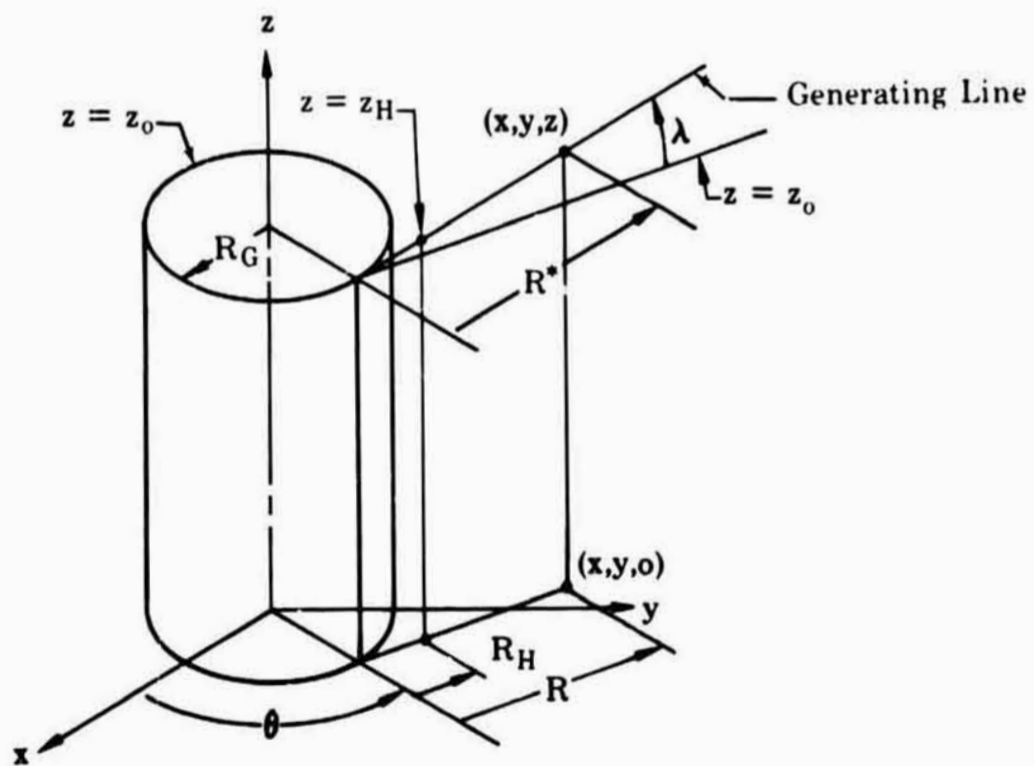


Figure 24. Geometric Parameters of Middle Surface of Inducer Blade

FD 25602A

(2) Finite Element Breakup

The use of discrete triangular elements for the stress analysis of three dimensional surfaces is discussed by Argyris, Cheung, Petyt, Zienkiewicz and others. In this instance, the surface is replaced by flat triangular elements that are joined at the vertices or nodes which lie on the original surface. Such analysis requires that the coordinates of the node be expressed in a common and local rectangular coordinate system. A right hand local system was chosen so that the base of each triangle lies on a generating line which defines the \bar{x} axis while the third vertex lies on an adjacent generator. The \bar{y} axis lies in the plane of the triangle in a right-hand sense as shown in figure 25. In this manner the coordinates of the nodes of each triangle are well defined because they always lie on generating lines whose coordinates are known.

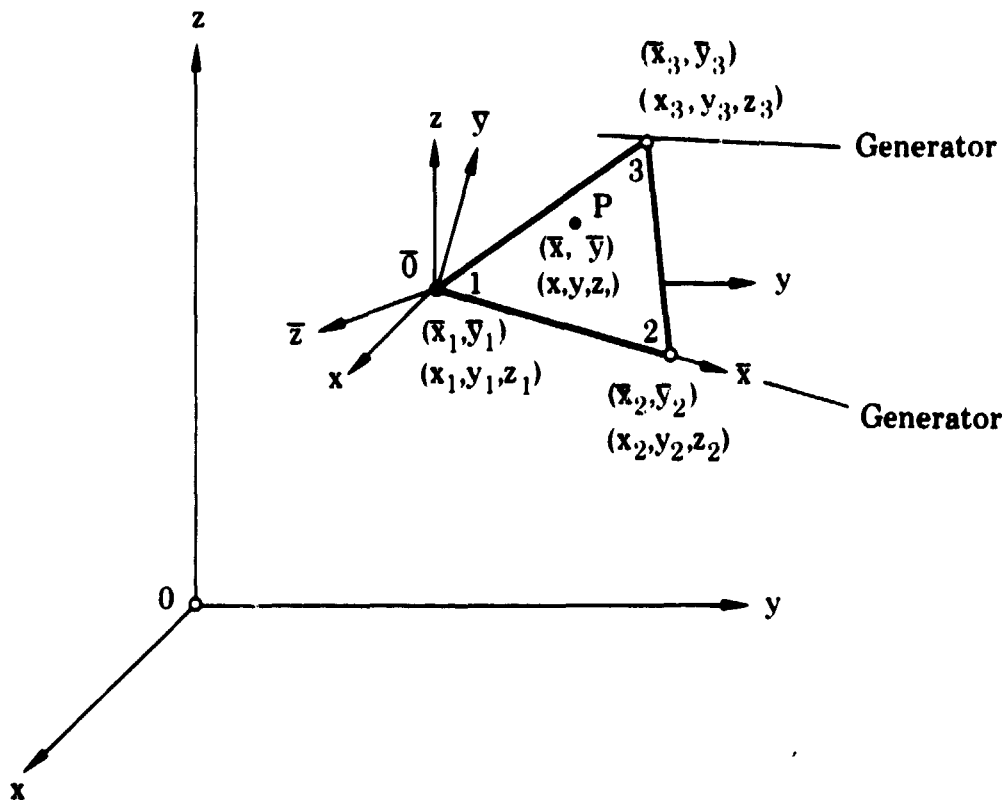


Figure 25. Local $|\bar{x}, \bar{y}, \bar{z}|$ and Common $|x, y, z|$ Rectangular Coordinate System for Triangular Element FD 25629

Nodal points are equally spaced on a generator between the hub radius R_H^* and tip radius R_T^* and establish the triangulation of the inducer blade as shown in figure 26. The common coordinates of the vertices are then used to calculate the direction cosine matrix $[R_1]$ by equation 46. This matrix establishes the relation between the directions of the local coordinate axes relative to the common coordinate axes for each element and is defined as:

$$[R_1] = \begin{bmatrix} \cos(x, \bar{x}), \cos(x, \bar{y}), \cos(x, \bar{z}) \\ \cos(y, \bar{x}), \cos(y, \bar{y}), \cos(y, \bar{z}) \\ \cos(z, \bar{x}), \cos(z, \bar{y}), \cos(z, \bar{z}) \end{bmatrix}$$

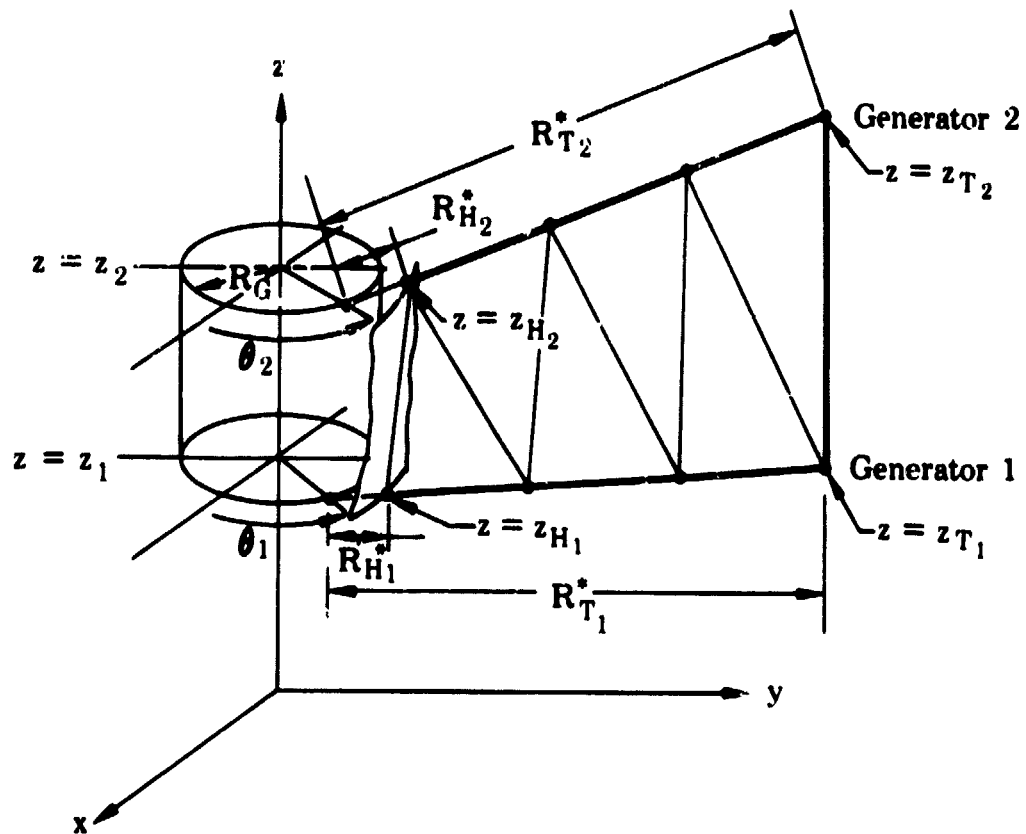


Figure 26. Triangulation of Inducer Blade

FD 25630A

This matrix is used later for transforming stiffness and mass matrices and is used to calculate the local nodal coordinates by the following relations:

$$\left\{ \bar{\psi}_1 \right\}_N = \begin{Bmatrix} \bar{x}_1 \\ \bar{y}_1 \\ \bar{z}_1 \end{Bmatrix} = \left\{ 0 \right\}$$

$$\left\{ \bar{\psi}_2 \right\}_N = \begin{Bmatrix} \bar{x}_2 \\ 0 \\ 0 \end{Bmatrix} = \left[R_1 \right]^T \begin{Bmatrix} x_2 - x_1 \\ y_2 - y_1 \\ z_2 - z_1 \end{Bmatrix}$$

$$\left\{ \bar{\psi}_3 \right\}_N = \begin{Bmatrix} \bar{x}_3 \\ y_3 \\ 0 \end{Bmatrix} = \left[R_1 \right]^T \begin{Bmatrix} x_3 - x_1 \\ y_3 - y_1 \\ z_3 - z_1 \end{Bmatrix}$$

or in matrix form:

$$\left\{ \bar{\psi} \right\}_N = \left[R_1 \right]^T \left\{ \psi - \psi_1 \right\}_N$$

where

$$\left[\psi \right]_N = \begin{bmatrix} x_1, x_2, x_3 \\ y_1, y_2, y_3 \\ z_1, z_2, z_3 \end{bmatrix}$$

(3) Displacement Functions for Triangular Elements

The use of triangular elements for finite element analysis is discussed extensively by Argyris, Cheung, Clough, Hermann, Melosh, Petyt, Tocher, Utku, Zienkiewicz, and others. Methods which are directly applicable to the three-dimensional inducer problem are discussed by Argyris, Cheung, Petyt, and Zienkiewicz.

The accuracy of the displacement method depends upon the selection of an appropriate displacement function; polynomial functions usually being the most appropriate.

For the triangular element under in-plane membrane loading the expressing of local membrane displacements \bar{u} and \bar{v} as linear functions of \bar{x} and \bar{y} yields a uniform strain field in the triangular element. Such a function provides compatibility at the interface between adjacent elements and involves six coefficients that are determined in terms of the six nodal displacements and six nodal coordinates of the vertices of the triangle. Linear displacement functions are used in the derivation of the membrane stiffness matrix $[\bar{K}_M]$ and the membrane inertia matrix $[\bar{M}_M]$ in paragraphs B2d(5) and B2d(10), respectively.

An appropriate displacement function for triangular elements under bending is more difficult to set up because in addition to a lateral deflection, \bar{w} , there are rotations, $\bar{\theta}_x$ and $\bar{\theta}_y$. Thus, there will be nine nodal displacements for each triangular element. If a cubic polynomial deflection function with terms like; const., \bar{x} , \bar{y} , \bar{x}^2 , \bar{xy} , \bar{y}^2 , \bar{x}^3 , $\bar{x}^2\bar{y}$, \bar{xy}^2 , \bar{y}^3 , is selected, one of the 10 terms will have to be deleted because only nine conditions can be satisfied, and hence the displacement function can have only nine coefficients. Although compatibility of edge displacement and slope in the direction of edges at an interface exists for the cubic displacement function, there is no guarantee that the normal slope in a direction perpendicular to the edges is continuous. It is not known how much error will be caused by such nonconformity. Clough, Zienkiewicz, and others discuss methods of obtaining conforming displacement functions but they are too complicated for use on the inducer program.

Pratt & Whitney Aircraft has had success in other problem areas with the Adini polynomial displacement function

$$w = \bar{a}_1 + \bar{a}_2\bar{x} + \bar{a}_3\bar{y} + \bar{a}_4\bar{x}^2 + \bar{a}_5\bar{y}^2 + \bar{a}_6\bar{x}^3 + \bar{a}_7\bar{x}^2\bar{y} + \bar{a}_8\bar{xy}^2 + \bar{a}_9\bar{y}^3$$

where the uniform twist term, \bar{xy} , in the 10 term cubic polynomial is omitted to maintain symmetry as discussed by Clough. This displacement function is used for the inducer program, and it is hoped that comparison of test cases with theoretical solutions can be used to determine the error caused by using this function.

c. Methods of Analysis

(1) Stress Program

(a) Forces and Displacements

The matrix displacement method using discrete triangular elements is used for these programs. In this method generalized nodal forces are expressed as linear functions of generalized nodal displacements in matrix form. These matrices are derived in paragraph B2d, below, and are determined for triangular elements in the local coordinate system. The force and displacement systems are right-handed, and the components are shown in figures 27 and 28. Moments and rotations are treated as vectors in the same manner as forces and displacements, as is done by Petyt and Zienkiewicz. This prevents confusion when transforming matrices to a rotated coordinate system. The matrix relation for the local system is then:

$$\begin{bmatrix} \bar{F}_{x_1} \\ \bar{F}_{y_1} \\ \bar{F}_{x_2} \\ \bar{F}_{y_2} \\ \bar{F}_{x_3} \\ \bar{F}_{y_3} \\ \bar{F}_{z_1} \\ \bar{M}_{x_1} \\ \bar{M}_{y_1} \\ \bar{F}_{z_2} \\ \bar{M}_{x_2} \\ \bar{M}_{y_2} \\ \bar{F}_{z_3} \\ \bar{M}_{x_3} \\ \bar{M}_{y_3} \end{bmatrix}_N = \begin{bmatrix} \bar{K}_M & 0 \\ 0 & \bar{K}_B \end{bmatrix} \begin{bmatrix} \bar{u}_1 \\ \bar{v}_1 \\ \bar{u}_2 \\ \bar{v}_2 \\ \bar{u}_3 \\ \bar{v}_3 \\ \bar{w}_1 \\ \bar{\theta}_{x_1} \\ \bar{\theta}_{y_1} \\ \bar{w}_2 \\ \bar{\theta}_{x_2} \\ \bar{\theta}_{y_2} \\ \bar{w}_3 \\ \bar{\theta}_{x_3} \\ \bar{\theta}_{y_3} \end{bmatrix}_N \quad (35)$$

(6x6)
(6x9)
(9x6)
(9x9)
(15 x 1)
(15 x 15)
(15 x 1)

where \bar{K}_M and \bar{K}_B are the local membrane and bending stiffness matrices whose composite form is \bar{K} , and \bar{F}_N and $\bar{\delta}_N$ are generalized nodal force and displacement column matrices or vectors. Displacements and moments in the local \bar{z} direction are assumed zero as is discussed by Zienkiewicz. These terms, however, will appear in this common system and are retained for convenience.

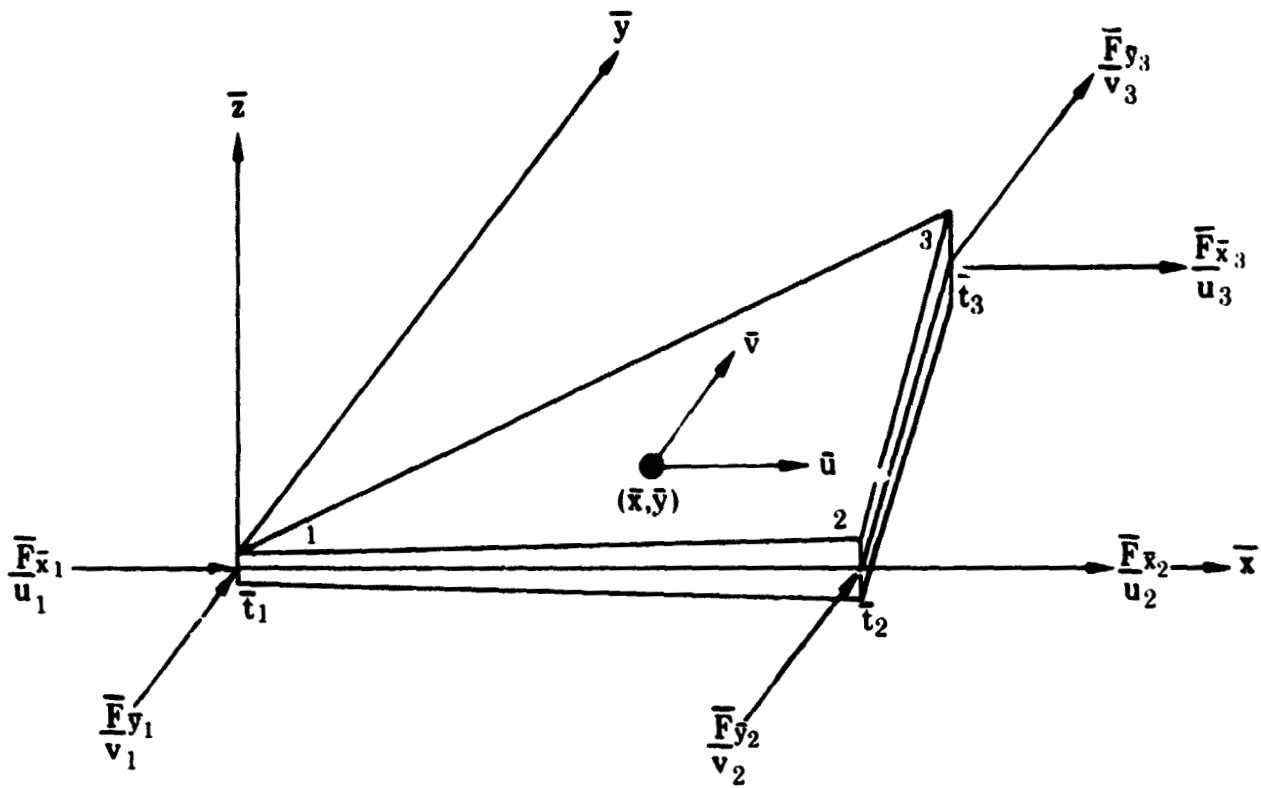


Figure 27. Generalized Nodal Local Membrane Displacements and Forces On Flat Triangular Element FD 25631A

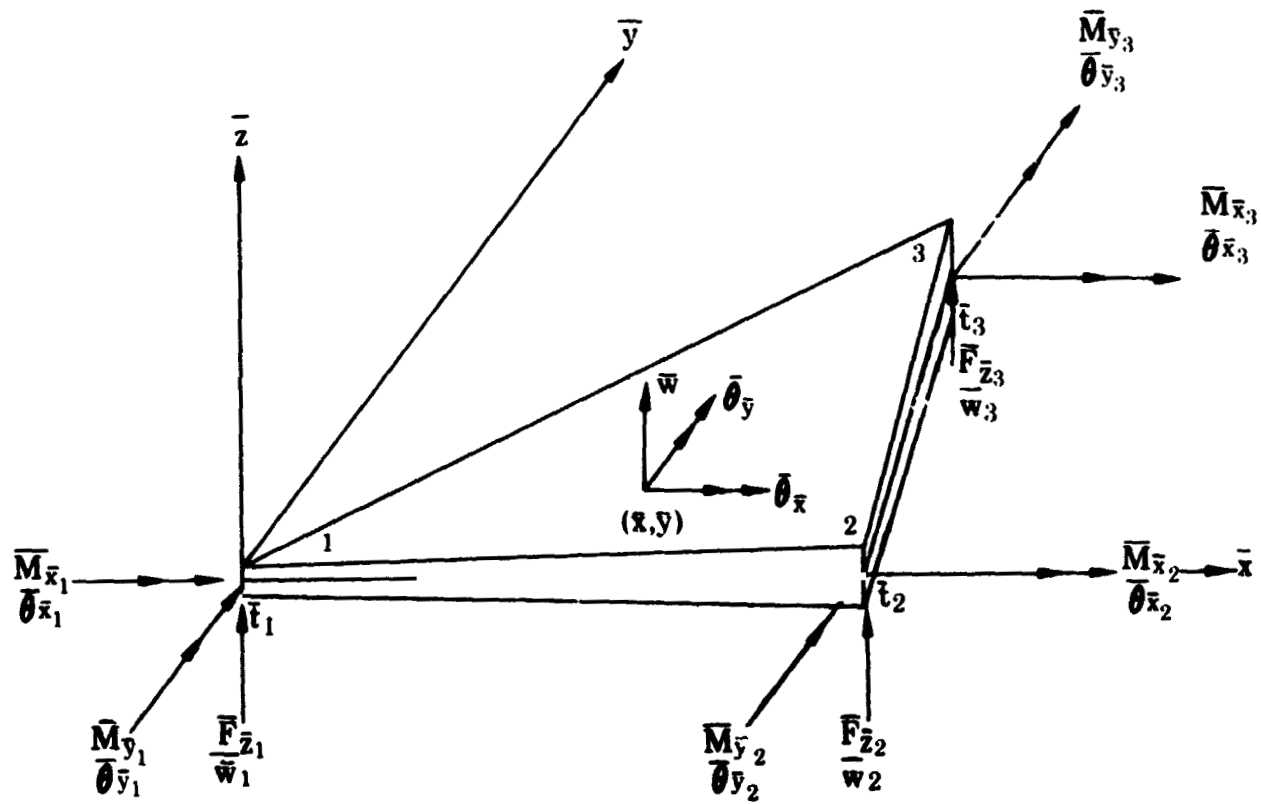


Figure 28. Generalized Nodal Bending Displacements and Forces On Flat Triangular Element FD 25652A

Generalized nodal pressure force matrices $\{\bar{F}_p\}_N$ and generalized nodal centrifugal force matrices $\{\bar{F}_c\}$, which have been derived in paragraphs B2d(7) and B2d(8), are also column matrices or vectors of the same order as $\{\bar{F}\}_N$. With these forces acting the general nodal force-displacement relation for a triangular element in local coordinates is:

$$\{\bar{F}\}_N = [\bar{K}]\{\bar{\delta}\}_N - \{\bar{F}_p\}_N - \{\bar{F}_c\}_N \quad (36)$$

To solve the three-dimensional stress problem, all generalized forces and displacements in this local system must be broken into components along the axes in the common system. This is accomplished by applying the direction cosine matrix $[R_1]$ to triplets of generalized forces and displacements in the local system. Because there are 6 degrees of freedom per node the stiffness matrix for a triangular element will be of order (18 x 18) and the generalized force and displacement matrices will be of order (18 x 1). To make the local matrices compatible, they must be of the same order. This is accomplished by placing zeros in appropriate positions; $\{\bar{F}_p\}_N$ and $\{\bar{F}_c\}_N$ are also expressed as an (18 x 1) column matrix by inserting zeros in appropriate locations.

$$\begin{array}{c}
 \begin{array}{c}
 F_{x_1} \\
 F_{y_1} \\
 F_{z_1} \\
 \hline
 F_{x_2} \\
 F_{y_2} \\
 F_{z_2} \\
 \hline
 F_{x_3} \\
 F_{y_3} \\
 F_{z_3} \\
 \hline
 M_{x_1} \\
 M_{y_1} \\
 M_{z_1} \\
 \hline
 M_{x_2} \\
 M_{y_2} \\
 M_{z_2} \\
 \hline
 M_{x_3} \\
 M_{y_3} \\
 M_{z_3}
 \end{array} \\
 (18 \times 1)
 \end{array}
 \cdot
 \begin{array}{c}
 \begin{array}{c}
 u_1 \\
 v_1 \\
 w_1 \\
 \hline
 u_2 \\
 v_2 \\
 w_2 \\
 \hline
 u_3 \\
 v_3 \\
 w_3 \\
 \hline
 \theta_{x_1} \\
 \theta_{y_1} \\
 \theta_{z_1} \\
 \hline
 \theta_{x_2} \\
 \theta_{y_2} \\
 \theta_{z_2} \\
 \hline
 \theta_{x_3} \\
 \theta_{y_3} \\
 \theta_{z_3}
 \end{array} \\
 (18 \times 1)
 \end{array}
 =
 \begin{array}{c}
 \left[\begin{array}{c}
 [R_1] \\
 \hline
 [R_1] \\
 \hline
 [R_1] \\
 \hline
 [R_1] \\
 \hline
 [R_1] \\
 \hline
 [R_1] \\
 \hline
 [R_1] \\
 \hline
 [R_1] \\
 \hline
 [R_1] \\
 \hline
 [R_1] \\
 \hline
 [R_1] \\
 \hline
 [R_1] \\
 \hline
 [R_1] \\
 \hline
 [R_1]
 \end{array} \right]
 \begin{array}{c}
 \begin{array}{c}
 \bar{F}_{x_1} \\
 \bar{F}_{y_1} \\
 \bar{F}_{z_1} \\
 \hline
 \bar{F}_{x_2} \\
 \bar{F}_{y_2} \\
 \bar{F}_{z_2} \\
 \hline
 \bar{F}_{x_3} \\
 \bar{F}_{y_3} \\
 \bar{F}_{z_3} \\
 \hline
 \bar{M}_{x_1} \\
 \bar{M}_{y_1} \\
 \bar{M}_{z_1} \\
 \hline
 \bar{M}_{x_2} \\
 \bar{M}_{y_2} \\
 \bar{M}_{z_2} \\
 \hline
 \bar{M}_{x_3} \\
 \bar{M}_{y_3} \\
 \bar{M}_{z_3}
 \end{array} \\
 (18 \times 1)
 \end{array}
 \cdot
 \begin{array}{c}
 \begin{array}{c}
 u_1 \\
 v_1 \\
 w_1 \\
 \hline
 u_2 \\
 v_2 \\
 w_2 \\
 \hline
 u_3 \\
 v_3 \\
 w_3 \\
 \hline
 \theta_{x_1} \\
 \theta_{y_1} \\
 \theta_{z_1} \\
 \hline
 \theta_{x_2} \\
 \theta_{y_2} \\
 \theta_{z_2} \\
 \hline
 \theta_{x_3} \\
 \theta_{y_3} \\
 \theta_{z_3}
 \end{array} \\
 (18 \times 1)
 \end{array}$$

(18 x 18) SYMMETRIC

or, in matrix notation

$$\{F\}_N = [R_6] \{\bar{F}\}_N \tag{38}$$

$$\{\delta\}_N = [R_6] \{\bar{\delta}\}_N \tag{39}$$

The general force-displacement matrix relation for a triangular element in the common system is obtained conventionally by transforming (36) using (38) and (39) from which

$$\{\bar{F}\}_N = [R_6]^T \{F\}_N \text{ and } \{\bar{\delta}\}_N = [R_6]^T \{\delta\}_N$$

Then (36) transforms from

$$\{\bar{F}\}_N = [\bar{K}] \{\bar{\delta}\}_N - \{\bar{F}_P\}_N - \{\bar{F}_C\}_N$$

to

$$[R_6]^T \{F\}_N = [\bar{K}] [R_6]^T \{\delta\}_N - [R_6]^T \{F_P\}_N - [R_6]^T \{F_C\}_N$$

or

$$\{F\}_N = [R_6] [\bar{K}] [R_6]^T \{\delta\}_N - \{F_P\}_N - \{F_C\}_N$$

Thus, the general force-displacement matrix relation for a triangle in the common system is expressed by

$$\{F\}_N = [K] \{\delta\}_N - \{F_P\}_N - \{F_C\}_N \quad (40)$$

where the elements on the right side are obtained directly from the local system properties by the relations

$$\{F_P\}_N = [R_6] \{\bar{F}_P\}_N$$

$$\{F_C\}_N = [R_6] \{\bar{F}_C\}_N$$

$$[K] = [R_6] [\bar{K}] [R_6]^T$$

The generalized nodal displacement matrix relation for the triangulated surface was assembled by considering a representative node that is common to neighboring triangular elements as shown in figure 29. Because each node has 6 degrees of freedom there will be 6n degrees of freedom for a system with n free nodes. Thus all column matrices will be of order (6n x 1) and the stiffness matrix will be of order (6n x 6n). The operations that yield the displacement matrix relation are:

1. Add the elements of $\{F_P\}_N$ and $\{F_C\}_N$ which are associated with a common node. This yields the system matrices $\{F_P\}_T$ and $\{F_C\}_T$
2. Sum all of the elements of $\{F\}_N$ which are associated with a common node to zero in order to satisfy internal nodal equilibrium
3. Equate generalized displacements of vertices that have a common node.
4. Add elements of stiffness matrices which are associated with a common node. This will yield the system stiffness matrix $[K]_T$.

The generalized displacement matrix equation for the system is then

$$\left[K \right]_T \left\{ \delta \right\}_N - \left\{ F_P \right\}_T - \left\{ F_C \right\}_T = \left\{ 0 \right\} \quad (41)$$

The solution to this set of simultaneous equations yields the generalized nodal displacements $\left\{ \delta \right\}_N$. These are then transformed back to the local system by

$$\left\{ \bar{\delta} \right\}_N = \left[R_6 \right]^T \left\{ \delta \right\}_N$$

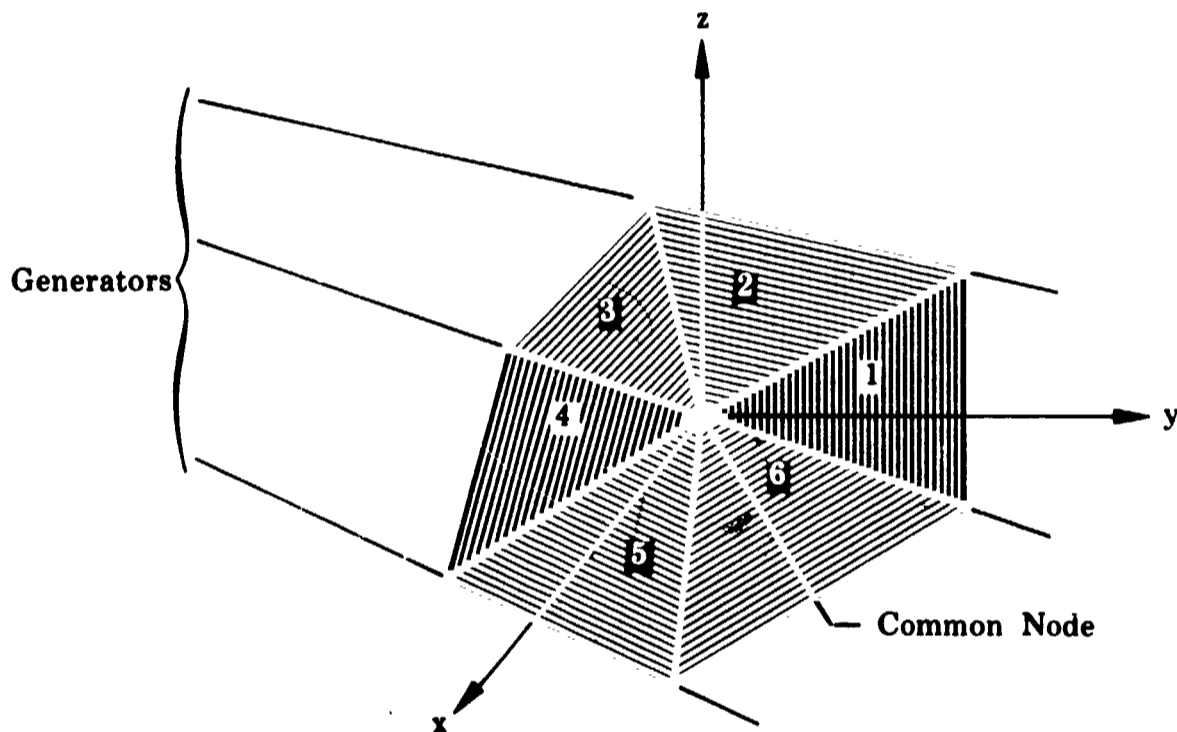


Figure 29. Common Node of 6 Neighboring Triangles

FD 25667A

(b) Stresses

The membrane stress and bending moment in terms of the local system are then given by

$$\left\{ \bar{\sigma} \right\}_M = \begin{Bmatrix} \bar{\sigma}_{xx} \\ \bar{\sigma}_{yy} \\ \bar{\tau}_{xy} \end{Bmatrix}_M = \left[\bar{E}_M \right] \left[\bar{w}_M \right] \left[\bar{A}_M \right]_N^{-1} \left\{ \bar{\delta} \right\}_M$$

$$\left\{ \bar{M} \right\}_B = \begin{Bmatrix} \bar{M}_x \\ \bar{M}_y \\ \bar{M}_{xy} \end{Bmatrix}_B = \left[\bar{D} \right] \left[\bar{v}_B \right] \left[\bar{E}_B \right] \left[\bar{A}_B \right]_N^{-1} \left\{ \bar{\delta} \right\}_B$$

where the symbols are defined in paragraph d. The bending moments are linear functions of \bar{x} and \bar{y} and are evaluated at the centroid C to yield the centroidal bending stresses.

$$\left\{ \bar{\sigma}_B \right\} = \left\{ \begin{array}{c} \bar{\sigma}_x \\ \bar{\sigma}_y \\ \bar{\tau}_{xy} \end{array} \right\}_B = \frac{6 \bar{M}_c}{E_c^2}$$

(c) Development of Subsystems

The direct solution of the set of simultaneous equations (41) is time-consuming and uneconomical when a large number of unknowns is involved. For this reason, the execution time was reduced by subsystem analysis. This was accomplished by providing an option to divide the system into subsystems as shown in figure 30. Each subsystem has common boundary nodes a and internal nodes b. The internal nodes include all nodes that do not lie on a common boundary. The general force-displacement relation for each subsystem is of the form (40) and becomes

$$\left\{ F \right\}_{N^{ss}} = \left[K \right]_{ss} \left\{ \delta \right\}_{N^{ss}} - \left\{ F_p \right\}_{N^{ss}} - \left\{ F_c \right\}_{N^{ss}}$$

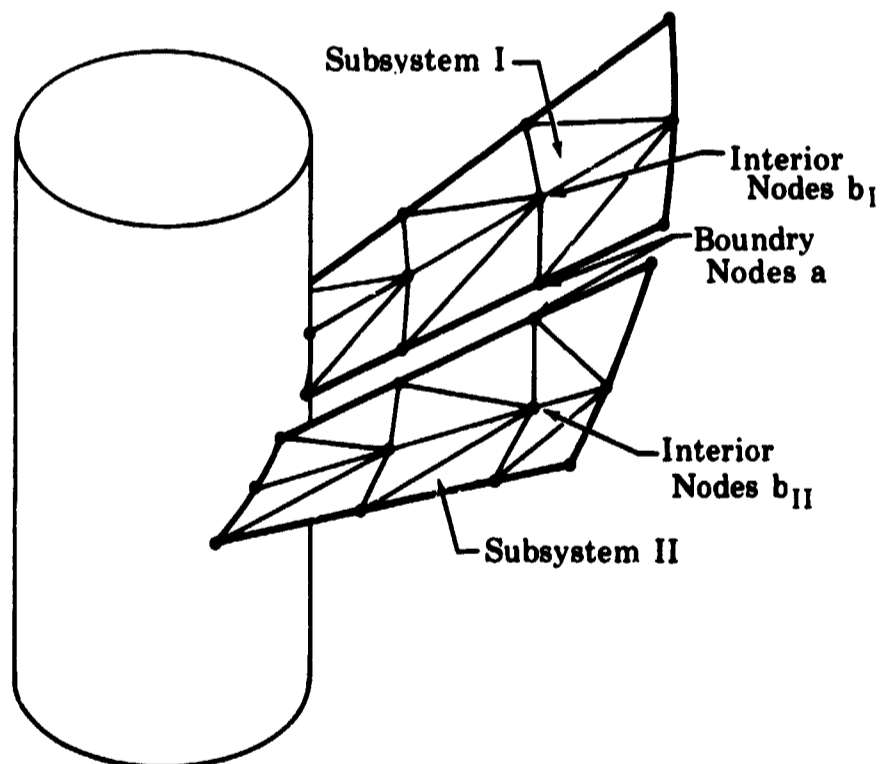


Figure 30. Division of System Into Subsystems

FD 25668A

Then, the subsystem matrix was partitioned to separate boundary nodes from internal nodes in the following manner since the summation of nodal forces at internal points is zero.

$$\left\{ F \right\}_{N^{ss}} = \left\{ \begin{array}{c} F_a \\ 0 \end{array} \right\}_{N^{ss}} = \left[\begin{array}{c|c} K_{aa} & K_{ab} \\ \hline K_{ba} & K_{bb} \end{array} \right] \left\{ \begin{array}{c} \delta_a \\ \delta_b \end{array} \right\}_N - \left\{ \begin{array}{c} F_{pa} \\ F_{pb} \end{array} \right\}_N - \left\{ \begin{array}{c} F_{ca} \\ F_{cb} \end{array} \right\}_N$$

This partitioning yields two matrix equations

$$\begin{aligned} [K_{aa}] \{\delta_a\}_N + [K_{ab}] \{\delta_b\}_N - \{F_{pa}\}_N - \{F_{ca}\}_N &= \{F_a\}_N \\ [K_{ba}] \{\delta_a\}_N + [K_{bb}] \{\delta_b\}_N - \{F_{pb}\}_N - \{F_{cb}\}_N &= 0 \end{aligned} \quad (42)$$

By eliminating the internal nodal deflections $\{\delta_b\}$ from the expressions, the generalized boundary force $\{F_a\}$ in terms of the generalized boundary deflection and the internal properties of the subsystem is obtained. Thus,

$$\begin{aligned} \{F_a\}_{Nss} &= [K_{aa} - K_{ab} K_{bb}^{-1} K_{ba}] \{\delta_a\}_N \\ &\quad - \left[\{F_{pa} - K_{ab} K_{bb}^{-1} \{F_{pb}\}\}_N \right. \\ &\quad \left. - \{F_{ca} - K_{ab} K_{bb}^{-1} \{F_{cb}\}\}_N \right] \end{aligned}$$

At the boundaries common to the subsystems, the displacements $\{\delta_a\}_N$ are equated and forces $\{F_a\}_N$ are summed to zero. This yields a set of simultaneous equations with the boundary displacements $\{\delta_a\}_N$ as unknowns. These equations are solved for $\{\delta_a\}_N$, and $\{\delta_b\}_N$ is then found from (42) by

$$\{\delta_b\}_N = [K_{bb}]^{-1} \left[- [K_{ba}] \{\delta_a\}_N + \{F_{pb}\}_N + \{F_{cb}\}_N \right]$$

Execution times on this program have been reduced by a factor of up to 25 by means of this technique.

(2) Vibration Program

For the vibration program, the surface of the inducer is triangulated in the same manner as the stress program and the same local stiffness matrices $[K_M]$ and $[K_B]$ are used. In addition to these matrices the triangular elements have local membrane inertia matrices $[M_M]$ and bending inertia matrices $[M_B]$, which are defined in Paragraph d. The associated local nodal inertia force matrix, assuming harmonic vibrations of frequency ω and amplitudes $\{\bar{q}\}_N$ is similar to 37 and is

$$\begin{bmatrix} \bar{F}_{x_1} \\ \bar{F}_{y_1} \\ \bar{F}_{x_2} \\ \bar{F}_{y_2} \\ \bar{F}_{x_3} \\ \bar{F}_{y_3} \\ \hline \bar{F}_{z_1} \\ \bar{M}_{x_1} \\ \bar{M}_{y_1} \\ \bar{F}_{z_2} \\ \bar{M}_{x_2} \\ \bar{M}_{y_2} \\ \bar{F}_{z_3} \\ \bar{M}_{x_3} \\ \bar{M}_{z_3} \\ \hline \bar{M}_{z_1} \\ \bar{M}_{z_2} \\ \bar{M}_{z_3} \end{bmatrix} = -\omega^2 \begin{bmatrix} \bar{M}_M & 0 \\ \hline \text{SYMMETRIC} & \bar{M}_B \end{bmatrix} \begin{bmatrix} \bar{u}_1 \\ \bar{v}_1 \\ \bar{u}_2 \\ \bar{v}_2 \\ \bar{u}_3 \\ \bar{v}_3 \\ \hline \bar{w}_1 \\ \bar{\theta}_{x_1} \\ \bar{\theta}_{y_1} \\ \bar{w}_2 \\ \bar{\theta}_{x_2} \\ \bar{\theta}_{y_2} \\ \bar{w}_3 \\ \bar{\theta}_{x_3} \\ \bar{\theta}_{y_3} \\ \hline \bar{\theta}_{z_1} \\ \bar{\theta}_{z_2} \\ \bar{\theta}_{z_3} \end{bmatrix} = -\omega^2 \left[\bar{M} \right] \left[\bar{q} \right]_N$$

It was now assumed that the vibration of the inducer blade is normal to the inducer surface. For this reason a right-handed rectangular coordinate different from the common system used in the stress program was adopted and is shown in figure 31. The z axes of this system are in the mean directions of the four normals to triangular elements that have common vertices at a node and a common generator, and the x axis is in the direction of the generator.

The directions of the normals are obtained from the direction cosine matrix $[R_1]$. Because the y axes are normal to the x axes, the direction of y is established, resulting in a new direction cosine matrix $[R_1]_n$ as defined in Paragraph d. The generalized inertia force matrix relation for a triangular element in the quasi-normal system is obtained in the same manner as the generalized static force-displacement matrix (37).

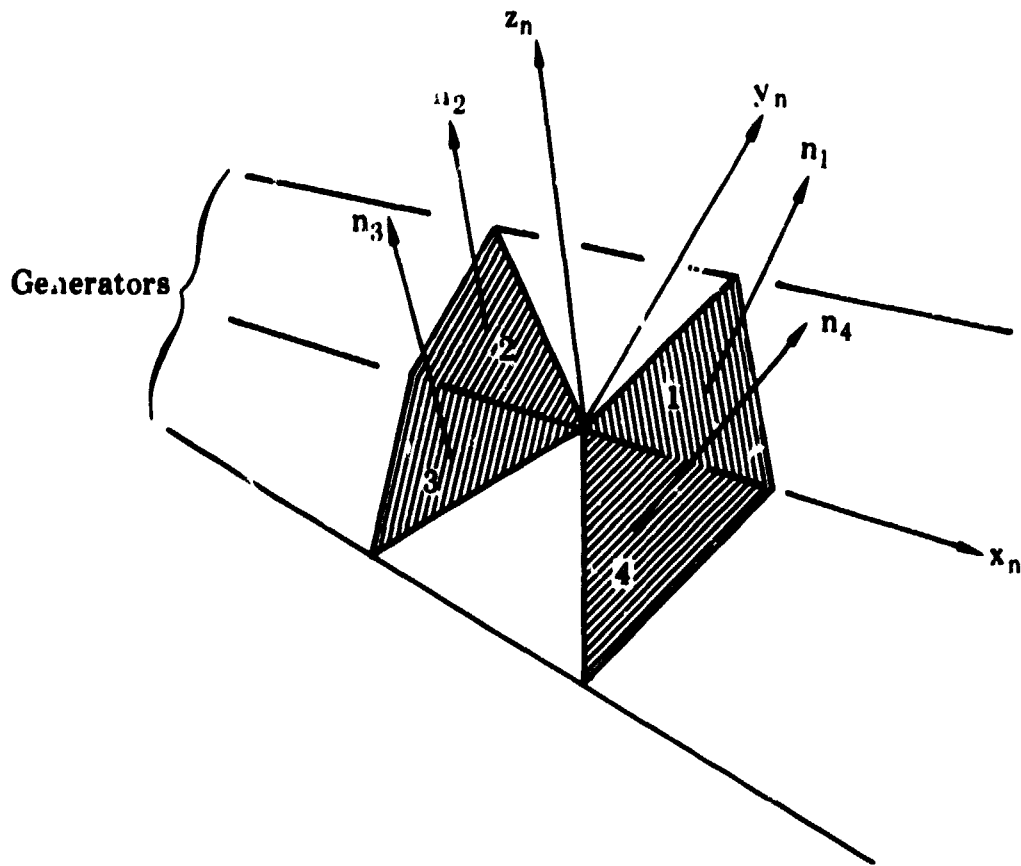


Figure 31. Definition of Quasi-Normal Coordinate System

FD 25669A

Thus,

$$\{\bar{F}\}_N = -\omega^2 \{\bar{M}\} \{\bar{q}\}_N \quad (43)$$

From (38) and (39)

$$\{\bar{F}\}_N = [R_{6n}]^T \{F\}_N \text{ and } \{\bar{q}\}_N = [R_{6n}]^T \{q\}_N$$

Then (43) transforms to

$$[R_{6n}]^T \{F\}_N = -\omega^2 \{\bar{M}\} [R_{6n}]^T \{q\}_N$$

or

$$\{F\}_N = -\omega^2 [R_{6n}] \{\bar{M}\} [R_{6n}]^T \{q\}_N$$

Thus, the generalized inertia force matrix relation for a triangular element in the quasi-normal system is expressed by

$$\{F\}_N = -\omega^2 \{M\} \{q\}_N$$

where the mass matrix $[M]$ is defined by

$$[M] = [R_6]_n [\bar{M}] [R_6]_n^T$$

The stiffness and mass matrices are now assembled in the same manner that was used in the stress program. Elements of stiffness and mass matrices, which are associated with a common node, are added and displacements at common nodes are equated. The matrix equation of motion of free nodes of the system is then

$$\{F\}_N = [-\omega^2 [M]_T + [K]_T] \{q\}_N = \{0\}$$

The associated eigen-value equation is then

$$|-\omega^2 I [M]_T + [K]_T| = 0$$

Because each free node has six degrees of freedom, the eigen-value matrix will be of order $(6n \times 6n)$ for a system with n free nodes. This allows only eight free nodes to describe the inducer geometry because the capacity of an existent IBM 360 eigen-value program is limited to 50 eigen-values. Because eight free nodes are insufficient to describe a typical inducer, the number of degrees of freedom per node was reduced to one by matrix condensation techniques following a procedure recommended by Guyan*. This is accomplished by rearranging and partitioning by which the nodal force-displacement relation can be expressed in the matrix form

$$\begin{matrix} \{F\}_N \\ (6n \times 1) \end{matrix} = \begin{bmatrix} \begin{matrix} [A] \\ (n \times n) \end{matrix} & \begin{matrix} [C]^T \\ (n \times 2n) \end{matrix} & | & \begin{matrix} [E]^T \\ (3n \times 3n) \end{matrix} \\ \hline \begin{matrix} [C] \\ (2n \times n) \end{matrix} & \begin{matrix} [B] \\ (2n \times 2n) \end{matrix} & | & \begin{matrix} [D] \\ (3n \times 3n) \end{matrix} \\ \hline & \begin{matrix} [E] \\ (3n \times 3n) \end{matrix} & | & \end{bmatrix} \begin{matrix} \begin{matrix} w \\ \theta_x \\ \theta_y \end{matrix} \\ \hline \begin{matrix} u \\ v \\ \theta_z \end{matrix} \end{matrix} \begin{matrix} (3n \times 1) \\ (3n \times 1) \end{matrix}$$

It is now assumed that if the plate vibrates normally to the surface u , v , and θ_z are zero. This can be accomplished by deleting the rows and columns containing the matrices $[D]$, $[E]$, and $[E]^T$. After deletion and further partitioning, the nodal force-displacement matrix relation is

$$\begin{matrix} \{F\}_N \\ (3n \times 1) \end{matrix} = \begin{matrix} \begin{matrix} [F_1] \\ (n \times 1) \end{matrix} \\ \hline \begin{matrix} [F_2] \\ (2n \times 1) \end{matrix} \end{matrix} = \begin{bmatrix} \begin{matrix} [A] \\ (n \times n) \end{matrix} & \begin{matrix} [C]^T \\ (n \times 2n) \end{matrix} \\ \hline \begin{matrix} [C] \\ (2n \times n) \end{matrix} & \begin{matrix} [B] \\ (2n \times 2n) \end{matrix} \end{bmatrix} \begin{matrix} \begin{matrix} w \\ \theta_x \\ \theta_y \end{matrix} \\ \hline \end{matrix} \begin{matrix} (n \times 1) \\ (2n \times 1) \end{matrix}$$

Letting $F_2 = 0$ for condensation as recommended by Guyan yields two matrix equations

$$\{F_1\}_N = [A] \{w\}_N + [C]^T \{\theta\}_N$$

$$\{0\} = [C] \{w\}_N + [B] \{\theta\}_N$$

*See Appendix A, section 3.

where

$$\left\{ \theta \right\}_N = \begin{Bmatrix} \theta_x \\ \theta_y \end{Bmatrix}_N$$

Eliminating θ

$$\left\{ F \right\}_N = \begin{bmatrix} \left[A \right] & \left[C \right]^T \\ \left[C \right] & \left[B \right] \end{bmatrix} \begin{bmatrix} \left\{ w \right\}_N \\ -\left[B \right]^{-1} \left[C \right] \left\{ w \right\}_N \end{bmatrix} \quad (44)$$

or

$$\left\{ F \right\}_N = \begin{bmatrix} \left[A \right] - \left[C \right]^T \left[B \right]^{-1} \left[C \right] \end{bmatrix} \left\{ w \right\}_N = \left[K \right]^* \left\{ w \right\}_N \quad (45)$$

$(n \times 1) \qquad \qquad (n \times n) \qquad \qquad (n \times 1)$

Thus, the reduced stiffness matrix is

$$\left[K \right]^* = \left[\left[A \right] - \left[C \right]^T \left[B \right]^{-1} \left[C \right] \right]$$

This operation reduces the number of degrees of freedom to n while still retaining the physical properties of the original system. Examination of (44) and (45) indicates that it amounts to a coordinate transformation as discussed by Guyan, i.e.

$$\left\{ q \right\}_N = \begin{Bmatrix} w \\ \theta \end{Bmatrix}_N = \left[T \right] \left\{ w \right\}_N$$

where

$$\left[T \right] = \left[\left[A \right] - \left[C \right]^T \left[B \right]^{-1} \left[C \right] \right]$$

Thus, if the internal strain energy is to be preserved under this transformation

$$U = \frac{1}{2} \left\{ q \right\}_N \left[K \right] \left\{ q \right\}_N = \frac{1}{2} \left\{ w \right\}_N \left[T \right]^T \left[K \right] \left[T \right] \left\{ w \right\}_N = \frac{1}{2} \left\{ w \right\}_N \left[K \right]^*_T \left\{ w \right\}_N$$

Thus, the reduced system stiffness matrix is of the form

$$\left[K \right]^*_T = \left[T \right]^T \left[K \right] \left[T \right]$$

The kinetic energy must also be preserved under this transformation. Thus,

$$T = \frac{1}{2} \left\{ \dot{q} \right\}_N \left[M \right] \left\{ \dot{q} \right\}_N = \frac{1}{2} \left\{ \dot{w} \right\}_N \left[T \right]^T \left[M \right] \left[T \right] \left\{ \dot{w} \right\}_N = \frac{1}{2} \left\{ \dot{w} \right\}_N \left[M \right]^*_T \left\{ \dot{w} \right\}_N$$

The reduced system mass matrix is then

$$\left[M \right]^*_T = \left[T \right]^T \left[M \right] \left[T \right]$$

Using these reduced matrices, the equation of motion becomes

$$\left[-\omega^2 [M]_T^* + [K]_T^* \right] \{w\}_N = \{0\}$$

The associated eigen-value equation then involves only n degrees of freedom and is

$$\left| -\omega^2 I + [M]_T^{*-1} [K]_T^* \right| = 0$$

d. Derivations of Basic Relations

The derivations of the various relations in matrix form are discussed in the following sections, as outlined below. These are separated into relations that are common to both the stress and vibration programs and those that apply specifically to only one of the programs.

Both Programs

- (1) Direction Cosine Matrix $\{R_1\}$
- (2) Nodal Coordinate Matrix $\{\bar{\psi}\}_N$
- (3) Triangular Surface Coordinate Matrix $\{\psi\}$
- (4) Thickness Matrix Relation
- (5) Membrane Stiffness Matrix $\{\bar{K}_M\}$
- (6) Bending Stiffness Matrix $\{\bar{K}_B\}$

Stress Program

- (7) Pressure Force Matrix $\{\bar{F}_P\}_N$
- (8) Centrifugal Force Matrix $\{F_C\}_N$
- (9) Approximate Centrifugal Force Matrix $\{F_C\}_N$

Vibration Program

- (10) Membrane Inertia Matrix $\{\bar{M}_M\}$
- (11) Bending Inertia Matrix $\{\bar{M}_B\}$
- (12) Normal Direction Cosine Matrix $\{R_1\}_n$

Integration of expressions containing variable thickness is accomplished by the Gaussian quadrature formula, using 100 internal nodal values of the integrand in the triangular element.

(1) Direction Cosine Matrix $[R_1]$ (See Figure 32.)

The direction cosine or rotation matrix $[R_1]$ establishes the relation between the directions of the axes of the common coordinate system and the local coordinate system. It is obtained by three operations:

1. Direction of \bar{z} axis is obtained by determining direction of vector product of vectors in directions of two sides of triangle.
2. Direction of \bar{x} axis is obtained by projection.
3. Direction of \bar{y} axis is obtained by determining direction of vector product of vector along \bar{z} axis and \bar{x} axis.

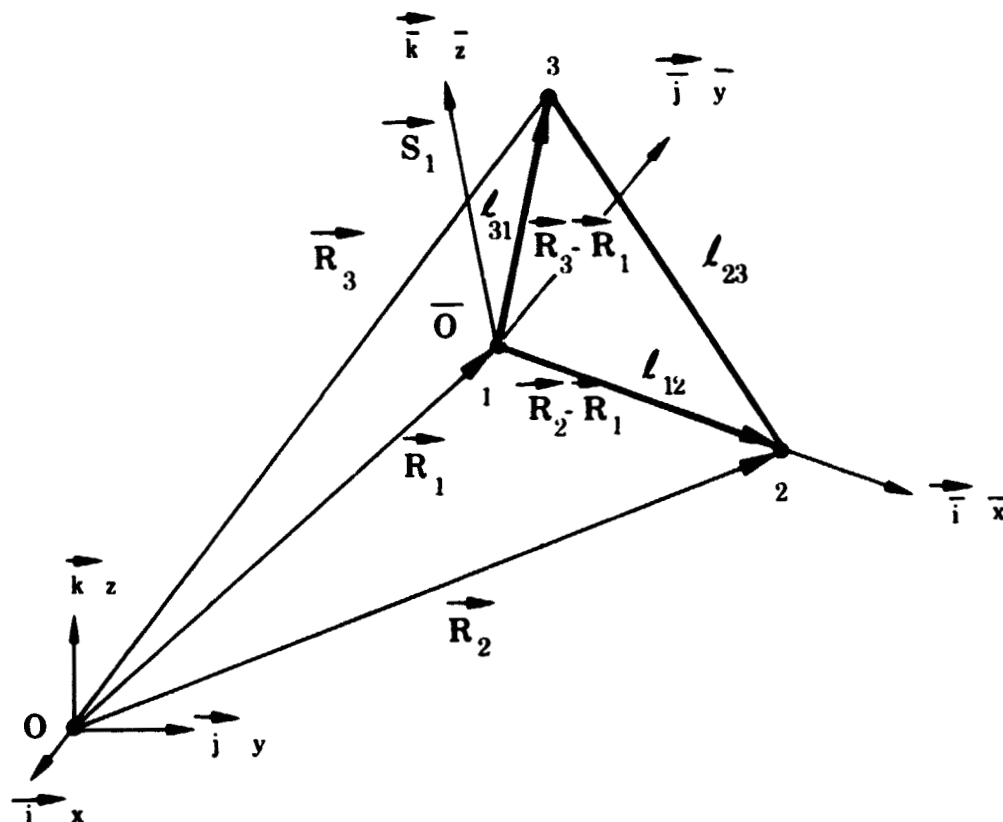


Figure 32. Geometry for Deriving $[R_1]$

FD 25843A

1. \bar{z} Direction

Vector area of triangle relative to common system, (one half of vector product)

$$\begin{aligned} \vec{S}_1 &= \frac{1}{2} (\vec{R}_2 - \vec{R}_1) \times (\vec{R}_3 - \vec{R}_1) \\ &= \frac{1}{2} \begin{vmatrix} \vec{i} & \vec{j} & \vec{k} \\ x_2 - x_1 & y_2 - y_1 & z_2 - z_1 \\ x_3 - x_1 & y_3 - y_1 & z_3 - z_1 \end{vmatrix} \end{aligned}$$

$$S_{1x} = \frac{1}{2} \left[(y_2 - y_1)(z_3 - z_1) - (y_3 - y_1)(z_2 - z_1) \right]$$

$$S_{1y} = \frac{1}{2} \left[(z_2 - z_1)(x_3 - x_1) - (z_3 - z_1)(x_2 - x_1) \right]$$

$$S_{1z} = \frac{1}{2} \left[(x_2 - x_1)(y_3 - y_1) - (x_3 - x_1)(y_2 - y_1) \right]$$

$$S_1 = \frac{1}{2} \sqrt{S_{1x}^2 + S_{1y}^2 + S_{1z}^2}$$

$$\vec{S}_1 = \vec{i} S_{1x} + \vec{j} S_{1y} + \vec{k} S_{1z}$$

$$\vec{k} = \vec{i} \frac{S_{1x}}{S_1} + \vec{j} \frac{S_{1y}}{S_1} + \vec{k} \frac{S_{1z}}{S_1}$$

$$\therefore \cos(x, \vec{z}) = \vec{i} \cdot \vec{k} = \frac{S_{1x}}{S_1}$$

$$\cos(y, \vec{z}) = \vec{j} \cdot \vec{k} = \frac{S_{1y}}{S_1}$$

$$\cos(z, \vec{z}) = \vec{k} \cdot \vec{k} = \frac{S_{1z}}{S_1}$$

2. \vec{x} Direction

By inspection,

$$\cos(x, \vec{x}) = \frac{x_2 - x_1}{l_{12}}$$

$$\cos(y, \vec{x}) = \frac{y_2 - y_1}{l_{12}}$$

$$\cos(z, \vec{x}) = \frac{z_2 - z_1}{l_{12}}$$

$$l_{12} = \sqrt{(x_2 - x_1)^2 + (y_2 - y_1)^2 + (z_2 - z_1)^2}$$

3. \bar{y} Direction

\bar{y} axis is in direction of vector product, $\vec{S}_1 \times (\vec{R}_2 - \vec{R}_1)$

$$\vec{S}_1 \times (\vec{R}_2 - \vec{R}_1) = \begin{vmatrix} \vec{i} & \vec{j} & \vec{k} \\ S_{1x} & S_{1y} & S_{1z} \\ x_2 - x_1 & y_2 - y_1 & z_2 - z_1 \end{vmatrix}$$

$$= \vec{i} \left[S_{1y}(z_2 - z_1) - S_{1z}(y_2 - y_1) \right] +$$

$$\vec{j} \left[S_{1z}(x_2 - x_1) - S_{1x}(z_2 - z_1) \right] +$$

$$\vec{k} \left[S_{1x}(y_2 - y_1) - S_{1y}(x_2 - x_1) \right]$$

$$S_2 = \sqrt{\left[S_{1y}(z_2 - z_1) - S_{1z}(y_2 - y_1) \right]^2 +$$

$$\sqrt{\left[S_{1z}(x_2 - x_1) - S_{1x}(z_2 - z_1) \right]^2 +$$

$$\sqrt{\left[S_{1x}(y_2 - y_1) - S_{1y}(x_2 - x_1) \right]^2}$$

$$S_{2x} = S_{1y}(z_2 - z_1) - S_{1z}(y_2 - y_1)$$

$$S_{2y} = S_{1z}(x_2 - x_1) - S_{1x}(z_2 - z_1)$$

$$S_{2z} = S_{1x}(y_2 - y_1) - S_{1y}(x_2 - x_1)$$

$$\vec{S}_2 = \vec{i} S_{2x} + \vec{j} S_{2y} + \vec{k} S_{2z}$$

$$\vec{j} = \vec{i} \frac{S_{2x}}{S_2} + \vec{j} \frac{S_{2y}}{S_2} + \vec{k} \frac{S_{2z}}{S_2}$$

$$\therefore \cos(x, \bar{y}) = \vec{i} \cdot \vec{j} = \frac{S_{2x}}{S_2}$$

$$\cos(y, \bar{y}) = \vec{j} \cdot \vec{j} = \frac{S_{2y}}{S_2}$$

$$\cos(z, \bar{y}) = \vec{k} \cdot \vec{j} = \frac{S_{2z}}{S_2}$$

The direction cosine matrix is then:

$$[R_1] = \begin{bmatrix} \cos(x, \bar{x}), \cos(x, \bar{y}), \cos(x, \bar{z}) \\ \cos(y, \bar{x}), \cos(y, \bar{y}), \cos(y, \bar{z}) \\ \cos(z, \bar{x}), \cos(z, \bar{y}), \cos(z, \bar{z}) \end{bmatrix} = \begin{bmatrix} \frac{x_2 - x_1}{l_{12}} & \frac{s_{2x}}{s_2} & \frac{s_{1x}}{s_1} \\ \frac{y_2 - y_1}{l_{12}} & \frac{s_{2y}}{s_2} & \frac{s_{1y}}{s_1} \\ \frac{z_2 - z_1}{l_{12}} & \frac{s_{2z}}{s_2} & \frac{s_{1z}}{s_1} \end{bmatrix} \quad (46)$$

(2) Nodal Coordinate Matrix. $[\bar{\Psi}]_N$ (See Figure 33.)

The matrix $[\bar{\Psi}]_N$ establishes the local coordinates of the nodes of the triangle in terms of the common coordinates of the nodes of the triangle. It is obtained by two operations:

1. Translation of origin of local coordinate system to origin of common coordinates system.
2. Rotation of axes of local coordinate system to axes of common system.

The operation $[\Psi - \Psi_1]_N$ or

$$[\Psi - \Psi_1]_N = \begin{bmatrix} 0, x_2 - x_1, x_3 - x_1 \\ 0, y_2 - y_1, y_3 - y_1 \\ 0, z_2 - z_1, z_3 - z_1 \end{bmatrix}$$

translates the local coordinate system to the origin of the reference system. This operation, together with rotation of the axes, yields:

$$[\bar{\Psi}_1]_N = \begin{bmatrix} \bar{x}_1 \\ \bar{y}_1 \\ \bar{z}_1 \end{bmatrix} = \begin{bmatrix} 0 \\ 0 \\ 0 \end{bmatrix}$$

$$[\bar{\Psi}_2]_N = \begin{bmatrix} \bar{x}_2 \\ 0 \\ 0 \end{bmatrix} = \begin{bmatrix} (x_2 - x_1) \cos(\bar{x}, x) + (y_2 - y_1) \cos(\bar{x}, y) + (z_2 - z_1) \cos(\bar{x}, z) \\ (x_2 - x_1) \cos(\bar{y}, x) + (y_2 - y_1) \cos(\bar{y}, y) + (z_2 - z_1) \cos(\bar{y}, z) \\ (x_2 - x_1) \cos(\bar{z}, x) + (y_2 - y_1) \cos(\bar{z}, y) + (z_2 - z_1) \cos(\bar{z}, z) \end{bmatrix}$$

$$\left| \bar{\Psi}_3 \right|_N = \begin{Bmatrix} \bar{x}_3 \\ \bar{y}_3 \\ 0 \end{Bmatrix} = \begin{Bmatrix} (x_3 - x_1) \cos(\bar{x}, x) + (y_3 - y_1) \cos(\bar{x}, y) + (z_3 - z_1) \cos(\bar{x}, z) \\ (x_3 - x_1) \cos(\bar{y}, x) + (y_3 - y_1) \cos(\bar{y}, y) + (z_3 - z_1) \cos(\bar{y}, z) \\ (x_3 - x_1) \cos(\bar{z}, x) + (y_3 - y_1) \cos(\bar{z}, y) + (z_3 - z_1) \cos(\bar{z}, z) \end{Bmatrix}$$

or

$$\begin{Bmatrix} \bar{x}_2 \\ 0 \\ 0 \end{Bmatrix} = \begin{bmatrix} \cos(\bar{x}, x) & \cos(\bar{x}, y) & \cos(\bar{x}, z) \\ \cos(\bar{y}, x) & \cos(\bar{y}, y) & \cos(\bar{y}, z) \\ \cos(\bar{z}, x) & \cos(\bar{z}, y) & \cos(\bar{z}, z) \end{bmatrix} \begin{Bmatrix} x_2 - x_1 \\ y_2 - y_1 \\ z_2 - z_1 \end{Bmatrix}$$

$$\begin{Bmatrix} \bar{x}_3 \\ \bar{y}_3 \\ 0 \end{Bmatrix} = \begin{bmatrix} \cos(\bar{x}, x) & \cos(\bar{x}, y) & \cos(\bar{x}, z) \\ \cos(\bar{y}, x) & \cos(\bar{y}, y) & \cos(\bar{y}, z) \\ \cos(\bar{z}, x) & \cos(\bar{z}, y) & \cos(\bar{z}, z) \end{bmatrix} \begin{Bmatrix} x_3 - x_1 \\ y_3 - y_1 \\ z_3 - z_1 \end{Bmatrix}$$

In matrix notation:

$$\left| \bar{\Psi} \right|_N = [R]^T [\Psi - \Psi_1]_N \quad (47)$$

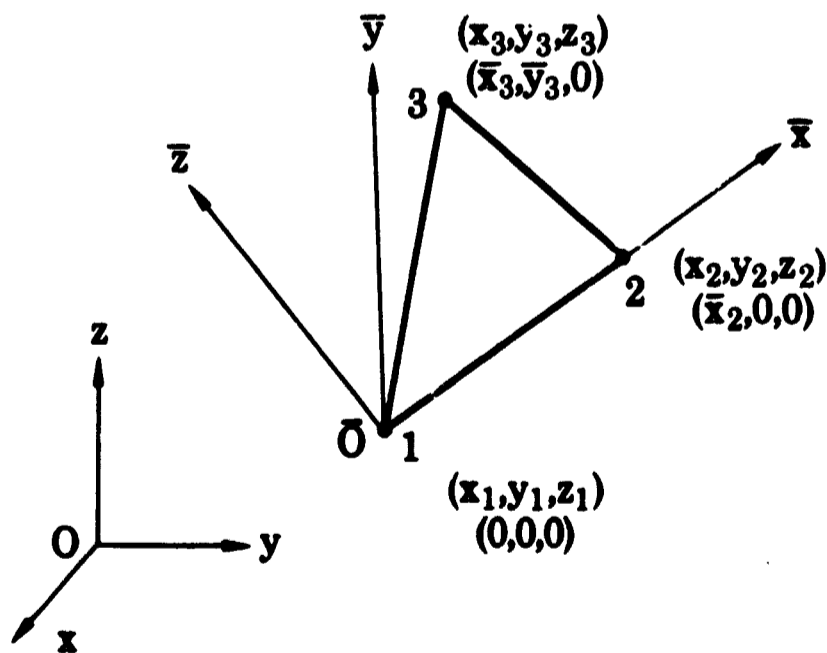


Figure 33. Geometry for Deriving $\left| \Psi \right|_N$

FD 25842

(3) Triangular Surface Coordinate Matrix $\left[\Psi \right]$ (See Figure 34.)

The matrix $\left[\Psi \right]$ establishes the relation between the local coordinates of points in the plane of the triangle and the common coordinates of these points. It is obtained by two operations:

1. Translation of origin of local system to origin of common system.
 2. Rotation of axes of local system to axes of common system.
- (From figure 34.)

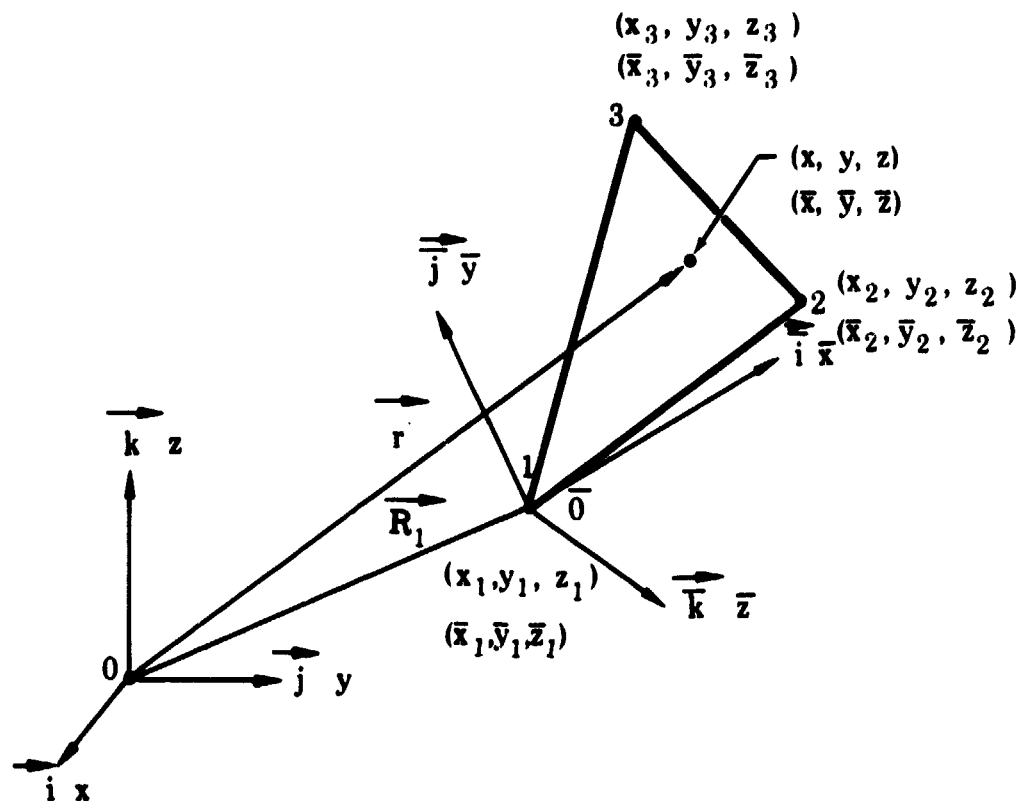


Figure 34. Geometry for Deriving $\left[\Psi \right]$

FD 25841A

$$\vec{r} = \vec{R}_1 + \vec{i}\bar{x} + \vec{j}\bar{y} + \vec{k}\bar{z}$$

But

$$\vec{i} = \vec{i} \cos(\bar{x}, x) + \vec{j} \cos(\bar{x}, y) + \vec{k} \cos(\bar{x}, z)$$

$$\vec{j} = \vec{i} \cos(\bar{y}, x) + \vec{j} \cos(\bar{y}, y) + \vec{k} \cos(\bar{y}, z)$$

$$\vec{k} = \vec{i} \cos(\bar{z}, x) + \vec{j} \cos(\bar{z}, y) + \vec{k} \cos(\bar{z}, z)$$

$$\begin{aligned} \therefore \vec{i}x + \vec{j}y + \vec{k}z &= \vec{i}x_1 + \vec{j}y_1 + \vec{k}z_1 + \\ &\quad \bar{x} \left[\vec{i} \cos(\bar{x}, x) + \vec{j} \cos(\bar{x}, y) + \vec{k} \cos(\bar{x}, z) \right] + \\ &\quad \bar{y} \left[\vec{i} \cos(\bar{y}, x) + \vec{j} \cos(\bar{y}, y) + \vec{k} \cos(\bar{y}, z) \right] + \\ &\quad \bar{z} \left[\vec{i} \cos(\bar{z}, x) + \vec{j} \cos(\bar{z}, y) + \vec{k} \cos(\bar{z}, z) \right] \end{aligned}$$

$$\begin{aligned} \therefore x &= x_1 + \bar{x} \cos(x, \bar{x}) + \bar{y} \cos(x, \bar{y}) + \bar{z} \cos(x, \bar{z}) \\ y &= y_1 + \bar{x} \cos(y, \bar{x}) + \bar{y} \cos(y, \bar{y}) + \bar{z} \cos(y, \bar{z}) \\ z &= z_1 + \bar{x} \cos(z, \bar{x}) + \bar{y} \cos(z, \bar{y}) + \bar{z} \cos(z, \bar{z}) \end{aligned}$$

or

$$\begin{bmatrix} x \\ y \\ z \end{bmatrix} = \begin{bmatrix} x_1 \\ y_1 \\ z_1 \end{bmatrix} + [R_1] \begin{bmatrix} \bar{x} \\ \bar{y} \\ \bar{z} \end{bmatrix}$$

In matrix form

$$[\Psi] = [\Psi_1] + [R_1][\bar{\Psi}]$$

(4) Thickness Matrix Relation (See Figure 35.)

This relation expresses the thickness at a point in the plane of the triangle in terms of the thicknesses at the three vertices, when the thickness is assumed to vary linearly with \bar{x} and \bar{y} over the triangle. It is derived by determining the coefficients of the linear form by matrix algebra.

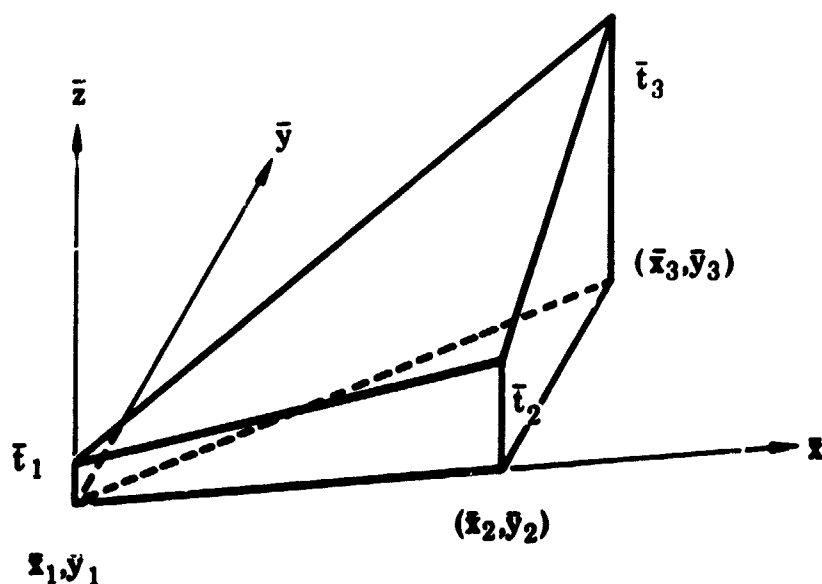


Figure 35. Geometry of Triangular Element With Linearly Varying Thickness

FD 25840A

Assume

$$\bar{t} = \bar{a}_1 \bar{x} + \bar{a}_2 \bar{y} + \bar{a}_3 = \begin{bmatrix} \bar{x} & \bar{y} & 1 \end{bmatrix} \begin{Bmatrix} \bar{a}_1 \\ \bar{a}_2 \\ \bar{a}_3 \end{Bmatrix} = [\bar{A}] \{\bar{\alpha}_T\}$$

For nodal values, $\bar{t}_1, \bar{t}_2, \bar{t}_3,$

$$\begin{Bmatrix} \bar{t}_1 \\ \bar{t}_2 \\ \bar{t}_3 \end{Bmatrix} = \begin{bmatrix} \bar{x}_1 & \bar{y}_1 & 1 \\ \bar{x}_2 & \bar{y}_2 & 1 \\ \bar{x}_3 & \bar{y}_3 & 1 \end{bmatrix} \begin{Bmatrix} \bar{a}_1 \\ \bar{a}_2 \\ \bar{a}_3 \end{Bmatrix}$$

$$\therefore \{\bar{\alpha}_T\} = \begin{Bmatrix} \bar{a}_1 \\ \bar{a}_2 \\ \bar{a}_3 \end{Bmatrix} = \begin{bmatrix} \bar{x}_1 & \bar{y}_1 & 1 \\ \bar{x}_2 & \bar{y}_2 & 1 \\ \bar{x}_3 & \bar{y}_3 & 1 \end{bmatrix}^{-1} \begin{Bmatrix} \bar{t}_1 \\ \bar{t}_2 \\ \bar{t}_3 \end{Bmatrix} = \frac{1}{2\text{AREA}} \begin{bmatrix} \bar{y}_2 - \bar{y}_3 & \bar{y}_3 - \bar{y}_1 & \bar{y}_1 - \bar{y}_2 \\ \bar{x}_3 - \bar{x}_2 & \bar{x}_1 - \bar{x}_3 & \bar{x}_2 - \bar{x}_1 \\ \bar{x}_2 \bar{y}_3 - \bar{x}_3 \bar{y}_2 & \bar{x}_3 \bar{y}_1 - \bar{x}_1 \bar{y}_3 & \bar{x}_1 \bar{y}_2 - \bar{x}_2 \bar{y}_1 \end{bmatrix} \begin{Bmatrix} \bar{t}_1 \\ \bar{t}_2 \\ \bar{t}_3 \end{Bmatrix}$$

$[\bar{A}_t]_N^{-1}$

in matrix form

$$\begin{aligned} \bar{t} &= [\bar{A}_t] \{\bar{\alpha}_t\} \\ \{\bar{t}\}_N &= [\bar{A}_t]_N \{\bar{\alpha}_t\} \quad \text{or} \quad \{\bar{\alpha}_t\} = [\bar{A}_t]_N^{-1} \{\bar{t}\}_N \\ \therefore \bar{t} &= [\bar{A}_t] [\bar{A}_t]_N^{-1} \{\bar{t}\}_N \end{aligned}$$

(5) Membrane Stiffness Matrix $[\bar{K}_M]$ (See Figure 36.)

The matrix $[\bar{K}_M]$ expresses the linear relation between fictitious nodal forces and nodal displacements in the plane of the triangle. It is derived by obtaining the internal strain energy in the form:

$$\bar{U}_M = \frac{1}{2} \{\bar{\delta}_M\}_N \left[\quad \right] \{\bar{\delta}_M\}_N$$

where $\{\bar{\delta}_M\}_N$ is the local nodal membrane displacement column matrix and the middle matrix $\left[\quad \right]$ is the local membrane stiffness matrix $[\bar{K}_M]$.

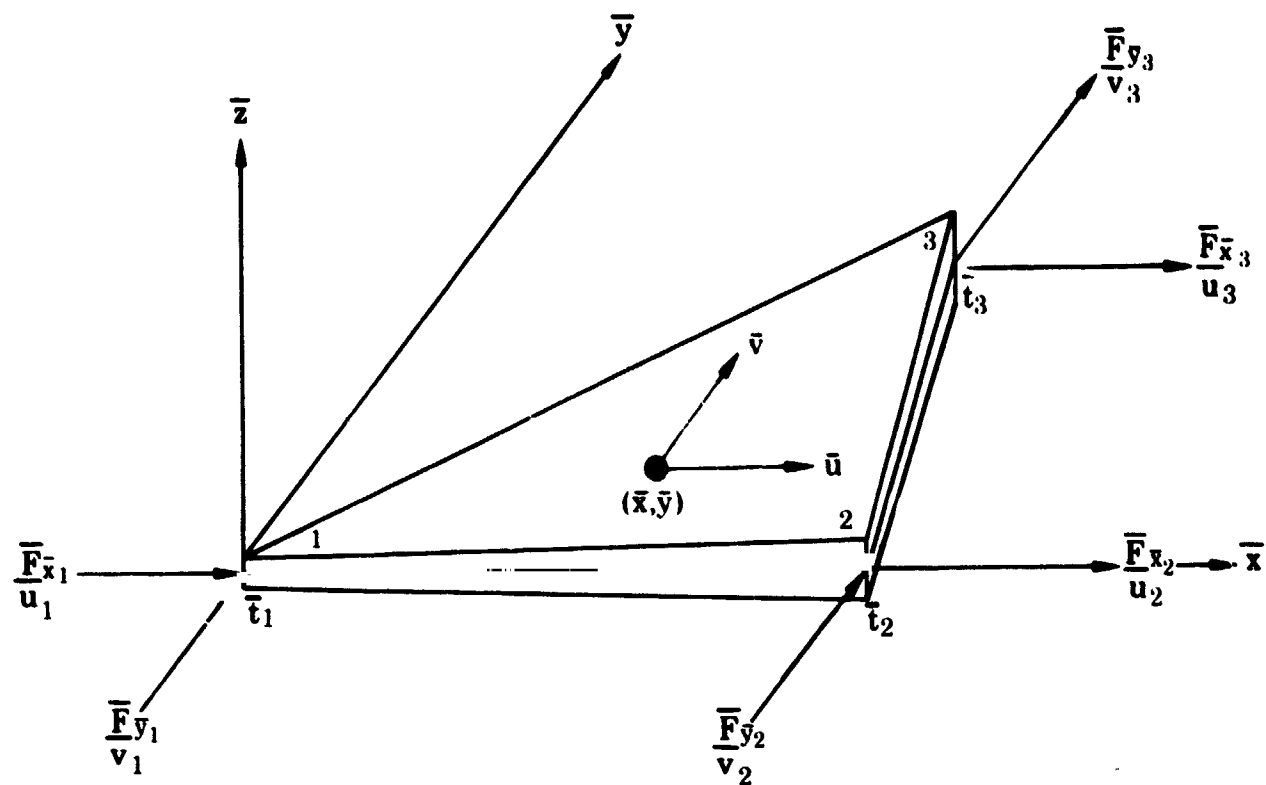


Figure 36. Generalized Nodal Local Membrane Displacements and Forces On Flat Triangular Element

FD 25631

Letting

$$\begin{Bmatrix} \bar{u} \\ \bar{v} \end{Bmatrix} = \begin{bmatrix} \bar{x} & 0 & \bar{y} & 0 & 1 & 0 \\ 0 & \bar{x} & 0 & \bar{y} & 0 & 1 \end{bmatrix} \begin{Bmatrix} \bar{a}_1 \\ \bar{a}_2 \\ \bar{a}_3 \\ \bar{a}_4 \\ \bar{a}_5 \\ \bar{a}_6 \end{Bmatrix}$$

or, in matrix form

$$\begin{Bmatrix} \bar{\delta}_M \end{Bmatrix} = \begin{bmatrix} \bar{A}_M \end{bmatrix} \begin{Bmatrix} \bar{\alpha}_M \end{Bmatrix}$$

For nodal values

$$\begin{Bmatrix} \bar{u}_1 \\ \bar{v}_1 \\ \bar{u}_2 \\ \bar{v}_2 \\ \bar{u}_3 \\ \bar{v}_3 \end{Bmatrix} = \begin{bmatrix} \bar{x}_1 & 0 & \bar{y}_1 & 0 & 1 & 0 \\ 0 & \bar{x}_1 & 0 & \bar{y}_1 & 0 & 1 \\ \bar{x}_2 & 0 & \bar{y}_2 & 0 & 1 & 0 \\ 0 & \bar{x}_2 & 0 & \bar{y}_2 & 0 & 1 \\ \bar{x}_3 & 0 & \bar{y}_3 & 0 & 1 & 0 \\ 0 & \bar{x}_3 & 0 & \bar{y}_3 & 0 & 1 \end{bmatrix} \begin{Bmatrix} \bar{a}_1 \\ \bar{a}_2 \\ \bar{a}_3 \\ \bar{a}_4 \\ \bar{a}_5 \\ \bar{a}_6 \end{Bmatrix}$$

$$\begin{bmatrix} \bar{A}_M \end{bmatrix}_N$$

or, in matrix form

$$\begin{Bmatrix} \bar{\delta}_M \end{Bmatrix}_N = \begin{Bmatrix} \bar{A}_M \end{Bmatrix}_N \begin{Bmatrix} \bar{r}_M \end{Bmatrix}$$

$$\therefore \begin{Bmatrix} \bar{\alpha}_M \end{Bmatrix} = \begin{Bmatrix} A_M \end{Bmatrix}_N^{-1} \begin{Bmatrix} \bar{\delta}_M \end{Bmatrix}_N$$

$$\text{and } \begin{Bmatrix} \bar{\delta}_M \end{Bmatrix} = \begin{Bmatrix} \bar{A}_M \end{Bmatrix} \begin{Bmatrix} \bar{A}_M \end{Bmatrix}_N^{-1} \begin{Bmatrix} \bar{\delta}_M \end{Bmatrix}_N$$

using

$$\text{Strain Matrix } \begin{Bmatrix} \bar{\epsilon}_M \end{Bmatrix} = \begin{Bmatrix} \epsilon_{xx} \\ \epsilon_{yy} \\ \epsilon_{xy} \end{Bmatrix} \begin{Bmatrix} \frac{\partial \bar{u}}{\partial \bar{x}} \\ \frac{\partial \bar{v}}{\partial \bar{y}} \\ \frac{\partial \bar{u}}{\partial \bar{y}} + \frac{\partial \bar{v}}{\partial \bar{x}} \end{Bmatrix} = \begin{bmatrix} 1 & 0 & 0 & 0 & 0 & 0 \\ 0 & 0 & 0 & 1 & 0 & 0 \\ 0 & 1 & 1 & 0 & 0 & 0 \end{bmatrix} \begin{Bmatrix} \bar{\alpha}_M \end{Bmatrix}$$

$$\begin{Bmatrix} \bar{w}_M \end{Bmatrix}$$

$$\therefore \begin{Bmatrix} \bar{\epsilon}_M \end{Bmatrix} = \begin{Bmatrix} \bar{w}_M \end{Bmatrix} \begin{Bmatrix} \bar{\alpha}_M \end{Bmatrix} = \begin{Bmatrix} \bar{w}_M \end{Bmatrix} \begin{Bmatrix} \bar{A}_M \end{Bmatrix}_N^{-1} \begin{Bmatrix} \bar{\delta}_M \end{Bmatrix}_N$$

using

$$\text{Stress Matrix } \begin{Bmatrix} \bar{\sigma}_{xx} \\ \bar{\sigma}_{yy} \\ \bar{\sigma}_{xy} \end{Bmatrix} = \begin{bmatrix} E_{11} & E_{12} & 0 \\ E_{12} & E_{22} & 0 \\ 0 & 0 & E_{44} \end{bmatrix} \begin{Bmatrix} \bar{\epsilon}_{xx} \\ \bar{\epsilon}_{yy} \\ \bar{\epsilon}_{xy} \end{Bmatrix} = \frac{E}{1-\nu^2} \begin{bmatrix} 1 & \nu & 0 \\ \nu & 1 & 0 \\ 0 & 0 & \frac{1-\nu}{2} \end{bmatrix} \begin{Bmatrix} \bar{\epsilon}_{xx} \\ \bar{\epsilon}_{yy} \\ \bar{\epsilon}_{xy} \end{Bmatrix}$$

$$\therefore \begin{Bmatrix} \bar{\sigma}_M \end{Bmatrix} = \begin{Bmatrix} \bar{E}_M \end{Bmatrix} \begin{Bmatrix} \bar{\epsilon}_M \end{Bmatrix}$$

Internal strain energy

$$\begin{aligned}
 \bar{U}_M &= \frac{1}{2} \int \{\bar{\epsilon}_M\} \{\bar{a}_M\} d\bar{v} = \int \{\bar{\epsilon}_M\} \{\bar{E}_M\} \{\bar{\epsilon}_M\} d\bar{v} \\
 &= \frac{1}{2} \int \{\bar{\delta}_M\}_N \left[\bar{A}_M \right]_N^{-1T} \left[\bar{w}_M \right]^T \left[\bar{E}_M \right] \left[\bar{w}_M \right] \left[\bar{A}_M \right]_N^{-1} \{\bar{\delta}_M\}_N d\bar{v} \\
 &= \frac{1}{2} \{\bar{\delta}_M\}_N \left[\left[\bar{A}_M \right]_N^{-1T} \left(\int \left[\bar{w}_M \right]^T \left[\bar{E}_M \right] \left[\bar{w}_M \right] d\bar{v} \right) \left[\bar{A}_M \right]_N^{-1} \right] \{\bar{\delta}_M\}_N \\
 \therefore \left[\bar{K}_M \right] &= \left[\bar{A}_M \right]_N^{-1T} \left(\int \left[\bar{w}_M \right]^T \left[\bar{E}_M \right] \left[\bar{w}_M \right] d\bar{v} \right) \left[\bar{A}_M \right]_N^{-1} \quad (48)
 \end{aligned}$$

where $d\bar{v} = \bar{t}d\bar{x}d\bar{y}$

and

$$\left[\bar{A}_M \right]_N^{-1} = \frac{1}{2\text{AREA}} \begin{bmatrix} \bar{y}_2 - \bar{y}_3 & 0 & \bar{y}_3 - \bar{y}_1 & 0 & \bar{y}_1 - \bar{y}_2 & 0 \\ 0 & \bar{y}_2 - \bar{y}_3 & 0 & \bar{y}_3 - \bar{y}_1 & 0 & \bar{y}_1 - \bar{y}_2 \\ \bar{x}_3 - \bar{x}_2 & 0 & \bar{x}_1 - \bar{x}_3 & 0 & \bar{x}_2 - \bar{x}_1 & 0 \\ 0 & \bar{x}_3 - \bar{x}_2 & 0 & \bar{x}_1 - \bar{x}_3 & 0 & \bar{x}_2 - \bar{x}_1 \\ \bar{x}_2 \bar{y}_3 - \bar{x}_3 \bar{y}_2 & 0 & \bar{x}_3 \bar{y}_1 - \bar{x}_1 \bar{y}_3 & 0 & \bar{x}_1 \bar{y}_2 - \bar{x}_2 \bar{y}_1 & 0 \\ 0 & \bar{x}_2 \bar{y}_3 - \bar{x}_3 \bar{y}_2 & 0 & \bar{x}_3 \bar{y}_1 - \bar{x}_1 \bar{y}_3 & 0 & \bar{x}_1 \bar{y}_2 - \bar{x}_2 \bar{y}_1 \end{bmatrix}$$

(6) Bending Stiffness Matrix $\left[\bar{K}_B \right]$ (See Figure 37.)

The matrix $\left[\bar{K}_B \right]$ expresses the linear relation between fictitious nodal forces and nodal bending displacements in the triangle. It is derived by obtaining the internal strain energy in the form:

$$\bar{U}_B = \frac{1}{2} \left[\bar{\delta}_B \right]_N \left[\quad \right] \left[\bar{\delta}_B \right]_N$$

where $\{\bar{\delta}_B\}_N$ is the local nodal bending displacement column matrix and the middle matrix $[\bar{A}_B]$ is the local bending stiffness matrix $[R_B]$.

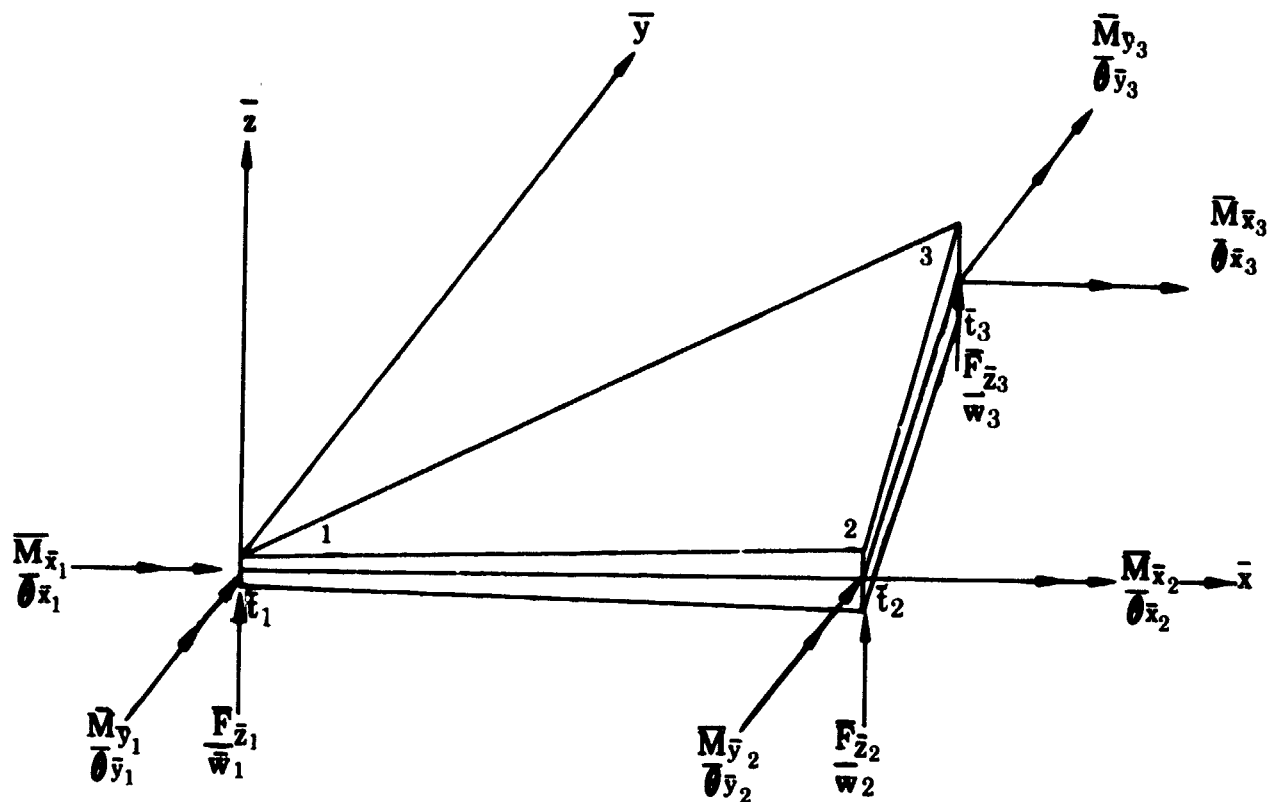


Figure 37. Generalized Nodal Bending Displacements and Forces On Flat Triangular Element

FD 25652

Using displacement function

$$\bar{w} = \bar{a}_1 + \bar{a}_2 \bar{x} + \bar{a}_3 \bar{y} + \bar{a}_4 \bar{x}^2 + \bar{a}_5 \bar{y}^2 + \bar{a}_6 \bar{x}^3 + \bar{a}_7 \bar{x}^2 \bar{y} + \bar{a}_8 \bar{x} \bar{y}^2 + \bar{a}_9 \bar{y}^3$$

$$\begin{Bmatrix} \bar{w} \\ \bar{\theta}_{\bar{x}} \\ \bar{\theta}_{\bar{y}} \end{Bmatrix} = \bar{\delta}_B = \begin{Bmatrix} \bar{w} \\ \frac{\partial \bar{w}}{\partial \bar{y}} \\ -\frac{\partial \bar{w}}{\partial \bar{x}} \end{Bmatrix} = \begin{bmatrix} 1 & \bar{x} & \bar{y} & \bar{x}^2 & \bar{y}^2 & \bar{x}^3 & \bar{x}^2 \bar{y} & \bar{x} \bar{y}^2 & \bar{y}^3 \\ 0 & 0 & 1 & 0 & 2\bar{y} & 0 & \bar{x}^2 & 2\bar{x} \bar{y} & 3\bar{y}^2 \\ 0 & -1 & 0 & -2\bar{x} & 0 & -3\bar{x}^2 & -2\bar{x} \bar{y} & -\bar{y}^2 & 0 \end{bmatrix} \begin{Bmatrix} \bar{a}_1 \\ \bar{a}_2 \\ \bar{a}_3 \\ \bar{a}_4 \\ \bar{a}_5 \\ \bar{a}_6 \\ \bar{a}_7 \\ \bar{a}_8 \\ \bar{a}_9 \end{Bmatrix} = [\bar{A}_B] \{\bar{\alpha}\}$$

In matrix form

$$\{\bar{\delta}_B\} = [\bar{A}_B] \{\bar{\alpha}_B\}$$

For nodal values

$$\begin{aligned} \{\bar{\delta}_B\}_N &= [\bar{A}_B]_N \{\bar{\alpha}_B\} \\ \therefore \{\bar{\alpha}_B\} &= [A_B]_N^{-1} \{\bar{\delta}_B\}_N \\ \text{and } \{\bar{\delta}_B\} &= [\bar{A}_B] [\bar{A}_B]_N^{-1} \{\bar{\delta}_B\}_N \end{aligned}$$

using

$$\text{Curvature Matrix } \{\bar{c}\} = \begin{Bmatrix} -\bar{w}_{yy} \\ -\bar{w}_{xx} \\ \bar{w}_{xy} \end{Bmatrix} = \begin{bmatrix} 0 & 0 & 0 & 0 & -2 & 0 & 0 & -2\bar{x} & -6\bar{y} \\ 0 & 0 & 0 & -2 & 0 & -6\bar{x} & -2\bar{y} & 0 & 0 \\ 0 & 0 & 0 & 0 & 0 & 0 & 2\bar{x} & 2\bar{y} & 0 \end{bmatrix} \{\bar{\alpha}_B\}$$

or

$$\{\bar{c}\} = [\bar{E}_B] \{\bar{\alpha}_B\} = [\bar{E}_B] [\bar{A}_B]_N^{-1} \{\bar{\delta}_B\}_N$$

Internal strain energy,

$$\begin{aligned} \bar{U}_B &= \frac{1}{2} \int \bar{D} \left[\bar{w}_{xx}^2 + \bar{w}_{yy}^2 + 2\nu \bar{w}_{xx} \bar{w}_{yy} + 2(1-\nu) \bar{w}_{xy}^2 \right] d\bar{x}d\bar{y} \\ &= \frac{1}{2} \int \bar{D} \begin{bmatrix} -\bar{w}_{yy} & -\bar{w}_{xx} & \bar{w}_{xy} \end{bmatrix} \begin{bmatrix} 1 & \nu & 0 \\ \nu & 1 & 0 \\ 0 & 0 & 2(1-\nu) \end{bmatrix} \begin{Bmatrix} -\bar{w}_{yy} \\ -\bar{w}_{xx} \\ \bar{w}_{xy} \end{Bmatrix} d\bar{x}d\bar{y} \\ &= \frac{1}{2} \int \bar{D} \{\bar{c}\} [\bar{V}_B] \{\bar{c}\} d\bar{x}d\bar{y} \\ &= \frac{1}{2} \int \bar{D} \{\bar{\delta}_B\}_N [A_B]_N^{-1T} [\bar{E}_B]^T [\bar{V}_B] [\bar{E}_B] [\bar{A}_B]_N^{-1} \{\bar{\delta}_B\}_N d\bar{x}d\bar{y} \end{aligned}$$

$$\bar{U}_B = \frac{1}{2} \{\bar{\delta}_B\}_N \left[[\bar{A}_B]_N^{-1T} \left(\int \bar{D} [\bar{E}_B]^T [\bar{V}_B] [\bar{E}_B] d\bar{x}d\bar{y} \right) [\bar{A}_B]_N^{-1} \right] \{\bar{\delta}_B\}_N$$

$$\therefore [\bar{K}_B] = [A_B]_N^{-1T} \left(\int \bar{D} [\bar{E}_B]^T [\bar{V}_B] [\bar{E}_B] d\bar{x}d\bar{y} \right) [\bar{A}_B]_N^{-1} \quad (49)$$

$$\bar{D} = \frac{Et^3}{12(1-\nu^2)}$$

(7) Nodal Pressure Force Matrix $\left\{ \bar{F}_p \right\}_N$ (See Figure 38.)

The matrix $\left\{ \bar{F}_p \right\}_N$ is the column matrix of fictitious local nodal forces which resist bending deflections caused by a uniform pressure load. This is derived by obtaining the potential energy in the form:

$$\bar{V}_p = \left[\bar{\delta}_B \right]_N \left\{ \right\}_N$$

where $\left[\bar{\delta}_B \right]_N$ is local nodal bending displacement row matrix and the latter matrix $\left\{ \right\}_N$ is the desired local pressure force matrix $\left\{ \bar{F}_p \right\}_N$.

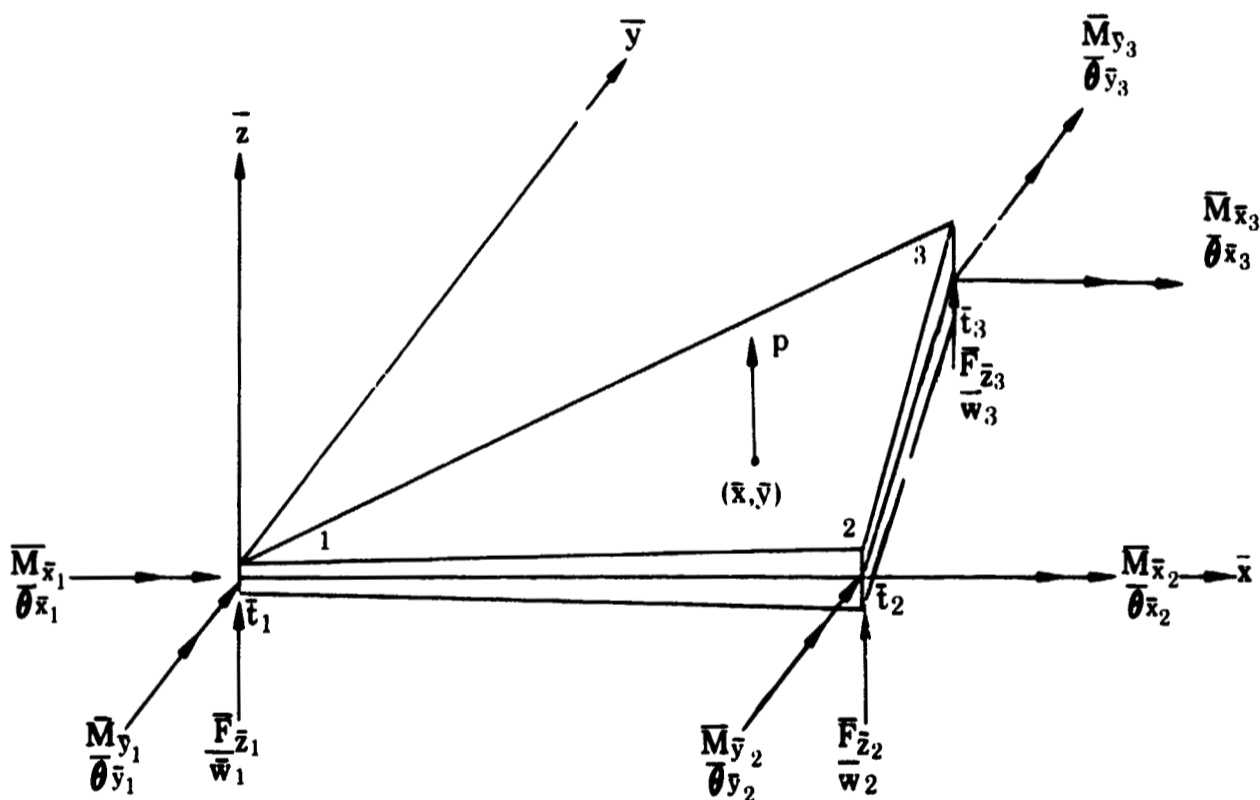


Figure 38. Generalized Nodal Bending Displacements and Forces on Flat Triangular Element

FD 25652B

In local coordinates,

$$\bar{w} = \bar{a}_1 + \bar{a}_2 \bar{x} + \bar{a}_3 \bar{y} + \bar{a}_4 \bar{x}^2 + \bar{a}_5 \bar{y}^2 + \bar{a}_6 \bar{x}^3 + \bar{a}_7 \bar{x}^2 \bar{y} + \bar{a}_8 \bar{x} \bar{y}^2 + \bar{a}_9 \bar{y}^3$$

or

$$\left[\bar{\delta}_B \right] = \begin{Bmatrix} \bar{w} \\ \bar{w}_{,\bar{y}} \\ -\bar{w}_{,\bar{x}} \end{Bmatrix} = \left[\bar{A}_B \right] \left\{ \bar{\alpha}_B \right\}$$

For nodal values

$$\left[\bar{\delta}_B \right]_N = \left[\bar{A}_B \right]_N \left\{ \bar{\alpha}_B \right\}$$

$$\begin{aligned} \therefore \{\bar{\alpha}_B\} &= [\bar{A}_B]_N^{-1} \{\bar{\delta}_B\}_N \\ \text{or } \{\bar{\delta}_B\} &= [\bar{A}_B] [\bar{A}_B]_N^{-1} \{\bar{\delta}_B\}_N \\ \text{and } \{\bar{\delta}_B\} &= \{\bar{\delta}_B\}_N [\bar{A}_B]_N^{-1T} [\bar{A}_B]^T \end{aligned}$$

$$\begin{aligned} \therefore \bar{w} &= \begin{Bmatrix} \{\bar{\delta}_B\} \\ 0 \\ 0 \end{Bmatrix} \\ &= \{\bar{\delta}_B\}_N [\bar{A}_B]_N^{-1T} [\bar{A}_B]^T \begin{Bmatrix} 1 \\ 0 \\ 0 \end{Bmatrix} \end{aligned}$$

The potential energy due to pressure loading is

$$\bar{V}_p = \int p \bar{w} d\bar{x} d\bar{y} = \{\bar{\delta}_B\}_N \int p [\bar{A}_B]_N^{-1T} [\bar{A}_B]^T \begin{Bmatrix} 1 \\ 0 \\ 0 \end{Bmatrix} d\bar{x} d\bar{y}$$

$$\text{or } \bar{V}_p = \{\bar{\delta}_B\}_N \{\bar{F}_p\}_N$$

Therefore,

$$\{\bar{F}_p\}_N = \int p [\bar{A}_B]_N^{-1T} [\bar{A}_B]^T \begin{Bmatrix} 1 \\ 0 \\ 0 \end{Bmatrix} d\bar{x} d\bar{y} \quad (50)$$

(8) Nodal Centrifugal Force Matrix $\{\bar{F}_C\}_N$ (See Figure 39.)

The matrix $\{\bar{F}_C\}_N$ is the column matrix of fictitious local nodal forces which resist displacements caused by rotation. This is derived by obtaining the potential energy in the form:

$$V_C = \{\bar{\delta}\}_N \{\bar{F}_C\}_N$$

where $\{\bar{\delta}\}_N$ is the local nodal displacement row matrix and the latter matrix $\{\bar{F}_C\}_N$ is the desired local centrifugal force column matrix $\{\bar{F}_C\}_N$.

The potential energy due to rotation is

$$\begin{aligned} V_C &= \int \rho \omega^2 \bar{r} \delta_r dA \\ &= \int \rho \omega^2 \bar{r} \left[u \cos(r,x) + v \cos(r,y) + w \cos(r,z) \right] dA \\ &= \int \rho \omega^2 \bar{r} \left[uvw \right] \begin{Bmatrix} \cos(r,x) \\ \cos(r,y) \\ \cos(r,z) \end{Bmatrix} dA \end{aligned}$$

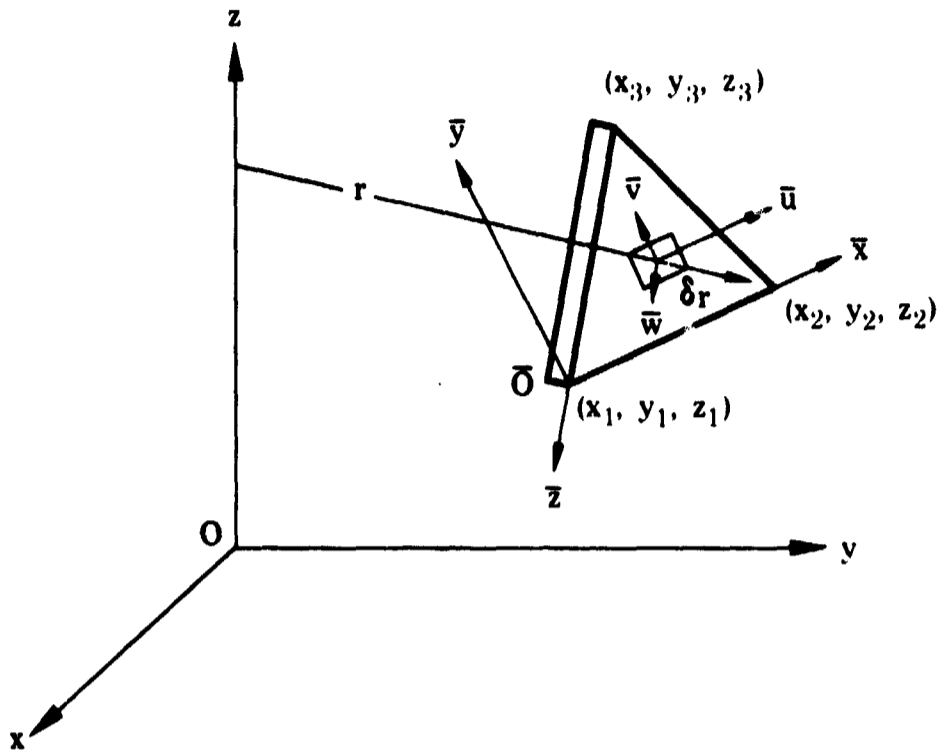


Figure 39. Geometry of Rotating Triangular Element

FD 25844

But

$$\begin{aligned} \begin{bmatrix} uvw \end{bmatrix} &= \begin{bmatrix} \bar{u} \bar{v} \bar{w} \end{bmatrix} \begin{bmatrix} \cos(x, \bar{x}) & \cos(y, \bar{x}) & \cos(z, \bar{x}) \\ \cos(x, \bar{y}) & \cos(y, \bar{y}) & \cos(z, \bar{y}) \\ \cos(x, \bar{z}) & \cos(y, \bar{z}) & \cos(z, \bar{z}) \end{bmatrix} \\ &= \begin{bmatrix} \bar{u} \bar{v} \bar{w} \end{bmatrix} \begin{bmatrix} R_1 \end{bmatrix}^T \end{aligned}$$

$$\therefore \delta_r = \begin{bmatrix} \bar{u} \bar{v} \bar{w} \end{bmatrix} \begin{bmatrix} R_1 \end{bmatrix}^T \begin{bmatrix} \cos(r, \bar{x}) \\ \cos(r, \bar{y}) \\ \cos(r, \bar{z}) \end{bmatrix}$$

Or

$$\delta_r = \begin{bmatrix} \bar{u} \bar{v} \bar{w} \end{bmatrix} \begin{bmatrix} R_1 \end{bmatrix}^T \begin{bmatrix} x/r \\ y/r \\ 0 \end{bmatrix}$$

Since $\cos(\tau, z) = 0$, from (34)

$$\begin{bmatrix} x \\ y \\ 0 \end{bmatrix} = \begin{bmatrix} x_1 \\ y_1 \\ z_1 - z \end{bmatrix} + \begin{bmatrix} R_1 \end{bmatrix} \begin{bmatrix} \bar{x} \\ \bar{y} \\ 0 \end{bmatrix}$$

From which

$$z - z_1 = \bar{x} \cos(z, \bar{x}) + \bar{y} \cos(z, \bar{y})$$

Therefore

$$\begin{bmatrix} x \\ y \\ 0 \end{bmatrix} = \begin{bmatrix} x_1 \\ y_1 \\ -\bar{x} \cos(z, \bar{x}) - \bar{y} \cos(z, \bar{y}) \end{bmatrix} + \begin{bmatrix} R_1 \end{bmatrix} \begin{bmatrix} \bar{x} \\ \bar{y} \\ 0 \end{bmatrix}$$

and

$$V_c = \int \rho \omega^2 \epsilon [\bar{u} \bar{v} \bar{w}] [R_1]^T \left[\begin{array}{c} \bar{x}^1 \cos(z, \bar{x})^1 - \bar{y}^1 \cos(z, \bar{y})^1 \\ \bar{x}^1 \cos(z, \bar{x})^1 - \bar{y}^1 \cos(z, \bar{y})^1 \\ 0 \end{array} \right] + [R_1] \left[\begin{array}{c} \bar{x} \\ \bar{y} \\ 0 \end{array} \right] dA$$

expanding

$$[\bar{u} \bar{v} \bar{w}] = [\bar{u} \bar{v} \bar{w} \bar{\theta}_x \bar{\theta}_y \bar{\theta}_z] \begin{bmatrix} 1 & 0 & 0 \\ 0 & 1 & 0 \\ 0 & 0 & 1 \\ 0 & 0 & 0 \\ 0 & 0 & 0 \\ 0 & 0 & 0 \end{bmatrix} = \{\bar{\delta}\} \begin{bmatrix} I_3 \\ 0_3 \end{bmatrix}$$

where

$$I_3 = \begin{bmatrix} 100 \\ 010 \\ 001 \end{bmatrix}$$

$$0_3 = \begin{bmatrix} 000 \\ 000 \\ 000 \end{bmatrix}$$

Therefore

$$\begin{bmatrix} \bar{u} \\ \bar{v} \\ \bar{w} \end{bmatrix} = \begin{bmatrix} 1 & 0 & 0 & 0 & 0 & 0 \\ 0 & 1 & 0 & 0 & 0 & 0 \\ 0 & 0 & 1 & 0 & 0 & 0 \end{bmatrix} \begin{bmatrix} \bar{u} \\ \bar{v} \\ \bar{w} \\ \bar{\theta}_x \\ \bar{\theta}_y \\ \bar{\theta}_z \end{bmatrix}$$

Also

$$\{\bar{\delta}\} = \begin{bmatrix} [\bar{A}_M] [\bar{A}_M]^{-1} & 0 & 0 \\ 0 & [\bar{A}_B] [\bar{A}_B]^{-1} & 0 \\ 0 & 0 & 0 \end{bmatrix} \{\bar{\delta}\}_N$$

Therefore

$$\begin{aligned}
 & \quad \quad \quad [H] \\
 \left\{ \bar{\delta} \right\} = \left\{ \bar{\delta} \right\}_N & \begin{bmatrix} \left[\bar{A}_M \right]_N^{-1T} & \left[\bar{A}_M \right]^T & 0 & 0 \\ 0 & \left[\bar{A}_B \right]_N^{-1T} & \left[\bar{A}_B \right]^T & 0 \\ 0 & 0 & 0 & 0 \end{bmatrix}
 \end{aligned}$$

In matrix form

$$\begin{aligned}
 \left\{ \bar{\delta} \right\} &= [H] \left\{ \bar{\delta} \right\}_N \\
 \left\{ \bar{\delta} \right\}_N &= \left\{ \bar{\delta} \right\}_N [H]^T
 \end{aligned}$$

$$\therefore v_c = \rho \omega^2 \left\{ \bar{\delta} \right\}_N \int_S \bar{t} [H]^T \begin{Bmatrix} I_3 \\ 0_3 \end{Bmatrix} [R_1]^T \begin{Bmatrix} x_1 \\ y_1 \\ -\bar{x} \cos(z, \bar{x}) - \bar{y} \cos(z, \bar{y}) \end{Bmatrix} + [R_1] \begin{Bmatrix} \bar{x} \\ \bar{y} \\ 0 \end{Bmatrix} dx dy$$

and

$$\left\{ F_c \right\}_N = \rho \omega^2 \int_S \bar{t} [H]^T \begin{Bmatrix} I_3 \\ 0_3 \end{Bmatrix} [R_1]^T \begin{Bmatrix} x_1 \\ y_1 \\ -\bar{x} \cos(z, \bar{x}) - \bar{y} \cos(z, \bar{y}) \end{Bmatrix} + [R_1] \begin{Bmatrix} \bar{x} \\ \bar{y} \\ 0 \end{Bmatrix} dx dy \quad (51)$$

Then, in local coordinates

$$\left\{ \bar{F}_c \right\}_N = [R_6]^T \left\{ F_c \right\}_N$$

(9) Approximate Centrifugal Force Matrix $\left\{ F_c \right\}_N$

$$\left\{ F_c \right\}_N = \begin{bmatrix} F_{x_1} \\ F_{y_1} \\ F_{z_1} \\ M_{x_1} \\ M_{y_1} \\ M_{z_1} \\ F_{x_2} \\ F_{y_2} \\ F_{z_2} \\ M_{x_2} \\ M_{y_2} \\ M_{z_2} \\ F_{x_3} \\ F_{y_3} \\ F_{z_3} \\ M_{x_3} \\ M_{y_3} \\ M_{z_3} \end{bmatrix} = \frac{\rho \omega^2 \bar{A}_i \bar{t}_i}{3} \begin{bmatrix} x_1 \\ y_1 \\ 0 \\ 0 \\ 0 \\ 0 \\ x_2 \\ y_2 \\ 0 \\ 0 \\ 0 \\ 0 \\ x_3 \\ y_3 \\ 0 \\ 0 \\ 0 \\ 0 \end{bmatrix} \quad (52)$$

- \bar{A}_i = Area of ith element
- \bar{t}_i = Average thickness of ith element
- ρ = Density
- ω = Angular velocity

x, y, z (N common coordinates)

This matrix (52) is used in lieu of (51) because of its simplicity. It should provide better accuracy than (51), particularly in cases where bending stresses are predominant; however, more experience is needed with this matrix (52) form before it can be used with a high degree of confidence. For this reason, the computer program contains in option that permits selection of either matrix (51) or (52).

(10) Membrane Inertia Matrix $\left[\bar{M}_M \right]$ (See Figure 36)

The matrix $\left[\bar{M}_M \right]$ is the matrix of fictitious nodal masses and inertias which resist vibratory membrane motion in the plane of the triangle. It is derived by obtaining the kinetic energy of motion in the form:

$$\bar{T} = \frac{1}{2} \left[\dot{\bar{q}}_N \right]^T \left[\bar{M}_M \right] \left[\dot{\bar{q}}_N \right]$$

where $\left[\bar{q} \right]_N$ is the local nodal vibratory membrane displacement column matrix and the middle matrix $\left[\bar{M}_M \right]$ is the desired local membrane inertia matrix.

$$\text{Kinetic Energy} = \int_s \frac{1}{2} \rho \bar{t} \left(\dot{\bar{u}}^2 + \dot{\bar{v}}^2 \right) d\bar{x}d\bar{y} = \int \frac{1}{2} \rho \bar{t} \dot{\bar{q}}^2 d\bar{x}d\bar{y}$$

Membrane Displacement Matrix

$$\left[\bar{q}_M \right] = \begin{Bmatrix} \bar{u} \\ \bar{v} \end{Bmatrix} = \begin{bmatrix} \bar{x} & 0 & \bar{y} & 0 & 1 & 0 \\ 0 & \bar{x} & 0 & \bar{y} & 0 & 1 \end{bmatrix} \begin{Bmatrix} \bar{a}_1 \\ \bar{a}_2 \\ \bar{a}_3 \\ \bar{a}_4 \\ \bar{a}_5 \\ \bar{a}_6 \end{Bmatrix}$$

or

$$\left[\bar{q}_M \right] = \left[\bar{A}_M \right] \left[\bar{\alpha}_M \right]$$

For nodal values

$$\left[\bar{q}_M \right]_N = \left[\bar{A}_M \right] \left[\bar{\alpha}_M \right]_N^{-1} \left[\bar{q}_M \right]_N$$

$$\left[\dot{\bar{q}}_M \right]_N = \left[\bar{A}_M \right] \left[\dot{\bar{\alpha}}_M \right]_N^{-1} \left[\dot{\bar{q}}_M \right]_N$$

and

$$\text{Kinetic Energy} = \int \frac{1}{2} \rho \bar{t} \left[\dot{\bar{q}}_M \right] \left[\dot{\bar{q}}_M \right] d\bar{x}d\bar{y}$$

$$= \frac{1}{2} \left[\dot{\bar{q}}_M \right]_N \rho \left[\bar{A}_M \right]_N^{-1T} \left(\int \bar{t} \left[\bar{A}_M \right]^T \left[\bar{A}_M \right] d\bar{x}d\bar{y} \right) \left[\bar{A}_M \right]_N^{-1} \left[\dot{\bar{q}}_M \right]_N$$

$$= \frac{1}{2} \left[\dot{\bar{q}}_M \right]_N \left[\bar{M}_M \right] \left[\dot{\bar{q}}_M \right]_N$$

∴ Membrane inertia matrix is

$$[\bar{M}_M] = \rho [\bar{A}_M]_N^{-1T} \left(\int \bar{t} [\bar{A}_M]^T [\bar{A}_M] d\bar{x}d\bar{y} \right) [\bar{A}_M]_N^{-1} \quad (53)$$

(11) Bending Inertia Matrix $[\bar{M}_B]$ (See Figure 37)

The matrix $[\bar{M}_B]$ is the matrix of fictitious nodal masses and inertias which resist vibratory transverse bending motion of the triangle. It is derived by obtaining the kinetic energy of motion in the form:

$$\bar{T} = \frac{1}{2} \left[\dot{\bar{q}} \right]_N \left[\quad \right] \left[\dot{\bar{q}} \right]_N$$

where $\left[\dot{\bar{q}} \right]_N$ is the local nodal vibratory transverse bending displacement column matrix and the middle matrix $\left[\quad \right]$ is the desired local bending inertia matrix $[\bar{M}_B]$.

$$\text{Kinetic Energy} = \int_V \frac{1}{2} \rho \bar{t} \left(\frac{\partial \bar{q}}{\partial t} \right)^2 d\bar{x}d\bar{y}$$

Transverse Displacement

$$\bar{q} = \bar{a}_1 + \bar{a}_2 \bar{x} + \bar{a}_3 \bar{y} + \bar{a}_4 \bar{x}^2 + \bar{a}_5 \bar{y}^2 + \bar{a}_6 \bar{x}^3 + \bar{a}_7 \bar{x}^2 \bar{y} + \bar{a}_8 \bar{x} \bar{y}^2 + \bar{a}_9 \bar{y}^3$$

or

$$\bar{q} = [\bar{A}_B] [\bar{\alpha}_B]$$

Using nodal values

$$\left[\bar{q}_B \right]_N = [\bar{A}_B]_N [\bar{\alpha}]_N$$

$$\left[\bar{\alpha} \right]_N = [\bar{A}_B]_N^{-1} \left[\bar{q}_B \right]_N$$

$$\bar{q} = [\bar{A}_B] [A_B]_N^{-1} \left[\bar{q}_B \right]_N$$

$$\dot{\bar{q}} = [\bar{A}_B] [A_B]_N^{-1} \left[\dot{\bar{q}}_B \right]_N$$

$$\begin{aligned}
\text{Kinetic Energy} &= \frac{1}{2} \rho \int_V \bar{t} \left[\dot{\bar{q}} \right] \left[\dot{\bar{q}} \right] d\bar{x}d\bar{y} \\
&= \frac{1}{2} \left[\dot{\bar{q}} \right]_N \left[\rho \left[\bar{A}_B \right]_N^{-1T} \left(\int \bar{t} \left[\bar{A}_B \right]^T \left[\bar{A}_B \right] d\bar{x}d\bar{y} \right) \left[\bar{A}_B \right]_N^{-1} \right] \left[\dot{\bar{q}} \right]_N \\
&= \frac{1}{2} \left[\dot{\bar{q}} \right]_N \left[\bar{M}_B \right] \left[\dot{\bar{q}} \right]_N
\end{aligned}$$

∴ Bending inertia matrix is

$$\left[\bar{M}_B \right] = \rho \left[\bar{A}_B \right]_N^{-1T} \left(\int \bar{t} \left[\bar{A}_B \right]^T \left[\bar{A}_B \right] d\bar{x}d\bar{y} \right) \left[\bar{A}_B \right]_N^{-1} \quad (54)$$

(12) Normal Direction Cosine Matrix $\left[R_1 \right]_N$

The matrix $\left[R_1 \right]_N$ establishes the relation between the directions of the axes of the common coordinate system and the axes of the quasi-normal system. It is obtained by averaging the directions of the \bar{y} and \bar{z} axes of the four triangular elements that have a common node and a common generator, with the x axis lying in the direction of the generator as shown in figure 40. The directions of the local axes of the individual triangular elements are obtained directly from the direction cosine matrix $\left[R_1 \right]$.

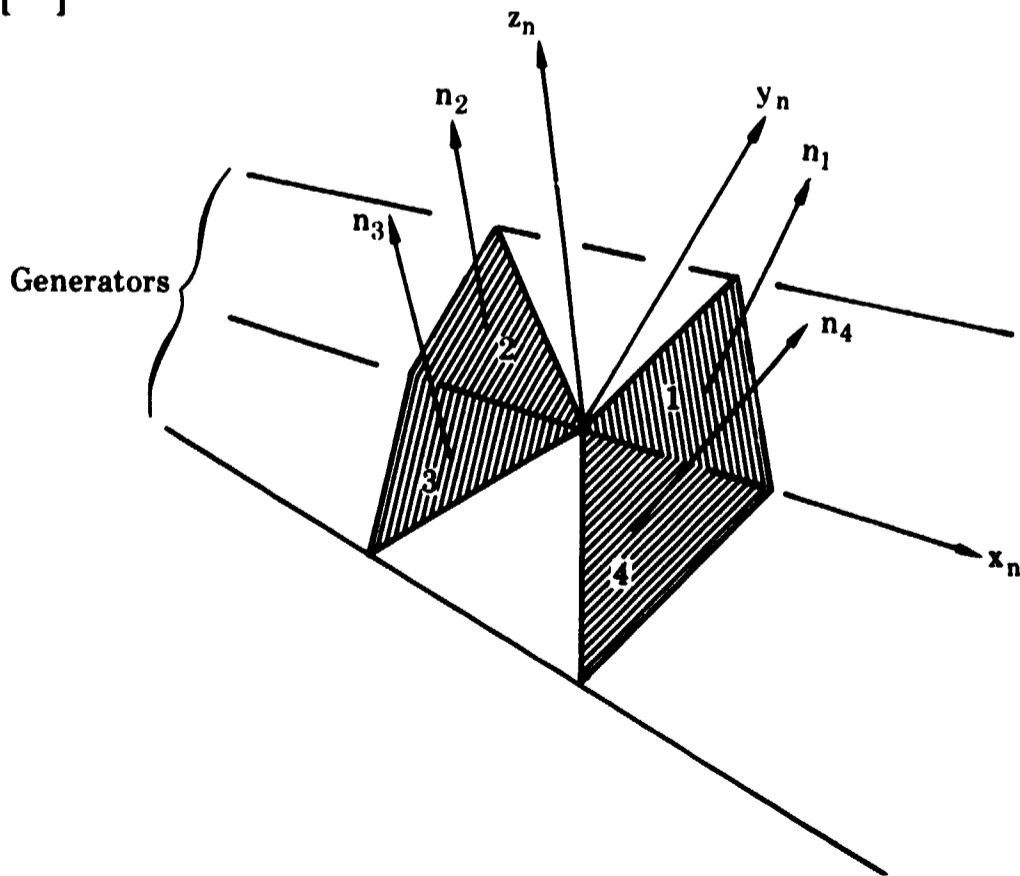


Figure 40. Definition of Quasi-Normal Coordinate System

FD 25669

e. Discussion of Typical Results of Analyses

(1) Stress Program

(a) Sectors

Test cases were first run on 45 degree flat sectors with 9 (figure 41) and 30 (figure 42) free nodes under uniform transverse load and centrifugal loading. There was a decided improvement in radial deflection for the centrifugal load case in going from 9 to 30 nodes as is shown in figure 43. Radial membrane stresses on interior triangular elements just about straddled the estimated stress curve when they were plotted for the centroid* of the appropriate triangle as is shown in figure 44. Approximate stresses and deflections were estimated by direct integration assuming that the radial pull is independent of polar angle. Averaging the stresses at each node by averaging the stresses in the triangles immediately surrounding a node also agreed fairly well with the estimated curve as is shown in figure 45.

The displacements under bending load also were improved in going from 9 to 30 nodes as is shown in figure 46. Radial bending stresses on interior triangular elements also straddled the estimated curve as is shown in figure 47. These stresses were also averaged at the center nodes and are presented in figure 48. Stresses were obtained from the moment distribution on a cantilever beam of linearly varying width and deflections were approximated by the moment-area method.

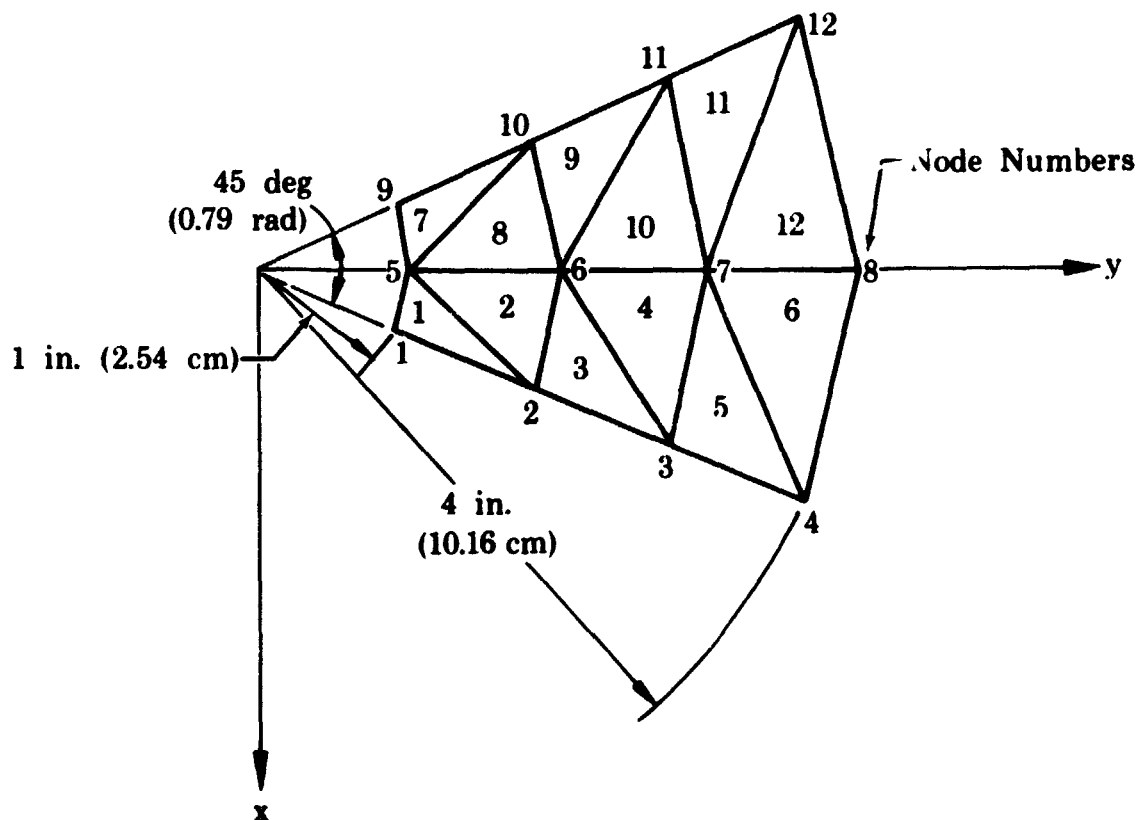


Figure 41. Breakup of 45-Degree Sector Into 12 Triangular Elements and 9 Free Nodes FD 25670

* Gerstenkoro presents data at the centroid of triangular elements for the solution of the thick-walled cylinder using finite elements, and Zienkiewicz discusses this and other methods of averaging stresses in triangular elements.

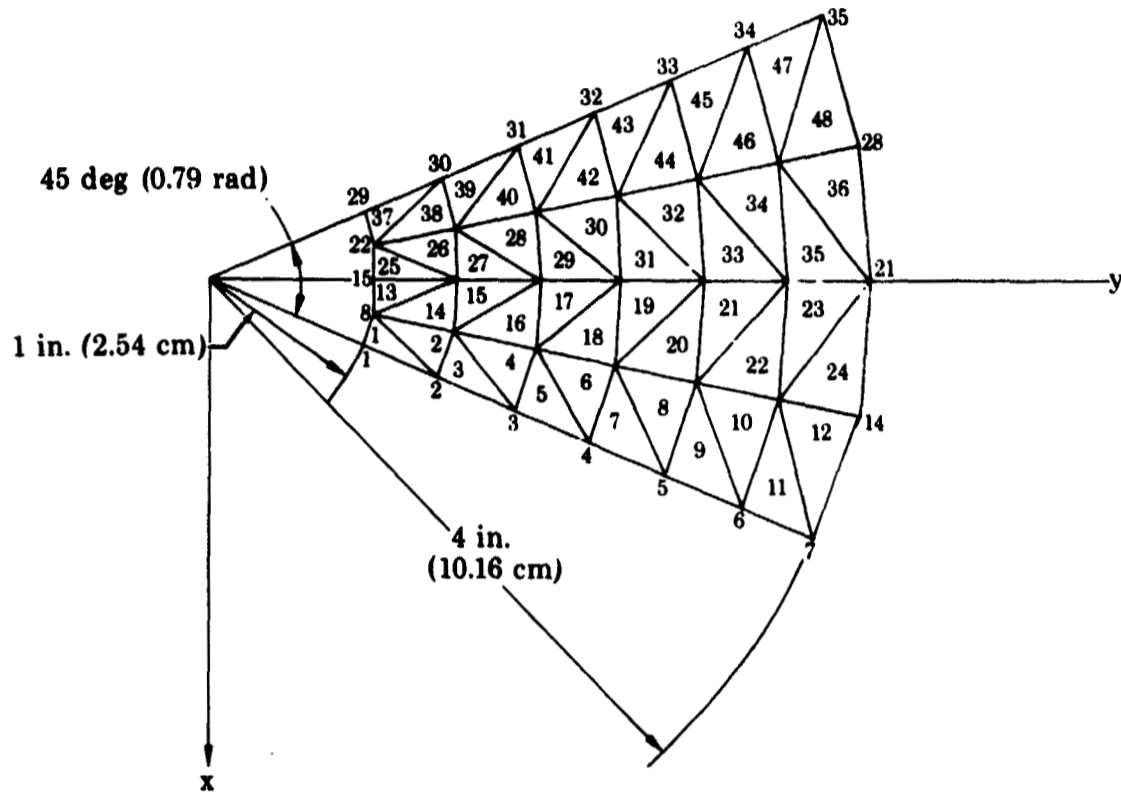


Figure 42. Breakup of 45-Degree Sector Into 48 Triangular Elements and 30 Free Nodes FD 25672

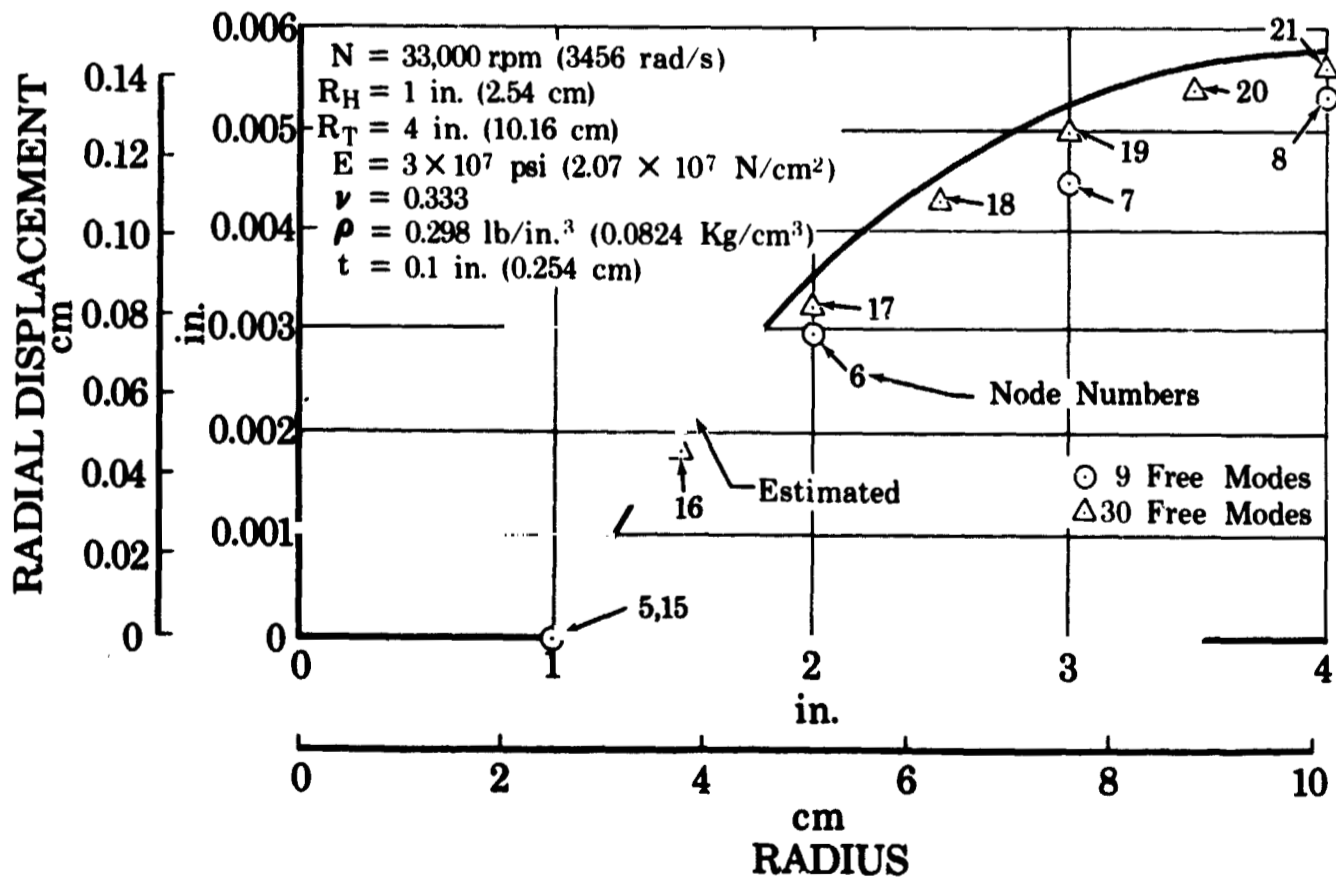


Figure 43. Radial Displacements In Rotating 45-Degree Sector FD 25335A

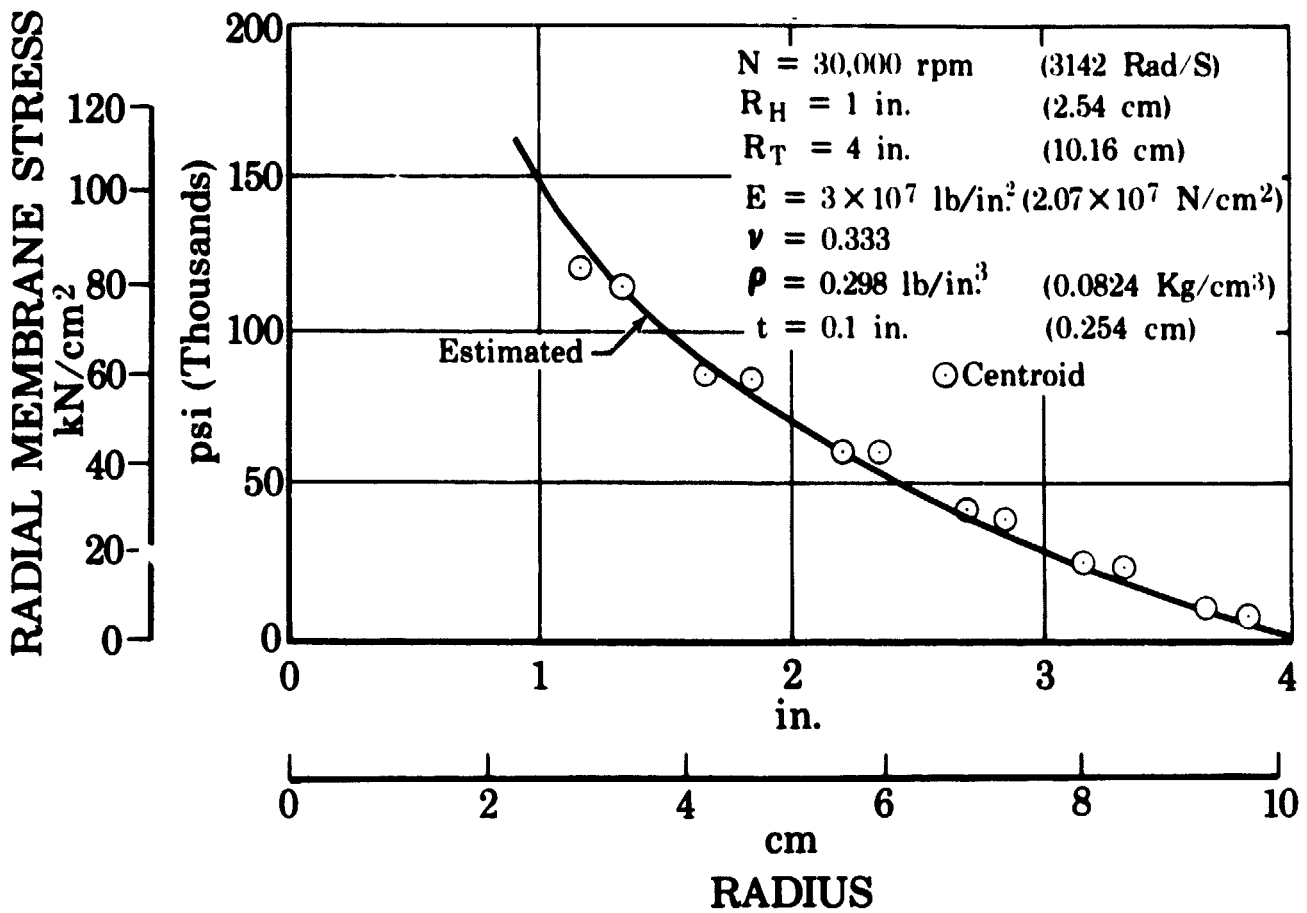


Figure 44. Radial Membrane Stresses In Rotating 45-Degree Sector With 30 Free Nodes FD 25657

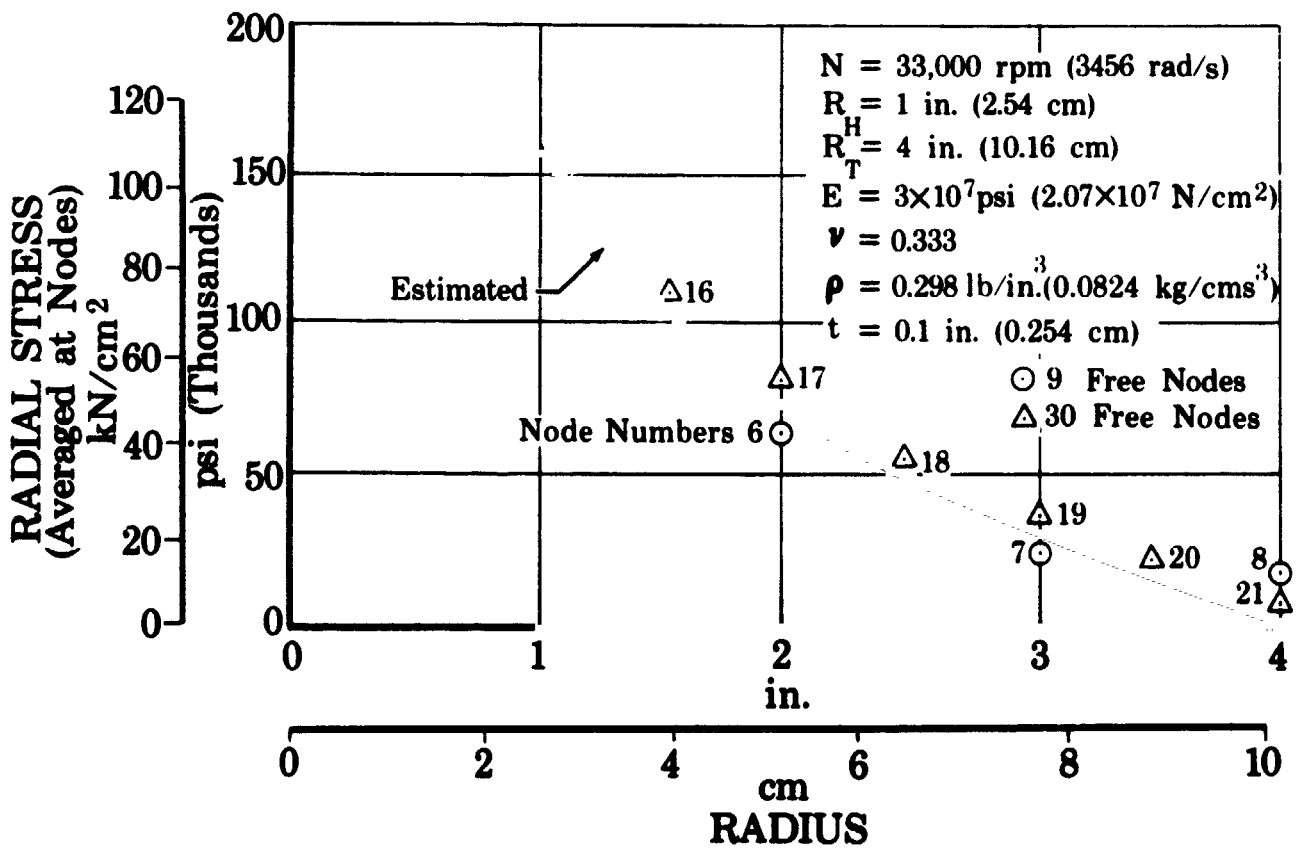


Figure 45. Radial Membrane Stresses In Rotating 45-Degree Sector at Midchord FD 25786A

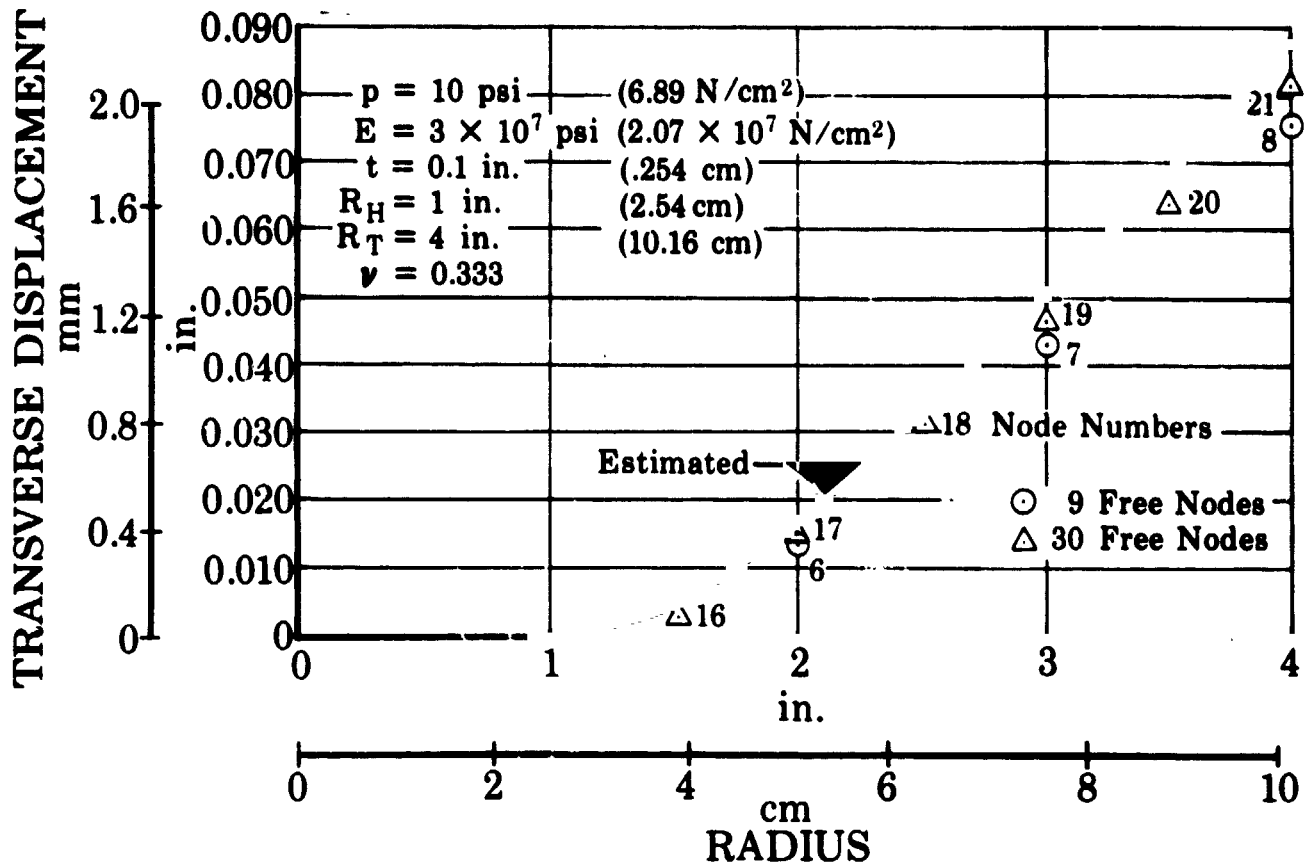


Figure 46. Transverse Midchord Displacement of Uniformly Loaded 45-Degree Cantilevered Sector FD 25787A

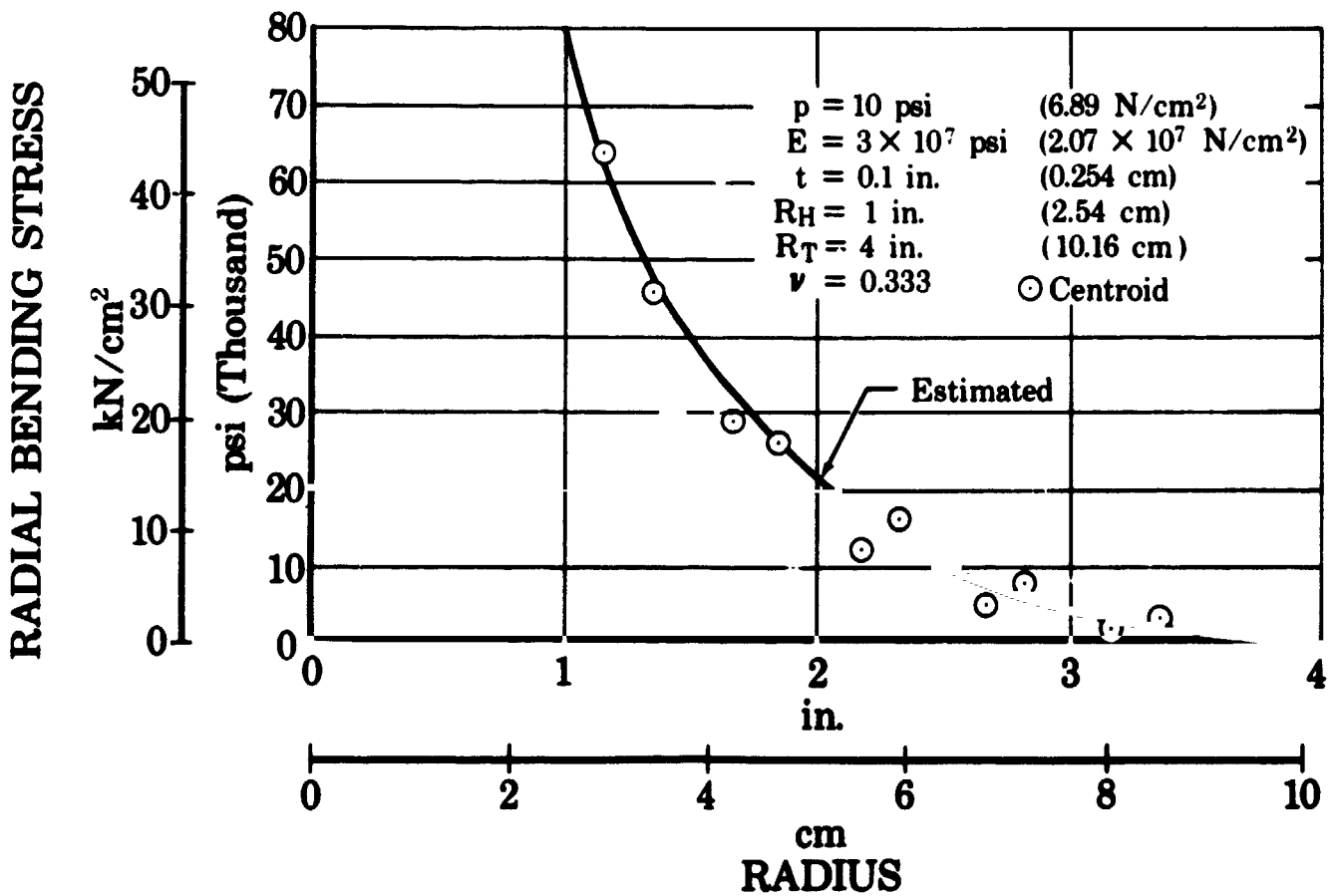


Figure 47. Radial Bending Stresses In Uniformly Loaded 45-Degree Cantilever Sector With 30 Free Nodes FD 25788A

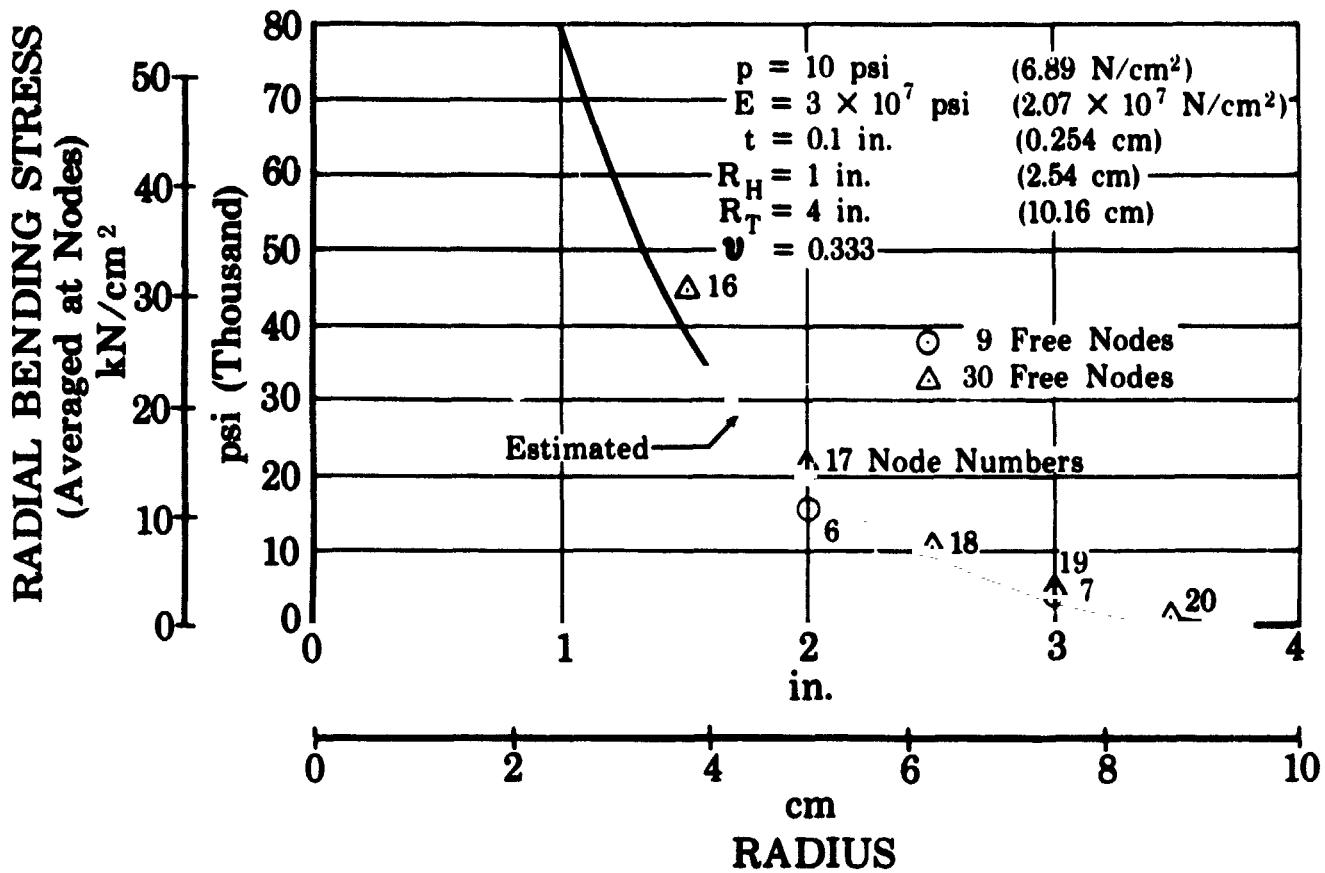


Figure 48. Radial Bending Stresses In Uniformly Loaded 45-Degree Cantilevered Sector |Midchord|

FD 25789A

(b) Rectangles

Similar test cases were run on 2 by 3 in. (5.08 by 7.62 cm) rectangles as shown in figures 49 through 53. Good agreement was achieved in all cases. Displacements always agreed better than the stresses.

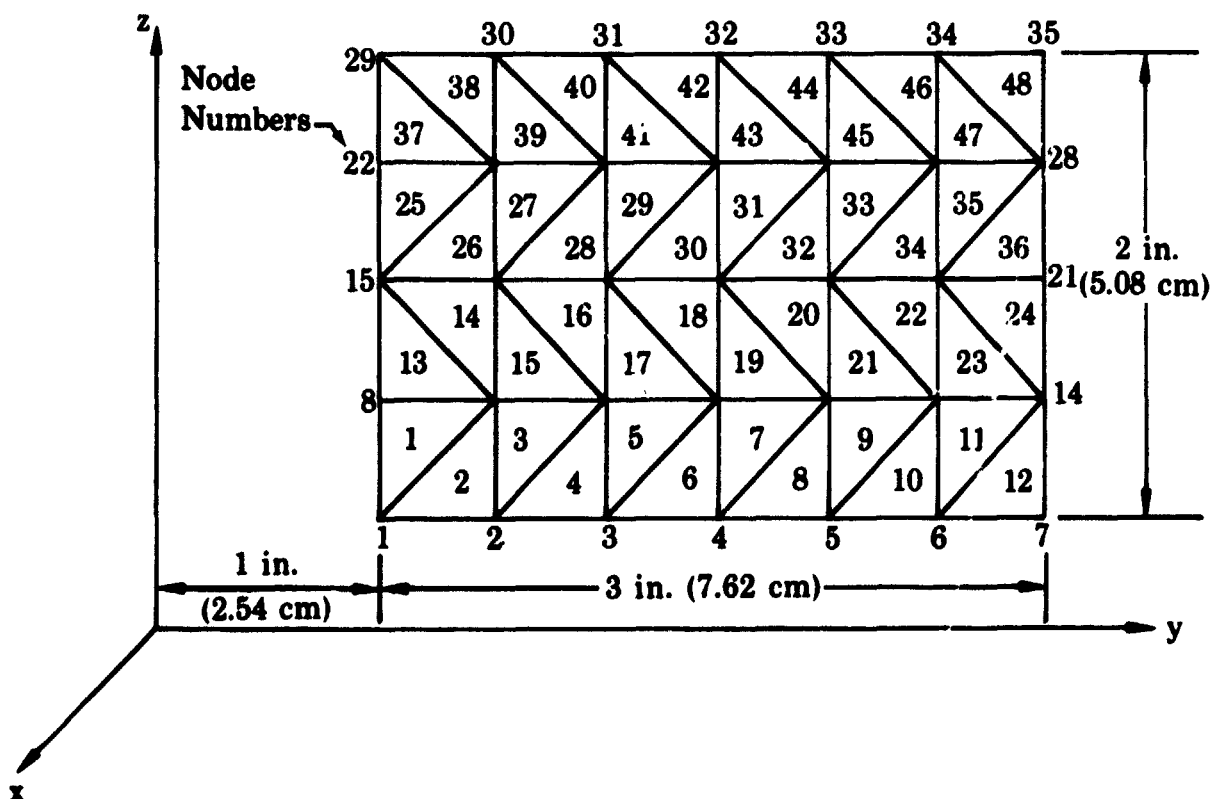


Figure 49. Breakup of 2-Inch by 3-Inch Rectangle Into 48 Triangular Elements and 30 Free Nodes

FD 25673

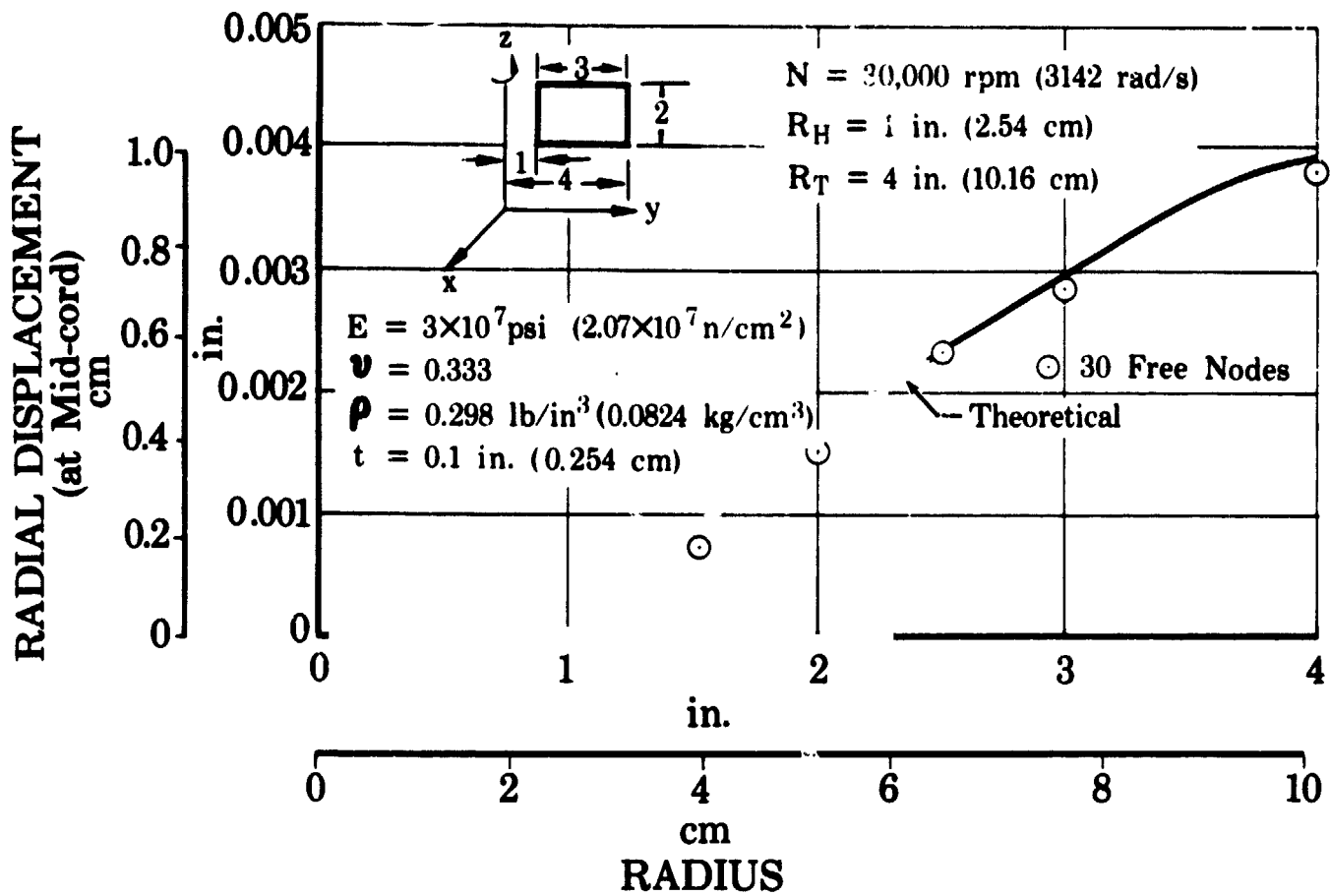


Figure 50. Radial Displacements In Rotating Rectangle With 30 Free Nodes FD 25790

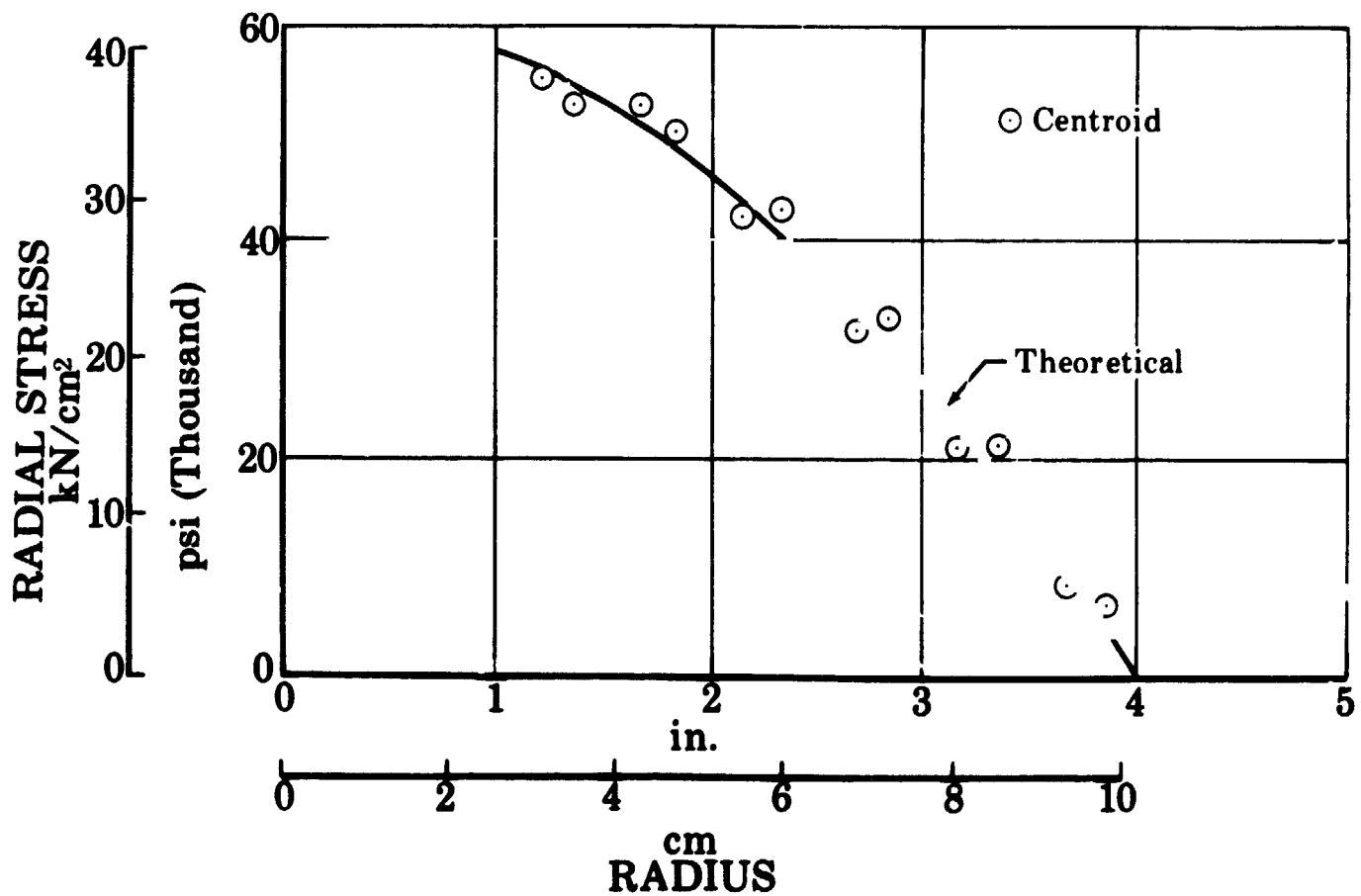


Figure 51. Radial Stresses In Rotating Rectangle With 30 Free Nodes FD 25791

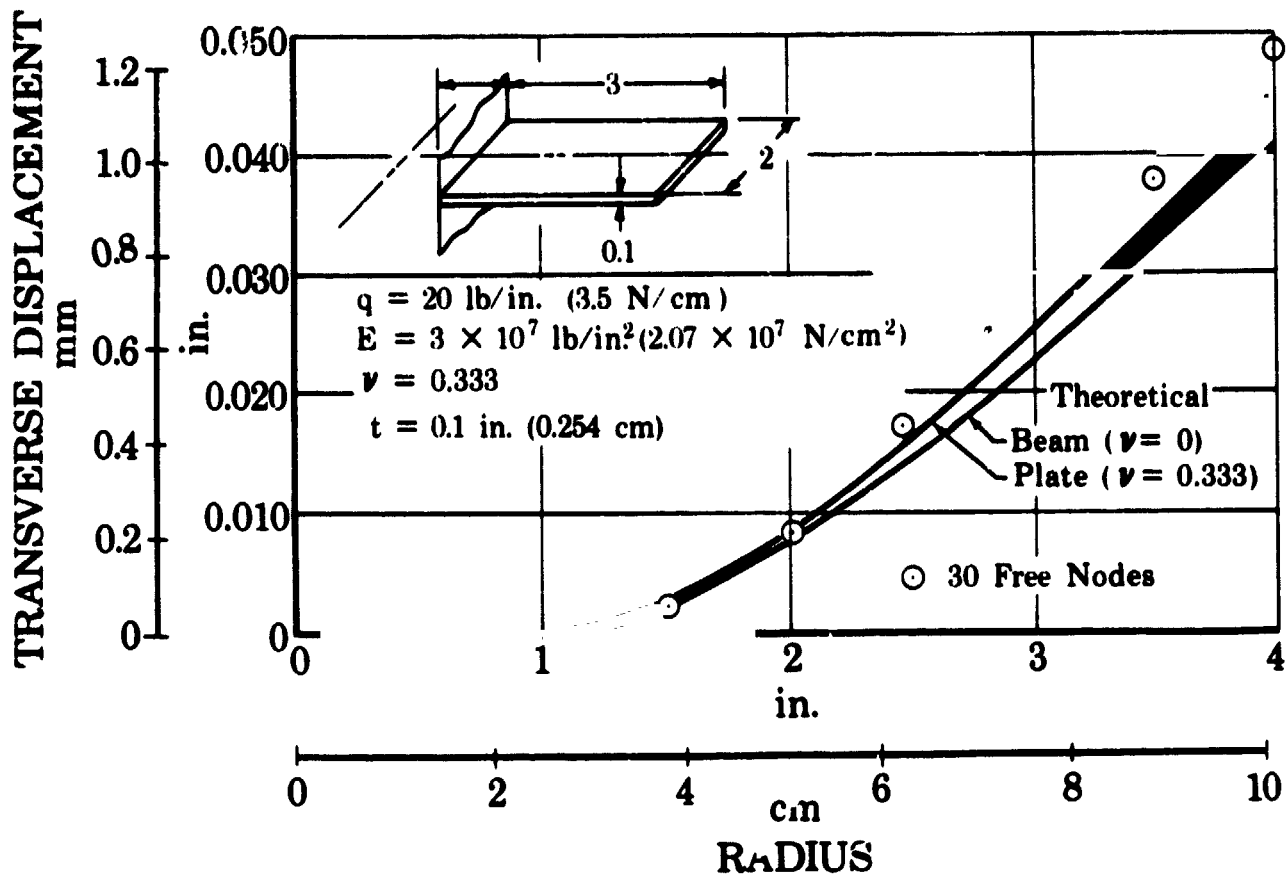


Figure 52. Transverse Midchord Displacement of Uniformly Loaded Cantilever With 30 Free Nodes

FD 25792A

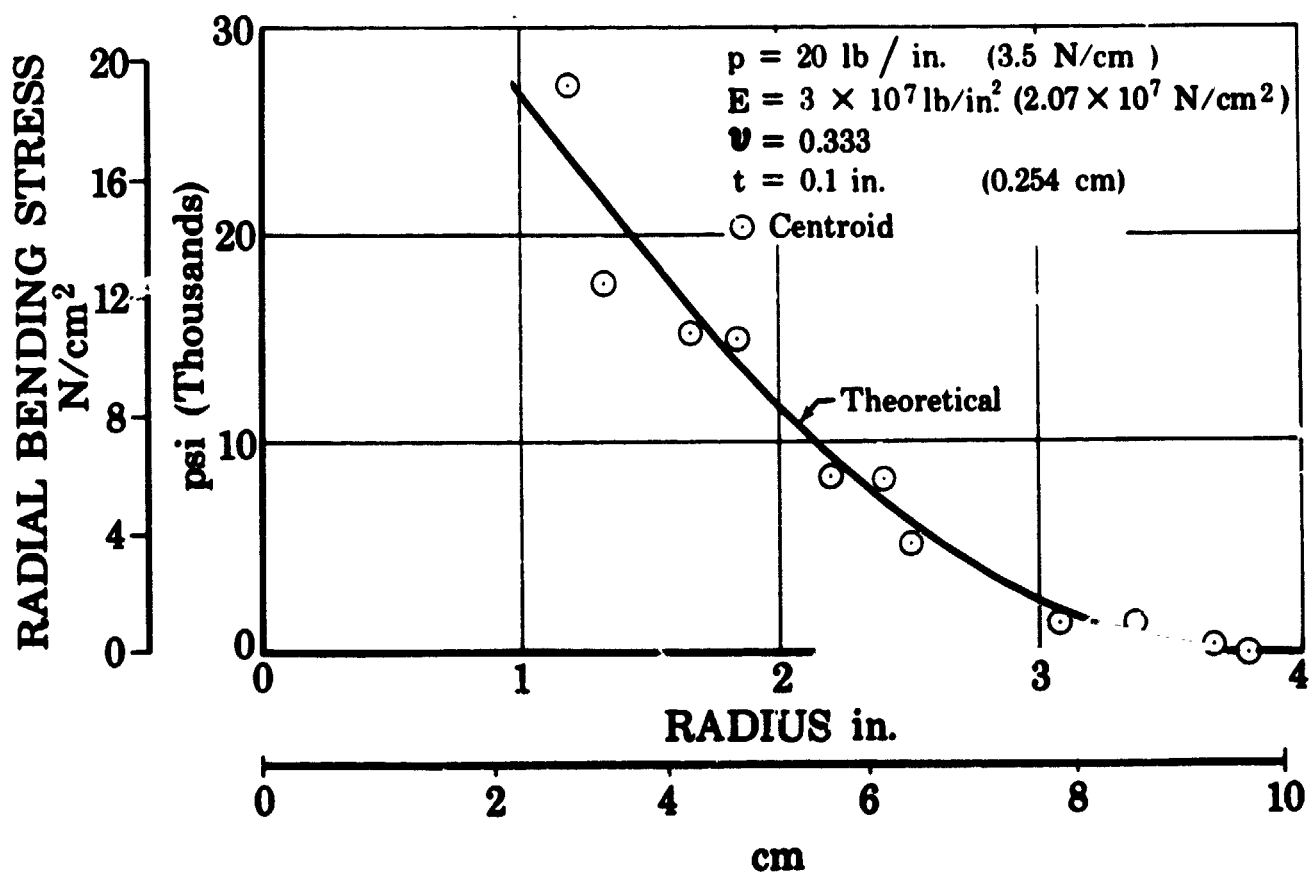


Figure 53. Radial Bending Stress In Uniformly Loaded Cantilever With 30 Free Nodes

FD 25793

(c) Circular Disk

A test case for a solid bore spinning disk with 48 free nodes (figure 54) was evaluated next. Displacements again agreed with theoretical results as shown in figure 55. Results were compared with the theoretical plane stress solution for a disk and with results from an existing program which is used by Pratt & Whitney Aircraft for compressor and turbine disk design, with $\nu = 0.300$. Stresses that were averaged at the nodes did not agree as closely as those for sectors and rectangles as is shown in figure 56. Pertaining to stress interpretation in general and figure 56 in particular, stresses at the hub and free edges cannot be evaluated directly because the correct stress gradient cannot be accounted for in a triangle over which the membrane stress is assumed constant or the bending stress is assumed to vary linearly. Such stresses can be obtained by using either extrapolation, smaller elements, or judicious weighing of element stresses as discussed by Zienkiewicz. It is expected that a finer breakup would reduce the error.

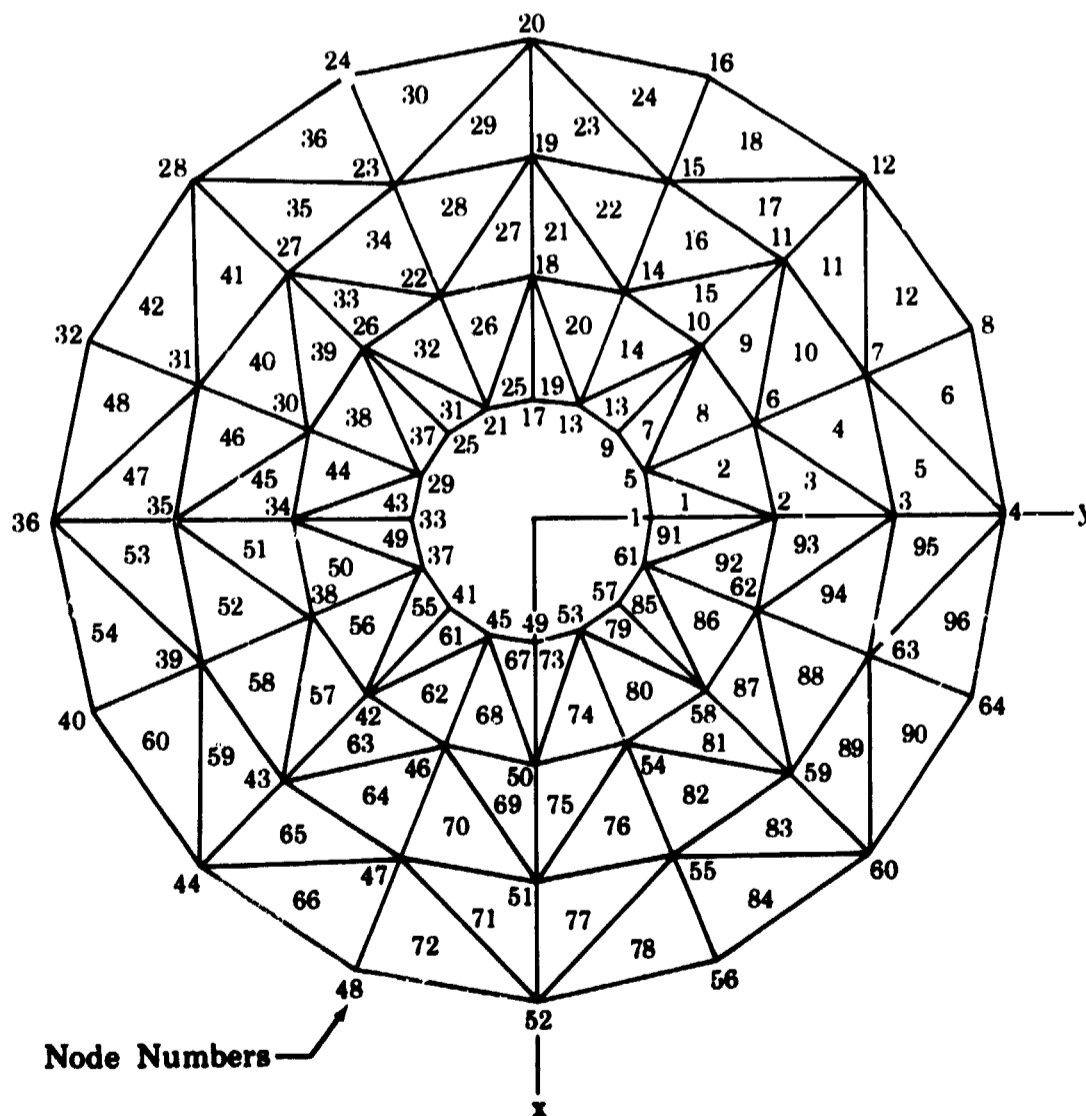


Figure 54. Breakup of Circular Disk into 96 Triangular Elements and 48 Free Nodes

FD 25655

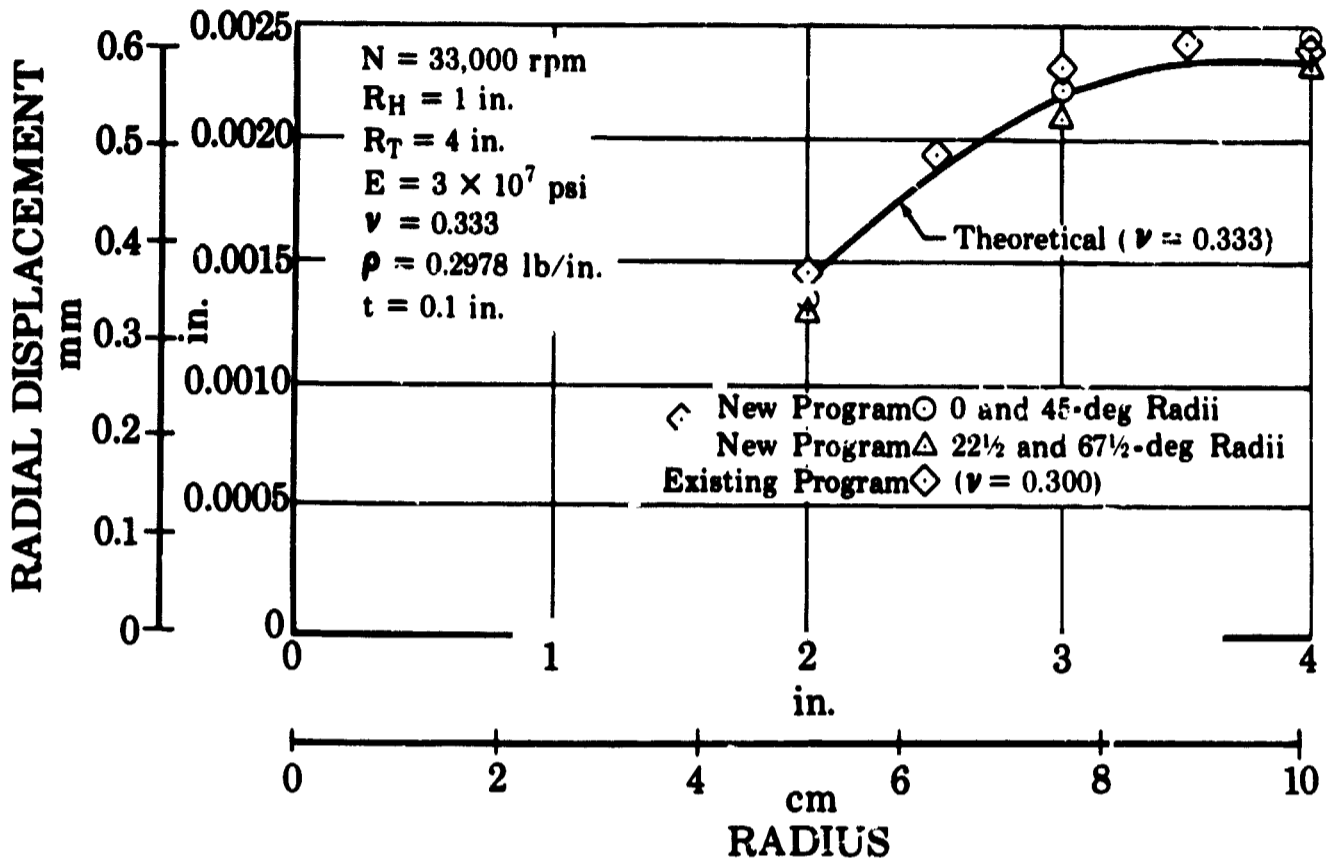


Figure 55. Radial Displacements In 48 Node Spinning Disk FD 25794A

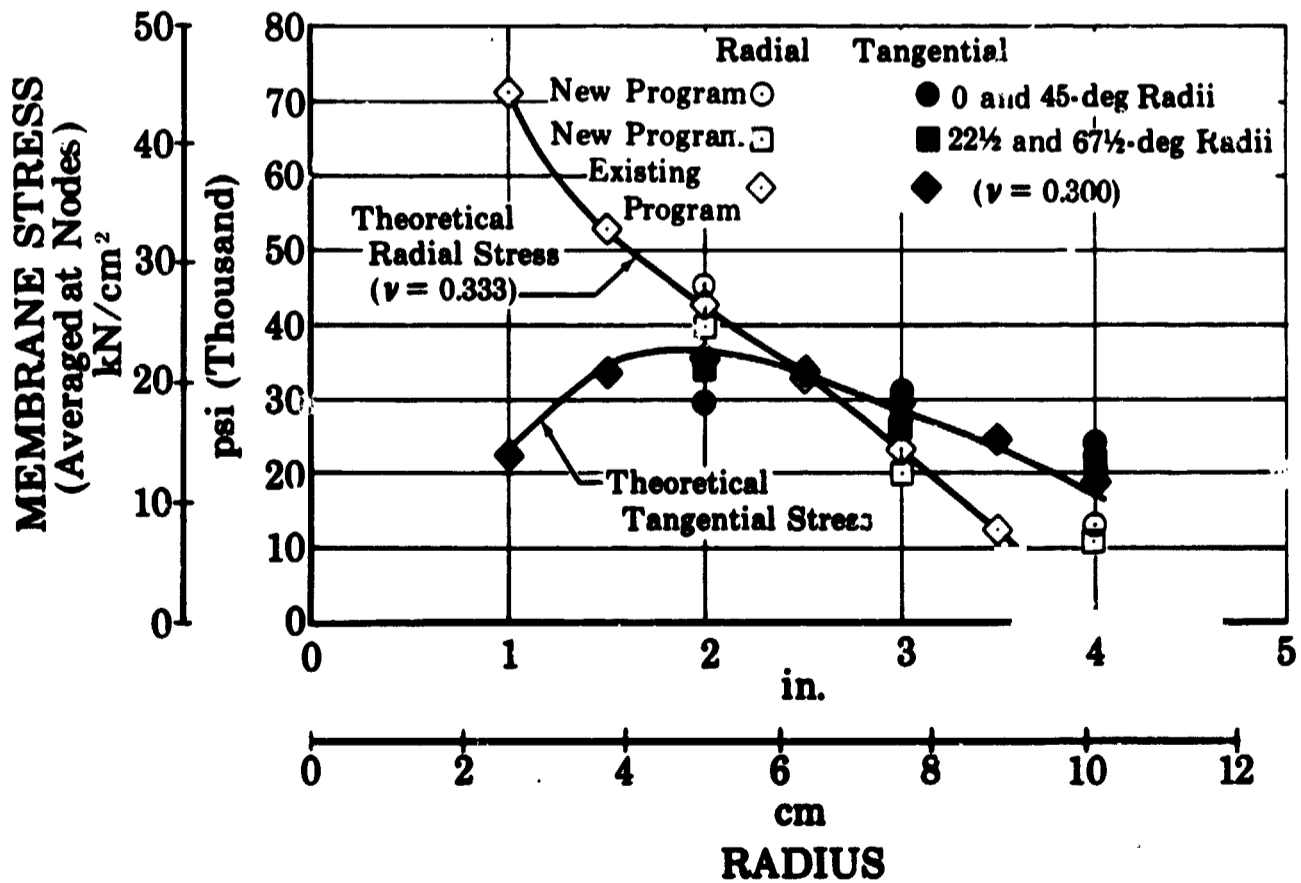


Figure 56. Radial and Tangential Membrane Stresses In 48 Node Spinning Disk FD 25795A

(2) Vibration Program

(a) Rectangular Plate

A test case on a 1 by 2 in. (2.5 by 5.1 cm) rectangular plate with 40 free nodes (figure 57) yielded the results shown in table I. Comparison with the first four known mode shapes (Barton) was in good agreement, as is shown in figures 58 through 61. The predicted frequency of the first torsional mode (1/0 mode), however, was high, and is still being investigated.

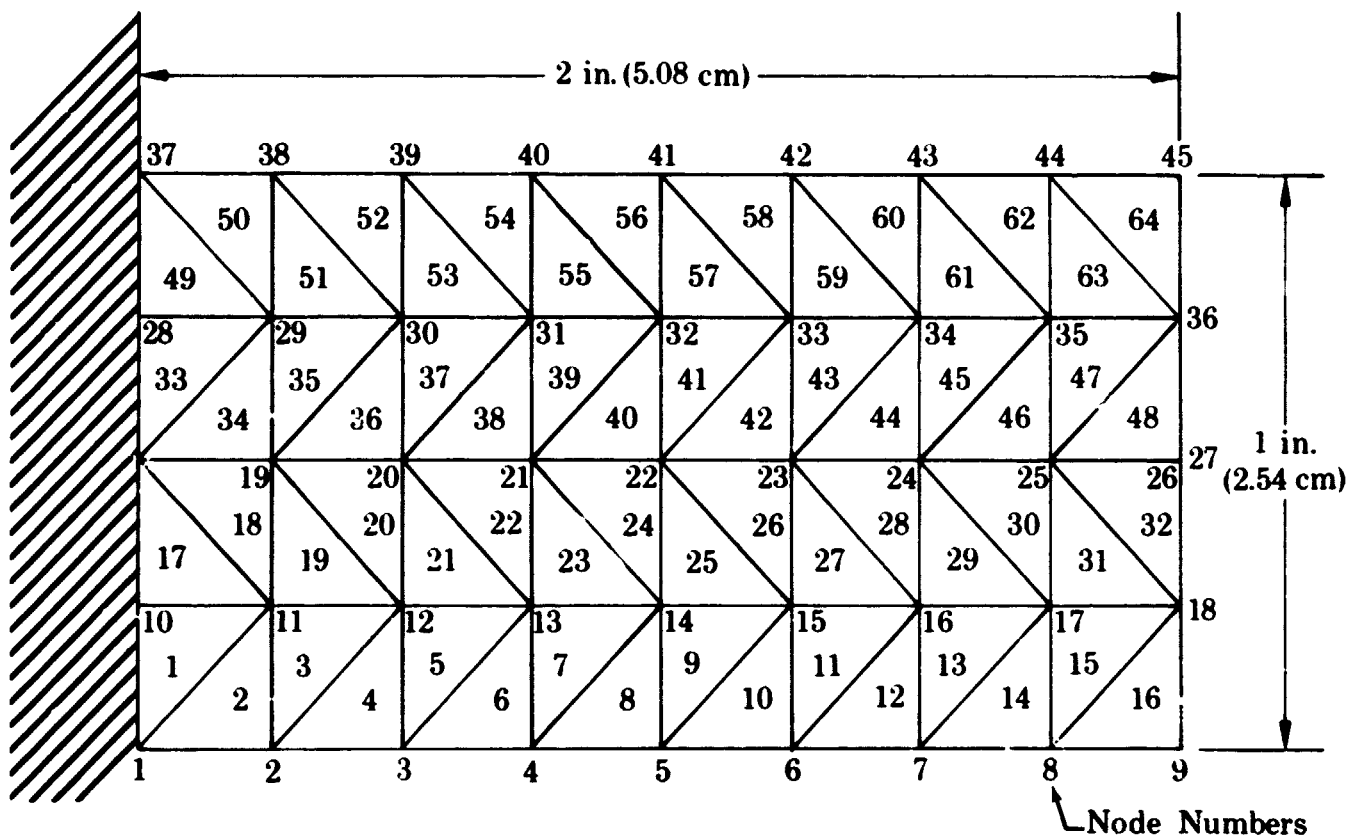
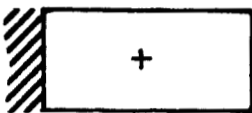
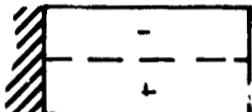
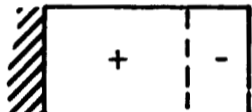
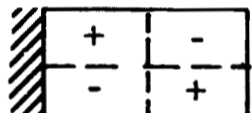
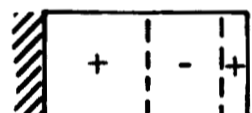
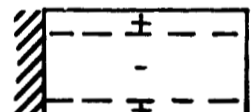
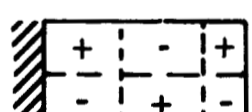
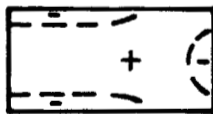
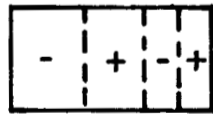
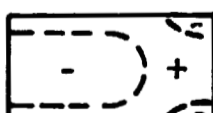
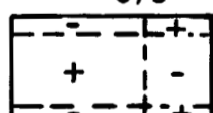
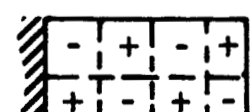


Figure 57. Breakup of 1-Inch by 2-Inch Rectangular Plate Into 64 Triangular Elements and 40 Free Nodes

FD 25656

Table I. Comparison of Exact and Computed Modes and Natural Frequencies of 1 by 2 by 0.1 in. Thick Cantilevered Rectangular Steel Plates

Mode	Frequencies, cps		
	Exact*	Existing Program	Present Program
 0/0	846	844	720
 1/0	3,638	3,584	4,942
 0/1	5,266	5,301	4,513
 1/1	11,870	11,802	14,648
 0/2		15,185	12,532
 2/0		23,011	21,563
 1/2		23,340	25,165
		 29,469	 24,459
		 31,190	 35,039
			2/1
 1/3		38,331	38,175

* Refer to Barton in Appendix A

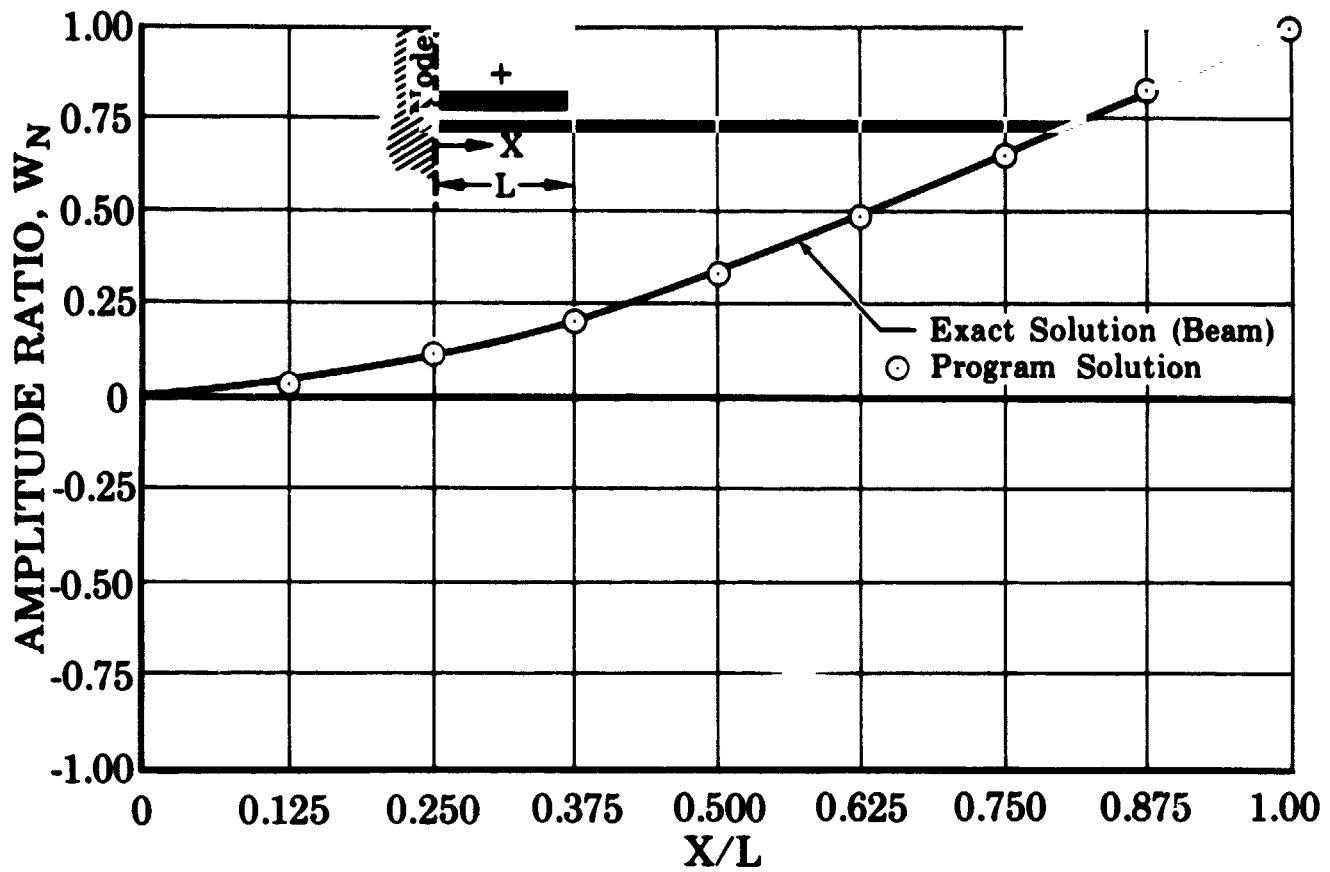


Figure 58. First Bending Mode of Cantilever Plate

FD 25895

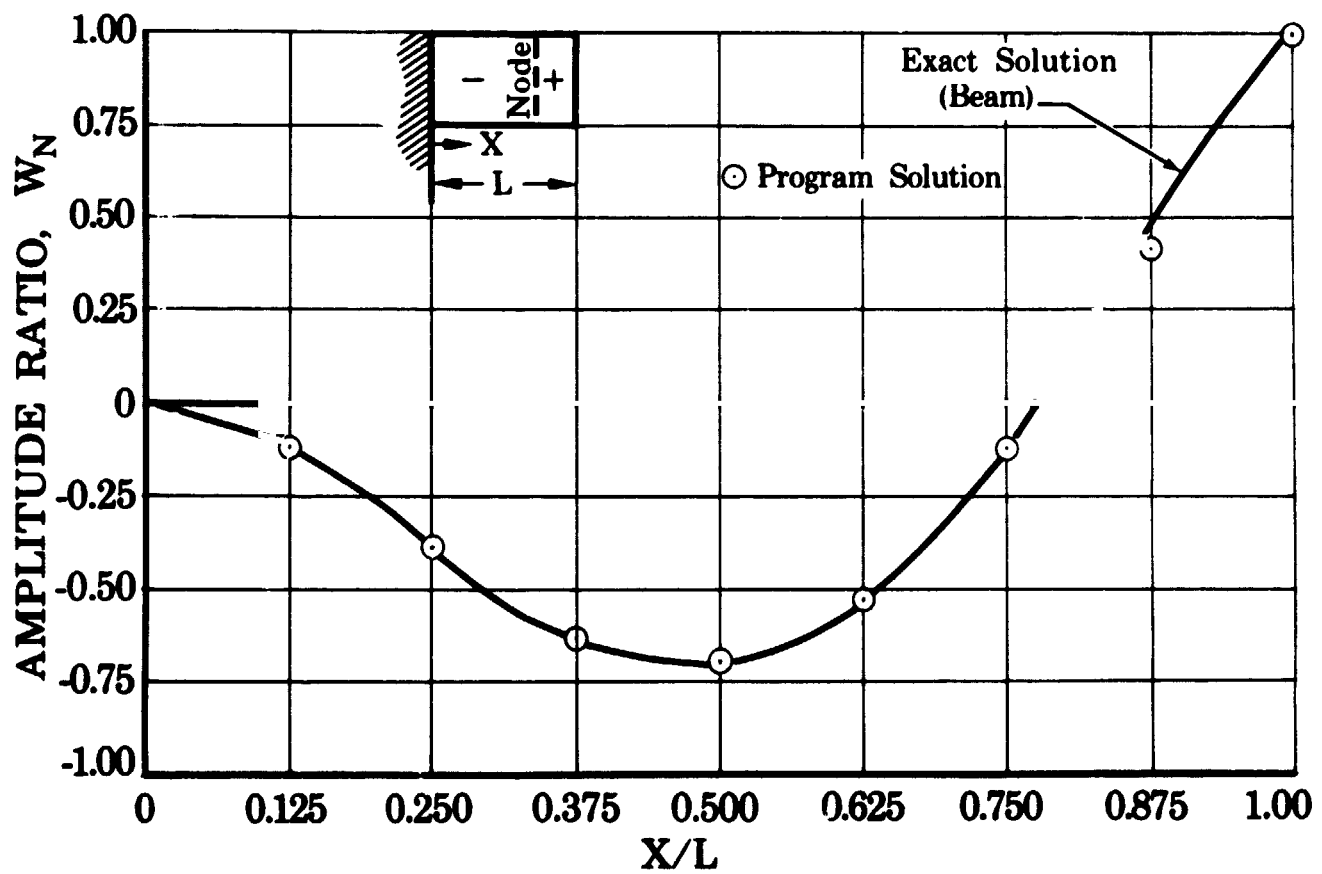


Figure 59. Second Bending Mode of Cantilever Plate

FD 25797

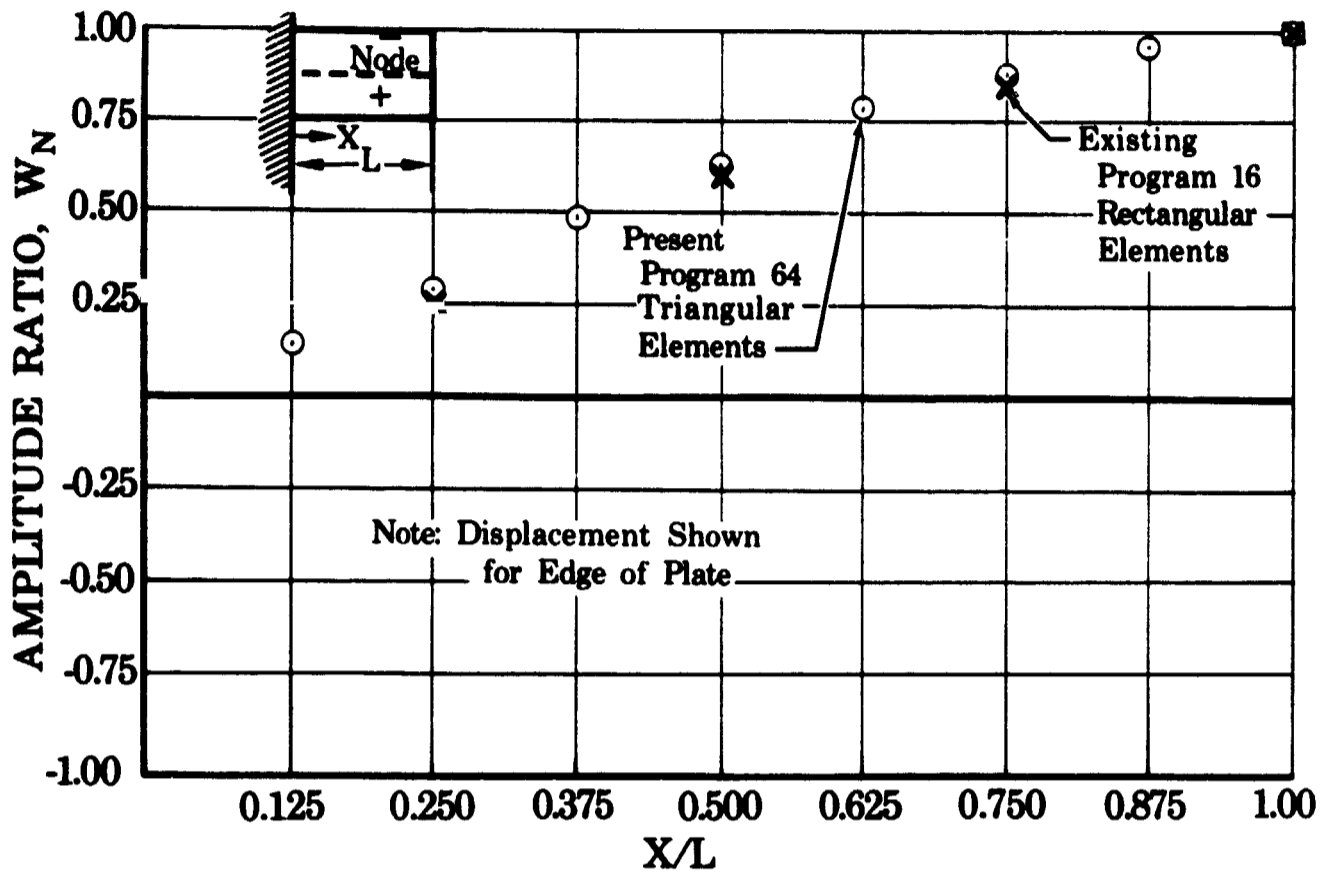


Figure 60. First Torsion Mode of Cantilever Plate

FD 25796

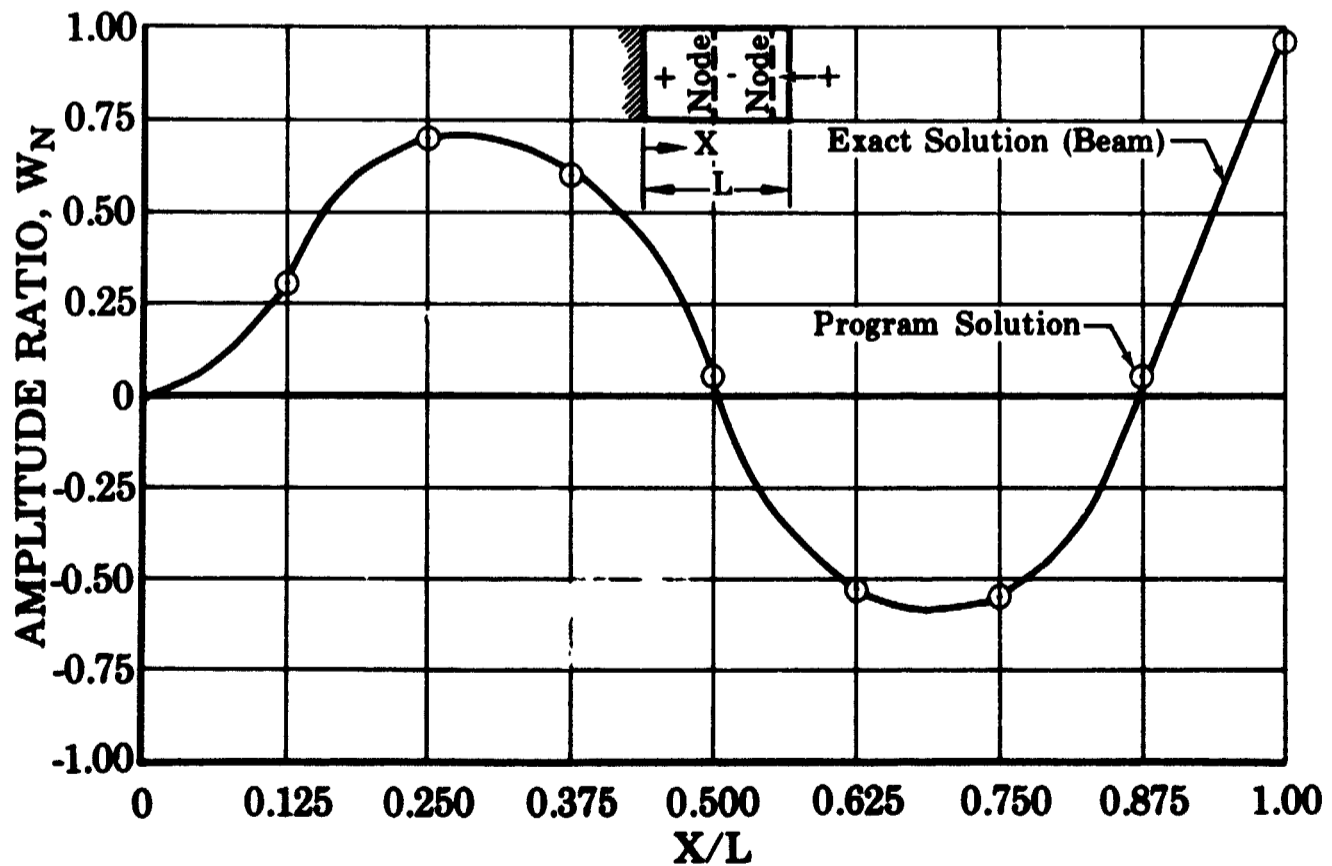


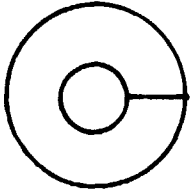
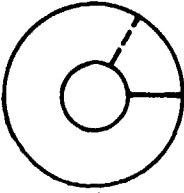
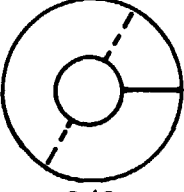
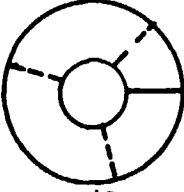
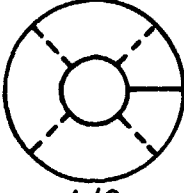
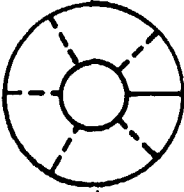
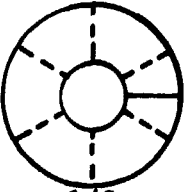
Figure 61. Third Bending Mode of Cantilever Plate

FD 25894A

(b) Six-Degree Inducer

A test case for a 6-degree inducer with a 438-degree wrap angle was conducted and results compared with test data as shown in table II. The results were in fairly good agreement, at least through the fifth mode.

Table II. Mode Shapes and Comparison of Natural Frequencies of 6-Degree (0.105-rad) Inducer

Mode	Frequency (cps)	
	Test Data	Calculated (Present Program)
 0/0	441	483
 1/0	575	540
 2/0	---	606
 3/0	---	709
 4/0	831	840
 5/0	---	994
 6/0	957	1170

C. TASK III - DESIGN OF TEST INDUCER

1. Hydrodynamic Design and Analysis

a. Preliminary Design

(1) Requirements

Task III work requirements called for the preliminary design of an inducer to be instrumented and tested in Task VI, both in static rigs and a closed flow loop. Test results will be used in the development of the computer programs formulated in Task II.

The following performance characteristics were established as design goals:

1. Test Fluid - Water
2. Minimum Flow Coefficient (ϕ) - 0.065
3. Minimum Head Coefficient (ψ) - 0.15
4. Minimum Suction Specific Speed (N_{SS}) - 40,000.

During the Task III preliminary design phase, it was found that, although our studies showed that a suction specific speed of 40,000 could be obtained, the low blade angles and thin blades required would limit instrumentation and compromise the acquisition of extensive and accurate test data. Therefore, the blade thickness and stagger angle were selected to provide good instrumentation coverage, and the other inducer parameters varied to obtain maximum suction specific speed.

(2) Selection of Basic Parameters

Three blades were selected, and zero taper angle was used to provide adequate tip thickness for instrumentation and low hub blockage for good suction performance. To obtain various hydrodynamic loading conditions, the meridional area was reduced by 15% at the exit, and the blade was cambered by 2 deg at the tip. An inlet tip angle of 8 deg was selected to provide adequate room for instrumentation while maintaining a low angle for good suction performance.

For simplicity and ease of rig modification, a constant OD flowpath was used. A high solidity was specified to obtain a high work level as well as good suction performance. The tip speed was limited to 150 ft/sec (46 m/sec) to preclude cavitation damage. A maximum OD and minimum ID were used to provide the largest blade surface for instrumentation. The basic design parameters are listed in table III.

Table III. Basic Design Parameters

	Inlet	Exit
Hub Diameter, in. (cm)	2.8 (7.1)	3.74 (9.5)
Blade Angle-Tip, deg (rad)	8 (0.14)	10 (0.18)
Blade Angle-Hub, deg (rad)	19.35 (0.339)	18.25 (0.318)
Tip Diameter, in. (cm)	7.0 (17.8)	
Blade Thickness, in. (cm)	0.130 (0.330)	
Number of Blades	3	
Flow Coefficient	0.07	
Head Coefficient	0.24	
Suction Specific Speed (100% Head Falloff)	30,000 (min)	
Flow Rate, gpm (m^3/S)	1060 (0.067)	
Rotor Speed, rpm (rad/s)	4900 (513)	

b. Flow Path and Blading Design

The hub contour and blade angle distribution are shown in figure 62. The tip blade angle was held constant at 8 deg for a tangential gap/chord ratio of approximately one. The blade angle profile from this point to the exit followed the power distribution shown in figure 62. This blade design is patterned after the "J" blade concept. This design technique, in incorporating a noncambered inlet for a tangential solidity of one, allows the leading edge incidence to be removed before turning the flow in the cambered section of the blade to produce the desired head. In doing this, the blade pressure loading due to leading edge incidence diminishes before the loading due to blade camber begins. This prevents addition of loadings due to incidence and camber near the blade leading edge.

After the blade angle distribution was determined, the channel flow area could then be held constant so that an acceptable mean line relative velocity profile would be obtained. With flow area and tip diameter constant and the blade angle distribution specified, an approximate hub contour was determined. Because of the test rig requirement that the inducer exit flow be axial, some departure from this desired hub contour was necessary to turn the flow to axial.

The mean relative velocity profiles, as determined from the hydrodynamic program, are shown in figure 63. The velocity profiles shown are both smooth and devoid of any excessive diffusion other than in the region of the leading edge, where some rapid diffusion exists. This diffusion in the region of the leading edge, which is the result of the rapid turning due to leading edge incidence, will appear in any inducer design. It can be tolerated (if the diffusion velocity ratio is not extremely high) because the boundary layers are still very thin near the leading edge.

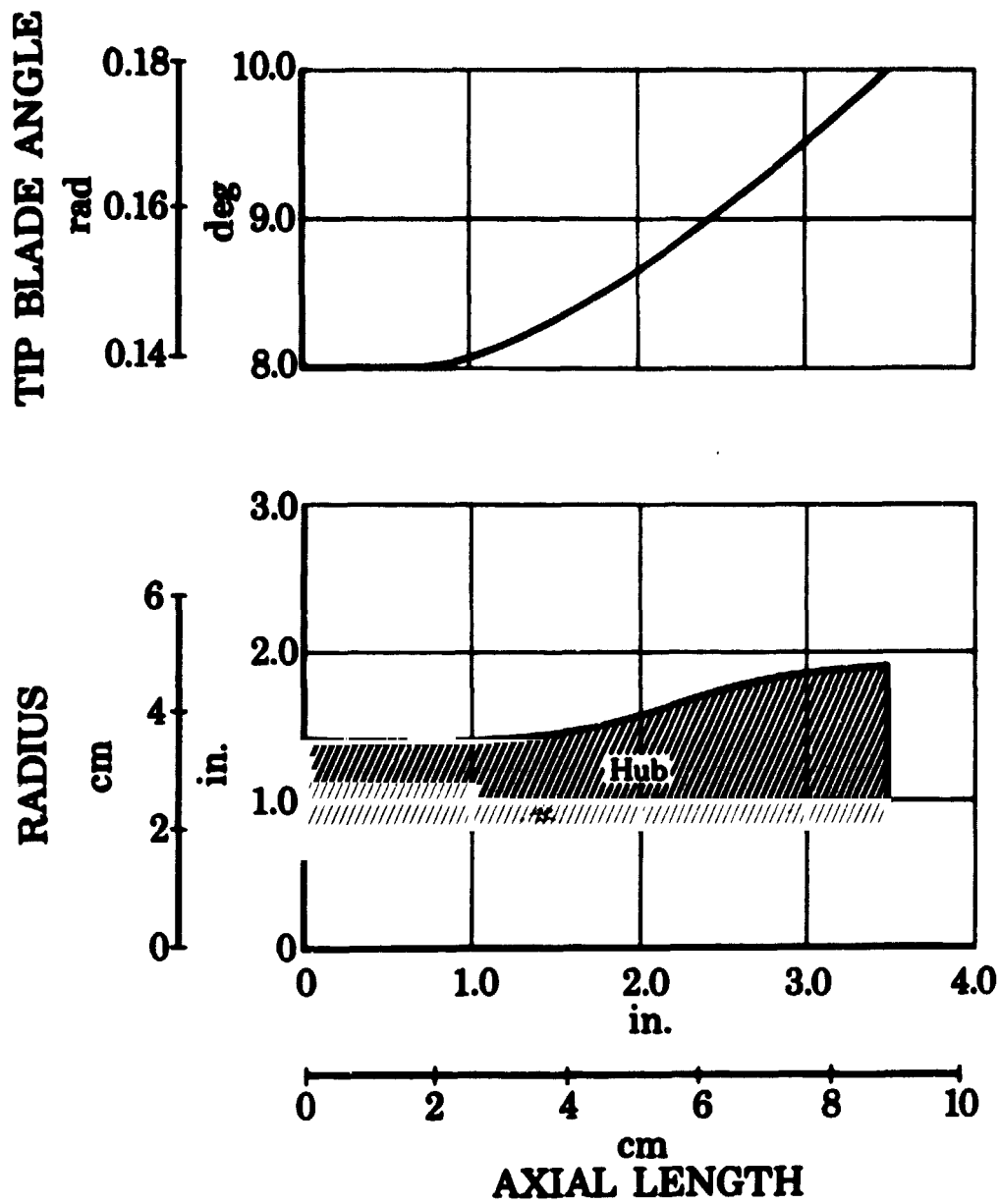


Figure 62. Task III Inducer Flow Path and Blade Angle Distribution

FI 25798A

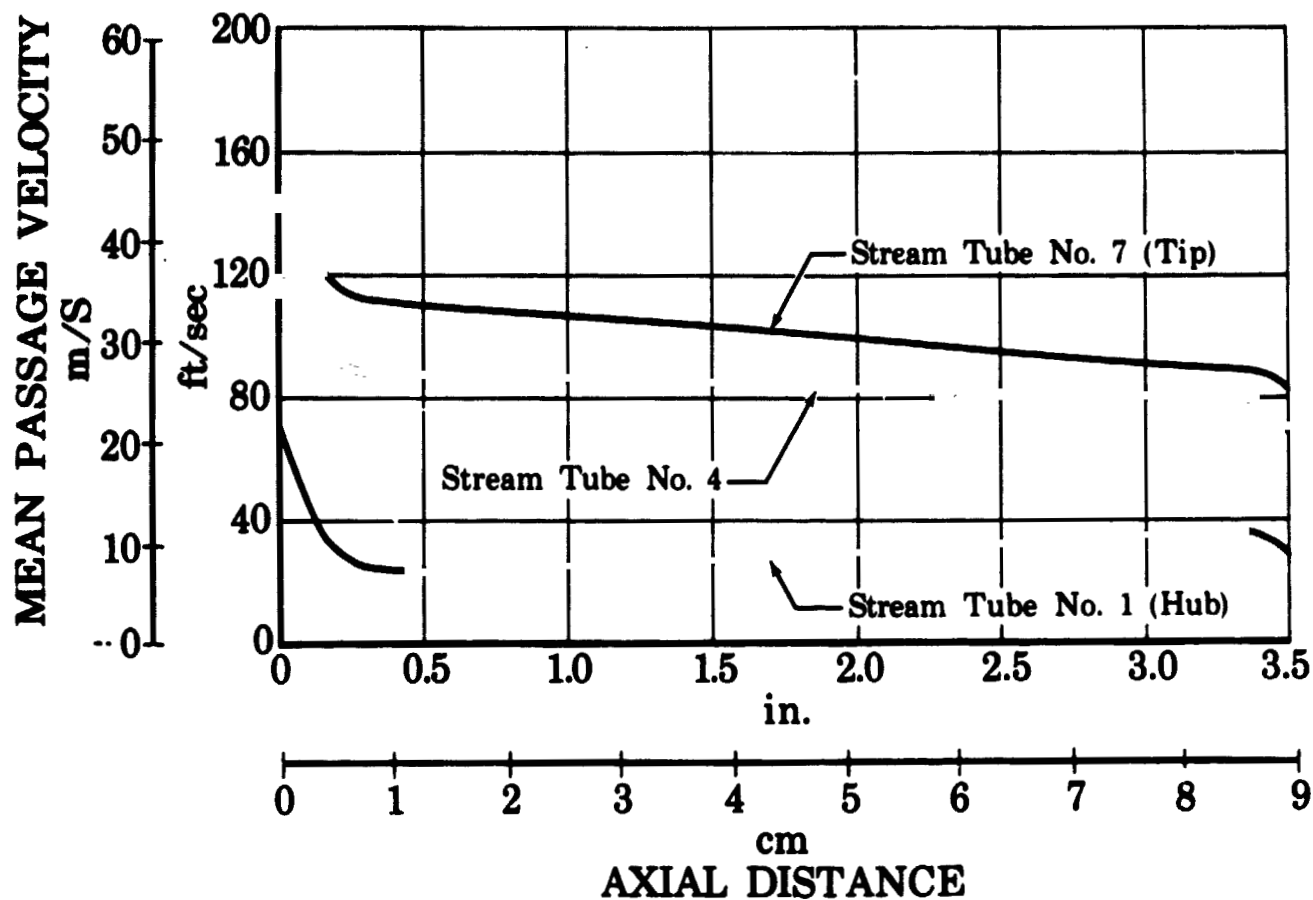


Figure 63. Task III Inducer Mean Passage Velocity Profile FD 25800

c. Performance Evaluation

(1) Noncavitating

The predicted inducer performance operating under noncavitating conditions is shown in figure 64. Based on the noncavitating results of the NASA 12-deg (0.21-rad) helical inducer discussed in paragraph Bld, above, it would appear that some falloff in actual head coefficient would result at the lower inlet flow coefficients. Although no requirement for hydrodynamic efficiency was established, it is felt that the predicted design efficiency is typical of many inducer designs.

(2) Cavitating

As previously discussed, some compromise in inducer suction performance was made to allow proper installation of pressure and strain gage instrumentation. As shown by figure 65, a predicted net positive suction head of approximately 8 ft (2.4 m), corresponding to a suction specific speed of 33,300, can be reached at complete head falloff.

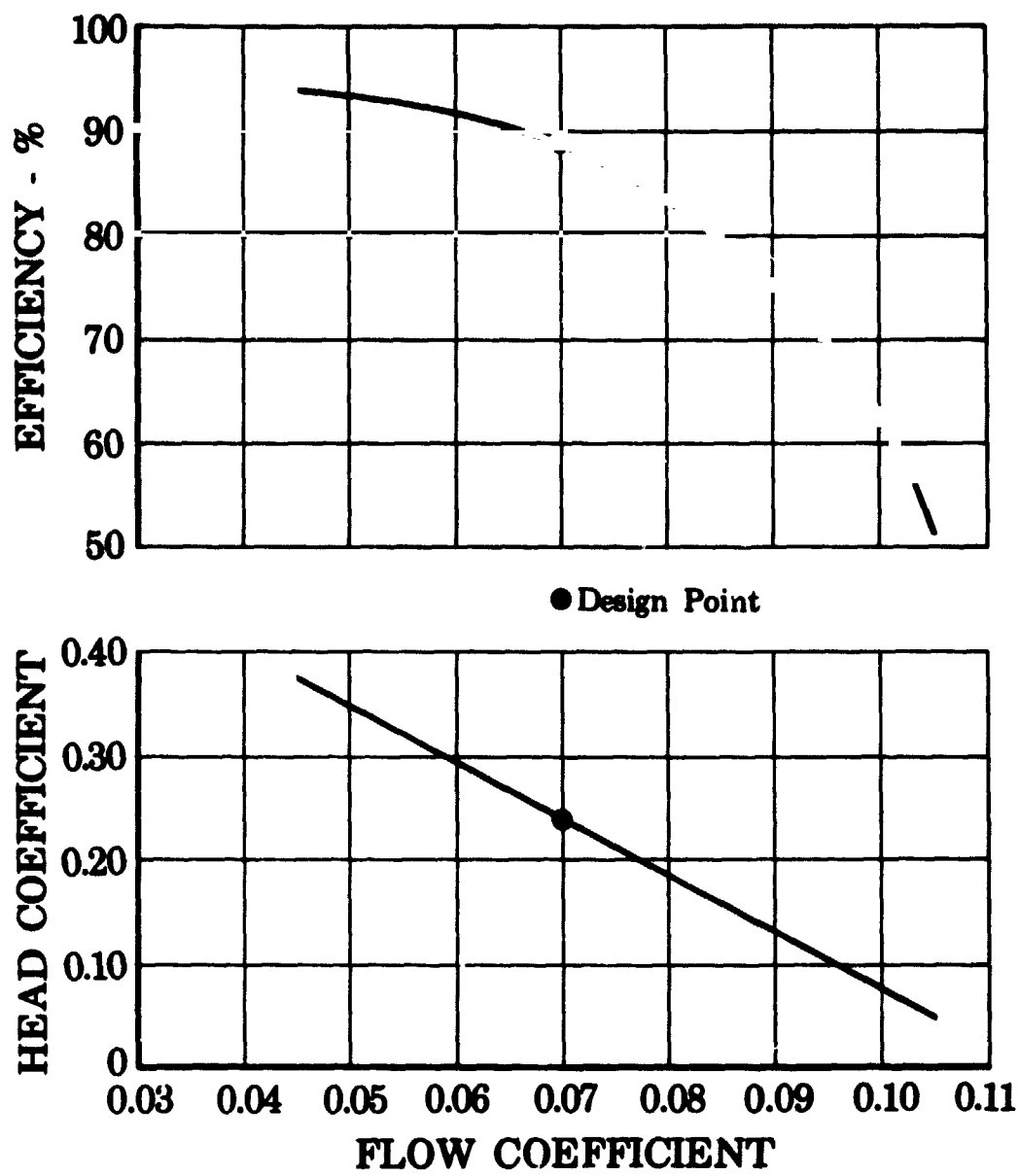


Figure 64. Task III Inducer Noncavitating Performance

FD 25799

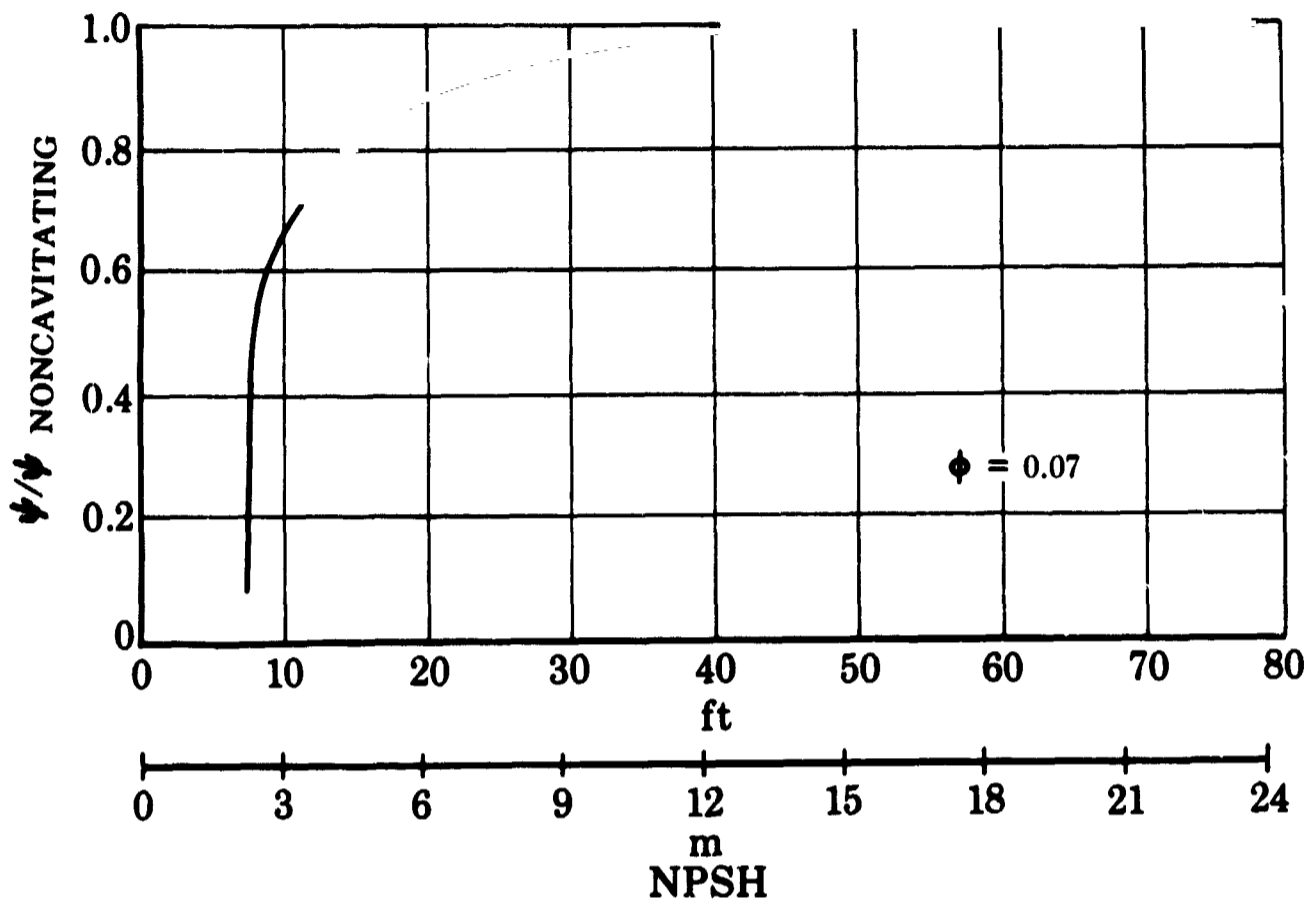


Figure 65. Task III Inducer Cavitating Performance

FD 25887A

2. Stress Analysis

a. Hydrodynamic Loading

The blade pressure loadings were obtained from the hydrodynamic analyses discussed above. These loadings are shown for noncavitating operation at 100% speed and 100% flow in figure 66. This figure shows isobars plotted on a frontal view of the inducer. Regions for varying level of hydrodynamic loading are indicated.

Note that the hydrodynamic loading is highest near the leading edge and decays rapidly away from the leading edge. This indicates that the highest loadings are caused by incidence turning of the flow. Further investigation of the loading relation previously discussed shows that these high tangential loadings are caused primarily by diffusion of the flow.

Figure 67 shows the hydrodynamic loading for the cavitating case at 100% speed, 100% flow, and NPSH = 20 ft (6.1 m) at approximately 10% head falloff. The reduction of peak hydrodynamic loading level is obvious on comparing figures 66 and 67. As previously discussed, the vapor cavity has grown to "spread" the flow turning over a longer distance and reduce the peak pressure gradients. Note, however, that far away from the leading edge the flow is still turning as the cavity develops so that moderate loading levels persist at a significant distance from the leading edge. In fact, the analysis indicates that the peak loading has shifted from the leading edge a significant distance into the inducer.

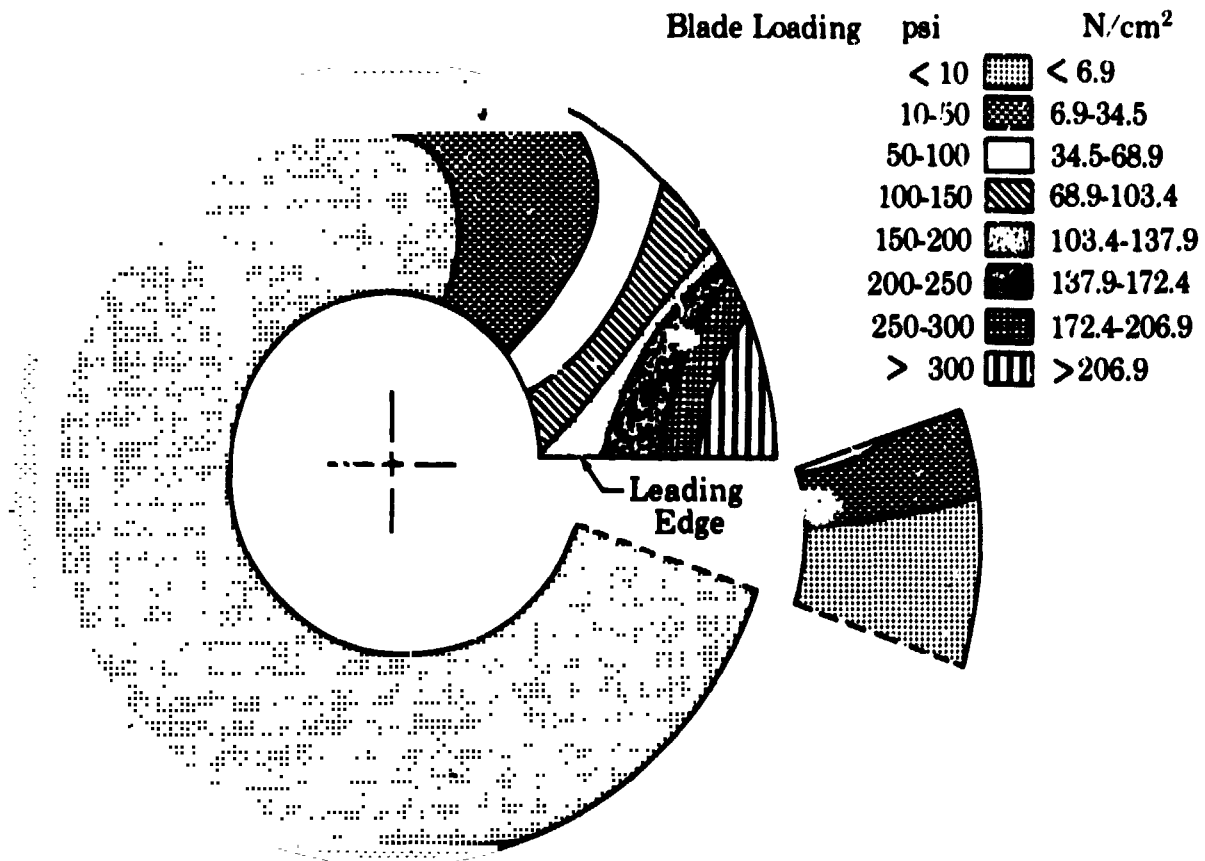


Figure 66. Task III Inducer Design Blade Loading Distribution, 100% Speed, 100% Flow [No Cavity]

FD 25571A

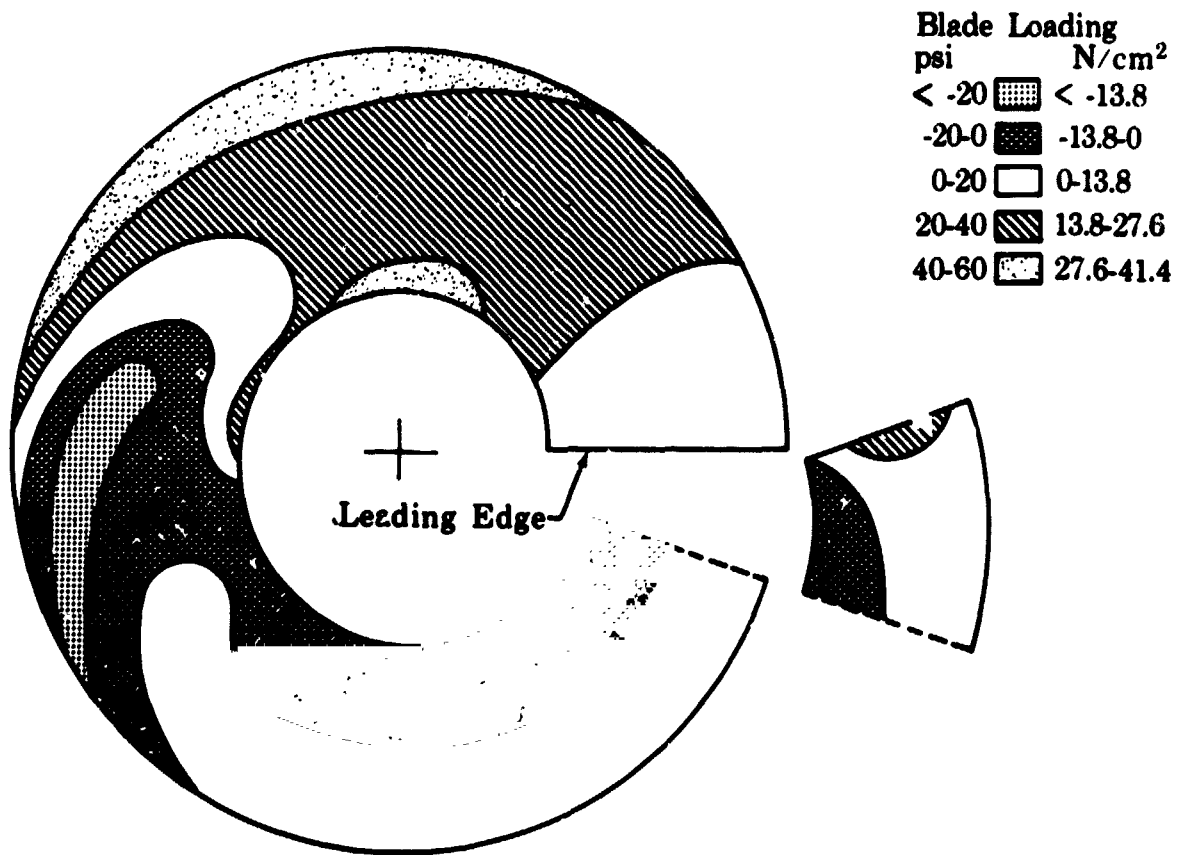


Figure 67. Task III Inducer Design Blade Loading Distribution, 100% Speed, 100% Flow, NPSH = 20 ft [6.1m]

FD 25878A

It should be noted that it was necessary to input a very high inlet pressure (very low suction specific speed) to obtain a noncavitating condition; i.e., a pressure on the suction surface of the blade higher than saturation pressure. The absence of any vapor cavity then allowed the hydrodynamic loadings to become very high, as indicated in figure 66. For the practical level of suction specific speed, the program predicts that there actually will exist a small vapor cavity. This prediction seems to be confirmed by visual observations of vapor cavities in inducers operating at relatively low suction specific speeds. Although this cavity is small enough so that it does not significantly affect overall performance, it still has a considerable effect on reducing the hydrodynamic loading.

Figure 68 shows the loading levels obtained from the hydrodynamic analysis at an inlet NPSH of 65 ft (213 m). The effect of the cavity in reducing the loadings quite significantly can be seen by comparing figures 66 and 68. The peak pressure loading has been reduced by almost a factor of four. Although the effect of this cavity on loading is very important in reducing stresses, it has, as previously stated, no significant effect on inducer performance. This can be seen in figure 65 at an NPSH value of 65 ft (213 m).

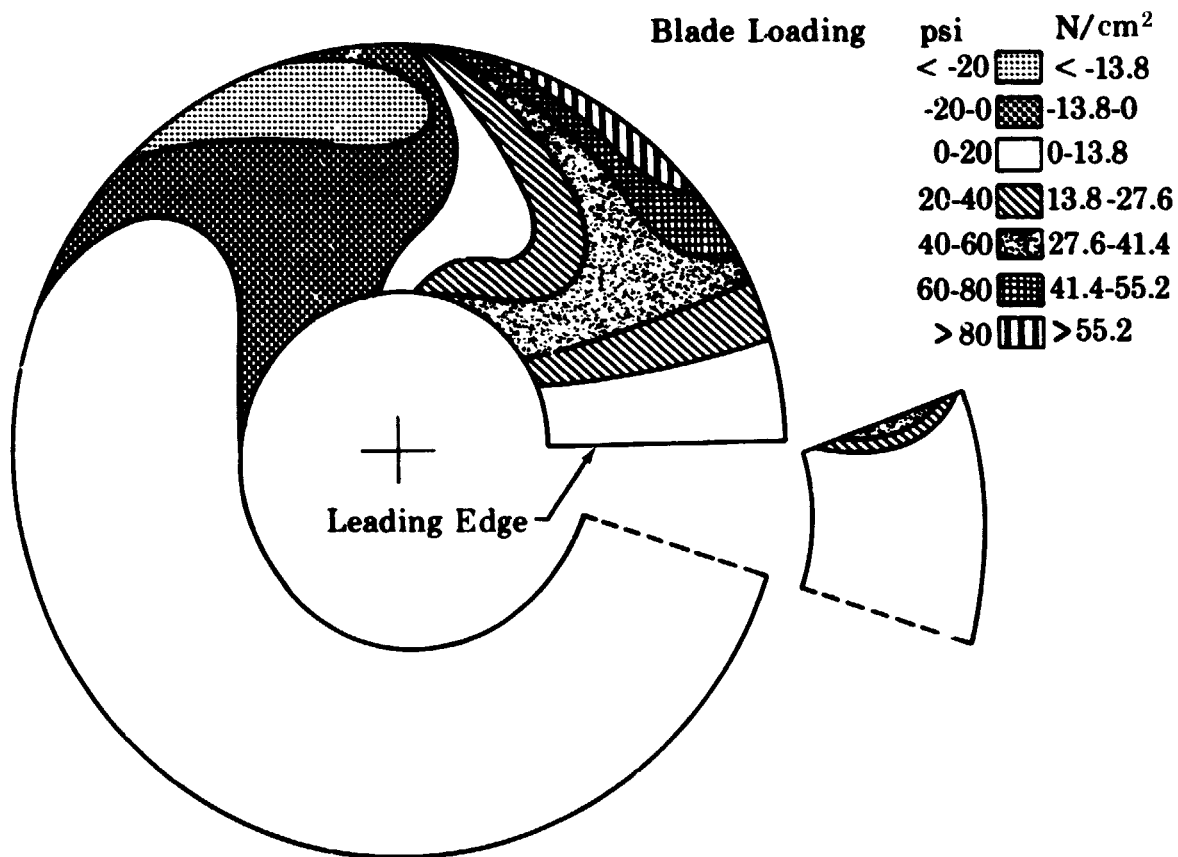


Figure 68. Task III Inducer Design Blade Loading Distribution, 100% Speed, 100% Flow, NPSH = 65 ft [19.8M]

FD 25880A

Figures 67 and 68, both resulting from analyses where cavities are present, show negative loadings. These loadings occur near the position where the cavity collapses on the surface of the blade. Because of the shape assumed for the cavity, the flow curvature and velocity gradient reverse after the point of maximum cavity height. (See figure 69.) As previously discussed, the shape of the cavity was arbitrarily assumed to be symmetric about the point of maximum height. Therefore, the accuracy of the loading in this region may be questionable. Further evaluation of these indications will be made in Task VI, both experimentally and theoretically, in the development of the computer programs. Specifically, a better model for the cavity shape will be sought.

The hydrodynamic loading for 100% speed and 80% flow was evaluated and was found to be comparable to the 100% flow condition. From this result, it was concluded that the hydrodynamic loading, and therefore the stresses, would not vary significantly over the range of flow of 80% to 120%.

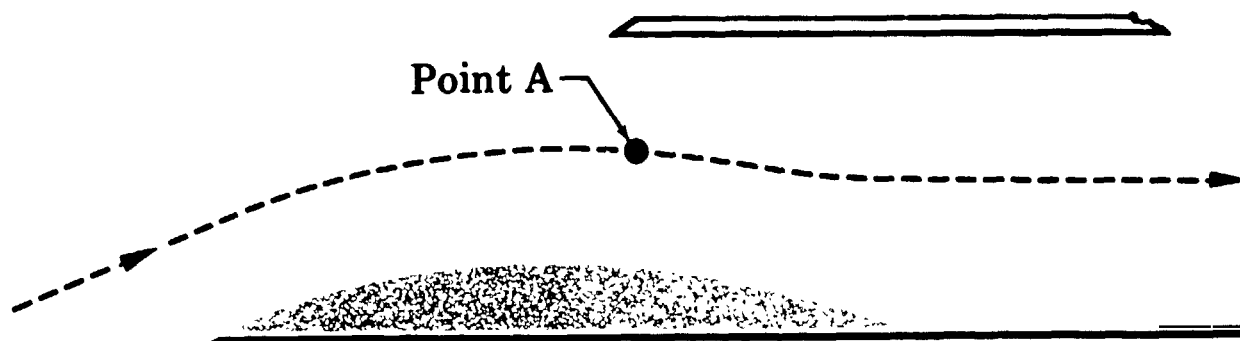


Figure 69. Effect of Cavity Shape On Streamline Curvature FD 25570

b. Stress Calculations

The hydrodynamic loads presented above were input to the stress analyses, using the computer program formulated in Task II. Three operating conditions were run and the results have been plotted as effective stress contours on a frontal view of the inducer, similar to the loading plots:

- Figure 70 - Noncavitating, 100% speed, 100% flow (no cavity)
- Figure 71 - Noncavitating, 100% speed, 100% flow, NPSH = 65 ft (21.3 m)
- Figure 72 - Cavitating, 100% speed, 100% flow, NPSH = 20 ft (6 m)

The 100% speed, 100% flow, no cavity case (figure 70) had the highest peak effective stress, a value of approximately 80,000 psi (55,158 N/cm²) at the hub leading edge. However, since the rig tests will not be run at the high level of pressure required to completely eliminate the cavity, this level of stress should never be reached.

Figure 71 shows the stress levels anticipated in the Task VI test program for the "noncavitating" case. These stresses are calculated from the loadings obtained with NPSH = 65 ft (21.3 m). The peak stress is only about 16,000 psi (11,031 N/cm²) and occurs at the hub blade leading edge.

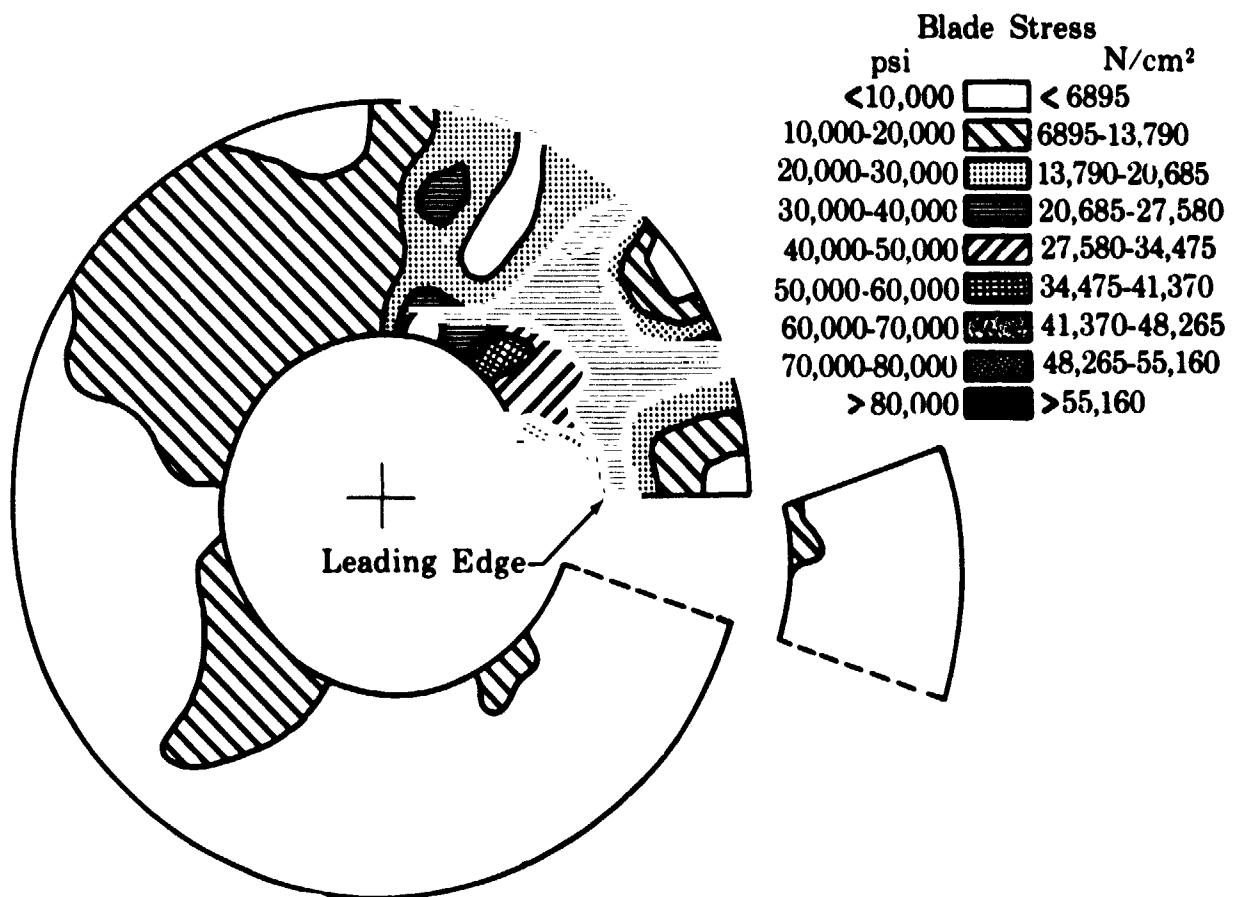


Figure 70. Task III Inducer Design Stress Level Distribution, 100% Speed, 100% Flow [No Cavity]

FD 25879A

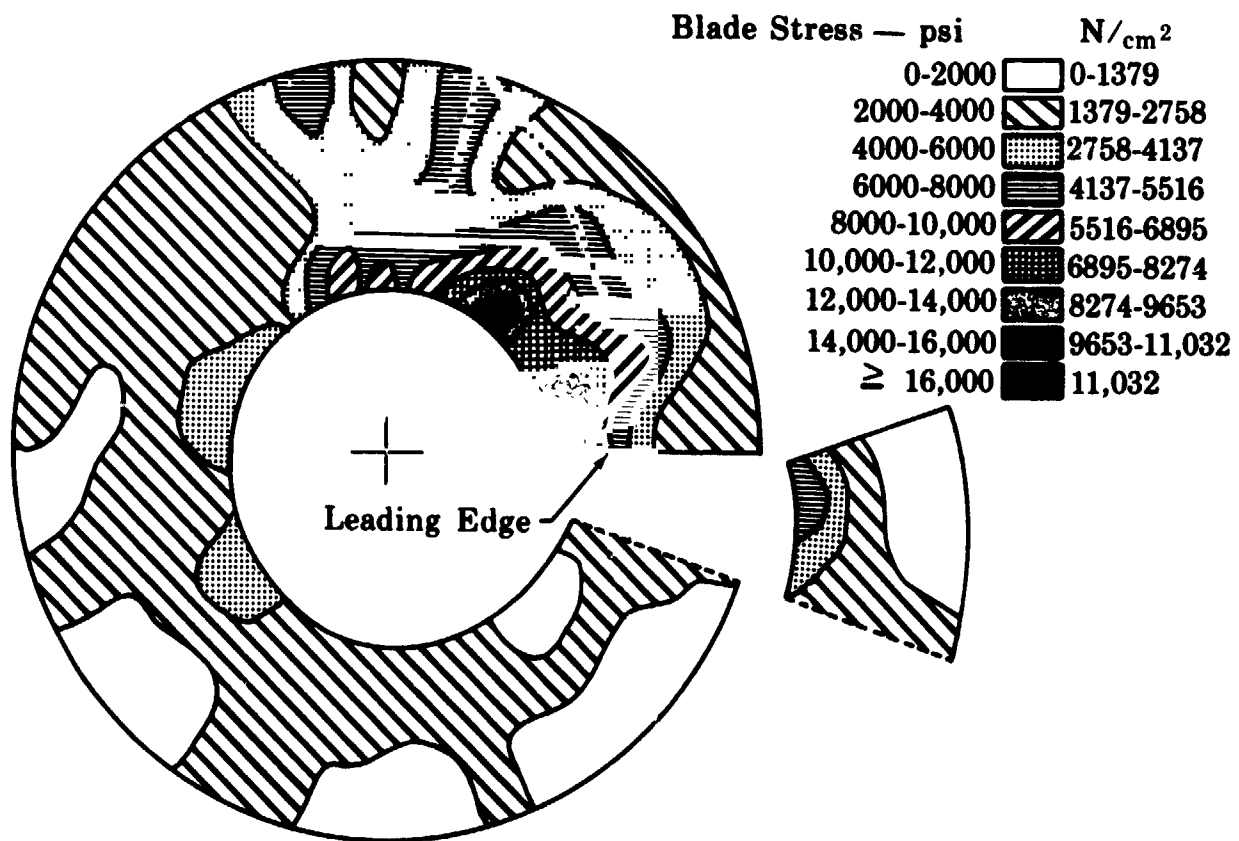


Figure 71. Task III Inducer Design Stress Level Distribution, 100% Speed, 100% Flow, NPSH = 65 ft [19.8M]

FD 25886A

Figure 72 shows that the cavitating case has about the same stress level as the "noncavitating" case at the hub on the blade leading edge. However, further back in the inducer, the collapse of the cavity caused a higher stress of approximately 24,000 psi (16,547 cm). However, it is recalled that the loadings at that point are questionable due to the assumption concerning the cavity shape

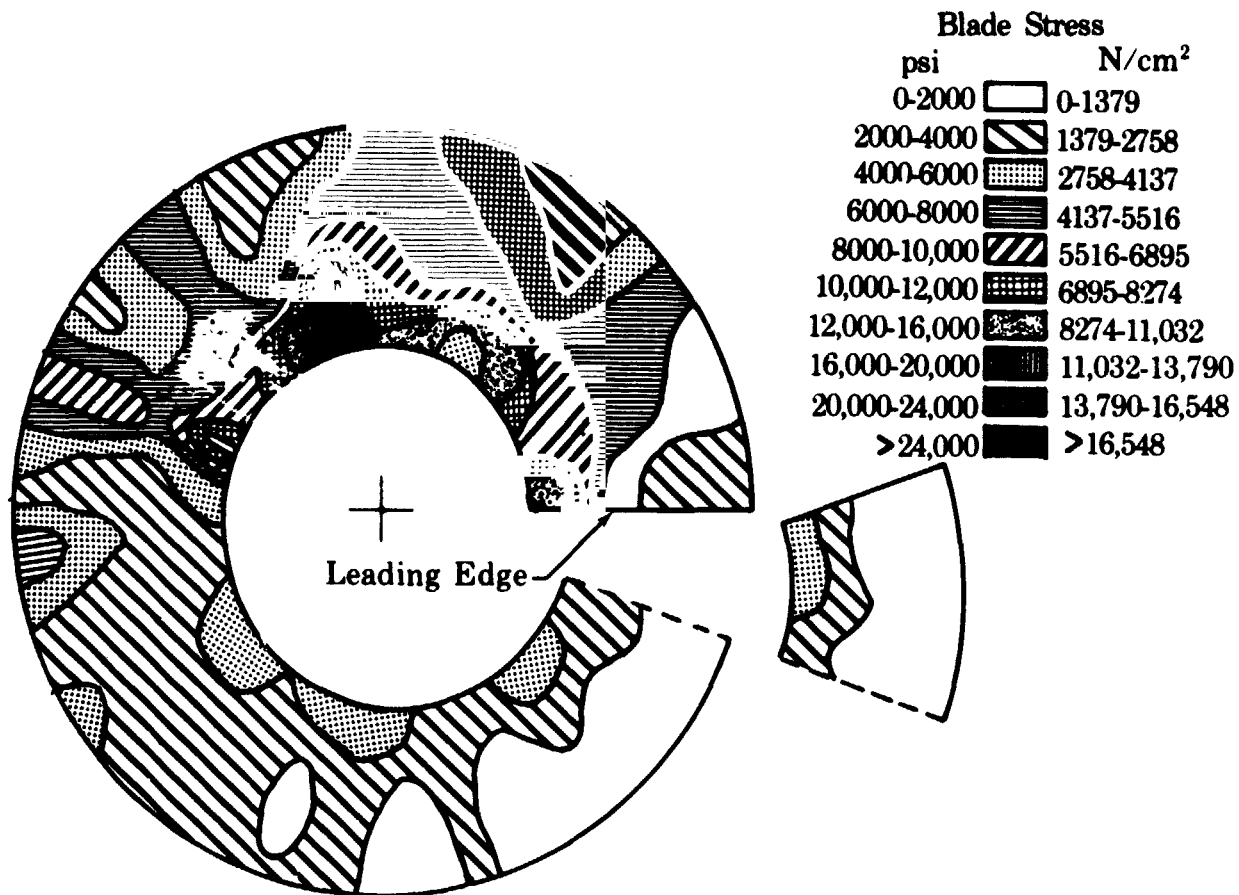


Figure 72. Task III Inducer Design Stress Level Distribution, 100% Speed, 100% Flow, NPSH = 20 ft [6.1m]

FD 25888A

3. Vibration Analysis

Vibratory characteristics of the Task III inducer were obtained using the vibrations program formulated in Task II. Mode shapes and frequencies for the first four modes of vibration are shown in figure 73. The lowest natural frequency was found to be much greater than any system excitation frequency that will be experienced during normal operating conditions.

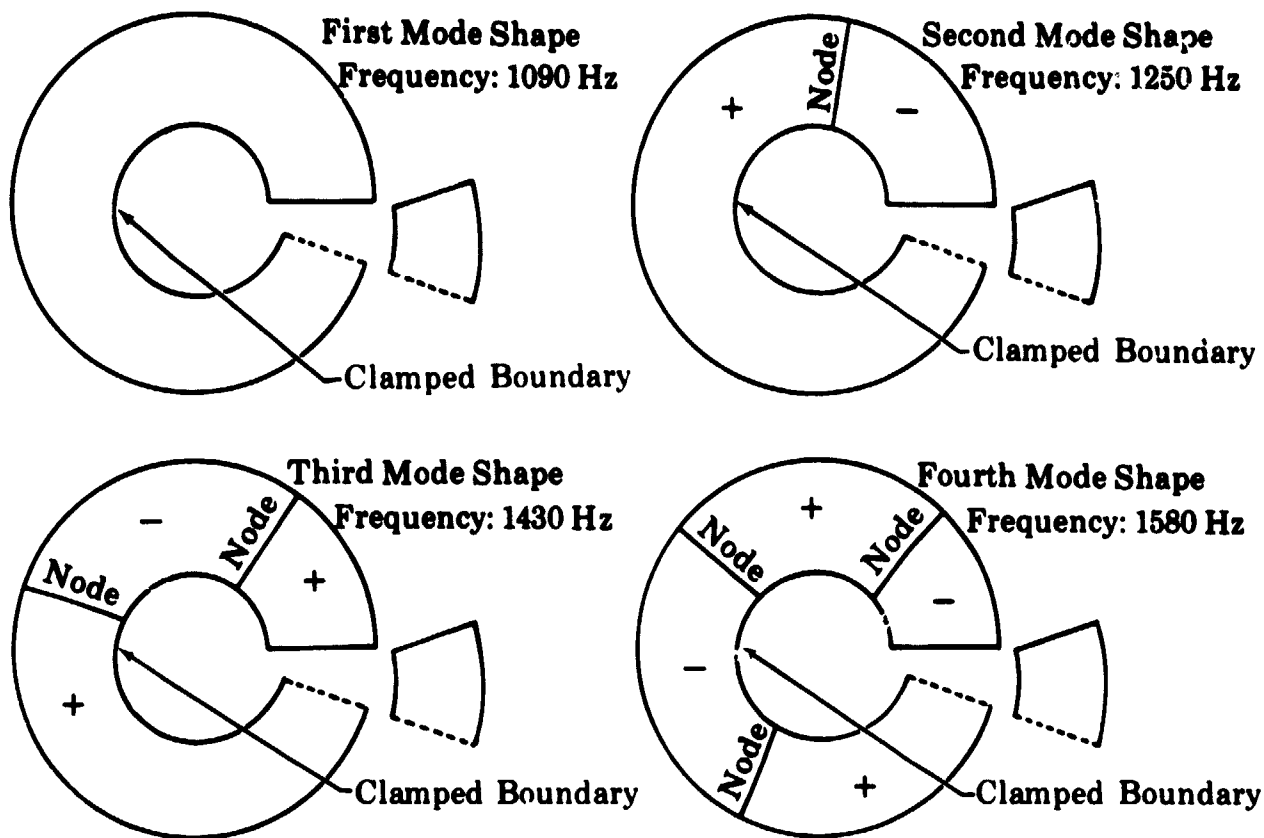


Figure 73. Task III Inducer First Four Vibratory Mode Shapes

FD 25900A

4. Instrumentation Design

Instrumentation provisions were designed into the inducer for measurement of the following data:

1. Blade steady-state strain
2. Blade vibration strain
3. Blade and hub steady-state surface pressures
4. Blade vibratory surface pressures.

Space limitations on the inducer blades and slip ring capacity necessitated that the data be obtained from two test series: the first for steady-state and vibratory strain and the second for steady-state and vibratory pressures. Some strain gages will be common to both test series to ensure data continuity.

Steady-state strains will be measured with eighteen three-direction strain gage rosettes located as shown in figure 74. These locations coincide with the maximum stress areas of figure 70. The use of rosettes instead of single direction gages at each location will permit determination of stress and stress direction at each point. Six of the rosettes will be placed on each of the three blades to facilitate routing the leads down the blades and into the inducer hub. All rosettes will be at different locations except at the inlet root. This is the area of maximum stress, and all blades will have a rosette at this location to ensure that gage failure does not prevent measurement of maximum stress. These common rosettes will also be used to check the degree of stress similarity

between blades in laboratory static load tests. Slip ring capacity will limit the number of rosettes recorded to twelve. Rosettes indicated as spare in figure 74, together with two of the inlet root rosettes, will be connected to the slip ring and recorded only if primary rosettes should fail. All gages will be located on the blade pressure surface for measurement of total strain (bending plus membrane).

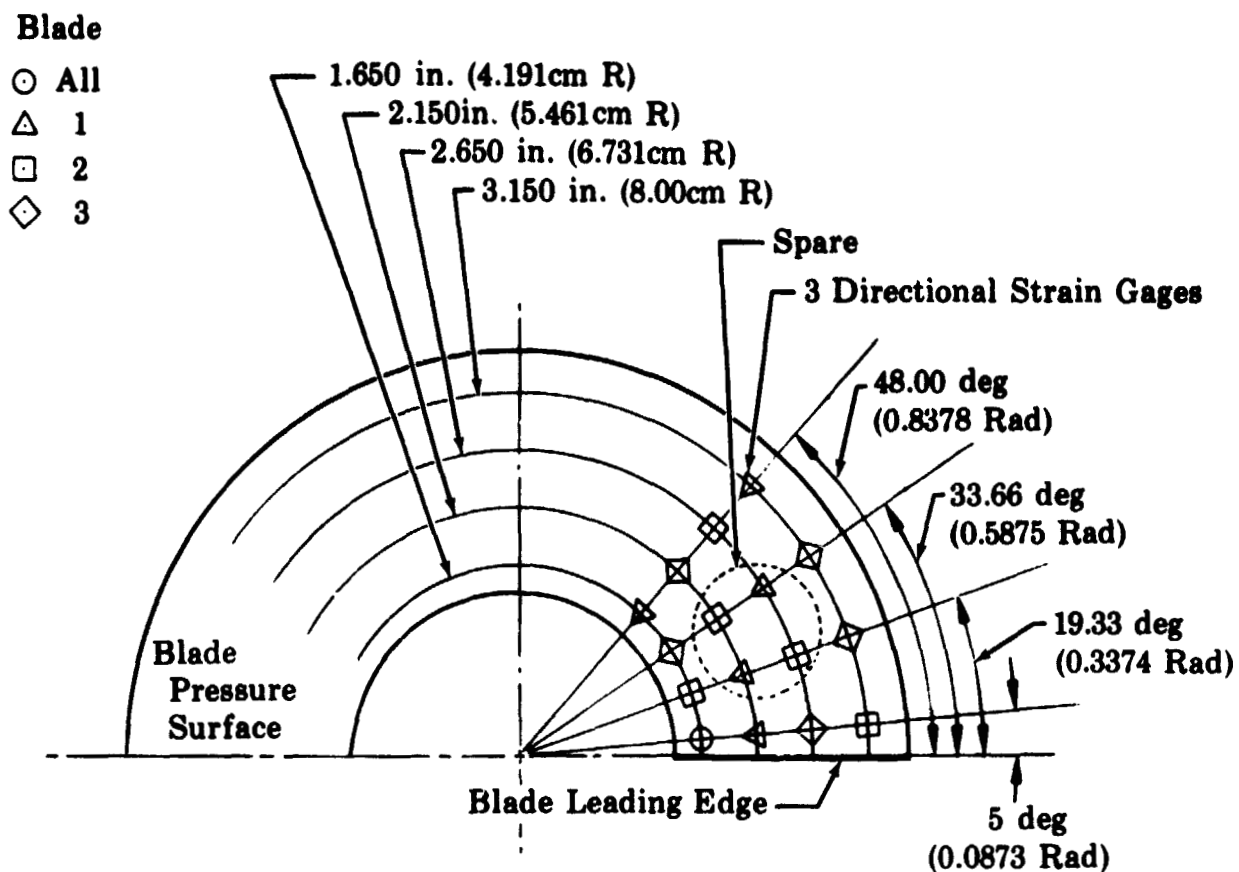


Figure 74. Strain Gage Locations - Blades No. 1, 2, and 3

FD 25877A

Vibratory strains will be measured with the same gages shown in figure 74 by running several additional tests and recording vibratory strain signals. These strains are expected to be minor, however; and it is expected that the most useful vibratory data will be obtained from shaker table tests with gages located according to inducer nodal patterns.

Steady-state blade and hub surface pressures will be measured by installing pressure taps flush with the blade and hub surfaces. The taps will be installed by machining grooves in the blade surfaces and holes through the inducer hub to accommodate 0.040-in. (1.016-mm) diameter tubing. Tubing will then be laid in the grooves and routed to the inducer inner cavity through the holes in the hub. Epoxy cement will be used to fill the groove, fair the blade surface, and hold the tube in place. Each pressure tap tube will then be connected to a pressure scanning valve* - transducer assembly mounted in the

*Scanivalve Co., San Diego, California, Model No. 48D9.

inducer hub as shown in figure 75. The scanning valve is capable of connecting 48 pressures sequentially to a single transducer. A schematic of the valve is shown in figure 76. The transducer will be a differential type with the reference side connected to a total pressure tap in the inducer nosepiece. Electrical leads from the valve drive solenoid, scanning position indicator, and transducer will be routed through the rig shaft for connection to a slip ring assembly in the rig drive train.

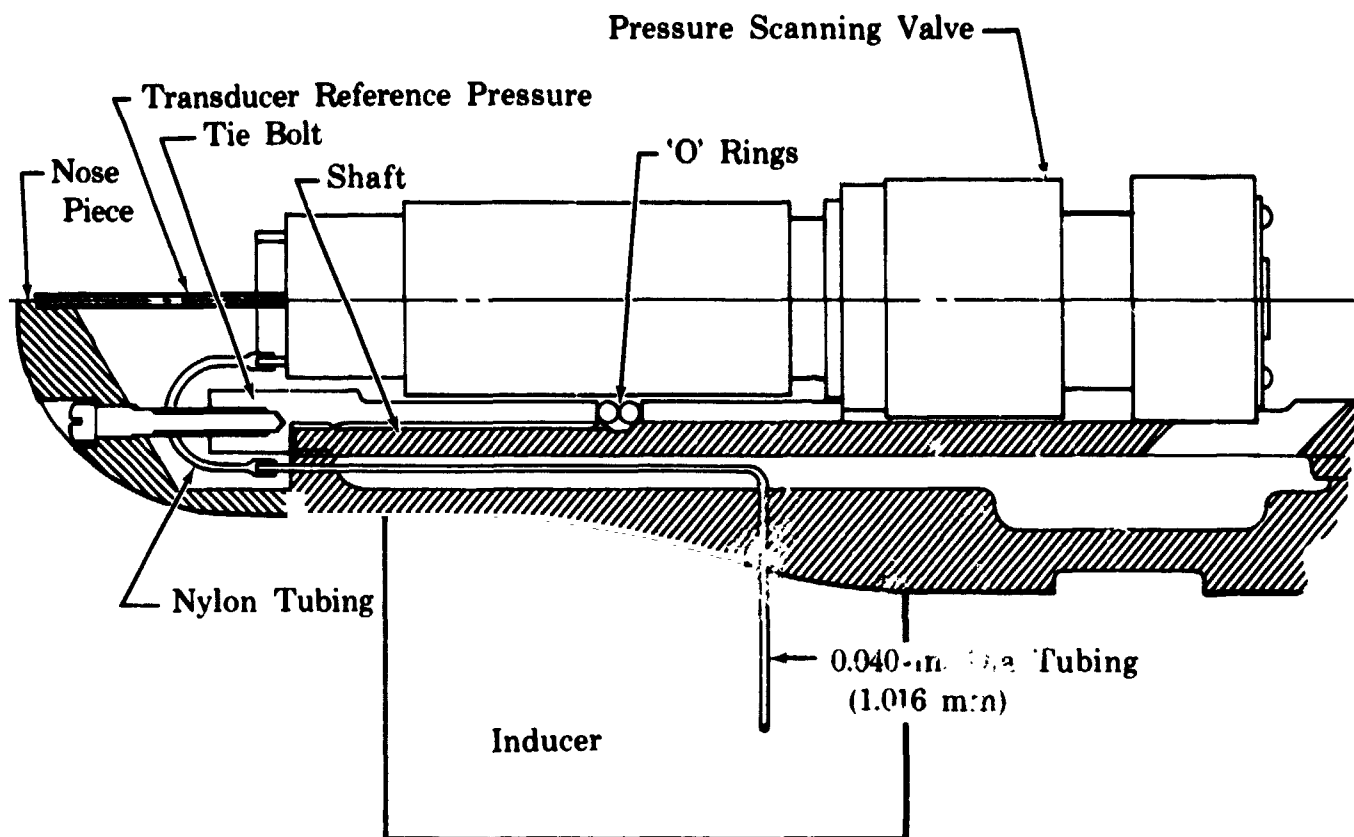


Figure 75. Pressure Scanning Valve In Inducer Hub

FD 25812

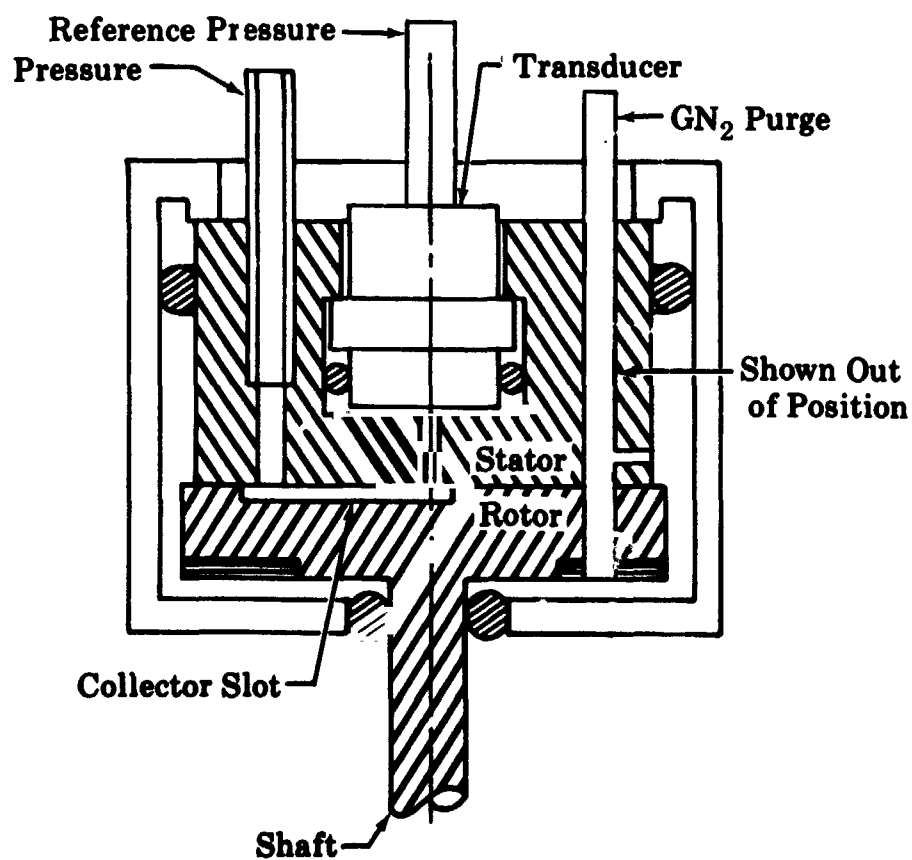


Figure 76. Schematic of Pressure Scanning Valve

FD 21392B

Pressure tap locations in the inducer blade and hub are shown in figure 77. The taps are located along four design point streamlines at nineteen axial blade positions. The same tubes will be used to sense pressures at all four radial locations by running a series of four tests. Pressures at outer radii will be measured first after which the inducer will be removed, outer taps plugged, and new taps drilled at the next inner radius. Two of the three inducer blades will be used to accommodate the pressure taps with each blade having alternate pressure and suction taps along its chord to avoid back-to-back grooves in the blade. Pressure surface taps at locations 2, 8, and 13 will be installed and read for all pressure tests to ensure data continuity within the pressure test series. One strain gage, at the inlet root, will also be installed on blade No. 3 for the first pressure test to check continuity with the strain gage test series.

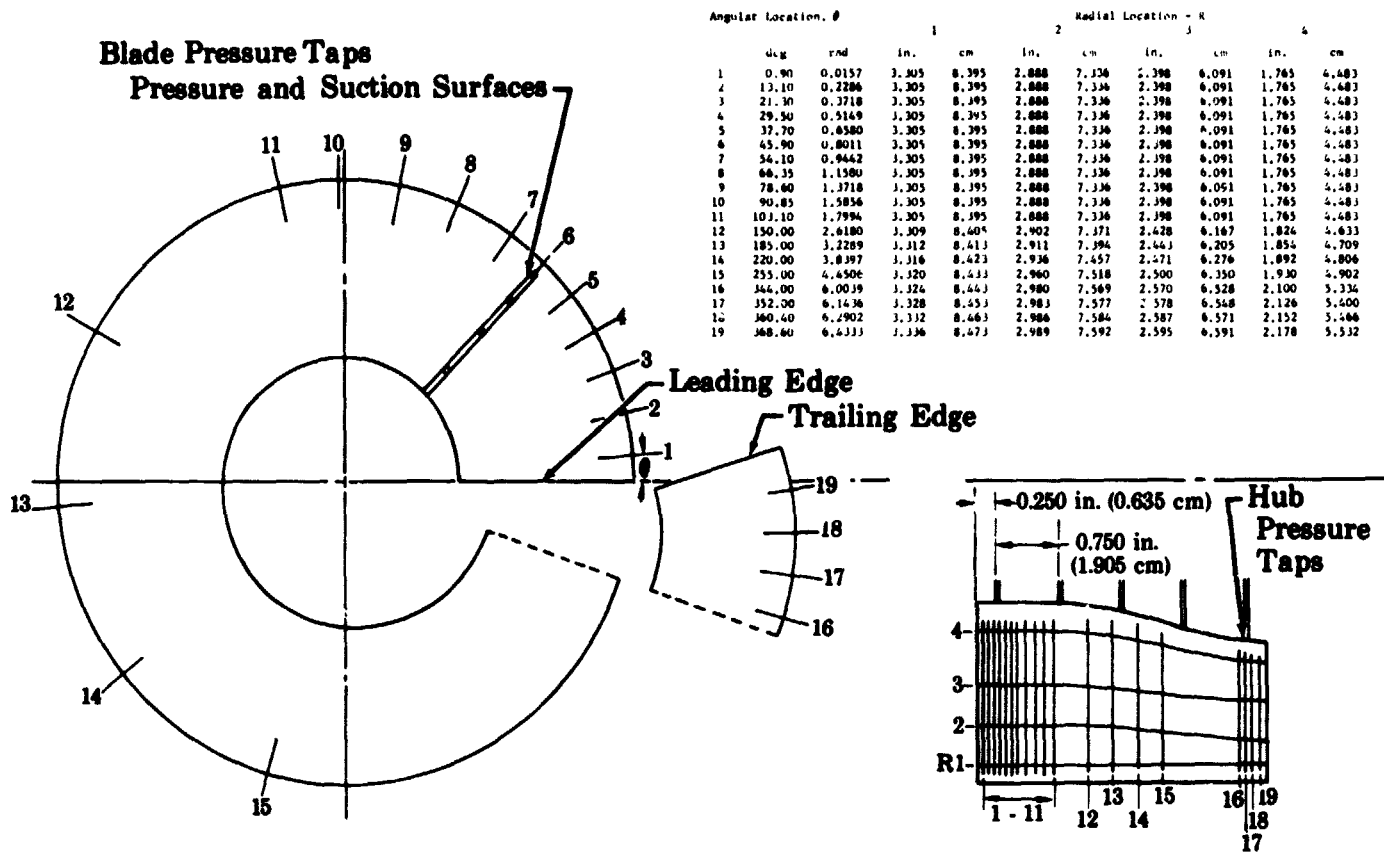


Figure 77. Pressure Tap Locations - Blades 1 and 2

FD 25876

Pressure tap measurements will be complicated somewhat by the centrifugal effect on the fluid in the radial tubes. The readings can be easily corrected, but the fluid in the tap tube must be single phase of known density. This will not be the case when blade surface pressure at the tap is lower than vapor pressure plus centrifugal pressure in the tap tube. To correct this, a modified pressure scanning valve will be ordered with a pressure connection into the space behind the valve and a hole through the rotor one space ahead of the collector slot. This space will be connected with 0.040-in. (1.016-mm) diameter tubing to a sealed annulus on the test rig drive shaft. GN₂ pressure applied at the annulus will then purge each pressure tube just prior to its being connected to the transducer, and it can be assumed that the tube will be completely filled with GN₂ at the transducer measured pressure.

Pressure fluctuation magnitude and frequency will be measured during the first pressure test with six miniature strain gage transducers (Kulite) installed flush with the suction surface of blade No. 3. The transducers will be located near the blade tip, as shown in figure 78, for measurements of pressure fluctuations in the most severe cavitation area.

Angular Location, θ

	deg	rad
1	6.00	0.1025
2	21.30	0.3718
3	37.70	0.6580
4	55.88	0.9753
5	84.37	1.4725
6	111.57	1.9472

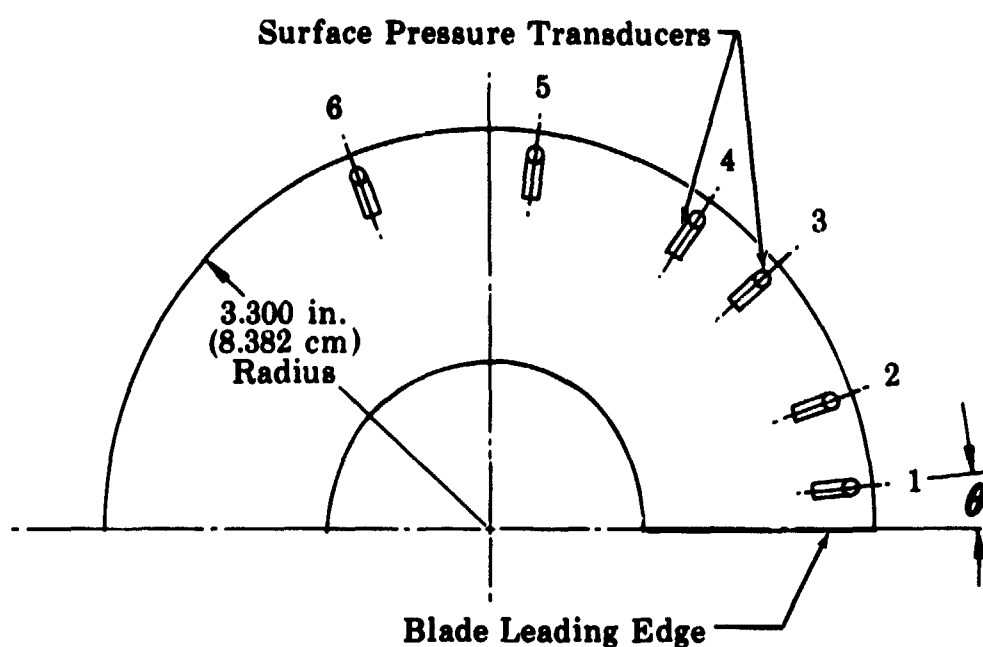


Figure 78. Miniature Transducer Locations - Blade No. 3

FD 25858

5. Test Rig Design

The inducer and instrumentation were designed into an existing water loop test rig as shown in figure 79. Strain gage, scanning valve, and miniature transducer leads will be routed through the drive shaft to a slip ring assembly in the drive train at the rear of the rig. The inducer is overhung from the drive shaft with the pressure scanning valve in its hub. An acrylic plastic (Dupont Lucite) sleeve is used to house the inducer and permit observation of cavitating flow. The sealed annulus at the rear of the rig will be used to purge the pressure scanning valve and inducer pressure tap tubes.

The rig shaft assembly first critical speed was calculated as 6200 rpm (649.3 rad/s). This is well above maximum test speed of 4900 rpm (513.1 rad/s). Stresses at critical areas were also calculated for all operating conditions, and all parts were found to have adequate safety margins.

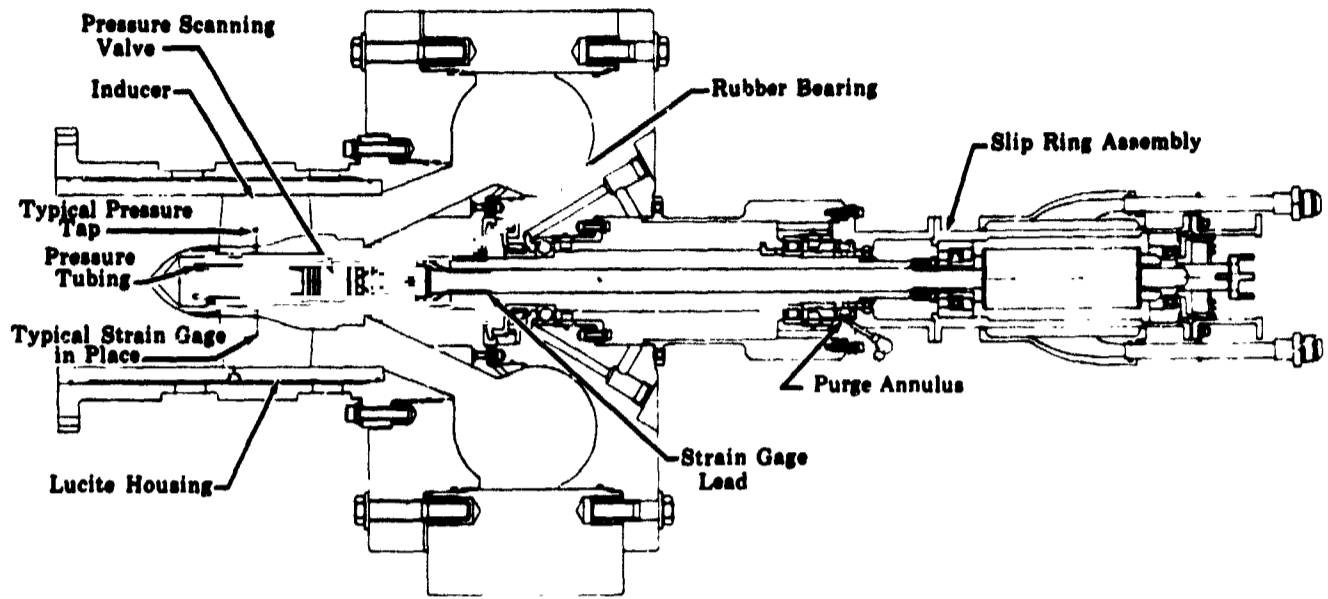


Figure 79. Inducer Test Rig

FD 21423B

SECTION III
CONCLUDING REMARKS

Computer programs have been written for the prediction of:

- Inducer performance (noncavitating and cavitating) and blade pressure loading
- Inducer blade stress distribution due to pressure and centrifugal loading
- Inducer blade resonant frequencies and associated stress distributions.

The computer programs have been correlated against a number of experimental and exact solution test cases with satisfactory results.

An inducer and test rig have been designed with provisions for measurement of:

- Blade steady pressure distribution
- Blade vibratory pressure magnitude and frequency
- Blade steady strain distribution
- Blade vibratory strain magnitude and frequency.

A series of tests in water are planned, and test data will be correlated with computer program predictions.

PRECEDING PAGE BLANK NOT FILMED.

APPENDIX A
LITERATURE SURVEY

1. VANE HYDRODYNAMIC LOADING UNDER CAVITATING AND NONCAVITATING CONDITIONS

a. Velocity and Pressure Distribution.

1. Acosta, A. J., "An Experimental and Theoretical Investigation of Two-Dimensional Centrifugal Pump Impellers," *Trans. ASME* 76, 5, 749-763, July 1954. An experimental and theoretical investigation on a series of two-dimensional centrifugal-pump impellers has been made in an effort to determine the usefulness of potential theory for the description of the flow. Computed values of the developed head and pressure distribution on the vane surfaces are compared with measurements on two-, four-, and six-vaned logarithmic spiral impellers. The agreement between the observed and predicted quantities is reasonably good for operating points where the influence of the inlet turn on the internal flow is least. The discrepancies which occur at other flow rates are attributed to real fluid effects which are observed in the impeller passages.
2. Betz, A., "On the Calculation of Cascade Flow at Fairly Great Distances Between the Blades," (in German), *ZAMM* 33, 4, 113-116, April 1953. The singularity method for calculating the flow around airfoils in cascade was developed by the author in 1931. The fundamental idea of this method consists in replacing the airfoils in cascade either by single vortices or by continuous distributions of vortices. The flow around each airfoil will then be found by the superposition of three flows: (1) The flow which is not being disturbed by the airfoil in cascade ("mean flow"); (2) the flow which is induced by the airfoil in question; (3) the flow which is induced by the remaining airfoils. By application of sources and sinks one can also take into consideration the shape (thickness) of the airfoils. The calculations following this method can generally be executed only by a graphical integration. In this case both principal tasks - (a) calculation of the shape of the airfoils, and (b) study of the effect of any existing airfoils in cascade - can be solved with any sufficient exactness. (See, e.g., *AFM* 462, 1952.)
In this paper, the author considers infinitely thin airfoils in cascade. The third of the above-mentioned flows is represented by a series development. Only the first term need be used when there are sufficiently great distances between the airfoils in cascade. The consideration of a certain distribution of vorticity along the airfoil's length l is reduced to turning points and moments of inertia of the distribution of vorticity. This means a considerable abridgment of the calculational work, and sufficient exactness will be obtained for large distances between the airfoils in cascade.
3. Brown, R. L., and R. G. Trout, "Axially-Symmetric Flow Between Prescribed Surfaces and Pump Inlet Design," *ASME-Paper 63-AMGT-32* for Meeting 3 to 7 March 1963, 5 p. Study to determine actual velocity distributions between surfaces of revolution from experimental data, and design of impeller on this basis to see to what extent performance could be improved; test data were run on water at 530,000 Re, and on air at 180,000 Re; results compared with potential pattern predicted on basis of nonviscous fluid flow.
4. Carter, A. D. S., "Blade Profiles for Axial-Flow Fans, Pumps, Compressors, etc.," *Proc. Instn. Mech. Engrs. (Appl. Mech.)* 175, 15, 775-806, 1961. In this paper the basic factors controlling blade-section performance are first examined. It is shown that substantial differences in performance may be expected from profiles having different fluid surface velocity distributions. Thus some distributions favor a wide working range while another may be more suitable for very high-speed operation, and so on. A desired velocity distribution may be achieved by appropriately selecting the various physical parameters, such as maximum thickness, position of maximum thickness, position of maximum camber, etc. which define the blade profile. Thus if a particular performance in terms of inlet angle, deflection, Mach number, and incidence and Mach number range is specified, there will be a particular blade profile to do the job. These conditions will have been determined by the overall design consideration, and the various features which the profile designer can then choose to meet them are fully discussed in the second part of the paper.
In the final section the requirements of some illustrative applications are discussed. It is shown that, on the basis of the earlier parts of this paper, certain applications demand significantly different blade profiles. Evidence is given that substantial gains have been achieved by using the appropriate blade profile for some duties, from which it is concluded that proper attention to the selection of profiles for all duties must lead to an all-round improvement in the performance of these machines.
5. Costello, G. R., R. L. Cummings, and J. T. Sinnette, Jr., "Detailed Computational Procedure for Design of Cascade Blades with Prescribed Velocity Distributions in Compressible Potential Flows," *NACA - Report 1060*, 1952, 16 p. diagrams, charts, tables. Supersedes *NACA - Tech Note 2281* indexed in *Engineering Index* 1951 p 486.
A detailed step-by-step computational outline is presented for the design of two-dimensional cascade blades having a prescribed velocity distribution on the blade in a potential flow of the usual compressible fluid. This outline is based on the assumption that the magnitude of the velocity in the flow of the usual compressible nonviscous fluid is proportional to the magnitude of the velocity in the flow of a compressible nonviscous fluid with linear pressure-volume relation. The computational procedure includes several ways

of adjusting the prescribed velocity to satisfy restrictions imposed by the method. Tables of coefficients are given for evaluating the necessary integrals, including the determination of the harmonic conjugate function. Numerical examples are included.

6. Durand, W.F., "Flow Through a Lattice Composed of Air Foils," p 91-96. *Aerodynamic Theory, Volume II (General Aerodynamical Theory - Perfect Fluids by T. von Karman and J. M. Burgers. First Edition, 1963.)* An exact solution is presented for the two-dimensional flow field through a lattice of flat, straight airfoils using conformal mapping techniques with use of a generalization of the Joukowski transformation. Treatment for both staggered and nonstaggered flat (uncambered) airfoils is given. Extension of the theory to include airfoils of various camber and thickness can be made. (See United Aircraft Research Department Report R-23010-12, Feb 23, 1953.)
7. Eichenberger, H.P., "Secondary Flow Within a Bend," *J. Math. Phys.* 32, 1, 34-42, Apr 1953. The paper presents a theoretical solution and comparison with experiment for the secondary flow within a bend of a tube with rectangular cross section. The theory neglects viscosity and compressibility and utilizes linearized equations of motion for the secondary flow. The equations are solved for the initial conditions of constant stagnation pressure in the radial direction and linear decrease from the center to the upper and lower walls. The theoretical results agree well with experiments at the 30° station of an 8-in. x 8-in. square tube with a 90° bend of mean radius 78 in. The agreement is, however, only slightly better than it is for the simplified theory of Squire and Winter, which assumes two-dimensional flow and neglects changes in the direction of increasing bend angle. It is concluded that, for cases the same as or less severe than that investigated, the simplified theory is adequate for corrections to the flow in the blade passages of a compressor.
8. Ellis, G.O., and J.D. Stanitz, "Two-Dimensional Compressible Flow in Centrifugal Compressor With Logarithmic-Spiral Blades," *NACA TN 2255*, 46 pp., Jan. 1951. Authors apply methods previously developed by the second author to investigate flow in a compressor where the center line of the flow passages lies in a right circular cone, the axis of which is coincident with the axis of the compressor. The quantitative results, obtained by relaxation-method techniques, indicate that a reduction in eddy flow may be attained with backward or forward curved blades as compared to radial blades. The suggestion of improved adiabatic efficiency follows immediately. Indicated constancy of static pressure ratio between straight and curved blades suggest that the diffuser problem is less critical with backward curved blades.
Not intended for establishing design criteria, the computed results clearly indicate the desirability of experimental investigations upon which design criteria may be based.
9. Fanti, R., "Elementary Incompressible Solution for the Performance of Airfoils of Arbitrary Shape in an Arbitrary Cascade," *United Aircraft Corporation Research Department, Report R-23010-12*, Feb 23, 1953. A solution for the incompressible, two-dimensional pressure distribution on an arbitrary airfoil in cascade is derived using a combination of the conformal transformation and singularity methods. The conformal mapping technique is used to transform the flow about a circle in one plane into a lattice of staggered flat-plate airfoils in another plane. Source and sink potentials are then distributed along the surfaces of the flat-plate airfoils to produce the contribution of velocity potential resulting from airfoil thickness and shape. The solution is presented in the form of an integral equation, which is easily solved by iterative procedure, and is rapidly convergent.
10. Gruber, J., "Design of Blade Profiles for Axial-Flow Turbomachines," (in German), *Maschinenbau-Technik* 2, 5, 209-217, May 1953. A simplification of Theodoreson's "Theory of Wing Sections of Arbitrary Shape" (*NACA TR 411*) has been presented by Thwaites (*Acro. Res. Council. Rep. Mem. nos. 2166, 2167*). Present paper simplifies Thwaites' method, particularly as to calculation of effect of blade curvature. Simplified method can be used for calculation of velocity and pressure distribution around relatively thin, slightly curved blades of arbitrary section, and for reverse problem. Paper includes useful review of fundamental theory.
11. Hargest, T.J., "The Theoretical Pressure Distribution Around Some Conventional Turbine Blades in Cascade," *Aero. Res. Council. Lond. Rep. Mem. 2765*, 10 pp., Mar. 1950, published 1953. This report presents comparative results between theoretical pressure distributions around a specific series of turbine blades in cascade arrangement and the observed aerodynamic performance of blades of the same shape as tested in the No. 3 high-speed cascade tunnel of the National Gas Turbine Establishment.
The theoretical pressure distributions around the blades were determined over the range of incidence covered in the aerodynamic tests by means of Relf's analogy between aerodynamic streamline flow and electric potential flow. It is shown that these theoretical pressure distributions and their variation with incidence can explain the corresponding cascade test results and can form a basis of general comparison of the turbine cascades.

12. Johnson, I.A., and A. Ginsburg. "Some NACA Research on Centrifugal Compressors," Trans. ASME 75, 5, 805-814, July 1953. Paper represents effort to replace some of the "art" of centrifugal compressor design with a better understanding of the flow processes taking place. It summarizes some of the results obtained in the NACA theoretical and experimental research program on centrifugal compressors. First section deals with impeller research, discussing the inducer function and the impeller function. These were investigated and analyzed separately as much as possible, and the effect of configuration on performance noted. Second section deals with vaneless diffuser research. Purpose of paper is to establish general trends of good design practice rather than to establish specific rules.
13. Krumer, J.J., M.O. Stockman, and R.J. Born, "Incompressible Nonviscous Blade-to-Blade Flow Through a Pump Rotor With Splitter Vanes," NASA TN D-1186, 31 pp., Apr. 1962. Report describes an application of an established method of analysis (Krumer, Trans. ASME 80, 1, 236-275, Jan. 1958) to the study of the inviscid flow in a mixed flow pump impeller in which splitter vanes are placed between the main vanes. Differential equation for the "blade-to-blade" stream function is solved numerically. Calculations indicate:
 (i) flow upstream of leading edge of splitter vanes is little affected by their presence,
 (ii) slip factor and head rise are increased by inserting splitter vanes.
 Authors report that calculations are very sensitive to assumed position for rear stagnation point, and suggest that this might be determined from experiment. Reviewer suggests trailing edges of blades might have been made much thinner, both for purposes of calculation and in practice.
14. Lakshminarayana, B. and J.H. Horlock, "Review: Secondary Flows and Losses in Cascades and Axial-Flow Turbomachines," Intern. J. Mech. Sci. 5, 3, 287-307, July 1963. Very useful review of secondary flow and losses, with extensive bibliography (127 items). Comparisons are given of various theoretical relationships and of experimental data where possible, together with recommended expressions in light of existing knowledge. Nearly all approaches are valid only for incompressible, inviscid flow; authors recommend attention to compressibility, rotational effects, radial flow and interaction of leakage with cascade secondary flow.
15. Leist, K., "Experimental Arrangement for Measurement of Pressure Distribution on High-Speed Rotating Blade Rows," An Soc Mech Engrs - Trans v 79 n 3 Apr 1957 p 617-26. New research staff of Institute for Turbomachines of Aachen Technical University, Germany, carried out measurements on rotating turbine blading; program is part of comprehensive effort directed toward investigation of 3-dimensional flow through axial flow turbomachines. Paper 56-GTP-13.
16. Linhardt, H.D. and A.J. Acosta, "Note on Application of Cascade Theory to Design of Axial-Flow Pumps," ASME-Paper 62-WA-222 for meeting Nov 25-30 1962. Theoretical and experimental results are presented which assure usefulness of 2-dimensional cascade theories for design of axial flow pumps; it is necessary to include effect of blade thickness upon impeller flow, found to be responsible for reported discrepancies between predictions of thin airfoil theories and performance of axial flow pumps characterized by high stagger angle and low aspect ratio.
17. MacGregor, C.A., "Two Dimensional Losses in Turbine Blades," J Aeronautical Sciences, v 19 n 6 June 1952 p 404-8. Tests on three typical blades in 2-dimensional cascade tunnel were run at varying angles of attack, stagger angle, solidity, and downstream survey stations at Mach Number of about 0.4 and Reynolds Number of 6.5×10^5 ; static pressure distribution about blade was measured by 27 static pressure taps; wake behind blade row was surveyed and loss determined.
18. Marble, F.E. and I. Michelson, "Analytical Investigation of Some Three-Dimensional Flow Problems in Turbomachines," NACA TN 2614, 109 pp., Mar. 1952. Paper collects further useful contributions to linear theory of axially symmetrical flow of incompressible, inviscid fluid in axial-flow turbomachines (see also Marble, AMR 1, Rev. 1400). Linearization means that radial velocity and deviation of axial velocity from mean through-flow velocity are considered small, and are calculated to first-order approximation. Axially symmetrical solution (infinite number of blades) provides corrections accounting for most of three-dimensional effects neglected by cascade theory, especially for low pitch-chord ratios.
 Theory distinguishes three (additive) components of flow, viz., (1) uniform through-flow, (2) radial equilibrium solution, correct for upstream and downstream of the blade row, (3) fine-structure accounting for radial acceleration. Tables of an influence function, for hub ratio 0.6, permit rapid evaluation of fine structure by punch-card method; two numerical examples are given.
 A simple, actuator-disk approximation to fine-structure solution is applied, with a numerical example in each case, to the discussion of (1) transients in the first few stages of a multistage machine, (2) fluctuations of the axial velocity distribution within the deeply embedded stages (see also Wu and Wolfenstein, AMR 4, Rev. 1316), (3) performance, in its dependence on the radius and on the aspect ratio, of a single-blade row with prescribed distribution of flow angle at trailing edge; (4) off-design performance of a blade row. In addition to their immediate interest, the examples provide a useful introduction to how theoretical knowledge of the fine-structure solution can be employed to obtain simple, approximate answers to practical questions.
 A modified linear theory is proposed for the case of a through-flow velocity varying with the radius. The linearized solution is also given for a machine such that hub and casing are conical cones with common vertex.
19. Morelli, D.A. and R.D. Bowerman, "Pressure Distributions on the Blade of Axial-Flow Propeller Pump," Trans. ASME-75, 6, 1007-1012, Aug. 1953. In the design of screw propellers, the demand for uniform energy input at all radii is satisfied by a blade circulation constant over the radius. With the authors' additional assumption of linear increase of circulation strength in axial direction, an approximate formula is given for the disturbance velocities in the blade space dependent on radius and distance from the blade's leading edge; they effect a curvature of the free streamlines which require a curvature of the blade profile computed according to airfoil theory.
 Using this formula a propeller pump has been designed; its pressure distribution has been investigated by means of a rotating manometer under various working conditions. The measurements approximately agree with potential-theoretical pressure distributions. In design condition, the energy supply proves to be really uniform over the radius; hereby, the practical use of this design method is shown.
20. Oba, R., "Linearized Theory of Supercavitating Flow Through an Arbitrary Form Hydrofoil," (in English), ZAMM 41, 9, 354-363, Sept. 1961. Faster and more powerful hydraulic machines result in cavitation problems such as drop in efficiency, damage due to erosion and vibration and noise. Author suggests that supercavitating hydrofoil such as Tulin hydrofoil be used. Problem is treated in two dimensions. A linearized theory is presented including (a) method to estimate hydrofoil form for given pressure distribution and (b) method to estimate characteristics of hydrofoil form. Numerical examples of hydrofoil computation are also presented.
21. Seidel, B.S., "Asymmetric Inlet Flow in Axial Turbomachines," Trans. ASME 86 A (J. Engrg. Power) 1, 18-28, Jan. 1964. Paper improves on the prediction of the attenuation of a distorted flow approaching blade rows in axial turbomachinery. The previous analysis of Rannie and Marble (AMR 12 (1959), Rev. 5708) and Ehrich (J. Aero. Sci. 24, 6, 413-417, June 1957) utilized the actuator-disk approach together with a blade force-flow angle relationship which was assumed to be the same as the uniform flow case. The essential, new feature of Seidel's paper is an improved blade force determination which accounts for the direct effect of the flow distortion.
 This paper also includes a rather nice comparison of theory and data.
22. Smith, L.H., Jr., S.C. Traugott, and G.F. Wislicenus, "A Practical Solution of a Three-Dimensional Flow Problem of Axial-Flow Turbomachinery," Trans. ASME 75, 5, 789-799, July 1953. Paper presents methods of determining the meridional flow pattern through turbomachines when there are strong departures from free vortex flow, arising from endeavor to design compressors and turbines for maximum head and flow, subject to Mach number limitations.
 Frictionless flow on infinite number of vanes, and axial symmetry are assumed, though authors themselves admit "that there is no known physical reason why this assumption should be considered as sufficiently accurate to describe the flow through actual vane systems of finite vane spacing."
 Methods of computation are described and results given of two worked examples, reference being made to N.S. theses by two of the authors for full details.
23. Stanitz, J.D., "Some Theoretical Aerodynamic Investigations of Impellers in Radial- and Mixed-Flow Centrifugal Compressors," ASME Gas Turb. Power Fall Meeting, Minneapolis, Sept. 1951. Paper 51-F-13, 25 pp. -- Trans. ASME 74, 4, 473-497, May 1952. Paper presents numerical results of relaxation solutions of flow of ideal fluid through a centrifugal impeller. Theory and results are given in dimensionless form. Two types of problems are treated: (1) Axial symmetry solutions in which blade forces are replaced by distributed body forces; (2) blade-to-blade solutions giving circumferential variation of pressure and velocity between blades.
 Equations for flow with axial symmetry are given for compressible fluids, but the two solutions presented are for incompressible flow through an arbitrary impeller profile with radial vanes, with and without inducer vanes. Results show that the form of streamlines in meridian section is little affected by presence of inducer vanes.

Blade-to-blade solutions are given for radial-flow impellers with constant flow area and with radial or log spiral blades, for compressible fluids in seven cases, and for incompressible fluids in one case, so that influence of change of impeller-tip Mach number, flow coefficient, angular blade spacing, blade angle and compressibility may be studied. Plots of streamlines, relative Mach numbers, and static pressure ratios allow easy qualitative comparison of different cases.

Author also presents simplified approximate methods of estimating velocity distributions along driving and trailing faces of blades and compares their accuracy with the relaxation solutions. He discusses qualitatively the influence of viscosity and boundary-layer development as affected by the frictionless flow pattern, and concludes that future centrifugal compressor development may lead to mixed-flow impellers with backward curved blades. He does not suggest, however, how the mechanical difficulties involved in producing a high-speed impeller of this type may be overcome.

The paper must be regarded as a valuable contribution to the literature on this difficult subject.

24. Stockman, N.O., and J.L. Kramer, "Method for Design of Pump Impellers Using a High Speed Digital Computer," NASA TN D-1562, 1963. Centrifugal pumps are being considered for space applications in chemical and nuclear-rocket engines using cryogenic fluids and in power-conversion systems using liquid metals. For these applications, the pumps should be of minimum size and weight, should have high efficiency, and should operate cavitation-free or with controlled cavitation at high rotational speeds. A knowledge and control of the internal flow are necessary to meet these requirements. The hub-shroud design method presented herein (with optional blade-surface computations) is a rapid and easy-to-use method. It enables the designer to proceed from a known streamline and its velocity distribution to an adjacent streamline and its velocity distribution. Thus, given the conditions along the hub, the entire hub-shroud profile is built up by proceeding from the hub streamline to the next streamline, and so on, until the shroud is reached.
25. Woods, L.C., D. Phil, and A. Thom, "A New Relaxational Treatment of the Compressible Two-Dimensional Flow About an Aerofoil With Circulation," *Aero. Res. Council. Lond. Rep. Mem. 2727*, 17 pp., Mar. 1950, published 1953. The two-dimensional incompressible and compressible flow over a profile is computed by relaxation in a grid with potential and stream functions as independent variables. Thus the profile appears as a straight line. Circulation is chosen in advance; angle of attack is found at the end of the computations. Boundary conditions at the profile are taken into account by successive approximations. Known circulation is used to formulate an approximate boundary condition at the outer edge of the relaxation field. Treatment of stagnation region is discussed in *AMR 6*, Rev. 1310. Comparison of theoretical and experimental results is carried out for profile NACA 16.
26. Wu, C.H., C.A. Brown, and V.D. Frian, "An Approximate Method of Determining the Subsonic Flow in an Arbitrary Stream Filament of Revolution Cut by Arbitrary Turbomachine Blades," *NACA TN 2702*, 46 pp., June 1952. A method is presented to obtain a relatively quick approximate determination of the detailed subsonic flow of a nonviscous fluid past arbitrary turbomachine blades. The method is illustrated with examples of compressible flow in a turbine cascade and in a centrifugal compressor. For these high-solidity blades, three terms of the Taylor series are found to give sufficient accuracy. Sufficient convergence is obtained in the turbine cascade after two cycles of computation and in the centrifugal compressor after four cycles of computation. The detailed flow variation obtained compares very well with an available numerical solution and experimental data for the turbine cascade, and with detailed experimental measurements for the centrifugal compressor.

b. Cavitation (Two-Phase Flow) - Theoretical

1. Cooper, P., "Application of Pressure and Velocity Criteria to Design of Centrifugal-Pump Impeller and Inlet," *ASME - Paper 63-ANGT-58* for meeting Mar 3-7 1963 12 p. Centrifugal pump impeller and inlet designed by use of criteria for distributions of pressure and velocity that lead to satisfactory performance at low net positive suction heads; calculations made for nonviscous, single-phase (liquid) flow with view toward minimizing bubble formation; tests run under cavitating and single-phase flow conditions; results show that design method leads to good suction performance.
2. Cooper, P. and H. B. Bosch, "Three-Dimensional Analysis of Inducer Fluid Flow," *NASA CR-54836*, Feb 11, 1966. Analytical studies were conducted to provide means for improving the design of inducers for high-speed, high-flow rocket engine pumps. Exact and approximate methods are presented for obtaining three-dimensional solutions to turbomachine flows with losses and vaporization, and results are presented for two sample inducers. The exact method solves four nonlinear differential equations of motion simultaneously by finite-difference and relaxation techniques that employ a "total residual" concept. The approximate method employs a finite difference solution of the basic flow equations in two dimensions and then superimposes an assumed solution in the third dimension, resulting in an approximate three-dimensional solution. Conclusions on inducer performance and design are made on the basis of several approximate solutions of both incompressible and two-phase flows, together with analysis of fluid thermal and scale effects. Fortran IV listings of the analysis computer programs are presented.

3. Goldman, K., R. Menkel, and R. P. Stein, "Equation for Critical Mass Velocity of Homogeneous Vapor-Liquid Mixtures at Low Pressures," *ASME - Paper 64-APM-12* for meeting June 9-11 1964 3 p; see also *AMR - Trans J Applied Mechanics v 31 n 3 Sept 1964 p 380-2*. Equations have been developed expressing critical mass velocity and isentropic expansion coefficient of single-component, homogeneous vapor-liquid mixtures at low pressures in terms of tabulated thermodynamic properties; two-phase flow relations are analogous to relations governing flow of single-phase compressible fluids, most readily formulated in terms of Mach numbers.
4. Jacobs, R. B., "Prediction of Symptoms of Cavitation," *US Bur Standards - J Research - Eng & Instrumentation v 65C n 3 July-Sept 1961 p 147-56*. Analysis of some basic problems in cavitation and which may permit prediction of cavitation characteristics of hydraulic equipment; application to pumps; practical results compared with theory; it is concluded that analysis may be applicable to prediction of symptoms of cavitation but that more information related to metastability, nucleation, and vapor phase dynamics is required.
5. Jakobsen, J. K., "On Mechanism of Head Breakdown in Cavitating Inducers," *ASME - Paper 63-ANGT-29* for meeting Mar 3-7 1963 15 p. Mechanism, as affected by thermodynamic properties of turbopump fluid and scale effects, is discussed; approach taken by other investigators and limitations to cavitation scaling in relation to experimental data; hypothesis introduced relates head breakdown process to acoustic shock phenomenon at point of leading-edge blade cavity collapse; integrated model for cavitating cascade blade is developed to correlate potential flow cavity cascade model with influence of thermodynamic properties, thermodynamic approach, and application of bubble dynamic studies to understand how suction performance is limited by inlet pressure; pertinence to propellant pumps.
6. Jakobsen, J. K., "Supercavitating Cascade Flow Analysis," *Trans ASME, J1 of Basic Engineering, Dec, 1964, p. 805-814*. An exact mathematical theory of supercavitating flow in cascades with arbitrary blade shapes is developed. Applying conformal mapping methods to the potential flow problem involved, a general mapping procedure is established. The geometric interpretation of the obtained mappings is discussed in general and completed in the case of the flat-plate cascade. All results assume infinitely long cavities. The application of the established mapping procedure to the case of a cascade with arbitrary blade shape requires the solution of a nonlinear integral equation for one of the mapping functions, or the approximation of this mapping function by a Fourier series whose coefficients must be determined from implicit conditions imposed by the blade shape.
7. Lewis, W. P., "Design of Centrifugal Pump Impellers for Optimum Cavitation Performance," *Instn Engrs. Australia - Elec & Mech Eng Trans v EN6 n 2 Nov 1964 p 67-74*. Examination of influence of velocity distributions in flow entering impeller to establish design procedure for flows with and without prerotation. 29 refs.
8. Sack, L. E., and H. B. Nottage, "System Oscillations Associated With Cavitating Inducers," *ASME-Paper 65-PE-14* for meeting June 7-9 1965 8 p. Nature and inception of pressure and flow-rate oscillations associated with high-speed cavitating inducer employed to extend suction performance capabilities of high-speed, high-flow pumps were investigated by nonlinear analog computer simulation; favorable accord between simulation findings and typical actual dynamic oscillation characteristics validates general technique for extension into inducer design analyses; it was found that nature and behavior of cavitation vapor volume and dynamic response characteristics of complete fluid circuit play key roles in incidence and suppression of oscillations.
9. Spraker, W. A., "Effects of Fluid Properties on Cavitation in Centrifugal Pumps," *ASME - Paper 64-WA/PE-14* for meeting Nov 29- Dec 3 1964 10 p. see also *ASME - Trans - J Eng for Power v 87 n 3 July 1965 p 309-18*. Analytical model of cavitation process in pump is developed assuming that flow is adiabatic, frictionless, steady, and irrotational; relationship is developed relating volume percentage of fluid vaporized during cavitation process to thermal cavitation parameter; experimental and analytical methods for determining cavitation characteristics of pumps handling petroleum-based hydrocarbon mixtures are described; cavitation data for two pipe-line pumps handling gasoline, fuel oil, and crude oil are presented.
10. Starkman, E. S., V. E. Shrock, K. F. Neusen, and D. J. Heneely, "Expansion of Very Low Quality Two-Phase Fluid Through Convergent-Divergent Nozzle," *ASME - Paper 63-ANGT-4* for meeting Mar 3-7 1963 8 p. Flow in de Laval nozzles of h-p steam water mixtures was investigated to determine mass flow rates and design criteria; qualities ranged from 0 to 20% and pressures up to 1000 psia; comparisons of data to isentropic expansion, frozen composition, and slip flow showed satisfactory correspondence except for qualities very close to saturated liquid; condition similar to shock resulted when nozzles were overexpanded; pertinence to very high heat flux heat power devices, e.g., nuclear reactors, with applications in nucleate boiling region.
11. Stepanoff, A. J., "Cavitation Properties of Liquids," *ASME - Paper 63-ANGT-22* for meeting Mar 3-7 1963 5 p. Method of representing thermal properties of liquids is offered such that cavitation behavior of centrifugal pumps handling any liquid molten metal, hydrocarbons, cryogenics can be accurately evaluated; there are sufficient test data to illustrate use of method.

12. Stepanoff, A. J., and M. A. Stahl, "Cavitation Criterion for Dissimilar Centrifugal Pumps," ASME - Paper 61-WA-139 for meeting Nov 26-Dec 1 1961. 5 p. Method of expressing net positive suction head for centrifugal pumps in terms of impeller design elements as they appear in inlet velocity triangle; procedure is applicable to pumps of different specific speeds, of different suction specific speeds, and to pumps having impellers of either overhung type or with shaft through eye.
13. Strippling, L. B., and A. J. Acosta, "Cavitation in Turbopumps," ASME - Papers 61-WA-112 13 p, 61-WA-98 11 p for meeting Nov 26-Dec 1 1961. Paper WA-112 (Pt. 1). Several simplified free streamline models suitable for flow through inducer discussed. Paper WA-98 (Pt. 2). Results are compared with tests on actual inducers; relevance to development of light weight turbomachine components for liquid rocket propulsion systems.
14. Wang, Y. L., and P. A. Longwell, "Laminar Flow-In Inlet Section of Parallel Plates," A.I.Ch.E. J v 10 n 3 May 1964 p 323-9. Numerical solutions of exact momentum equations for steady isothermal laminar flow of incompressible Newtonian fluid in inlet section of parallel plates; velocity distributions, pressure gradients, and overall pressure drop for two cases at Re 300; it was verified that usual boundary-layer assumptions are not valid near leading edge.
15. Warner, C. F., and D. W. Metzner, "Investigation of Flow Characteristics in Converging-Diverging Nozzles," ASME - Paper 63-WA-192 for meeting Nov 17-22 1963 9 p. Analytical method based on 1-dimensional model is presented for determining flow characteristics of 2-phase flow of liquid drops in gas stream expanding through converging-diverging nozzle; analysis can be utilized to predict liquid velocity, gas velocity, static pressure, and droplet diameter as function of axial distance along nozzle axis for flows containing approximately 10 times as much liquid as gas by weight.
16. Wu, T. Y. and D. P. Wang, "An Approximate Numerical Scheme for the Theory of Cavity Flows Past Obstacles of Arbitrary Profile," Trans. ASME, JI of Basic Engineering, Sept-1964, p 556-560. Previously one of the authors has developed an exact theory for the cavity flow past an obstacle of arbitrary profile at an arbitrary cavitation number by adopting a free-streamline wake model. In the present paper the authors introduce an approximate numerical method for the computation of the dual functional equations which result from the theory. The new method is shown to provide a drastic simplification to the computations while maintaining a high degree of accuracy of the numerical result.

c. Cavitation (Two-Phase Flow) - Experimental

1. "Facilities and Techniques Employed at Lewis Research Center in Experimental Investigations of Cavitation in Pumps," ASME - Symposium on Cavitation Research Facilities and Techniques, May 18-20 1964, p 60-76. Study of cavitation as it occurs in pumping of high-energy propellants (cryogenic liquids) used in chemical and nuclear rocket engines and alkali metals used in space-electric-power generation systems; paper lists and describes facilities and techniques utilized to supply experimental input to program studies; test fluids include water, cryogenic liquids, and alkali metals.
2. Grindell, A.G., "Correlation of Cavitation Inception Data for Centrifugal Pump Operating in Water and in Sodium-Potassium Alloy (NaK)," ASME-Trans-J Basic Eng v 82 Ser D n 4 Dec 1960 p 821-8. Static head at pump suction at time of cavitation inception was correlated for water and for 1500 F NaK on basis of differences of vapor pressures of two liquids; difference between vapor pressures, for same conditions of pump speed and liquid flow, was added to water test cavitation inception value; this proved to be good approximation to experimental value found for cavitation inception with NaK. Paper 59-A-156.
3. Hartmann, M.J. and R.F. Soltis, "Observation of Cavitation in Low Hub-Tip Ratio Axial-Flow Pump," ASME-Paper 60-HYD-14 for meeting Mar 6-9 1960, 12p. Cavitation formations in pump rotor are examined in attempt to determine important characteristics of flow model which may be used to indicate effects of cavitation; data were obtained at Lewis Water Tunnel at NASA Lewis Research Center; besides instrument surveys, high speed photographs were taken, for which latter purpose upper half of pump casing is of plastic.
4. Morie, C. and M. Oshima, "Experimental Study on Cavitation in Mixed Flow Pump Impellers," Japan Soc Mech Engrs - Bul v 7, n 25, Feb 1964, p. 62-70. Series of experimental studies of cavitation characteristics of mixed flow pump impellers was performed; report clarifies mainly how cavitation inception and performance decrease are influenced by number of vanes and shape of vane inlet edge; it was also found that certain amount of flow deviation must be taken into account in determination of vane inlet angles.
5. Jehat, W.K., "Reynolds Number and Incidence-Angle Effects on Inducer Cavitation," ASME-Paper WA/FE-31 for meeting Nov 17-22 1966, 9 p. Tests of various hubless inducers in water show that suction specific speed increases with Reynolds number and incidence angle; analysis is presented which reduces this observation to Reynolds number-dependency and approximate incidence-independency of newly defined "vane coefficient;" relations are general and apply to other inducer types and normal pump impellers. 22 refs.

6. Langteau, R.R. and E.R. Dodge, "Cavitation in Impeller-Looking from Inside Out," ASME-Paper 63-AMOT-30 for meeting Mar 3-7 1963 12 p. Low specific speed, double suction centrifugal pump was modified by splitting casing and impeller in half and incorporating transparent inserts and housings to permit visual observations of flow; "half pump" was operated in water test facility at prototype design heads with both Francis and radial-vaned inlet impeller design; photographic records of cavitating and noncavitating conditions at various points along pump characteristic are correlated with various performance parameters.
7. Miller, M.J., J.E. Crouse, and D.E. Sandercock, "Summary of Experimental Investigation of Three Axial-Flow Pump Rotors Tested in Water," ASME-Paper 66-WA/FE-24 for meeting Nov 27-Dec 1 1966, 11 p. Three rotors located immediately downstream of pump inducer were tested to study flow and performance across loaded axial-flow blade rows; principal design parameters varied were flow coefficient, blade loading parameter at tip, and hub-tip radius ratio; overall and blade element performances under noncavitating flow conditions are discussed; comparisons between measured, three-dimensional design parameters and those computed from two-dimensional cascade correlations; performance obtained during operation of rotors in unstable flow and cavitating flow conditions.
8. Seemann, V., "What Engineers Should Know About Cavitation and NPSH," Pipe Line Industry v 15 n 1 July 1961 p 55-61. Relationship between pump suction characteristics and fluid properties has been obtained; satisfactory performance of pumps on hydrocarbons with less net positive suction head available than required by cold water was studied; data collected and theory developed aim at accurate prediction of pump suction requirements for all liquids, on basis of cold water requirements; causes of cavitation; test stand, instrumentation, results, and benefits of investigation.
9. Soltis, R. F., D. A. Anderson, and D. M. Sandercock, "Investigation of the Performance of a 78° Flat-Plate Helical Inducer," NASA TND-1170, 1962. The coupling of a cavitating inducer with a pump, in order to realize the advantages of higher mechanical speeds, has found wide use in missile applications. An effective and quite easily fabricated blade shape employed in the inducer has been the flat-plate helix. This report presents the measured performance of an inducer of this type. The rotor, 5 inches in diameter, consisted of three blades with a hub-tip ratio of 0.5 and a helix angle of 78 degrees at the tip. All tests were made in water. Performance results over a range of flows are presented at both cavitating and noncavitating conditions. This includes both the overall performance and radial distributions of flow conditions and selected blade-element performance parameters. In addition, photographs that visually describe flow conditions at various modes of operation are presented. A comparison of the measured axial velocity distributions with those computed assuming simple radial equilibrium provides a check on the validity of the radial equilibrium assumption.
10. Wood, G.M., "Visual Cavitation Studies of Mixed Flow Pump Impellers," Trans. ASME 85 D (J. Basic Engrg.) 1, 17-28, Mar. 1963. Three mixed impellers (design parameters; 3800, 4920, 8500 rpm; 1760, 1545, 1245 gpm; 287, 235, 245 ft) have been tested in a closed water loop. Author compares cavitation curves at three test points at rpm 1900, 2460, 4250 with the high-speed photographic records. He concludes that cavitation occurs for all impellers at higher values of NPSH than those associated with a drop in the head rise. Cavitation in vane channels is cyclic, whereas cavitation near the vane leading edges was more stable. In author's opinion, the mean static pressure gradient is a prime variable in the determination of cavitation performance characteristics. Some data on vane channel cavitation frequency are presented.
11. Wood, G.M., J.S. Murphy, and J. Farquhar, "Experimental Study of Cavitation in Mixed Flow Pump Impeller," ASME-Trans-J Basic Eng v 82 Ser D n 4 Dec 1960 P 929-40. Hydraulic performance of impeller design tested with 6, 5, and 4 vanes in closed water loop; 2 idealized flow models for incipient cavitation were derived to illustrate limits of cavitation design; both vane blockage and solidity effects are important. Paper 60-Hyd-7.
12. Wright, M.K., "Design Comments and Experimental Results for Cavitation-Resistant Inducers up to 40,000 Suction Specific Speed," ASME-Paper 63-AMOT-59 for meeting Mar 3-7 1963 8 p. Paper considers general geometric considerations of inducer design, correlation of dimensionless design parameters, experimental data obtained from 2 models developed by Bell Aerosystems Co. and suggests several auxiliary means of augmenting cavitation resistance of inducer; inducer is axial flow pump capable of digesting large scale fluid vapor formations at its inlet without seriously affecting head generation.
13. Yokoyama, S., "Effect of Profile of Entrance of Centrifugal Pump Impeller on Cavitation," Japan Soc Mech Engrs-Bul v 5 n 19 Aug 1962 p 485-91. Velocity distribution just before vane entrance edge differs according to difference of impeller entrance profile; irrespective of velocity distribution, static pressure distribution at point just before vanes was almost same for all profiles; in comparison of cavitation occurrence for profiles designated A and C, no distinctive difference was observed except that head drop due to cavitation in large flow rate range was smaller for second profile.

14. Yokoyama, S., "Effect of Tip Shape at Entrance of Impeller Vane of Centrifugal Pump on Cavitation," Japan Soc Mech Engrs-Bul v 3 n 11 Aug 1960 p 326-32. Experiments were carried out on three different types of tip shape; in each case, head capacity curve, static pressure distribution on surfaces of vanes near entrance tips and modes of cavitation occurrence were measured; results indicate that at shockless entry there are more changes of cavitation for round tip vane than for other type vanes; for sharp tip vane no cavitation occurs in experiments.

2. VANE STRESSES (STRESSES IN CURVED PLATES)

a. Exact Solutions

1. Candela, F., "Structural Applications of Hyperbolic Paraboloidal Shells," J. Amer. Concr. Inst. 26, 5, 397-413, Jan. 1955. After a short exposition of the properties of the hyperbolic paraboloid, author gives in simple form Fucher's general equations of the stress system analysis. More especially, the warped parallelogram is studied, arising from consideration of a portion of a hyperbolic paraboloid limited by four straight generatrix. In general, the stress system is given for the following cases: (1) snow load; (2) dead load; (3) fill load. The $f(x), F(y)$ functions relative to the boundary conditions are to be determined in all aforesaid cases. The finite-differences method is recommended for the more complex solution of case (2).

Some existing examples are shown of constructions in Mexico City built up as associations of the warped parallelogram.

The possibilities of the use of these shells in reinforced-concrete construction makes this work particularly interesting.

2. Deverall, L. I. and C. J. Thorne, "Bending of Thin Ring-Sector Plates," J. appl. Mech. 18, 4, 359-363, Dec. 1951. Authors attack the problem by a method they used for rectangular plates in previous paper (AMR 4, Rev. 3837). General expressions for the deflection of plates whose planform is a sector of a circular ring are given for cases in which the straight edges have arbitrary but given deflection and bending moment. The solutions are given for all combinations of physically important edge conditions on the two circular edges. Sectors of circular plates are included as special cases. Solutions are given for a general load which is a continuous function of r and a sectionally continuous function of θ , where r and θ are the usual polar coordinates with the pole at the center of the ring. Several specific examples for angles of the sector 30° and 90° are given.
3. Griffin, D. S., "Stresses and Deflections of Thick, Curved Plates," ASME - Paper 64-WA/ME-8 for meeting Nov. 29-Dec. 4 1964 6 p.; See also ASME - Trans - J Eng - r Industry v 87 n 3 Aug 1965 p 303-8. Solution is obtained using linear theory of elasticity for stresses in long, thick, uniformly curved plate due to pressure on curved surfaces and forces or deflections specified on straight edges; maximum stresses are compared with those obtained by elementary thin beam theory, showing range of applicability of simpler theory; in general, accuracy of elementary theory depends on total plate angle, as well as mean-radius-to-thickness ratio.
4. Neas, A. M., "Design of Thin Concrete Shells: Vol. 1, Positive Curvature Index," New York, John Wiley & Sons, Inc., 1962, viii + 128 p. This book represents the first of a set of several volumes concerning various aspects of shell analysis, design, and construction that the author intends to publish. This first volume deals with the design and analysis of doubly curved shells of positive curvature and in particular axisymmetric shells.
- The book begins with a brief outline of the membrane theory of shells and a concise summary of the necessary relationships of differential geometry for the analysis of thin shells. Next, the membrane analysis of axisymmetric deformation of axisymmetric shells is formulated and a number of special cases pertaining to membrane stresses existing in symmetrically deformed shells of revolution are treated. These include the spherical dome, the elliptical dome, and conical shells subjected to various types of symmetric loads. Analytical as well as graphical solutions are discussed. The next chapter presents the case of unsymmetrically loaded shells of revolution and linear elastic theory is completely developed for this situation. Solutions involving expansions in terms of harmonic series are treated in detail for spherical shells and shells on discrete supports, and, lastly, various aspects of design consideration for such shells are discussed.
5. Knowles, J. K., and E. Reissner, "Torsion and Extension of Helicoidal Shell," Quarterly of Applied Mathematics, Vol 17, p 409-422, 1959. The authors determine the elastic behavior of a pretwisted strip in the form of a helicoidal shell when acted upon by axial forces and a twisting moment. In this instance the rotationally symmetric states of strain depend upon the states of displacement that are not rotationally symmetric. Torsional rigidity and axial stiffness are obtained as a function of pretwist by perturbation solutions.

6. Langhaar, M. L., "An Invariant Membrane Stress Function for Shells," J. appl. Mech. 20, 2, 178-182, June 1953. The equations of equilibrium of membrane stresses in a shell are shown to be satisfied with certain restrictions by a generalized Airy stress function. For shells of constant Gaussian curvature the stress function is shown to be unrestricted. For other shells, it is expressed as a function of the Gaussian curvature. Comparisons are made with Fucher's stress function. Shells of revolution with constant and variable curvature are discussed.

7. Langhaar, M. L. and D. R. Carver, "On The Strain Energy of Shells," J. appl. Mech. 21, 1, 81-82, Mar. 1954. In a previous paper (AMR 3, Rev. 1641) of the first author, the strain energy was derived with the assumption that only the linearized terms in the thickness coordinate s need be retained in the geometrical equations between the strains and the displacements of the middle surface. The present paper shows that, in general, the strain-energy density is only a rational function of s , and the evaluation of the strain energy in terms of the displacements is not difficult. In the simple example of the cantilever curved beam the authors point out that the linearizing of the geometrical equations in connection with the use of strain energy and calculus of variations leads to questionable approximations. The conditions of equilibrium are not satisfied; the net tension disagrees grossly. But if the shell is thin, the linearizing causes only a small error in the stresses.

8. Lew, H. G., J. A. Fox, and T. T. Loo, "Large Deflection Of Curved Plates," NACA TN 3684, 33 pp.; Oct. 1956. The specific problems treated are the deflections of doubly curved plates with normal edge loads, doubly curved plates under edge shear loads, and nearly cylindrical curved plates under longitudinal compression. The difference between the first two plates and the third one lies in the fact that the initial deflection is axially symmetric in the first two cases whereas the third plate is very close to a portion of a straight circular cylinder but has, in addition, a slight bulge along the length of it.

The principle of minimum potential energy, or equivalently the Ritz method, is used to determine the coefficients in the assumed expression for the stress function, and it is found that, for the initial deflections considered, only a few coefficients were necessary to represent the complete solution. This is, of course, merely another way of saying that if the initial deflection can be represented well by a few terms in a double sine series and if the loads such that the total deflections under load are similar in form to the initial deflection, then only a few terms in a double sine series will suffice equally well to describe the deformed state.

In addition to the determination of the stresses and deflections, the effective widths of the curved plates were calculated for several cases and compared to flat sheets and circular cylindrical curved panels.

9. Libai, A., "Invariant Stress and Deformation Functions for Doubly Curved Shells," Transactions of ASME, Vol 89, Series E, No. 1, Journal of Applied Mechanics, March 1967, p 43-54. Exact invariant stress and deformation functions for doubly curved (nondevelopable) shells are derived. The invariant stress function reduces the six shell equilibrium equations into a single equation in the stress function and moment resultants. The deformation function reduces the three surface strain-displacement relations into a single compatibility equation in the strains and deformation function, in terms of which the changes of curvature are also expressed. Application of these functions in the formulation of an approximate bending theory for shells is presented.

10. Reissner, E., "On Finite Twisting and Bending of Circular Ring Sector Plates and Shallow Helicoidal Shells," Quarterly of Applied Mathematics, Vol 11, 1963, p 473-483. The author considers the behavior of a thin circular ring sector plate subjected to two equal and opposite forces perpendicular to the plane of the plate and later analyzes an initially deflected helicoidal shell. Stress resultants and couples are assumed independent of the polar angle, θ , and transverse displacement is assumed proportional to θ . The solutions are obtained in terms of an Airy stress function.

11. Reissner, E., "Rotationally Symmetric Problems in the Theory of Thin Elastic Shells," Proc. Third U.S. Nat. Congr. Appl. Mech., June 1958; Amer. Soc. Mech. Engrs., 1958, 51-69. Paper presents an exhaustive and concise survey of linear and nonlinear theory of rotationally symmetric problems of thin elastic shells. Numerous important contributions to the subject by author and others are summarized with aim of constructing a unified and generalized theory.

Theory of shallow shells of revolution is treated for linear and small nonlinear deflections. Method for closed nonlinear solution of shallow spherical shell is given. In view of examination of applicability of membrane solutions, boundary-layer theory is summarized. Condition for existence of boundary-layer solution is developed for general case, thus generalizing known condition for spherical shell.

Second-order correction theory for influence coefficients of shell loaded on edges only is developed. General condition for negligibility of this correction is given, thus generalizing earlier result of author for cylindrical shell.

Other subjects treated are: Linear theory of pure bending of incomplete shells of revolution, shells of revolution with small variation of radial dimensions, asymptotic solutions for toroidal shells, and bending correction to membrane solution of closed ellipsoidal shell.

Lastly, differential equation of finite bending of thin-walled pressurized tubes of initial circular cross section is set up. Explicit solution is given by series expansion for case of initially straight center line.

Reviewer believes that paper is of major importance in thin-shell theory.

12. Vol'mir, A. S., "Survey of Investigations on the Theory of Flexible Plates and Shells (Covering the Period from 1941 to 1957)," NASA Tech. Transl. F-180, 45 pp., Oct. 1963. (From Raschet Prostranstvennykh Konstruktsii, 4, 451-475, 1958.) The literature on the theory of flexible plates and shells is reviewed, and information is abstracted on pertinent areas such as fundamental and approximate methods of solution, large deflections of plates and shells, and postbuckling deformations of plates and shells.

13. Wan, F. Y. M., "A Class of Unsymmetrical Stress Distributions in Helicoidal Shells," Quarterly of Applied Mathematics, Vol 24, No. 4, 1967. The author develops a theory for the elastic behavior of a helicoidal shell in which the displacements are multivalued in the polar angle, θ , while the strain distribution, although single valued in θ , is dependent upon θ . Ten strain displacement relations are used to set up the differential equations which govern the elastostatic behavior of the shell. The bending of a helicoidal shell by end moments is solved as an example.

b. Approximate Methods

1. Archer, J. S., "Consistent Matrix Formulations for Structural Analysis Using Finite-Element Techniques," AIAA Journal, Vol 3, No. 10, Oct 1965, p 1910-1918. The discrete-element stiffness matrix technique for formulation of linear structural problems in engineering mechanics is examined to develop techniques that give exact or closely approximate solutions for static load-displacement, elastic stability, and dynamic response problems. An exact relationship is derived for determining the coordinate load matrix equivalent to a general distributed load function. Use of the load matrix in static load-displacement problems results in an exact solution for the coordinate displacements consistent with the theoretical basis used for constructing the stiffness matrix. Explicit expressions are derived for a finite-displacement matrix for beam and plate elements for use in formulating the general elastic-stability problem. The approach discussed provides closely approximate buckling loads that are upper bounds to the precise solution. The dynamic problem, including elastic-stability considerations, is formulated using a consistent mass matrix approach. This approach provides closely approximate natural frequencies that are upper bounds to the exact solution. The data required for stiffness, load, finite-displacement, and mass matrices for a system composed of Timoshenko beam elements with linearly varying properties are provided. An example cantilever stepped beam problem is solved to illustrate the techniques involved and the exact or closely approximate nature of the solutions obtained.

2. Argyris, J.H., "Recent Advances in Matrix Methods of Structural Analysis," Progress in Aeronautical Sciences, Vol 4, The Macmillan Company, 1964. This book discusses methods of using matrices to solve aircraft structural problems by computer techniques. Methods of solving linear and nonlinear problems by matrix force-methods and matrix displacement methods are presented. These are many examples in which the results are compared with experimental test data with good agreement. Of particular interest is the general discussion on a method of approaching the problem of the curved cover by replacing the cover surface with triangular elements, as discussed in Appendix I.

3. Dawe, D.J., "A Finite Element Approach To Plate Vibration Problems," Journal of Mechanical Engineering Science, Vol 7, No. 1, p 28-32. A method of computing the natural frequencies of vibration of flat plates of arbitrary shape is outlined in which the plate is considered as an assemblage of elements.

Both stiffness and inertia matrices are derived for a rectangular isotropic plate element of uniform thickness, and these matrices are used to find the natural frequencies of square plates subject to various boundary conditions. Comparison of finite element frequencies with known exact, experimental, and energy solutions shows the method to give good results even for relatively few elements.

4. Dawe, D.J., "Vibration of Rectangular Plates of Variable Thickness," Journal of Mechanical Engineering Science, Vol 1, No. 1, p 42-51, 1966. In a previous paper the application of the finite element method to plate vibration problems was discussed. It was shown that the method gave good results when applied to the vibration of plates of uniform thickness.

The present paper extends the method to include plates of variable thickness. In particular, stiffness and inertia matrices are derived for an isotropic rectangular plate element of linearly variable thickness in one co-ordinate direction. These matrices are used to find the natural frequencies and mode shapes of a number of rectangular plenum cantilever plates of non-uniform thickness. Experimental results provide a basis for comparison with the finite element results.

5. Flügge, W., and S. C. Chou, "Large-Deformation Theory of Shells of Revolution," Transactions of ASME, Vol 89, Series E, No. 1, Journal of Applied Mechanics, March 1967, p 36-38. In this paper, nonlinear membrane equations are derived for a shell of revolution under the assumption that not only are the displacements and rotations large, but that, also, large strains are admitted. The equations, therefore, are aimed at shells which are not only very thin, but which are also made of a material which permits large elastic strains. The special difficulties resulting from this extension of the theory are discussed. As an example for the application of the equations, a circular toroid subjected to internal pressure is studied. Numerical results are given for a level of loading which lies clearly outside the domain of a large-deflection, small-strain theory.

6. Gallagher, R. N., R. A. Gellatly, J. Padig, and R. H. Mallett, "A Discrete Element Procedure for Thin-Shell Instability Analysis," AIAA Journal, Vol 3, No. 1, Jan 1967, p 138-145. The concepts of the matrix displacement approach to discrete element structural analysis are extended to predict general instability. Instability phenomena are accounted for by considering the influence of element membrane forces on element effective flexure stiffnesses. Particular attention is given to the problem of determining membrane force distributions that account for interelement membrane-flexure coupling. Representations of instability effects are formulated for several levels of approximation for an arbitrary quadrilateral plate element. Critical applied load intensities are predicted for plate, arch, and spherical cap structures to demonstrate convergence characteristics and to provide comparisons with test data and classical solutions.

7. Gerstenkoru, G. F. and A. S. Kobayashi, "Application of the Direct Stiffness Method to Plane Problems Involving Large, Time-Dependent Deformations," Journal of Basic Eng., Dec 1966, p 771-776. The direct stiffness method is used to formulate a numerical procedure for solving plane structural problems involving large, time-dependent deformations and nonhomogeneous, time-dependent material properties. The stiffness matrix in polar coordinates is derived for the state of plane strain. The nonlinear structural response is incrementally linearized by considering the deformation process to be linear within small time increments. The developed procedure is compared numerically with a known solution of creep deformations in a thick-walled cylinder subjected to internal pressure loading and elevated temperature.

8. Hermann, L. R., "A Bending Analysis for Plates," March 1965, Aerojet-General Corp., Technical Paper No. 7 SR0. In this paper, a general, approximate solution method applicable to the bending analysis of structural plates is presented and illustrated. The analysis includes the effects of shearing deformations and as a consequence, is applicable to both thin and moderately thick plates.

The plate bending equations (including shear deformations), written as functions of the transverse deflection, and the bending moments are expressed by means of a variational theorem. The plate to be analyzed is represented by a series of finite elements (triangles). Forms of the primary dependent variables (transverse deflection and moments) are assumed within each element and are related to their values at the element nodes (i.e., at the triangle vertices). The approximate solution is obtained by taking the variational of the function with respect to the node values of the unknowns, thus generating a set of linear algebraic equations that define these nodal values. The rotations and shears are calculated from the values of deflection and moments.

The consideration of transverse shear deformations permits the specification of three boundary conditions at each boundary point, instead of two, as in the case of the classical thin plate theory. Thus, for example, along a free edge of a plate, the actual boundary conditions may be applied (vanishing of the normal moment, normal shear, and twisting moment) instead of the rather artificial boundary conditions demanded by thin plate theory (vanishing of the normal moment and the "effective" transverse force).

The solution technique is utilized to analyze two significant problems, for which exact solutions are available, with excellent accuracy.

9. Holston, A., Jr., "Approximate Analytical Solutions of the Finite-Deflection Equations for a Shallow Spherical Shell," Transactions of ASME, Vol 89, Series E, No. 1, Journal of Applied Mechanics, March 1967, p 65-86. Approximate solutions are obtained, by Newton's method, for shells subjected to uniform and/or point loads in the prebuckled or postbuckled configurations. Comparison of results with numerical solutions shows maximum deviations of 5 percent for clamped shells subjected to uniform loads in the prebuckled configuration. Similar comparisons for other cases show larger deviations. A characteristic load is developed which compares favorably with numerical buckling loads.

10. Hrennikoff, A., "Solution of Problems of Elasticity by the Framework Method," Journal of Applied Mechanics, Trans. ASME 63, Dec 1941, p A169-A175. Because of mathematical difficulties which make the solution of differential equations of the theory of elasticity impossible in many cases, the author has been impelled to seek some other method of approach than one of pure mathematical analysis. The method outlined in this paper is of this character and may with some qualifications be applied to problems of two-dimensional stress, bending of plates, bending of cylindrical shells, the general case of three-dimensional stress, and a great variety of others. Essentially, the method consists in replacing the continuous material of the elastic body

- being studied by a framework of bars arranged according to a definite pattern, the elements of which are endowed with elastic properties suitable to the type of problem. This framework is then analyzed, according to the procedure outlined in the paper, for various types of elastic problems. Examples of the application of the principles involved are also given.
11. Kainius, A. and J. F. Lestings, "On Nonlinear Analysis of Elastic Shells of Revolution," Transactions of ASME, Vol 89, Series E No. 1, Journal of Applied Mechanics, March 1967, p 59-64. A multisegment method is developed for the solution of two-point boundary-value problems governed by a system of first-order ordinary nonlinear differential equations. By means of this method, rotationally symmetric shells of arbitrary shape under axisymmetric loads can be analyzed with any available nonlinear bending theory of shells. The basic equations required by the method are given for one particular theory of shells, and numerical examples of a shallow spherical cap and a complete torus subjected to external pressure are presented in detail. The main advantage of this method over the finite-difference approach is that the solution is obtained everywhere with uniform accuracy, and the iteration process with respect to the mesh size, which is required with the finite-difference method, is eliminated.
 12. Kaufman, S. and D. B. Hall, "Bending Elements for Plate and Shell Networks," AIAA Journal, Vol 3, No. 3, March 1967, p 402-405. Triangular bending elements that can be applied to irregular plate or shell networks are presented. Equilibrium as well as elastic properties of these elements are derived. Also presented are parallelogram plate bending elements whose elastic properties include core shear deformations for sandwich or thick plates. The elements presented are peculiar to the matrix force method with virtual work concepts forming the basis for computation of the elastic properties of the elements. A method of providing transition elements between triangular and parallelogram networks is also given.
 13. Khanna, J. and E. F. Hooley, "Comparison and Evaluation of Stiffness Matrices," AIAA Journal, Vol 4, No. 12, Dec 1966, p 2105-2111. Previous developments in the comparison and evaluation of stiffness matrices are reviewed. A simplification to the method of making comparisons on the basis of strain energy is presented, and it is shown that the results of element stiffness matrix comparisons apply to the structure. The theoretical basis for obtaining approximate qualitative comparisons from stiffness matrix eigenvalues is described, and the existing hypothesis on their use evaluated. Some plane stress stiffness matrices for square, isotropic elements are compared, and it is shown that it is reasonable to expect bounding of the strain energy by varying a stiffness matrix parameter. A method of comparing stiffness matrices of different orders is proposed. It also is shown that square elements generally will provide a better approximation to the strain energy than constant-stress triangular elements.
 14. Klein, B., "A Simple Method of Matrix Structural Analysis," Journal of Aero/Space Sciences, Jan 1957, p 39-41. A simple method of matrix structural analysis is presented which is believed to have certain distinct advantages over existing methods as explained in the text. The possible disadvantages of the method eventually may be minimized as the size and scope of automatic computing equipment are made larger. Certain two- and three-dimensional problems are worked to illustrate the ease and simplicity of the method.
 15. Klein, B., "A Simple Method of Matrix Structural Analysis: Part II - Effects of Taper and Consideration of Curvature," Journal of Aero/Space Sciences, Nov 1957, p 813-820. The matrix method of structural analysis presented previously in Part I is extended to include the effects of panel geometry and gage taper, stringer taper, and a consideration of curved elements. The resulting matrices are of the same form as the previous matrix and of comparable simplicity. Several problems are presented to illustrate the mechanics and simplicity of the extended method.
 16. Klein, B., "A Simple Method of Matrix Structural Analysis: Part III - Analysis of Flexible Frames and Stiffened Cylindrical Shells," Journal of Aero/Space Sciences, June 1958, p 385-394. The method presented in Part II (reference 2) is extended to cover the case of stiffened cylinders. Treatable loadings include those producing peak shear, such as in flexible frame problems, and those involving thermal stresses. Various structural irregularities may be accounted for, such as variable frame moment of inertia, tapered longerons, variable skin gage, cutouts, noncircular cylindrical shells, etc. A flexible frame problem is solved for illustration purposes.
 17. Klein, B., "A Simple Method of Matrix Structural Analysis: Part V - Structures Containing Plate Elements of Arbitrary Shape and Thickness," Journal of Aero/Space Sciences, Nov 1960, p 859-865. Simple equations are used to treat plate elements. The equations are basic equilibrium and force-displacement equations. The plate elements may be of any shape and have any thickness variation. The stresses in the elements may vary in a complex pattern. There need not be any edge members attached to the plates. All equations are simple to derive and simple in principle. Most equations contain definite integrals. Since in general the shapes and thicknesses of the plate elements are arbitrary, a simple numerical integration scheme is used to evaluate the integrals. Numerous numerical examples are worked out to illustrate the mechanics of the method and the accuracy attained.
 18. Klein, B., "A Simple Method of Matrix Structural Analysis, Part VI - Bending of Plates of Arbitrary Shape and Thickness Under Arbitrary Normal Loading," Journal of Aero/Space Sciences, March 1962, p 306-322. Method for analysis of general kinds of complex plates under complex normal loading; work is extension of previously given matrix method for solution of in-plane plate problems; method is of comparable simplicity; all boundary conditions are satisfied easily and directly; numerical examples illustrate mechanics of method. Part V indexed in Engineering Index 1961 p 1285.
 19. Lo, C. C., W. W. Niedenfuhr, and A. W. Leissa, "Further Studies in the Application of the Point Matching Technique to Plate Bending and other Harmonic and Biharmonic Boundary-Value Problems," Air Force Flight Dynamics Laboratory Technical Report AFFDL-TR-65-114, 175 pp. (Jan. 1966). Contract No. AF 33(657)-8772. This work is the second report summarizing work in applying the point matching technique to plate bending and other harmonic and biharmonic boundary value problems. Ideas to improve the numerical convergence are investigated. One idea involves using multiple poles of expansion; this is demonstrated by a torsion problem. Sources of round-off error are identified and means of minimizing it are described, along with examples. The concept of multiple poles is extended further to the use of a large number of origins located along the boundary itself. Singularity functions referred to these origins are used to represent concentrated forces and moments. Used in conjunction with point matching, a method results which is an approximation to the solution of singular integral equations, and yields excellent results for intricate shapes. Suitable equations are formulated for representing the boundary conditions by step function or polygonal function approximation for several classes of problems, including: conductive heat transfer, torsion, plate bending, and plane elasticity with mixed boundary conditions. Numerous numerical examples are presented which demonstrate the technique and convergence for these classes of problems.
 20. Lu, Z. A., J. Fenzien, and E. P. Popov, "Finite Element Solution for Thin Shells of Revolution," NASA CR-37, 76 pp., July 1964. (Prepared under Grant no. NSG-274-63 by Univ. of Calif., Berkeley, Calif.) Thin shells of revolution are widely used in flight structures and their analysis is of great importance to the design engineer. In such shells for symmetrical loadings and small displacements, the membrane stresses and the corresponding elastic displacements can be readily computed. However, due to the variations in thickness, ring-like reinforcements at openings and junctures with the adjoining shells and/or structures, very important bending stresses develop. The analysis of such stresses may be very complex. In fact, solutions are available only for the few simplest possible shapes of the meridian. Also very few solutions exist for the cases of variable thickness and, in some of the solutions which are available, the thickness variation is prescribed for reasons of mathematical expediency. On the other hand, functional and manufacturing requirements often demand arbitrary shape and thickness variation of the shell of revolution. To achieve a practical solution for such a general problem is the primary purpose of this investigation.
 21. "Matrix Methods in Structural Mechanics," (proceedings of the conference held at Wright-Patterson Air Force Base, Ohio, 26 to 28 October 1965), AFFDL-TR-66-80. The Conference on Matrix Methods in Structural Mechanics held at Wright-Patterson Air Force Base on 26 to 28 October 1965 was sponsored jointly by the Air Force Flight Dynamics Laboratory, Research and Technology Division, Air Force Systems Command, and the Air Force Institute of Technology, Air University. The purpose of the conference was to discuss the recent developments in the field of matrix methods of structural analysis and design of aerospace vehicles.
- The 36 papers presented were arranged into 6 sessions under 5 different themes: General Matrix Methods, Finite Element Properties, Nonlinear Effects, Dynamics, and Applications. The papers cover practically all major aspects of recent research and development work in the field of matrix methods of structural analysis and design.
22. Melosh, R. J., "Basis for Derivation of Matrices for the Direct Stiffness Method," AIAA Journal, Vol 1, No. 7, July 1963, p 1631-1637. Previous developments in the direct stiffness method are reviewed. The advantages of extending the definitions to make the method a variational approach are cited. The finite element formulation of the method of minimum potential energy is given. Explicit requirements of potential energy displacements are presented, and a criterion insuring monotonic convergence is developed. Illustrative displacements yielding matrices resulting in monotonic convergence are included. Available matrices are reviewed with respect to the extended developments.
 23. Melosh, R. J. and R. G. Merritt, "Evaluation of Spar Matrices for Stiffness Analyses," Journal of the Aero/Space Sciences, Vol 25, No. 9, Sept 1958, p 537-543. Convergence difficulties have been encountered in the deflection analysis of certain structures with most of the bending material in the skin using the stiffness method. The difficulties are attributed to the use of the elementary beam spar matrix. Two new spar matrices are developed and compared with the matrix based on elementary beam concepts. The error, as a function of the nodal breakdown and the structural parameters, is determined for a beam analyzed using the spar matrix for the web and stringer matrices for the flanges.

Convergence to the final stiffness coefficients is shown to be much more rapid using either of the new matrices for structures with most of the bending material in the skin.

An unswept box beam is analyzed to demonstrate convergence of the stiffness solutions and the superiority of the new moment-shear spar matrix in an actual problem characteristic of a wing. The stiffness method results are shown to converge to analytical results obtained with elementary bending theory including transverse shear deformation and shear lag corrections.

24. Percy, J. H., T. M. H. Pian, S. Klein, and D. R. Navaratna, "Application of Matrix Displacement Method to Linear Elastic Analysis of Shells of Revolution," *AIAA Journal*, Vol 3, No. 11, Nov 1965, p 2138-2145. The paper describes the application of the matrix displacement method to the linear elastic analysis of shells of revolution. The shell is idealized as a series of conical frusta, joined at nodal circles. In the present paper the use of the idealization to handle asymmetric deformations is demonstrated. Also shown is how approximations to the mass and stiffness matrices may be consistently derived; these may then be used to solve both static and dynamic problems. The effect on the results of static analyses of improving the approximation to the stiffness matrix, using the procedure suggested by Pian, is demonstrated and discussed. Results are presented of static analyses of several shell configurations, and these are compared with solutions by other methods. It is found that the method provides accurate solutions for shells of revolution under both axisymmetric and asymmetric loadings by using a reasonable number of elements.
25. Tuma, J. J., K. S. Havner, and S. E. French Jr., "Analysis of Flat Plates by Algebraic Carry-Over Method," *Oklahoma State Univ Eng Experiment Station, Publication 118*, Dec 1960, 230 p. Lagrange's 4th order partial differential equation of thin plate is replaced by 2nd order equations in terms of loads, moments and deflections; these equations together with boundary conditions are expressed by 2 sets of finite difference equations in algebraic form; numerical evaluation of these algebraic results is made by means of electronic computer; tables; references.
26. Turner, M. J., R. W. Clough, M. C. Martin, and L. J. Topp, "Stiffness and Deflection Analysis of Complex Structures," *Journal of the Aeronautical Sciences*, Vol 25, No. 9, Sept 1956, p 805-823. A method is developed for calculating stiffness influence coefficients of complex shell-type structures. The object is to provide a method that will yield structural data of sufficient accuracy to be adequate for subsequent dynamic and aeroelastic analyses. Stiffness of the complete structure is obtained by summing stiffnesses of individual units. Stiffnesses of typical structural components are derived in the paper. Basic conditions of continuity and equilibrium are established at selected points (nodes) in the structure. Increasing the number of nodes increases the accuracy of results. Any physically possible support conditions can be taken into account. Details in setting up the analysis can be performed by nonengineering trained personnel; calculations are conveniently carried out on automatic digital computing equipment. Method is illustrated by application to a simple truss, a flat plate, and a box beam. Due to shear lag and spar web deflection, the box beam has a 25 percent greater deflection than predicted from beam theory. It is shown that the proposed method correctly accounts for these effects. Considerable extension of the material presented in the paper is possible.
27. Turner, M. J., E. W. Dill, M. C. Martin, and R. J. Melosh, "Large Deflections of Structures Subjected to Heating and External Loads," *Journal of Aero/Space Sciences*, Feb 1960, p 97-106. The method of direct formulation of the stiffness matrix is extended to include the effects of nonuniform heating and large deflections. The purpose is to develop an analytical tool for the treatment of actual structures. In the solution of aeroelastic problems the relations between forces and deflections must be determined. The use of stiffness matrix formulation of this relationship is limited to small temperature changes and small deflections. For large temperature changes additional terms are required. Also the problem becomes geometrically nonlinear when large deflections are involved. To overcome the inherent difficulties of the nonlinear problem for practical structures either an iterative or a step-by-step procedure must be used. The force-deformation relations necessary for this step-by-step or iterative approach are derived for an axially loaded member and for a plate element including the effects of thermal strains.
28. Utku, S., "Stiffness Matrices for Thin Triangular Elements of Nonzero Gaussian Curvature," *AIAA Journal*, Vol 5, No. 9, Sept 1967, p 1659-1667. Flat triangular elements, when used to approximate shells, may cause geometrical idealization errors in addition to the errors associated with assumptions on deflection distributions. Taking into account average curvatures of the middle surface, these idealization errors may be reduced without additional grid refinement. The curved triangular elements are defined by joining the selected nodes with the geodesic lines of the middle surface. In computer applications, the average values of normal curvatures of a curved triangular element may be either input or computed from the cartesian coordinates of elemental nodes. A piecewise linear deflection field is assumed. The nodal values of this field are the undetermined parameters of the problem which yield a minimizing sequence

with grid refinement. Using the shallow shell theory, strains may be expressed in the natural coordinate system of the base triangle. Expressing the strain energy of the curved triangle in terms of its nodal deflections, the elemental stiffness matrix is obtained by the usual minimization process coupled with the condition that no nodal forces result from rigid body modes. By setting the average curvatures equal to zero, the stiffness matrix of a flat triangular element is obtained.

29. Utku, S., and R. J. Melosh, "Behavior of Triangular Shell Element Stiffness Matrices Associated with Polyhedral Deflection Distributions," *NASA Technical Report 32-1217*, 13 February 1968. Invariants of the triangular shell element stiffness matrices are examined. The stiffness matrix is considered as the sum of membrane, bending, and transverse shear stiffness matrices representing respective strain energies. For various geometries and curvatures, eigenvalues of these matrices are obtained numerically. By studying the eigenvalues, it is shown that stiffness matrices produced with the help of equilibrium requirements may display nonpositive behavior depending upon element geometry. The grave consequences of nonpositive behavior are demonstrated. Since equilibrium algorithms can be used to accelerate the convergence, two schemes are developed to correct the nonpositive behavior. These schemes are based on the observation that nonpositive behavior originates from the base matrix to which equilibrium algorithm is applied. The effect of thickness/area ratio on the overall behavior is studied. The behavior associated with true potential energy approach is demonstrated on several test cases. The effect of geometry is also discussed in the assembled matrix. Guidelines have been presented for the use of the triangular shell element in structural analysis.
30. Zienkiewicz, O. C. and Y. K. Cheung, "The Finite Element Method in Structural and Continuum Mechanics," McGraw-Hill, 1967. The powerful method of "finite elements" permits almost all problems of structural stress analysis, or the analysis of such field problems as heat transfer and fluid flow, to be presented in a mathematical form suitable for solution on a digital computer. This is indispensable if complex structures are to be economically designed, not only to serve the advanced needs of aeronautics, space flight, turbine design, and nuclear technology, but also for use in such general engineering fields as dam and bridge building. "The Finite Element Method in Structural and Continuum Mechanics" is the first comprehensive textbook on a subject that until now has been presented mainly in specialist papers. Although it begins with first principles and is a relatively simple treatment of a wide subject, the book takes the reader up to the frontiers of present-day research. It also includes many examples of solutions to practical problems, such as those relating to the design of dams, nuclear reactors, and turbines, as well as those concerned with rock mechanics and seepage in civil engineering projects. A final chapter gives details of typical computer programs written in FORTRAN language with comments on data preparation and digital solutions.
- c. Experimental Methods
1. Isler, H., "Experimental Shell Design," *Proceedings of the Symposium on Shell Research*, New York, John Wiley & Sons, Inc., 1962, p 356-358. Experimental methods are described, helping to solve shell problems at different levels: to find new shapes; to visualize design; to elaborate accurate shape; to determine stresses and deflections; to analyze stability; to check built shells. Applications in prestressed concrete and reinforced plastics are shown.
2. Rowe, R. E., "Tests on Four Types of Hyperbolic Shell," *Proceedings of the Symposium on Shell Research*, New York, John Wiley & Sons, Inc., 1962, p 16-35. Tests are described and principal results are reported. One test was performed on a 1/10 scale model of one quarter of a square shell roof, with edge beams, made of reinforced cement mortar. Another test was on a similar model without edge beams. The third model was a square mushroom roof on a central column made of reinforced mortar to 1/6 scale. The fourth model was a grillage of Perspex plastic beams welded with chloroform, simulating to 1/32 scale the construction of part of a composite hyper roof from precast concrete units. In these tests bending stresses were shown to have the same order of magnitude as membrane stresses.
3. VANE VIBRATIONS (VIBRATIONS OF CURVED PLATES)
- a. Exact Solutions
1. Cummings, B. E., "Large Amplitude Vibration and Response of Curved Panels," *AIAA Journal*, Vol 2, 4, p. 709-716, Apr 1964. The dynamic nonlinear shallow-shell equations are examined in the special case of a cylindrical shell segment. Different developments are given for two systems: in system A, the stress boundary conditions are satisfied exactly, and compatibility is satisfied on the average; in system B, compatibility is satisfied exactly, and the stress boundary conditions are satisfied on the average. Perturbation and exact integral expressions are found for the frequencies of vibration. The response to delta-function, step-function, and harmonic-function loading is examined. Dynamic buckling is predicted by shock response method.
2. Galletly, G. B., "On The In-Vacuo Vibrations of Simply Supported, Ring-Stiffened Cylindrical Shells," *Proceedings of the Second U. S. National Congress of Applied Mechanics* (1954), p 225-231. An analytical solution is presented for the problem of determining the in-vacuo frequencies of vibration of a simply supported thin cylindrical shell

which is reinforced by equally spaced, equal strength circular ring stiffeners. The displacement configuration assumed permits inter-ring deformation of the shell. Numerical calculations were made for a cylindrical shell with various sizes of stiffening rings, and curves were plotted which show the effect of the rings upon the frequency of vibration. The numerical values obtained were also compared with those calculated by approximate methods and were found to agree within ± 10 percent.

3. Guyan, R. J., "Reduction of Stiffness and Mass Matrices," AIAAJ, Volume 3, No. 2, p 380, February 1965. This paper discusses a matrix condensation technique by which the order of stiffness and mass matrices can be reduced. Reduction is accomplished by eliminating coordinates at which a zero force is applied. The reduced matrices retain the structural and mass properties of the original matrices in a complex form. This will be useful in the inducer vibration program by reducing the number of degrees of freedom per free node to one. In this manner, an existing FRDC eigenvalue or latent root program that is limited to 50 degrees of freedom will allow an inducer with a maximum of 50 free nodes to be analyzed.
 4. Kalnins, A., "Free Vibration of Rotationally Symmetric Shells," Journal of the Acoustical Society of America, Vol 36, No. 7, July 1964. This paper is concerned with a theoretical investigation of the free vibration of arbitrary shells of revolution by means of the classical bending theory of shells. A method is developed that is applicable to rotationally symmetric shells with meridional variations (including discontinuities) in Young's modulus, Poisson's ratio, radii of curvature, and thickness. By means of the method of this paper, the natural frequencies and the corresponding mode shapes of axisymmetric or nonsymmetric free vibration of rotationally symmetric shells can be obtained without a limitation on the length of the meridian of the shell. To illustrate the application of the method given in this paper to particular shells, some results of free vibration of spherical and conical shells obtained earlier by means of the bending theory are reproduced by the general method of this paper, and a detailed comparison is made. In addition, paraboloidal shells and a sphere-cone shell combination are considered, which have been previously analyzed by means of the inextensional theory of shells, and natural frequencies and mode shapes predicted by the bending theory are given.
 5. Kalnins, A., "Free Nonsymmetric Vibrations of Shallow Spherical Shells," Proceedings of the Fourth U.S. Congress of Applied Mechanics, Vol I, p 225-233, 1962. This paper is concerned with the investigation of the natural frequencies and mode shapes of free vibrations of shallow spherical shells with the use of the classical theory of shallow shells. Explicit solutions for the three displacement components of the middle surface are derived in terms of Bessel functions, and the frequency equation for a shallow spherical cap with a clamped edge is deduced. All natural frequencies within a certain frequency band are determined for various values of the circumferential wave number, curvature, and thickness of the shell. The mode shapes of the first six modes are calculated and their character is examined. It is found that the modes are such that either the longitudinal or the transverse displacement is predominant. The corresponding frequency equation given by the theory of transverse vibration is deduced and by comparing its frequencies to those of the classical theory the modes not predicted by the theory of transverse vibrations are determined.
 6. Palmer, F. J., "Natural Frequency of Vibration of Curved Rectangular Plates," Aeronautical Quarterly v 5 pt 2 July 1954 p 101-10. Vibration evaluated for fundamental extensional mode, thought to be applicable when plates are excited by uniformly distributed pressure as may occur with dynamic pressure wave; natural frequencies corresponding to this mode increase fairly rapidly with curvature of plate.
- b. Approximate Methods
1. Dawe, D. J., "A Finite Element Approach to Plate Vibration Problems," J. Mech. Engng. Sci. 7, 1, 28-32, Mar. 1965. Energy considerations are used to derive stiffness and inertia matrices for a rectangular isotropic plate element of uniform thickness. The deflected form of each element is assumed to contain terms proportional to $1, x, y, x^2, xy, y^2, x^3, x^2y, y^3, x^2y, xy^2$, and the twelve associated unknowns are determined from continuity of $v, \partial v/\partial x, \partial v/\partial y$ at the corner points. (See also Zienkiewicz and Cheung, *ASME* 88 (1965), Rev. 131). The matrices are used to find the natural frequencies of certain square plates, and comparisons with other solutions show that the method gives good results even for relatively few elements.
 2. Desk, A.L. and T.H.H. Pien, "Application of Smooth-Surface Interpolation to the Finite Element Analysis," AIAA Journal, Vol 5, No. 1, p 187-189, Jan 1967. Compatibility of the slopes along the normal of the inter-element boundaries of finite rectangular elements in bending is achieved by the use of special polynomial functions. Stiffness and mass matrices based upon these functions have been used to make static and dynamic analyses of rectangular plates. This method yields a considerable improvement in numerical solutions of displacements in numerical solutions of displacements and frequencies as obtained without the use of the interpolation functions.
 3. Laurson, M. I., R. P. Shubinski, and R. W. Clough, "Dynamic Matrix Analysis of Framed Structures," Proceedings of the Fourth U.S. Congress of Applied Mechanics, Vol I, 1962, p 99-105. The matrix methods developed in recent years for static analysis of structures can be used effectively to determine the natural frequencies of these structures. This can be accomplished by developing a dynamic stiffness matrix for the individual members and subsequently obtaining a dynamic stiffness matrix for the entire structure. Substitution of this matrix into the appropriate equilibrium expression results in an expression for the natural frequencies of the structure. Application of this technique is demonstrated here with several different examples. The results may be considered exact in the sense that the mass of all members is assumed to be distributed and the stiffness of all members is assumed to be finite.
 4. Leckie, F. A., "Application of Transfer Matrices to Plate Vibrations," Ingenieur-Archiv v 32 n 2 1963 p 100-11. Successful application of transfer matrices to computation of natural frequencies and normal modes of elastic systems described by single space variable suggested extension to include systems described by 2 space variables such as plates when, instead of plate, model suggested by A. Frey was used, problem could be reduced to one with finite degrees of freedom.
 5. "Matrix Methods in Structural Mechanics," (proceedings of the conference held at Wright-Patterson Air Force Base, Ohio, 26 to 28 October 1965), AFFDL-TR-66-80. The Conference on Matrix Methods in Structural Mechanics held at Wright-Patterson Air Force Base on 26 to 28 October 1965 was sponsored jointly by the Air Force Flight Dynamics Laboratory, Research and Technology Division, Air Force Systems Command, and the Air Force Institute of Technology, Air University. The purpose of the conference was to discuss the recent developments in the field of matrix methods of structural analysis and design of aerospace vehicles. The 36 papers presented were arranged into 6 sessions under 5 different themes: General Matrix Methods, Finite Element Properties, Nonlinear Effects, Dynamics, and Applications. The papers cover practically all major aspects of recent research and development work in the field of matrix methods of structural analysis and design.
 6. McGrattan, R. J., and E. L. North, "Vibration Analysis of Shells Using Discrete Mass Techniques," Transactions of ASME, November 1967, p 766-772. A method for analyzing thin shells by a discrete mass technique is presented. The shells and stiffeners are idealized as a system of lumped masses and an elastic framework having the equivalent mass and stiffness of the actual shell. This method is most useful for shells without rotational symmetry, since classical solutions are not available for these cases. Four examples are presented and a comparison with experimental results and classical theory is made for a case of a symmetrically stiffened cylinder.
 7. Navaratna, D. R., "Natural Vibrations of Deep Spherical Shells," AIAA Journal, Vol 4, No 11, p 2056-2058, Nov 1966. The author represents a shell of revolution by a series of discrete frustra of shells which satisfy the displacement and slope continuity at the common nodal circles. Stiffness and mass matrices are determined and the matrix frequency equation is solved for the natural frequencies and the generalized displacements. Calculations for spherical shells with free, hinged, and clamped edges agree satisfactorily with those obtained by other methods.
 8. Nowinski, J. L., "Large-Amplitude Oscillations of Oblique Panels with an Initial Curvature," AIAA J. 2, 6, 1025-1031, June 1964. Von Karman field equations for flexible oblique plates with an initial curvature are extended to a dynamical case. Using series representation of initial and additional deflections and Galerkin's procedure, the governing equation for an admissible mode time function is established. Using this single assumed modal deflection, and assuming built-in edge free to move in the inplane directions, the following particular cases are discussed: buckling of an oblique plate under uniaxial compressive load, free linear vibrations of a square plate, large deflections of a uniformly loaded square plate, snap-through phenomena of a curved oblique plate under uniform transverse load, and free nonlinear vibrations. A numerical example concerning a rhombic plate is discussed in more detail. The well-known fact of a decrease of the period of nonlinear vibrations with an increasing amplitude is corroborated, this relation being less pronounced for larger sweep angles.
 9. Patyt, Maurice, "Finite Element Vibration Analysis of Cracked Plates in Tension," Technical Report AFML-TR-67-396, January 1968. A finite element method of analysis is developed to determine the vibration characteristics of an aircraft fuselage panel containing a fatigue crack. Experimental observations show that as the length of the crack increases, the frequency of vibration reaches a minimum when the free edge of the crack buckles. The variation in this phenomena with increasing plate width is studied both experimentally and theoretically. The analysis is developed in a systematic manner and calculations are performed at each stage on problems with known solutions to determine the accuracy of the method. The problems considered include the vibrations of flat plates of varying planform, the vibrations of a cylindrical shell, the buckling of a rectangular plate, and the vibrations of a rectangular plate in compression. The method is finally applied to the problem of a cracked plate in tension and the results compared with experimental

measurements. The post buckling behavior is calculated using a step-by-step analysis to permit linearization of the governing equations. By considering the calculated stress distributions, the variation in buckling stress with crack length and plate width is explained.

10. Plass, M. J. Jr., J. M. Gaines, and C. D. Newson, "Application of Reissner's Variational Principle to Cantilever Plate Deflection and Vibration Problems," *Journal of Applied Mechanics*, March 1962, p 127-135. A variational principle due to K. Reissner has been rewritten in a form which is applicable to small deflection problems for thin plates. The modified principle is used to obtain approximations to static deflection and vibration problems of square and skew cantilever plates of uniform thickness.
11. Ross, E. W., Jr. and W. T. Matthews, "Frequencies and Mode Shapes for Axisymmetric Vibration of Shells," *Transactions of ASME, Vol 89, Series E, No. 1, Journal of Applied Mechanics*, March 1967, p 73-86. This paper treats the axisymmetric vibration of thin elastic shells. Estimates of natural frequencies and modes are obtained for a general class of domes by applying the approximations obtained in a previous paper by one of the authors. Numerical results are obtained for ellipsoidal shells, and one new theoretical result is found.
12. Witmer, E. A., H. A. Balmer, J. W. Leech, and T. M. H. Pien, "Large Dynamic Deformations of Beams, Rings, Plates, and Shells," *AIAA J. 1, 8, 1848-1857, Aug. 1963*. Authors develop a finite difference lumped-stringer type of formulation for the dynamic response of simple two-dimensional and axisymmetric structures subjected to impulse loadings which deform the structures into the plastic region. The method considers elastic strain-hardening behavior, strain rate and large deflections.
The resulting numerical solutions for particular cases are compared with limited experimental data - particularly some recent beam tests at Picatinny Arsenal. A comparison between authors' theory and experiment shows generally good agreement although there are some unexplained differences between predicted and observed time histories.
A major difficulty in applying their method is, as the authors note, the large number of difference equations which requires considerable computer time. Simpler, less time-consuming methods are desirable.
13. Zienkiewicz, O. C., and Y. K. Cheung, "The Finite Element Method in Structural and Continuum Mechanics," McGraw-Hill, 1967. The powerful method of "finite elements" permits almost all problems of structural stress analysis, or the analysis of such field problems as heat transfer and fluid flow, to be presented in a mathematical form suitable for solution on a digital computer. This is indispensable if complex structures are to be economically designed, not only to serve the advanced needs of aeronautics, space flight, turbine design, and nuclear technology, but also for use in such general engineering fields as dam and bridge building.
"The Finite Element Method in Structural and Continuum Mechanics" is the first comprehensive textbook on a subject that until now has been presented mainly in specialist papers. Although it begins with first principles and is a relatively simple treatment of a wide subject, the book takes the reader up to the frontiers of present-day research. It also includes many examples of solutions to practical problems, such as those relating to the design of dams, nuclear reactors, and turbines, as well as those concerned with rock mechanics and seepage in civil engineering projects. A final chapter gives details of typical computer programs written in FORTRAN language with comments on data preparation and digital solutions.

c. Experimental Methods

1. Hoppmann, W. H., II, and C. H. Baronet, "A Study of the Vibrations of Shallow Spherical Shells," *Trans. ASME 30 E (J. Appl. Mech.) 3, 329-334, Sept. 1963*. Paper is sequel to papers by senior author alone or with collaborators (see, for example, *ASME 15 (1962), Revs. 1370, 2026*) on vibration of spherical caps. Additional experimental results are presented and compared with results of theory previously presented for symmetrical vibration. New data are given for shells which have 12-inch chord; 0.5 and 1.6-inch rise; thicknesses of 1/16, 1/8, and 1/4 inch; and both clamped and hinged edges. Agreement is moderately good. Experimental results are also presented for asymmetrical vibration. As authors point out, it is interesting to note that frequencies for clamped and for momentless cases do not differ greatly. Appendix presents formulas for symmetrical vibration but no basic theory; the reader is referred to previous paper for the complete analytical treatment.

APPENDIX B
RESUMES OF SOURCE MATERIAL

1. HYDRODYNAMIC LOADING OF INDUCER BLADES

The following are resumes of those articles included in the Literature Survey (Appendix A) from which prediction methods were selected for use in formulating analytical models.

a. Exact Methods: Noncavitating

1. Durand, W. F., Aerodynamic Theory, Vol II (General Aerodynamic Theory - Perfect Fluids by Th. von Karman and J. M. Burgers), First Edition, 1963; "Flow Through a Lattice Composed of Airfoils," p 91-96.

An exact two-dimensional solution to the basic potential flow operations is presented for both staggered and unstaggered flat plate cascades. The solution to these potential flow equations employs the techniques of conformal mapping. A general form of the Joukowski transformation is used to map from the potential flow about a circle in one plane into the flow around a cascade of airfoils (staggered or unstaggered) in the real plane. This method considers ideal or no-loss flow only, while giving a solution to the flow field in two dimensions. Cavitation is not considered. This method of analysis, however, does allow determination of incidence effects on loading around the blade leading edge.

2. Fanti, R., "Elementary Incompressible Solution for the Performance of Airfoils of Arbitrary Shape in an Arbitrary Cascade," United Aircraft Corporation Research Department, Report R-23010-12, 23 February 1953.

An exact two-dimensional potential flow solution is presented for the case of incompressible flow through airfoils of arbitrary shape in an arbitrary cascade. This work is an expansion on the theory presented in Durand (Reference 1) by von Karman and Burgers. Sources and sinks are applied along the surfaces of the flat plate airfoils to simulate the effects of airfoil thickness and shape on the potential flow field. This method of flow analysis is completely theoretical and does not allow for internal flow losses but does accurately describe the deviations between the streamlines and the blade surface in the region of the airfoil leading edge. Cavitation is not considered, restricting use of the solutions presented to single-phase flow.

b. Exact Methods: Cavitating

1. Stripling, L. B. and A. J. Costa, "Cavitation in Turbo-pumps," Parts I and II, ASME Papers No. 61-WA-112 and 61-WA-98, 25 July 1961.

An exact two-dimensional solution to the potential flow equations for the case of supercavitating flow is presented in Part I. The method of solution employs conformal mapping techniques similar to those used in the articles presented by Durand and Fanti for noncavitating flow. Part II illustrates the cavitation performance data of several helical inducers for various flow coefficients correlated with the theory from Part I. With the use of semi-empirical correlating factors, the streamline theory presented in Part I is said to serve as a useful basis for design.

Basic assumptions made in the streamline model are listed below:

- A distinct vapor cavity is formed by a free streamline which is attached to the leading edge of all blades
- Flow is two-dimensional, irrotational, inviscid and nonoscillatory
- Cavity is infinite in length.

These assumptions result in measurable deviations from the actual flow case. In particular, the combination of radius changes and rotation of the inducer would result in significant blade loadings due to Coriolis effects, which are not accounted for in the two-dimensional analysis. Other important real effects include flow losses due to friction, leakage and diffusion and three-dimensional cavities that collapse within the inducer. This method is also restricted to flow through cascades composed of parallel flat plate airfoils. Although this type analysis would not result in satisfactory determination of the flow field within cambered inducer passages, the exact theory could be used to indicate flow incidence effects on and near the airfoil leading edge, including the effects of cavitation.

2. Jakobson, J. K., "Supercavitating Cascade Flow Analysis," ASME Paper No. 64-FE-11, 27 February 1964.

Exact two-dimensional potential flow theory is presented for incompressible flow through a cascade of arbitrarily shaped airfoils, including the effects of cavitation. The assumptions that are made are essentially the same as those made by Stripling and Acosta. Flow is two-dimensional, irrotational, inviscid, and nonoscillatory. Cavity representation is made by a distinct (vapor) cavity of infinite length. This latter assumption again allows an exact mathematical solution of the potential flow equations for special cases using the techniques of conformal mapping. The general theory for flow through any cascade composed of blades of arbitrary

shapes results in an integral equation that cannot be solved directly and must rely on numerical integration techniques for its solution. It is indicated that a numerical integration of resulting integrals for cambered blades could be complex, requiring experimentation to develop computer programs that would be convergent and efficient. Although this paper covers the theory for the most general type of two-dimensional, ideal (steady, irrotational, lossless), potential flow, that of cavitating flow in a cascade of arbitrary shaped airfoils, the complexity of the resulting exact solutions may be unattractive for use in this program.

c. Numerical or Approximate Methods

1. Cooper, P. and H. B. Bosch, "Three Dimensional Analysis of Inducer Fluid Flow," NASA CR-54836, 11 February 1966.

Solutions for the three-dimensional and quasi-three-dimensional potential flow fields are presented. The three-dimensional analysis, referred to as the "exact" analysis, results from a finite difference representation of the basic potential flow equations. The quasi-three-dimensional analysis, referred to as the "approximate" method, results from a finite difference solution of the basic flow equations in the hub-to-shroud direction with a superimposed assumed solution in the blade-to-blade direction.

Use of these basic flow equations and their finite difference solution in defining three-dimensional flow fields is similar to methods which have been employed at FRDC as well as by others. Reference is made to Stanitz (Reference 5) and Stockman (Reference 6) in the literature survey. Both employed types of quasi-three-dimensional solutions for describing flow fields. Use of the method presented in this report is unique, however, in its treatment of cavitating flow.

Both methods of analysis presented in this report account for internal flow losses due to friction and diffusion while also accounting for the effects of cavitation. The cavity model used in both models allows for cavities of finite length and consisting of a nonhomogeneous, two-phase mixture. This cavity model differs significantly from the cavity model assumed by Stiippling (Reference 2) and Jakobsen (Reference 4) who assumed a distinct cavity filled with saturated vapor and infinite in length.

The "exact" method completely describes the entire potential flow field including flow losses and cavitation effects. The "approximate" method, in describing the flow field two-dimensionally in the

hub-to-shroud direction only, cannot accurately account for the effects of leading edge loading (incidence) and trailing edge unloading (deviation). Both solutions compare favorably in the interior regions of the inducer.

The "exact" method, while representing a good design system capable of solving the most general of problems, including incidence effects, flow losses, cavitation, and general blade geometry, requires considerable computing time that would, in general, prohibit its use as a practical design tool.

2. STRESSES AND VIBRATIONS IN INDUCER BLADES

1. Argyris, J. H., "Recent Advances in Matrix Methods of Structural Analysis," Progress in Aeronautical Sciences, Vol 4, 1964, The MacMillan Company, Pergamon Press.

Sections of this book outline the technique by which a curved cover can be analyzed by replacing the surface with triangular elements. The vertices of the elements are first prescribed as coordinates of a common coordinate system. A local plane coordinate system is then defined for the element and the direction cosines of the axes of this system relative to the common system are determined. These direction cosines are then used to determine the local coordinates of the nodes. The stiffness matrix, which is a function of the local coordinates, can then be computed. This matrix is then transformed to the common axes by rotating local axes to the common axes.

2. McGrattan, R. J. and E. L. North, "Vibration Analysis of Shells Using Discrete Mass Techniques," Transactions of ASME, Journal of Engineering for Industry, 767-777, November 1967.

In this paper, thin shells are idealized by a framework of elastic beams that have the equivalent mass and stiffness of the shell. The interesting part of this paper is not the part involving the equivalent shell, but the method of transforming stiffnesses and determining flexibility matrices. Because the general surface is curved, the stiffnesses of the individual beams must be transformed by rotating their coordinate system to a common coordinate system and translating from the midpoint of the element to an appropriate joint. The resulting stiffnesses are then summed. This general method can be adapted to the inducer problem by transforming the stiffness matrices of the triangular elements in the same manner.

The flexibility matrix is determined by the conventional unit load method, in which the deflection vector due to a unit load is applied at the N joints.

3. Utku, Senol, "Stiffness Matrices for Thin Triangular Elements on Analyzed Gaussian Curvature," AIAA, Vol No. 9, pp 1659-1667, September 1967.

In this paper, curved surfaces with double curvature are triangulated and referred to a base triangle whose vertices are the nodes of the curved element. Shallow shell theory is used and the strain energy of the shell is expressed in terms of nodal displacements. If zero curvature for the element is assumed the curved elements degenerate into the flat triangular base plane elements as will be done for the inducer blade. The method of partitioning the bending, membrane, and shear stiffness matrices, and the method of avoiding the difficulty due to coupling of bending moments and membrane forces is discussed. These techniques should be applicable to the inducer blade problem.

4. Turner, M. J., R. W. Clough, H. C. Martin, and L. J. Topp, "Stiffness and Deflection Analysis of Complex Structures," Journal of the Aeronautical Sciences, Vol 25, pp 805-823, September 1956.

This is one of the basic papers from which the matrix analysis of structures was developed. Direct methods for determining stiffness matrices of frame elements, shear panels, box beams, spars, rectangular plates, and triangular plates are presented. These matrices are developed by considerations of statics and avoid the use of strain energy methods. Of particular interest is the membrane stiffness matrix for arbitrarily shaped triangular plates of uniform thickness.

PRECEDING PAGE BLANK NOT FILMED.

APPENDIX C

FORMULATION OF HYDRODYNAMIC COMPUTER PROGRAM

Contained in this Appendix is the engineering formulation for the hydrodynamic computer program.

INTERNAL PROGRAM CONSTANTS

$$H_o = \frac{P_T}{\rho}$$

$$\nu = \frac{\mu}{\rho}$$

$$NPSH = \frac{P_T - P_{sat}}{\rho}$$

$$\omega = 2\pi N$$

$$Q = \frac{\dot{m}}{\rho N_i N_b}$$

$$C_1 = \frac{\rho}{2g}$$

$$C_2 = \frac{2\pi}{N_b}$$

$$C_3 = \frac{\rho \omega^2}{2g}$$

1. INLET ROUTINE

$$\Delta R = R_{t(1)} - R_{H(1)}$$

$$U_T = \omega R_T$$

$$\tau_{cav} = \frac{2gNPSH}{U_T^2}$$

$$V_m = \frac{N_b Q}{\pi \left(R_{T(1)}^2 - R_{H(1)}^2 \right)}$$

$$\phi = \frac{v}{U_T} R$$

$$v = \frac{V_m}{\sin \alpha}$$

$$V_u = V \cos \alpha$$

$$p = P_T - C_1 V^2$$

$$\psi_T = \tan^{-1} \left[\frac{R_{T(2)} - R_{T(1)}}{Z(2) - Z(1)} \right]$$

$$\psi_H = \tan^{-1} \left[\frac{R_{H(2)} - R_{H(1)}}{Z(2) - Z(1)} \right]$$

Find R for each streamline (R_{ST}) by dividing the annulus area into N_i equal areas such that ΔR^2 between streamlines equals a constant, i.e.,
 $R_{ST(i)}^2 - R_{ST(i-1)}^2 = \text{constant}$

Find $\psi_{(i)}$ for each streamline by linear interpolation versus radius.

$$R_{(i)} = \frac{R_{ST(i-1)} + R_{ST(i)}}{2.0}$$

$$\tau_{(i)} = C_2 R_{(i)}$$

$$U = \omega R_{(i)}$$

$$HI_{o(i)} = \frac{UV_u}{g}$$

$$R \tan \beta^* = R_{T(1)} \tan \beta_{T(1)}^* - \frac{R_{T(1)} - R_{(i)}}{\Delta R} \left[R_{T(1)} \tan \beta_{T(1)}^* - R_{H(1)} \tan \beta_{H(1)}^* \right]$$

$$\beta_{(i)}^* = \tan^{-1} \left[\frac{R \tan \beta^*}{R_{(i)}} \right]$$

$$\beta_{(i)} = \tan^{-1} \left[\frac{V_m}{W_u} \right]$$

$$i_{o(i)} = \beta_{(i)}^* - \beta_{(i)}$$

$$W_{(i)} = \frac{V_m}{\sin \beta_{(i)}}$$

$$Q_D = C_1 (W_{(i)})^2$$

$$P_{rel(i)} = p + Q_D$$

a. Cavity Parameters (Stripling and Acosta)

$$k = \frac{p - P_{sat}}{Q_D}$$

$$W_c = W_{(i)} \sqrt{1 + k}$$

$$A = \left[\frac{W_c}{W_{(i)}} + \frac{W_{(i)}}{W_c} \right] \cos (i_{o(i)})$$

$$B = \left[\frac{W_c}{W_{(i)}} - \frac{W_{(i)}}{W_c} \right] \sin (i_{o(i)}) \cot \beta_{(i)}$$

$$W_2 = \frac{W_c}{2.0} \left[A + B - \sqrt{(A + B)^2 - 4.0} \right]$$

$$h_{o(i)} = \tau_{(i)} \sin \beta_{(i)}^* \left(1.0 - \frac{W_{(i)} \sin \beta_{(i)}}{W_2 \sin \beta_{(i)}^*} \right)$$

$$Tl = \left(\sin \beta_{(i)}^* + \left(\frac{W_{(i)}}{W_c} \right)^2 \cos \left(\frac{\pi}{2} + i_{o(i)} - \beta_{(i)} \right) \right) \cdot \ln \left[\frac{(W_c^2 - 2.0W_{(i)} \cos (i_{o(i)}) + W_{(i)}^2)}{(W_c^2 + 2.0W_{(i)} \cos (i_{o(i)}) + W_{(i)}^2)} \right]$$

$$T2 = 2.0 \left(\sin \beta_{(i)} \right) \left(\frac{W_{(i)}}{W_2} + \frac{W_{(i)} W_2}{W_c^2} \right) \ln \left(\frac{W_c - W_2}{W_c + W_2} \right)$$

$$T3 = 2.0 \left(\cos \beta_{(i)}^* + \left(\frac{W_{(i)}}{W_c} \right)^2 \sin \left(\frac{\pi}{2.0} + i_{o(i)} - \beta_{(i)} \right) \right) \cdot \tan^{-1} \left[\frac{2.0 W_{(i)} W_c \sin (i_{o(i)})}{W_c^2 - W_{(i)}^2} \right]$$

$$C_{o(i)} = (T1 - T2 + T3) \frac{\tau_{(i)}}{2\pi} \cdot$$

$$R_{c(i)} = \left(C_{o(i)}^2 + h_{o(i)}^2 \right) / (2.0 h_{o(i)})$$

$$\delta\beta_{c(i)} = 0.5 \tan^{-1} \left[\frac{C_{o(i)}}{(R_{c(i)} - h_{o(i)})} \right]$$

2. MAIN PROGRAM

$$\Delta Z_e = Z_{N_j} - Z_{(j)}$$

$$\Delta Z = Z_{(j)} - Z_{(j-1)}$$

$$\overline{RV}_u = \sum_{i=1}^{N_i} \frac{R_{(i)} V_{u(i)}}{N_i}$$

$$\Delta R = R_{T(j)} - R_{H(j)}$$

$$W_{u_e} = \frac{\omega R_{(i)} - \overline{RV}_u}{R_{(i)}}$$

$$W_{m_e} = \frac{W_{(i)} \sin \beta_{(i)} (\tau_{(i)} - b_{(i)})}{C_2 R_{(i)}}$$

$$\beta_e = \tan^{-1} \left[\frac{W_{m_e}}{W_{u_e}} \right]$$

$$R_{ST} = R_{H(j)} + PCR_{(i)} \Delta R$$

$$R_{(i)} = \frac{R'_{ST} + R_{ST}}{2.0}$$

$$\bar{R} = \frac{R_{(i-1)} + R_{(i)}}{2.0}$$

$$R \tan \beta^* = R_{T(j)} \tan \beta_{T(j)}^* - \left(R_{T(j)} - R_{(i)} \right) \left[\frac{R_{T(j)} \tan \beta_{T(j)}^* - R_{H(j)} \tan \beta_{H(j)}^*}{\Delta R} \right]$$

$$\Delta y_{(i)} = R_{ST} - R'_{ST} \text{ (For Hub and Tip Stream Tubes - } \Delta y_{(i)} = \Delta y_{(i)} - \delta^*)$$

$$t = t_{T(j)} + \gamma \left(R_{T(j)} - R_{(i)} \right)$$

$$\beta_{(i)}^* = \tan^{-1} \left[\frac{t \tan \beta^*}{R_{(i)}} \right]$$

$$\tau_{(i)} = C_2 R_{(i)} - \frac{t + 2.0 \delta^*}{\sin \beta_{(i)}^*} \quad \delta^* = 0 \text{ 1st time through}$$

$$\psi_T = \tan^{-1} \left[\frac{R_{T(j)} - R_{T(j-1)}}{Z_{(j)} - Z_{(j-1)}} \right]$$

$$\psi_H = \tan^{-1} \left[\frac{R_{H(j)} - R_{H(j-1)}}{Z_{(j)} - Z_{(j-1)}} \right]$$

$$\bar{\psi}_{(i)} = \psi_H + (\psi_T - \psi_H) \left[\frac{R_{(i)} - R_{H(i)}}{\Delta R} \right]$$

$$\Delta m_m = \frac{\Delta Z}{\cos \bar{\psi}_{(i)}}$$

$$\Delta m_{(i)} = \frac{\Delta m_m}{\sin \beta_{(i)}^*}$$

$$m_{(i)} = m'_{(i)} + \Delta m_{(i)}$$

a. Deviation Calculations

If cavity exists:

$$\theta_{(i)} = \tan^{-1} \left(\frac{(C_{o(i)} - m_{(i)}) \tan \beta_{(i)}^* + R_{c(i)} - h_{o(i)}}{R_{c(i)} \cos \theta_{(i)}} - 1.0 \right) \cot \beta_{(i)}^*$$

Iterate on $\theta_{(i)}$ until within tolerance.

$$b \sin = R_{o(i)} (\cos \theta_{(i)} - 1.0) + h_{o(i)}$$

$$b_{(i)} = \frac{b \sin}{\sin \beta_{(i)}^*}$$

$$\delta \beta^* = 0.5 \theta_{(i)}$$

If no cavity exists:

$$\delta \beta^* = 0.0$$

$$\text{Power}_1 = \frac{m_{(i)} N_b}{R_{(i)} \sin \beta_{(i)}^*}$$

$$\delta\beta_1 = \frac{(i_{o(i)} - \delta\beta_c(i))}{\sqrt{1.0 + e^{\text{Power}_1}}}$$

$$\text{Power}_2 = \frac{N_b \Delta Z_e}{R_{(i)} \sin^2 \beta_{(i)}^*}$$

$$\delta\beta_2 = \frac{(\beta_{(i)}^* - \delta\beta^* - \beta_e)}{\sqrt{1.0 + e^{\text{Power}_2}}}$$

$$\text{Power}_3 = - \frac{\pi |m_{(i)} - 2.0 C_{o(i)}|}{\tau_{(i)} \sin \beta_{(i)}^*}$$

$$\delta\beta_3 = 0.5 \delta\beta_c e^{\text{Power}_3}$$

If $m_{(i)} > 2.0 C_{o(i)}$ then $\delta\beta_3 = - \delta\beta_3$

$$\text{Deviation} = \delta\beta_1 + \delta\beta_2 + \delta\beta_3 + \delta\beta^*$$

b. Stream Tube - Flow Calculations

$$\beta_{(i)} = \beta_{(i)}^* - \text{Deviation}$$

$$\Delta\beta = \beta_{(i)} - \beta'_{(i)}$$

$$\left(\frac{d\beta}{dm}\right)_i = \frac{\Delta\beta}{\Delta m_{(i)}}$$

$$\Delta\psi = (\bar{\psi}_{(i)} - \bar{\psi}'_{(i)}) \left(\frac{2.0 \Delta m_{(i)}}{\Delta m_{(i)} + \Delta m'_{(i)}} \right)$$

$$\left(\frac{d\psi}{dm}\right)_{(i)} = \frac{\Delta\psi}{\Delta m_{(i)}}$$

$$\psi_{(i)} = \bar{\psi}'_{(i)} + \frac{\Delta\psi}{2.0}$$

$$\tau_{\ell} = \tau_{(i)} - b_{(i)}$$

$$A = \Delta y_{(i)} \tau_{\ell} \sin \beta_{(i)} \cos \psi_{(i)}$$

$$W_{(i)} = \frac{Q}{A}$$

$$Q_D = C_1 W_{(i)}^2$$

$$\bar{W} = \frac{W'_{(i)} + W_{(i)}}{2.0}$$

$$\bar{\tau}_{\ell} = \frac{\tau_{(i)} - b_{(i)} + \tau'_{(i)} - b'_{(i)}}{2.0}$$

$$\left(\frac{dW}{dm}\right)_{(i)} = \frac{W_{(i)} - W'_{(i)}}{\Delta m_{(i)}}$$

$$\bar{Q}_D = C_1 (\bar{W})^2$$

For hub and tip stream tubes:

$$D_H = \frac{4.0 A}{\tau_{\ell} \sin \beta^*_{(i)} + 2.0 \Delta y_{(i)}}$$

For other stream tubes:

$$D_H = \frac{2.0 A}{\Delta y_{(i)}}$$

c. Pressure Loss Calculation

Call Loss Routine (Calculate K_L and δ^*)

$$\Delta P_L = K_L \bar{Q}_D$$

$$P_{rel(i)} = P'_{rel(i)} + C_3 \left((R_{(i)})^2 - (R'_{(i)})^2 \right) - \Delta P_L$$

$$P_{(i)} = P_{rel(i)} - Q_D$$

d. Radial Pressure Gradient Calculation

$$\Delta P_r = P_{(i)} - P_{(i-1)}$$

$$\Delta r = R_{(i)} - R_{(i-1)}$$

$$\bar{R} = \frac{R_{(i)} + R_{(i-1)}}{2.0}$$

$$\bar{W} = \frac{W_{(i)} + W_{(i-1)}}{2.0}$$

$$\bar{\beta} = \frac{\beta_{(i)} + \beta_{(i-1)}}{2.0}$$

$$\bar{\psi} = \frac{\psi_{(i)} + \psi_{(i-1)}}{2.0}$$

$$\bar{\frac{d\psi}{dm}} = \frac{\left(\frac{d\psi}{dm}\right)_{(i)} + \left(\frac{d\psi}{dm}\right)_{(i-1)}}{2.0}$$

$$\bar{\frac{dW}{dm}} = \frac{\left(\frac{dW}{dm}\right)_{(i)} + \left(\frac{dW}{dm}\right)_{(i-1)}}{2.0}$$

$$\bar{\frac{d\beta}{dm}} = \frac{\left(\frac{d\beta}{dm}\right)_i + \left(\frac{d\beta}{dm}\right)_{(i-1)}}{2.0}$$

$$\left(\frac{dp}{dr}\right) = \frac{\rho}{g} \left[(\bar{R}\omega - \bar{W})^2 \sin \bar{\beta} \cos \bar{\psi} \bar{\frac{d\psi}{dm}} - (\bar{W})^2 \sin \bar{\psi} \cos \bar{\beta} \bar{\frac{d\beta}{dm}} - \bar{W} \sin \bar{\psi} \sin \bar{\beta} \bar{\frac{dW}{dm}} \right]$$

$$\text{Error} = \frac{\Delta P_r}{\Delta r} - \frac{dp}{dr}$$

e. Streamline Test and Adjustment Routine

The error is determined for each streamline and compared with some tolerance. If each streamline error is within the prearranged tolerance, the program continues. If all or anyone of the streamlines is not within this tolerance, the errors of that streamline and its adjacent streamlines are used in the adjustment for locating the new streamline positions. After each streamline adjustment has been made, the program returns to the R_{ST} equation in the Main Program (paragraph 2).

f. Blade Loading Calculation

$$\Delta p_{b(i)} = 2.0 \frac{\bar{\tau}}{\bar{l}} \frac{\bar{Q}_D}{\sin \beta_{(i)}^*} \left[\left(\frac{2.0\omega}{\bar{W}} - \frac{\cos \bar{\beta}}{\bar{R}} \right) \sin \bar{\psi}_{(i)} + \frac{d\beta}{dm} - \frac{\cot \bar{\beta}}{\bar{W}} \frac{dW}{dm} \right]$$

$$p_{s(i)} = p_{(i)} - \frac{\Delta p_{b(i)}}{2.0}$$

$$p_{p(i)} = p_{s(i)} + \Delta p_{b(i)}$$

$$W_{s(i)} = W_{(i)} \sqrt{1.0 + \frac{\Delta p_{b(i)}}{2.0 \bar{Q}_D}}$$

$$W_{p(i)} = W_{(i)} \sqrt{1.0 - \frac{\Delta p_{b(i)}}{2.0 \bar{Q}_D}}$$

g. Station Performance Calculations:

$$U = \omega R_{(i)}$$

$$V_m = W_{(i)} \sin \beta_{(i)}$$

$$W_u = W_{(i)} \cos \beta_{(i)}$$

$$V_u = U - W_u$$

$$\alpha = \tan^{-1} \left[\frac{V_m}{V_u} \right]$$

$$V = \frac{V_m}{\sin \alpha}$$

$$\text{Deviation} = (\beta_{(i)}^* - \beta_{(i)})$$

$$P_T = P_{(i)} + C_1 V^2$$

$$H = \frac{P_T}{\rho} - H_o$$

$$HI_{(i)} = \frac{U V_u}{g} - HI_{o(i)}$$

$$\eta = \frac{H}{HI_{(i)}}$$

If last "J" station, continue. If not last "J" station, return to beginning of Main Program (paragraph 2).

3. EXIT ROUTINE

$$U = \omega R_{(i)}$$

$$W_u = W_{(i)} \cos \beta_{(i)}$$

$$V_u = U - W_u$$

$$V_m = \frac{W_{(i)} \sin \beta_{(i)} (\tau_{(i)} - b_{(i)})}{C_2 R_{(i)}}$$

$$\alpha = \tan^{-1} \left[\frac{V_m}{W_u} \right]$$

$$V = \frac{V_m}{\sin \alpha}$$

$$\beta_e = \tan^{-1} \left[\frac{V_m}{W_u} \right]$$

$$\text{Deviation} = (\beta_{(i)}^* - \beta_e)$$

$$W_{(i)} = V_m \sin \beta_e$$

$$P_T = P_{(i)} + C_1 V^2$$

$$H = \frac{P_T}{\rho} - H_o$$

$$HI_{(i)} = \frac{U V_u}{g} - HI_{o(i)}$$

$$\eta = \frac{H}{HI_{(i)}}$$

4. OVERALL PERFORMANCE

$$H = \frac{\sum_{i=1}^{N_i} H}{N_i}$$

$$HII = \frac{\sum_{i=1}^{N_i} HI_{(i)}}{N_i}$$

$$\eta = \frac{H}{HII}$$

$$\psi_p = \frac{gH}{\omega R_T^2(1)}$$

$$R_N = \frac{\omega R_T^2(1)}{\nu}$$

END OF PROGRAM

FLOW LOSS SUBROUTINE

$$Re_x = \frac{W(i) m(i)}{\nu}$$

$$f = 0.0576 (Re_x)^{-1/5}$$

$$\delta^* = 0.04625 m(i) (Re_x)^{-1/5}$$

$$K_F = \frac{4.0 f \Delta m(i)}{D_H}$$

$$\phi_D = 114.6 \tan^{-1} \left[\left(\frac{A}{\pi \Delta m(i)^2} \right)^{1/2} \left(1.0 - \left(\frac{W(i)}{W'(i)} \right)^{1/2} \right) \right]$$

$$\text{If } b(i) > 0.0 \text{ \& } \phi_D > 0.0 \quad f(\phi) = 1.0$$

$$\text{If } \phi_D < 0.0 \quad f(\phi) = 0.0$$

$$\text{If } 0.0 < \phi_D \leq 14.0 \quad f(\phi) = (0.74506) \times 10^{-3} \phi_D^2 + (0.79874) \times 10^{-3} \phi_D - (0.4056) \times 10^{-4}$$

$$\text{If } 14.0 < \phi_D \leq 46.0 \quad f(\phi) = 0.02577 \phi_D - 0.1855$$

$$\text{If } \phi_D > 46.0 \quad f(\phi) = 1.0$$

$$K_D = 4.0 f(\phi) \left[\frac{W'(i) - W(i)}{W'(i) + W(i)} \right]^2$$

$$K_L = K_D + K_F$$

RETURN TO PROGRAM

PRECEDING PAGE BLANK NOT FILMED.

APPENDIX D
NOMENCLATURE

A. HYDRODYNAMIC

SYMBOL	DESCRIPTION	UNITS
A	Flow area normal to direction of relative velocity	ft ²
b	Tangential vapor cavity height	ft
C	Distance from leading edge to point of maximum vapor cavity height	ft
D _H	Hydraulic diameter	ft
Deviation	Total deviation angle	deg
F	Tangential blade pressure force	lb
f	Surface friction coefficient	
H	Head rise	ft
H _o	Absolute total head at inlet	ft
h	Normal vapor cavity height	ft
h _o	Maximum normal vapor cavity height	ft
H _I	Ideal head rise	ft
H _{I_o}	Absolute ideal total head at inducer inlet	ft
i _o	Incidence angle	deg
k	Cavitation number	
m	Length along streamline	ft
ṁ	Mass flow rate	lb/sec
N _b	Number of blades	
N	Inducer rotative speed	rev/sec
NPSH	Net positive suction head	ft
P _T	Total pressure	lb/ft ²
P	Static pressure	lb/ft ²
ΔP _b	Blade pressure loading	lb/ft ²
ΔP _L	Pressure loss along stream tube	lb/ft ²
Q	Volumetric flow rate	ft ³ /sec
Q _D	Relative dynamic head	ft
q	Relative dynamic pressure	lb/ft ²

SYMBOL	DESCRIPTION	UNITS
R	Radius	ft
Re _m	Reynolds number based on streamline path length	
R _c	Radius of circular arc approximating vapor cavity	ft
T	Torque	lb-ft
t	Blade thickness	ft
U	Inducer tangential velocity	ft/sec
V	Fluid absolute velocity	ft/sec
W	Fluid relative velocity	ft/sec
W _c	Fluid relative velocity along cavity surface	ft/sec
W.P.	Perimeter of wetted surface	ft
Δy	Radial distance between streamlines	ft
z	Axial dimension	ft
Δze	Axial distance from station to exit	ft
α	Angle between fluid absolute velocity and tangential direction	deg
β	Angle between fluid relative velocity and tangential direction	deg
β*	Angle between blade and tangential direction	deg
δβ*	Deviation angle due to vapor cavity	deg
δβ _c	Initial angle of vapor cavity	deg
δβ ₁	Deviation angle due to inlet incidence	deg
δβ ₂	Deviation angle due to vapor cavity and exit deviation	deg
δβ ₃	Deviation angle due to initial cavity shape	deg
γ	Blade taper angle	deg
δ*	Boundary layer displacement thickness	ft
η	Efficiency	
λ _L	Lean angle of blade generatrix	deg
μ	Absolute viscosity	lb/sec-ft
ν	Kinematic viscosity	ft ² /sec
ρ	Density	lb/ft ³

SYMBOL	DESCRIPTION	UNITS
τ	Blade tangential spacing	ft
τ_{cav}	Cavitation parameter	
τ_l	Tangential space between blades occupied by fluid	ft
τ_n	Blade spacing measured normal to blades	ft
ϕ	Flow coefficient	
ϕ_{eq}	Local equivalent diffusion angle	deg
ψ	Angle between relative velocity and axial direction or head rise coefficient	deg
ω	Inducer angular velocity	rad/sec

Superscripts

'	Previous value
-	Average value between axial stations
=	Average value between stream tubes

Subscripts

e	Exit
H	Hub
i	Streamline number, 1, 2, 3 ----
j	Axial station number, 1, 2, 3 ----
m	Along streamline
p	Pressure surface
rel	Relative
s	Suction surface
ST	Streamline
T	Tip
u	Tangential

B. STRESS AND VIBRATION

SYMBOL	DESCRIPTION	UNITS
$[A], [B], [C], [D], [E]$	Partitioned matrices of $[K]_T$	lb/in., lb-in./rad
$[\bar{A}]$	Displacement function coordinate matrix	Mixed
$[\bar{A}_T]$	Thickness function coordinate matrix	Mixed

SYMBOL	DESCRIPTION	UNITS
\bar{C}	Curvature matrix	rad/in.
\bar{D}	Flexual rigidity $\frac{Et^3}{12(1-\nu^2)}$	lb-in.
E	Modulus of elasticity	lb/in. ²
\bar{E}_B	Curvature coordinate matrix	Mixed
\bar{E}_M	Membrane elastic constants matrix	lb/in. ²
F_x, F_y, F_z	Force in coordinate direction	lb
$\{F\}_N$	Generalized nodal force column matrix $\{F_x, F_y, F_z, M_x, M_y, M_z\}^T$	lb, lb-in.
$[I]$	Unit diagonal matrix	
$[K]$	Stiffness matrix	lb/in., lb-in./rad
$[K]_T^*$	Reduced stiffness system matrix $[T]^T [K]_T [T]$	lb/in., lb-in./rad
M_x, M_y, M_z	Moment about coordinate axis	lb-in.
$[M]$	Inertia matrix	lb-sec ² /in., lb-sec ² -in.
$[M]_T^*$	Reduced inertia system matrix $[T]^T [M]_T [T]$	lb-sec ² /in., lb-sec ² -in.
p	Pressure, + ve in + ve direction of \bar{z}	lb/in. ²
$\{q\}$	Generalized vibratory amplitude	in., rad
R	Radius measured in x, y plane	in.
R*	Radius measured along generator	in.
R _G	Generator offset radius	in.
$[R_1]$	Rotation matrix	
T	Kinetic energy	lb-in.
$[T]$	Coordinate transformation matrix $[A] - [C]^T [B]^{-1} [C]$	lb/in., lb-in./rad
\bar{t}	Thickness of triangular element	in.
$\{\bar{t}\}_N$	Nodal thickness column matrix $\{\bar{t}_1 \bar{t}_2 \bar{t}_3\}$	in.

SYMBOL	DESCRIPTION	UNITS
U	Internal strain energy	lb-in.
u, v, w	Displacement in x, y, z directions	in.
V	Potential energy	lb-in.
$\left[\bar{V}_B \right]$	Bending elastic constant matrix	
$\left[\bar{W}_M \right]$	Membrane strain coordinate matrix	
x, y, z	Rectangular coordinates	in.
z_H	Lead height of generator measured at hub radius	in.
$\left[\bar{\alpha} \right]$	Displacement function coefficient column matrix	Mixed
$\left[\bar{\alpha}_T \right]$	Thickness function coefficient column matrix	Mixed
$\left[\delta \right]$	Generalized displacement column matrix $\left[u \ v \ w \ \theta_x \ \theta_y \ \theta_z \right]^T$	in., rad
$\bar{\epsilon}_{xx}, \bar{\epsilon}_{yy}$	Strain in x and y directions	in./in.
$\bar{\epsilon}_{xy}$	Shear strain	rad
$\left[\bar{\epsilon} \right]$	Membrane strain column matrix	in./in., rad
θ	Wrap angle	deg
$\theta_x, \theta_y, \theta_z,$	Rotation about coordinate axis	rad
λ	Generator lean angle	deg
ν	Poisson's ratio	
ρ	Density	lb/in. ³
$\left[\psi \right]$	Coordinate matrix	in.
ω	Natural frequency or angular velocity	rad/sec
$\left\{ \right\}$	Column matrix	
$\left \right $	Determinant	
$\cos(x, \bar{y}),$ etc.	Cosine of angle between x axis in common and \bar{y} axis in local system	

SYMBOLS	DESCRIPTION	UNITS
Superscripts		
-	Refers to local coordinate system	
$[]^T$	Transpose of matrix $[]$	
Subscripts		
B	Bending	
c	Centrifugal	
H	Inducer hub	
i	Parameter at node "i" (1,2,3)	
M	Membrane	
T	Inducer tip	
$[]_N$	Matrix of nodal parameters	
$[]_T$	System matrix	